



DEEP SEATED MAGMATISM, Its sources and plumes

Глубинный магматизм, его источники и плюмы



**MIASS
IRKUTSK
2009**

*Russian Academy of Sciences
Vinogradov Institute of Geochemistry
Siberian Branch
Institute of Mineralogy
Uralian Branch
Russian Foundation of Basic Research*



Deep-seated magmatism, its sources and plumes

(Глубинный магматизм, его источники и плюмы)

PROCEEDING
of XI International Workshop « Deep-seated
magmatism, its sources and plumes »
Edited by Dr. N.V. Vladykin

MIASS
IRKUTSK
2009

Deep-seated magmatism, its sources and plumes

Proceedings of the XI International Conference. Publishing House of the Institute of Geography SB RAS, 2009, 192 p., ISBN 978-5-94797-130-9. Vol.4.

The workshop on 2009 was held at the Mineralogical Institute, Uralian Branch, in Miass, the invited reports of which are presented in this book.

It describes many problems of deep-seated magmatism and its relationships with plume processes. The paper provides average compositions of magmas and mantle of intra-plate oceanic and continental environs, the pattern of space distribution of "hot spots" of the mantle of the recent Earth, magmatic and geodynamic evolution of the present super-continent. It also provides the data on solubility of carbon in the main minerals of the Earth's mantle, geochemistry of potassium magmatism of the Atlantic Ocean and oceanic islands. Some issues were disclosed relative to (i) the application of single mineral thermo barometry for reconstructing the structure of mantle lithosphere, regime of volatile components in the zones of diamond formation and pre-requisites of the mantle genesis of heavy hydrocarbons in the alkaline massifs of continental plates, (ii) basic physical-chemical parameters of natural mineral-forming fluids. The composition and temperature conditions of the mantle above the Angola pipes is measured based on the study of deep-seated xenocrysts of kimberlite pipes and distribution of rare elements in them. The conclusion has been made on the contribution of plume processes in formation of kimberlites in the north of the Russian platform.

The book might present interest to specialists involved in petrological and geochemical investigations as well as those studying deep alkaline and kimberlite magmatism.

*Published following the decision of the Scientific Council
of Vinogradov Institute of Geochemistry SB RAS*

Editor: Prof. N.V. Vladykin

Reviewers: Prof. O.M. Glasunov
Original-model: M.D. Sedunova, O.V. Logvanova

*Institute of Geography SB RAS
664033, Irkutsk, Ulanbatorskaja str.
1*

Published in Glazkovskaya printing House
Irkutsk, Gogol str., 53.
Order № 2155. Edition 150 copies.

ISBN 978-5-94797-130-9

© Institute of Geochemistry SB RAS, 2009

© Irkutsk Geography SB RAS, 2009

TABLE OF CONTENTS

1. Kovalenko V. I., Yarmolyuk V. V., and Bogatikov O. A Regularities of Spatio-Temporal Distribution of Mantle Hot Spots of the Modern Earth	5
2. Anfilogov V. N. Thermal Convection and Plumes in the Crystalline Earth Mantle.	13
3. Kogarko L. N. and Asavin A. M. Oceanic Potassic Magmas: An Example of the Atlantic Ocean	20
4. Kovalenko V. I., Naumov V. B., Girnis A. V., Dorofeeva V. A., and Yarmolyuk V. V. Magmas and Mantle Sources of Mid-Ocean Ridges and Intraplate Oceanic and Continental Basalts: The Data on Melt Inclusions and Quenched Glasses of Basalts	36
5. Ryabchikov I. D. Regime of Volatile Components in the Zones of Diamond Formation	80
6. Balashov Yu. A. Evolution aspects of geochemical heterogeneity of the lithosphere	87
7. Ashchepkov I. V., Vladykin N. V., Pokhilenko N. P., Logvinova A. M., Kuliashova L. V., Malygina L. V., Alymova N. V., Mityukhin S. I., M. Kopylova. Application of geochemical data for the reconstruction of the mantle lithosphere structure	99
8. Naumov V. B., Dorofeeva V. A., and Mironova O. F. Principal Physicochemical Processes in Mantle-Forming Fluids.	118
9. Kovalenko V. I., Yarmolyuk V. V., and Bogatikov O. A. The Recent Supercontinent: Evolution of the Northern Hemisphere of the Earth (North Pangea): Magmatic and Geodynamic Evolution.	152
10. Ashchepkov I. V., Rotman A. Y., Nossyko S., Somov S. V., Shimupi J., Vladykin N. V., Saprykin A. I., Khmelnikova O. S. Composition and thermal structure of mantle beneath the Kasai craton according to xenocrysts from Angola kimberlites	159
11. Asavin A. M. Trace Elements in Plutonic Alkaline Rocks from the Oceanic Islands	182
12. Sharygin V. V. Hendricksite and Zn-containing phlogopite from peralkaline igneous rocks of the Azov Region, Ukraine.	189

FOREWORD

The fact is well accepted that alkaline rocks represent unique formations on the Earth. They have been long attractive for research because large Nb, Ta, Zr, Y, TR, Cu and P deposits, gemstones of charoite, Cr-diopside, dianite are associated with them. For instance, in Australia diamonds are recovered in lamproites. The complicated processes of their formation provoked scientific disputes still going on. The newly developed analytical methods and techniques provided abundant information on the composition of alkaline rocks. The data on geochemistry of isotopes confirm the evidence on the mantle sources of the substance of alkaline rocks. The new concepts of plume tectonics are applied by scientists when studying alkaline rocks as the deep-seated geodynamics of the Earth is interpreted based on these data.

These problems were discussed at the international workshops held in 2001 at the Institute of Geochemistry in Irkutsk; in 2002 at the Far-East Geological Institute, Vladivostok; in 2003 at the Institute of Tectonics and Geophysics in Khabarovsk, in 2004 at Geological Institute in Ulan-Ude, in 2005 at the Institute of Volcanology and Seismology in Petropavlovsk-Kamchatsky), in 2006 in TSNIGRI JC "ALROSA" in Mirny, in 2007 in Irkutsk and Naples (Italy) in 2008 at the Far-East Geological Institute, Vladivostok. The workshop on 2009 was held at the Mineralogical Institute, Uralian Branch, in Miass, the invited reports of which are presented in this book.

It describes many problems of deep-seated magmatism and its relationships with plume processes. The paper provides average compositions of magmas and mantle of intra-plate oceanic and continental environs, the pattern of space distribution of "hot spots" of the mantle of the recent Earth, magmatic and geodynamic evolution of the present super-continent. It also provides the data on solubility of carbon in the main minerals of the Earth's mantle, geochemistry of potassium magmatism of the Atlantic Ocean and oceanic islands. Some issues were disclosed relative to (i) the application of single mineral thermo barometry for reconstructing the structure of mantle lithosphere, regime of volatile components in the zones of diamond formation and pre-requisites of the mantle genesis of heavy hydrocarbons in the alkaline massifs of continental plates, (ii) basic physical-chemical parameters of natural mineral-forming fluids. The composition and temperature conditions of the mantle above the Angola pipes is measured based on the study of deep-seated xenocrysts of kimberlite pipes and distribution of rare elements in them. The conclusion has been made on the contribution of plume processes in formation of kimberlites in the north of the Russian platform.

The book might present interest to specialists involved in petrological and geochemical investigations as well as those studying deep alkaline and kimberlite magmatism.

Chairman of Organizing Committee,
Chief Editor

Dr. N.V. Vladykin

UDK 550.42

Regularities of Spatial Distribution of Mantle Hot Spots of the Modern Earth

Kovalenko V. I., Yarmolyuk V. V., Bogatikov O. A

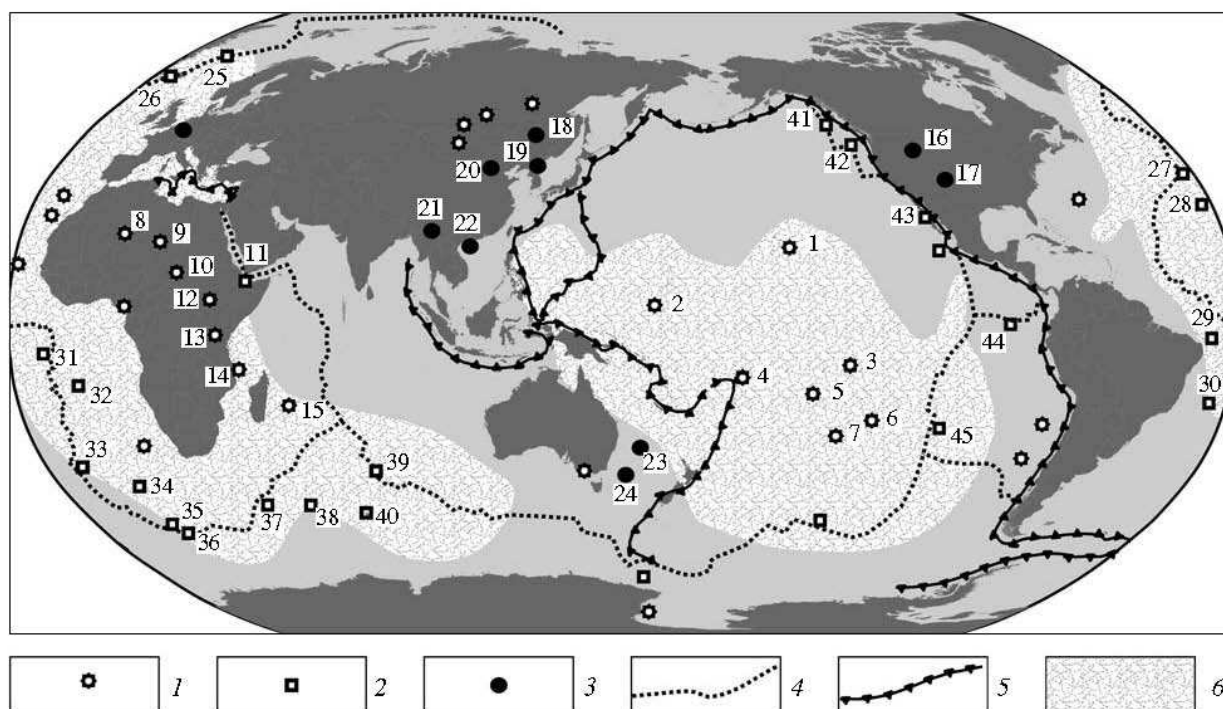
Institute of Ore Deposits, Geology, Petrography, Mineralogy, and Geochemistry, Russian Academy of Sciences, ul. Bol'shaya Gruzinskaya 10, Moscow, 123995 Russia; e-mail: yarm@igem.ru (Yarmolyuk V. V.)

The mantle hot spots of the modern Earth were first found by P. Morgan and G. Wilson as projections of the deep-earth material flows at the modern Earth's surface, uplifting under the moving lithospheric plates [1, 2]. Since that time, the study of interplate oceanic and continental magmatism and geodynamics associated with the mantle hot spots has advanced the development of this hypothesis. It has led to development of the patterns of their deep structure [3] on the one side, and, actually, negation of their deep structure, on the other side [4]. The most prominent achievement of modern geophysics and geology is the development of visual images of the mantle plumes on the basis of global and local seismic tomography. A recent review of such works is presented in [5]. The given work is devoted to discussion of a poorly studied problem, the estimation of regularities of the spatial distribution of the hot spots in the Earth and their connection with modern and ancient geodynamic processes. The number of hot spots at the Earth's surface varies according to different authors. In this work the set of modern hot spots with sufficiently studied deep structure with the methods of seismic tomography [3] is used for the analysis. These "hot spots" are shown in Fig. 1.

The hot spots shown in Fig. 1 are local interplate manifestations with sizes from hundreds to thousands of kilometers in diameter (properly, "hot spots") and vast super plumes with a diameter up to tens of thousands of kilometers. Among latter ones are the South Pacific and African Superplumes, including usually some local hot spots [6]. The most known hot spots of these super plumes are shown in Fig. 1 (no. 1–15).

Along with this situation, another distribution of hot spots, connected with their location along the boundaries of lithospheric plates, is possible. The following groups (Fig. 1) are distinguished: (1) hot spots confined to convergent boundaries of plates (zones of subduction and collision), (2) hot spots formed in

connection with the formation of divergent boundaries and caused by the formation and development of mid-oceanic ridges, (3) hot spots located out of zones of formation of lithospheric boundaries. The hot spots associated with the western boundary of North and South America and with the eastern margin of Asia and Australia (Fig. 1, no. 16–24) can be referred to the first group. The hot spot Eiffel (West Europe) is also close to the first group, so it is located close to the

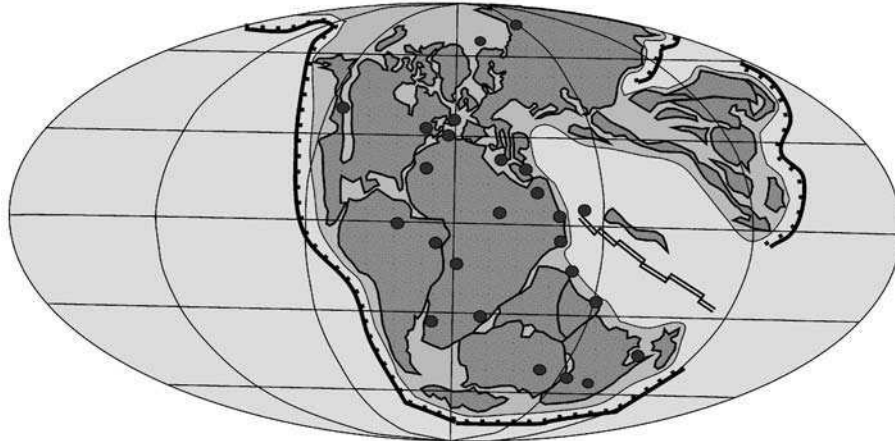


subduction zone of the Mediterranean (Tethys). The same situation is with the hot spots located along the eastern border of the Pacific (Fig. 1, no. 41–45). Part of these hot spots has a dual position that makes it possible to connect them with convergent boundaries, as well as with spreading centers.

Fig. 1. Scheme of the distribution of hot spots in the system of the lithospheric plates in the Earth.

1–3—Hot spots: 1—hot spots of inner parts of the lithospheric plates, 2—hot spots controlling the position of the mid-oceanic ridges (MOR), 3—hot spots connected with convergent boundaries of plates; 4–5—boundaries of lithospheric plates: 4—divergent (MOR), 5—convergent; 6—projections of mantle hot fields (super-plumes); 1–7—Hot spots of the South Pacific Superplume: 1—Hawaiian, 2—Karolinskaya, 3—Markizskaya, 4—Samoa, 5—Tahiti, 6—Pitcairn, 7—MacDonald; 8–15—hot spots of African Superplume: 8—Hoggar, 9—Tibesti, 10—Darfur, 11—Afar, 12—East African, 13—Victoria, 14—Comoro, 15—Reunion; 16–24—hot spots of convergent boundaries of plates: 16—Yellowstone, 17—Raton, 18—Wudalianchi, 19—Changbaishan, 20—Datong, 21—Tengchong, 22—Hainyan, 23—Lord Hoyer, 24—East Australian; 25–45—hot spots of mid-oceanic ridges: 25—Jan Maien, 26—Island, 27—Azores, 28—New England, 29—Fernando, 30—Trinidad, 31—Ascension, 32—Saint Helen, 33—Tristan, 34—Goff, 35—Meteor, 36—Buve, 37—Marion, 38—Kroze, 39—Amsterdam, 40—Kergelen, 41—Bovi, 42—Cobb, 43—Badzha, 44—Galapagos, 45—Paskhi.

The hot spots of the Atlantic Ocean are referred to the second group. They mark the boundary of the detachment zone between the continents of the Western and Eastern Hemispheres (Fig. 1, no. 25–36). The current position of the hot spots of the second group does not always coincide with the axis zone of the Mid-Oceanic Ridge. However, in the Late Paleozoic Pangaea, these hot spots were located in the detachment zones between America, Africa, Antarctica, and



Australia, taking part in the formation of the Atlantic and Indian oceans (Fig. 2).

Hot spots of the inner parts of the lithospheric plates, mainly located in the central parts of projections of the superplumes on the Earth's surface, are referred to the third group.

Fig. 2. Scheme of location of mantle hot spots in the structure of Pangaea. Reconstruction of the Pangaea prior to 190 Ma ago (after [15]). The position of the hot spots corresponds to their current location on the Earth's surface. The hot spots of the Atlantic MOR are located along the suture between Africa and both Americas.

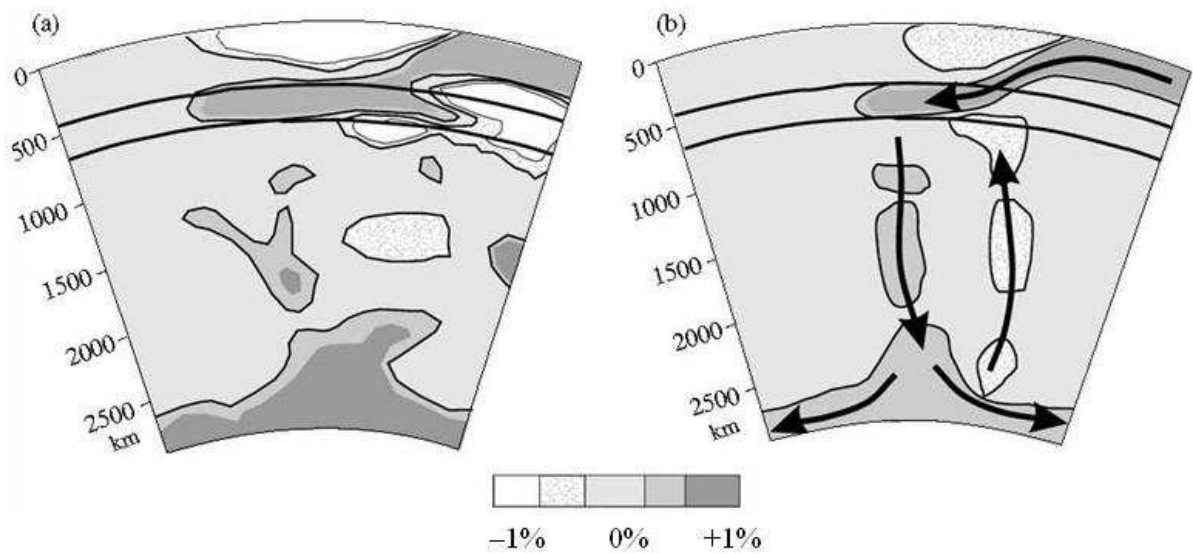


Fig. 3. Deep structure of the mantle (a) in zones of convergent boundaries of the western part of the Pacific according to the data [7] and the model of formation of convection flows at these boundaries (b).

In that way, all hot spots confirmed by seismic tomography occupy their own place in the given simple classification.

However, it is important to understand the geodynamic and physical sense of the connection of such hot spots with the main tectonic structures of the Earth, so the hot spots and above-mentioned structures manifest different depth formations. For this purpose, it is necessary to mention some hypothetical explanations of geodynamic processes taking place in the above-listed tectonic structures. The causes of the formation of mantle plumes are considered in the framework of two extreme groups, differing in the mechanisms of initiation of ascending mantle flows. According to one of these causes, subduction processes, or rather the mechanism of downlifting of slabs to the deep mantle and, accordingly, upward movement of low density mantle as plumes, are supposed to play the main role. This cause can be connected with the tectonics of the lithospheric plates. According to another cause, the processes on the core–mantle boundary were dominant and they promoted the existence of ascending flows of the hot mantle regardless of subduction process.

The model of subduction initiation of hot spots. First of all, it should be taken into account that hot spots are associated with the convergent boundaries of plates. The main process at these boundaries is known to be subduction of the cold lithosphere into the transition mantle, and then even to the basement of the mantle or the mantle-core boundary [6]. In spite of discussions on the causes of such downlifting, this fact is confirmed by seismic tomography. With the significant volume of the subducted lithospheric plates with formation of the “graveyard” of slabs, according to the vivid expression of S. Maruyama, the cooling of the transition mantle and then the entire mantle takes place. Downlifting of the lithosphere into the mantle creates the general mantle convection processes, filling the matter discharge in the zone of ascending superplumes and plumes under the mid-oceanic ridges and leading to the formation of local convection cells near the convergent boundaries. Similar local cells appear due to nonstationarity of subduction branches of the global convection loop, and, in particular, the occurrence of stagnated and discretely descending fragments of slabs [7] (Fig. 3).

This simple physical mechanism explains adequately the cause of the connection of hot spots of the subduction group with the zones of the convergent boundaries of the lithospheric plates [8].

The connection of the second group of hot spots with the area of the MOR also can be associated with the results of global subduction processes. It should be taken into account that the modern midocean ridges formed as a result of breakdown of the supercontinent Pangaea. For example, the Atlantic is considered

to have appeared under the division of America, Eurasia, and Africa being affected by the mantle plumes ascending from the core–mantle boundary, but not in the connection with spreading. The spreading is considered to be a secondary and nearly-surface process. The Atlantic hot spots listed above are responsible for the opening of the Atlantic Ocean. Due to the occurrence of the Atlantic plumes in the northern part of the supercontinent, the Atlantic was opened with the Eurasian basin to the north of it. Accordingly, the detachment of East Gondwana with separation of Africa, Antarctica, and Australia was connected with the activity of hot spots in the Indian Ocean and its western border with the South Atlantic (Fig. 2).

If the continent Pangaea was the initial position of the hot spots of the second group, then it should be supposed that the mantle under this supercontinent has to be cooled due to the long-term subduction of the lithosphere plates. Alternatively, it is difficult to imagine the mechanism itself of formation of supercontinents. Since the moment of breakdown of Gondwana, the North Pangaea existed as a supercontinent, but there was intervention of Atlantic plumes to its Arctic part [8, 12]. Due to the movement of plumes to the Arctic, the Eurasian basin of the North Arctic Ocean was probably yet to appear. However, up to the present, the activity of Arctic plumes was short-term and dampened by the subduction processes, which took place everywhere around North Pangaea. Consequently, for the second group of the hot spots, the same mechanism of the uplifting of the hot mantle by descending colder slabs and the formation of hot mantle plumes ascending in the cooled mantle in connection with the mass balance took place.

In this interpretation the formation of superplumes is hardly ever different from the supposed mechanism of formation of ordinary plumes. Their feature is in their huge sizes and duration of existence. As an example, according to known data, the Pacific superplume was active since the Riphean age, when, as supposed, the Pacific appeared. At the same time, the supercontinent Rodinia appeared as a result of the Grenwill orogeny, which according to data of many authors started to break down. The process of formation of the supercontinent Rodinia was the result of long-term subduction of the lithosphere plates from the Pantalassa Ocean. In Maruyama's opinion [6, 9] the “graveyard” of the Grenwill lithosphere plates is at present in the area of the South Pacific Superplume, surrounding it from the periphery. If this is so the case, the breakdown of Rodinia as a result of the appearance and the beginning of activity of the South Pacific Superplume could be connected most likely with the upward movement of hot mantle at the core–mantle boundary by descending cold slabs and uplifting of hot mantle as deep mantle plumes. In another words, the formation of super-plumes can be explained quite reasonably by subduction of the lithosphere plates, their subsidence to the mantle basement, and, accordingly, upward movement of hot mantle material. The sizes and duration of activity of superplumes can be caused by the duration of

subduction, accumulation of the high volume of plates at the mantle basement and an additional perturbation of the Earth's core with heat release due to convection with the cooling of the outer core under the affect of the "graveyard" of cold slabs. The latter fact is probably to be referred to the second model of the formation of mantle plumes.

The model of formation of mantle plumes due to the core–mantle interaction. This model is different from that discussed above by the mechanism of initiation of hot mantle flows, so it is based on the initial (and not induced subduction) nature of plumes. As supposed by [10], the superplumes form above ascending branches of convection cells in the liquid core of the Earth as a result of focused inflow of heat to the core–mantle boundary. The over-heated mantle of these sections attains buoyancy relative to the surrounding mantle, and during ascension it is manifested in the Earth's upper spheres as mantle plumes. The mechanisms of their interaction with the lithosphere can be different. From one side, the superplumes such as the African one stimulate the breakdown of continents and centrifugal recession of the lithosphere plates. From the other side, they can be overlapped by the lithosphere plates, as can be seen in the example of the Pacific Plume, especially in its eastern and southeastern parts (Fig. 1).

In accordance with this model, it can be supposed that the breakdown of the Late Paleozoic Pangaea took place due to thrusting of the southern (Gondwana) part of the supercontinent on the area of manifestation of the African Superplume. The data of sequential expansion of the interplate magmatism during the interval of 320–120 Ma into the Eurasian part and, then, to the Gondwana parts of the supercontinent [11]. The clearly manifested asymmetry in the deep structure of the supercontinent and its remnant fragments (Fig. 2) also corresponds to this representation. The Gondwana part of the supercontinent was initially located in the area of development of the hot mantle, which was fixed by the hot spots corresponding to the African Superplume. Otherwise, in the northern part of Pangaea, there are no active hot spots, and up to the present, it is distinguished by the thickest localization of the cold mantle at the basement, as well as by development of convergent boundaries around the framework. Over the last 300 Ma, the plume activity has begun a few times, which can firstly be connected with the activity of the Island Plume and, probably, mantle plume of the High Arctic. However, this activity was inhibited by subduction processes [8, 12] and did not lead to the breakdown of this, the biggest fragment of the supercontinent, as was to be expected in accordance with the first model. Moreover, the Island Plume corresponds to the African hot mantle field and its activity was probably controlled by the activity of this field. All of this makes it possible to suppose that Pangaea was really destroyed as a result of its thrusting into the African Superplume. In this case the hot spots associated with the MOR mark the traverses of zones of the detachment of the lithosphere plates [13]. The weakness of the model is that

upliftings of the geoid's surface correspond to the areas of the hot mantle; the mechanisms of thrusting of the lithosphere plates and, especially, supercontinents to these areas have still not been studied clearly.

This (the second) model of formation of the mantle allows us to regard some features of the formation of convergent boundaries and those specific conditions that specify the manifestation of plumes on these boundaries (first of all, on the boundaries of the West Pacific type). For this type of boundaries, corresponding to the convergent zone between the Asian continent and the Pacific plate, the significant wide (up to a thousand kilometers) and regular change of geological structures across the strike is typical. Their frontal parts are represented by island arcs (Kurily–Japan–IdzuBonin–Marianskaya–Philippine) which towards the continent changed by the back-arc seas and associated rift structures, and then, by the system of normal faults, superimposed on the continental boundary of the East Asia. Seismotomographic studies of mantle from these boundaries have revealed in its section the combination of low speed “hot” and high speed “cold” mantle, corresponding to the subducted ocean lithosphere [7]. The hot mantle is followed up to the lower mantle as large lenses, including divided subducted slabs (Fig. 3). Accumulation of the hot mantle in this part of the Pacific allows us to connect it with mantle plumes, satellites of the Pacific Superplume (Fig. 1). It is probable that the combination of subduction zones with mantle plumes at the convergent boundaries of the West Pacific type is caused by some specific geodynamic conditions of this part of the Earth. It can be supposed that manifestation of decompressed (hot) mantle under the cold ocean lithosphere led to the bowing of the lithosphere and, as a result, its fracture and subsidence of the hanging side of the cold oceanic plate into the mantle. This event corresponded to the moment of location of the subduction zone. The subsequent subsidence of the lithosphere into the mantle can be accompanied by occurrences of compensation and uplifting of hot matter from deep mantle horizons to the surface, as has been mentioned in the first model.

The considered models of formation of the mantle plumes are significantly different according to the mechanism of their formation. In the first model, the plumes have a secondary nature and form due to compensation processes, associated with cooling of the mantle by the lithosphere plates and their downlifting to the deep mantle. In the second model, plumes are of a primary nature; they form as a result of processes of heat exchange at the core–mantle boundary and contribute to the subsequent heat redistribution to the upper spheres of the Earth. It is most likely that in nature combinations of both mechanisms can take place. At least, in order to explain the spatial and time distribution of modern volcanism within the convergent boundaries of North Eurasia, the first model has mainly been used [12]. The ideas about mechanisms of the formation of mantle plumes presented in the given work have not been limited by only the main

physical interfaces in the mantle. They do not contradict the possibility of generation of plumes at the different depths in the intermediate and lower mantle, which was noted by Yu. M. Puscharovskii [14].

Along to the above-mentioned mechanisms, some other mechanisms of generation of mantle plumes may be possible. According to their nature, they can be thermal, as well as by water. Such nature of mantle plumes is supposed to explain the interpolate magmatism of South East Asia [6], including plumes under the margin basins on the convergent boundaries of the West Pacific type. The mechanism of generation of mantle plumes under the stagnation of the lithosphere plates in the intermediate zone of the mantle is proposed [7]. It is clear that development of all these ideas needs further serious many-sided explanation from the perspective of getting new information as a result of improvement of methods of seismic tomography, as well as from the perspective of physical and petrologic modeling.

ACKNOWLEDGMENTS

This work was supported by the Russian Foundation for Basic Research, project nos. 08-05-00347 and 08-05-00472, and the Program of the Presidium of RAS no. 16.

REFERENCES

1. **W. J. Morgan**, *Nature* 230, 42–43 (1971).
2. **J. T. Wilson**, *Can. J. Phys.* 41, 863–870 (1963).
3. **D. Zhao**, *Gondwana Res.* 12, 335–355 (2007).
4. **D. L. Anderson**, *Plates, Plumes and Paradigms. Special Pap.* 388, 31–54 (2005).
5. **B. Romanovicz**, *C. R. Geosci* 385, 23–25 (2003).
6. **S. Maruyama, M. Santosh, and D. Zhao**, *Gondwana Res.* 11, 7–37 (2007).
7. **D. Zhao**, *Gondwana Res.* 15, 297–323 (2009).
8. **V. I. Kovalenko, V. V. Yarmolyuk, and O. A. Bogatikov**, *Dokl. Akad. Nauk* 427 (3) (2009).
9. **Yu. M. Pushcharovsky, A. A. Mossakovsky, and S. V. Ruzhentsev**, *Dokl. Akad. Nauk* 364 (1), 88–91 (1999).
10. **N. L. Dobretsov, A. G. Kirdyashkin, and A. A. Kirdyashkin**, *Deep Geodynamics (Nauka, department GEO, Novosibirsk, 2001)*, p. 407 [in Russian].
11. **V. V. Yarmolyuk, V. I. Kovalenko, D. V. Kovalenko and M. Kozlovsky**, in *General and Regional Problems of Tectonics and Geodynamics (GEOS, Moscow, 2008)*, Vol. 2, pp. 516–520 [in Russian].
12. **V. I. Kovalenko, V. V. Yarmolyuk, and O. A. Bogatikov**, *Geotectonics*, No 5, 3–25 (2009).
13. **K. Burke and J. F. Dewey**, *J. Geol.* 81, 406–433 (1973).
14. **Yu. M. Puscharovsky and D. Yu. Pushcharovsky**, *Geotectonics*, No. 1, 3–14 (1999).
15. **C. R. Scotese**, *Paleogeographic Atlas. (University of Texas at Arlington, Arlington, 1994)*.

Thermal Convection and Plumes in the Crystalline Earth Mantle. Analysis of the Problem in Terms of the Similarity Laws and Physics of Solid and Liquid States

Anfilogov V.N.

Institute of mineralogy Ural division of Russian Academy of Sciences, Miass, Russia

The plate tectonics is based on the assumption, that the free circular flows of a hard material are generated in the nonuniformly heated crystalline earth mantle. It is suggested that these flows are able to move the lithospheric plaits which thickness is 100 – 150 km and horizontal size several thousands km. This idea is based on the following syllogism:

1. The crystalline materials behaves like liquid within certain conditions.
2. The free convection can be in nonuniformly heated liquid.
3. Consequently, the free convection can come into existence in crystalline material.

The plate tectonics theory assumes that the third position of this syllogism is realistic and uses up the similarity criteria which are employed for convective heat transfer description in liquid to crystalline mantle [9]. We believe that it is not obviously and the similarity of the heat transfer processes for liquid and crystalline mantle should be discussed. Nobel laureates L. Landau wrote: “ There is no convection in the non uniformly heated crystalline phase as it usually take place in liquid” [12].

Let us consider the possibility of the free convection and plumes realization in crystalline mantle in the contexts of similarity laws and physics of hard and liquid state. The elevated viscosity of crystalline material does not allow to reproduce the convective heat transfer in it. Because of this the only way to estimate the correctness of using for solid state the similarity parameters, which are used for liquid is absolute carrying out of the similarity criterias. Otherwise we can get formally correct, but physically unfeasible result [11]. For example, if we calculate the density gradient in the mantle convective cell, which size is 700 km, we must be sure that the mantle material is homogeneous in this interval. We have no the right to use the average mantle density to calculate the Reley's number, if minerals density difference is more than temperature density gradient. Density of the crystalline phases in mantle at 400 – 700 km interval varies from 4.1 g/cm³ for pyroxene to 3.6 g/cm³ for olivine [5]. This difference is much more then mantle

temperature density gradient. Because of that the equations, which describe the thermal transfer in homogeneous medium do not work for mantle.

The second strong violating of similarity low is connected with the density distribution in the upper mantle. Accordingly geophysics data there are some density bounds to 1000 km depth, which are due to phase transitions [4,14], Fig. 1. We thus have not right to build up the models, which convective cell has vertical size more than interval between the transition zones. Errors, which necessarily came into existence if this condition breaks down are due to a failure of the geometrical similarity between homogeneous liquid and layered mantle. This similarity is the first obligatory prerequisite for similarity of the physical phenomenon [15].

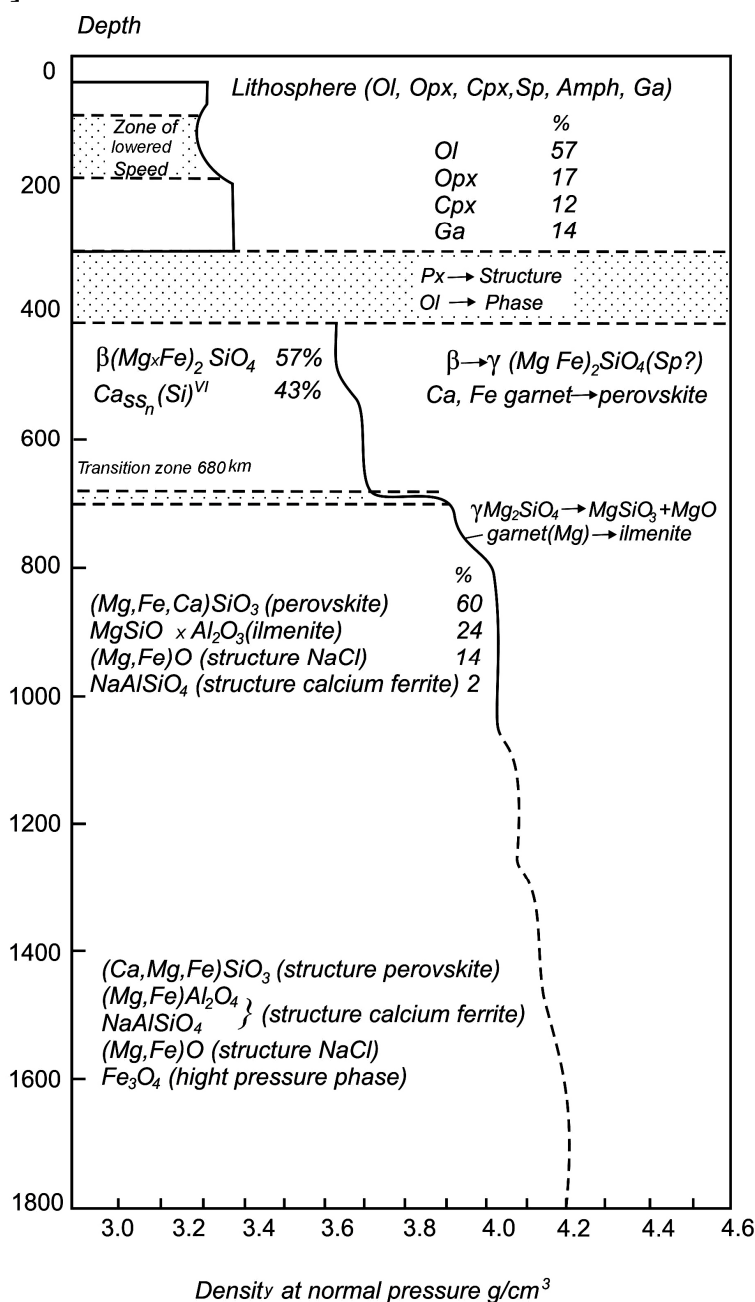


Fig. 1. Structure of upper mantle of the Earth [4]

The thermogravitational convection in liquid can be considered as the process of irreversible deformation, which is due to deviation of density distribution from adiabatic one. We will now look the basic principles of structural unit movements in the process of deformation in crystalline material and in liquid. The irreversible deformation in crystalline material is realized by two ways: by plastic current and by creep. The plastic deformation of crystalline material is the result of movement of the system of dislocations, when atoms or ions translate on the points of lattice. Viscosity of the isotropic solid body at plastic deformation is described by equation [13]:

$$\sigma_{ik} = 2\eta(u_{ik} - 1/3\delta_{ik}u_{ll}) + \xi u_{ll}\delta_{ik} \quad (1),$$

where σ_{ik} – dissipative tensor, η and ξ - viscosity coefficients, u_{ik} and u_{ll} – the time derivative of deformation tensor, δ_{ik} the unit tensor. An important point is that a complete analogy between solid and liquid is absent and equation (1) coincides with equation for tensor of deformation in liquid only formally [13].

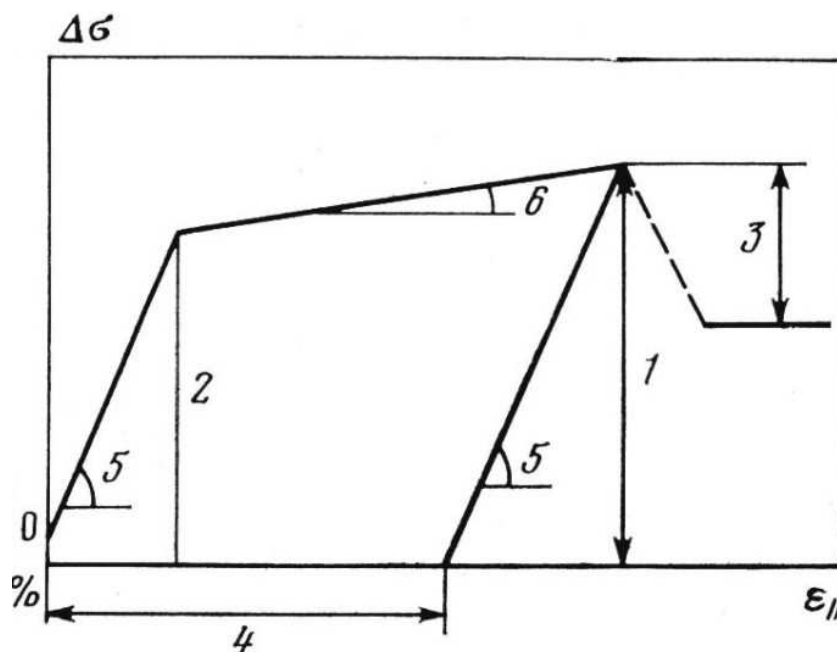


Fig. 2. The general view of deformation curve of rock [6]. 1- limit of strength; 2 – limit of elasticity; 3 – drop of strain at rock disruption; 4 – elasticity; 5 – module of strength; 6 – coefficient of deformational regdizion

Creep is the plastic deformation of solid body at high temperature and low speed of deformation [7]. It is effected by transverse slipping of dislocations, when dislocations crawls over from one plane to another. It rises to three-dimensional

saturation of crystals by dislocations with resulting deformation at low strain. The solid material viscosity at creep deformation is described by equation [7]:

$$\eta = \frac{2kTRL}{3BD\Omega} \quad (2),$$

L – the distance between grains; K – Boltzman's constant; T – temperature; R - radius of grain; D – coefficient of diffusion; Ω - atomic volume; B – constant. Equation (2) is used for the estimation of mantle viscosity [3], but if it is correct, then current units must be commensurable to grain size of mantle minerals.

The plastic deformation of solid body as opposed to liquid can not be reduced by internal forces. It appears if stress has progressed to limit of plasticity only, Fig. 2 [6]. On less stress there is elastic deformation only, which has been fully eliminated after stress is took out.

We can take lherzolite as a model of mantle material. The dependence of plasticity limit of lherzolite from temperature is shown on Fig. 3. At 1400°C it equal 250 bars [10]. The same stress must be in mantle to mantle material begin to flow. The plastic current is material moving in one direction. It never transform to circular current.

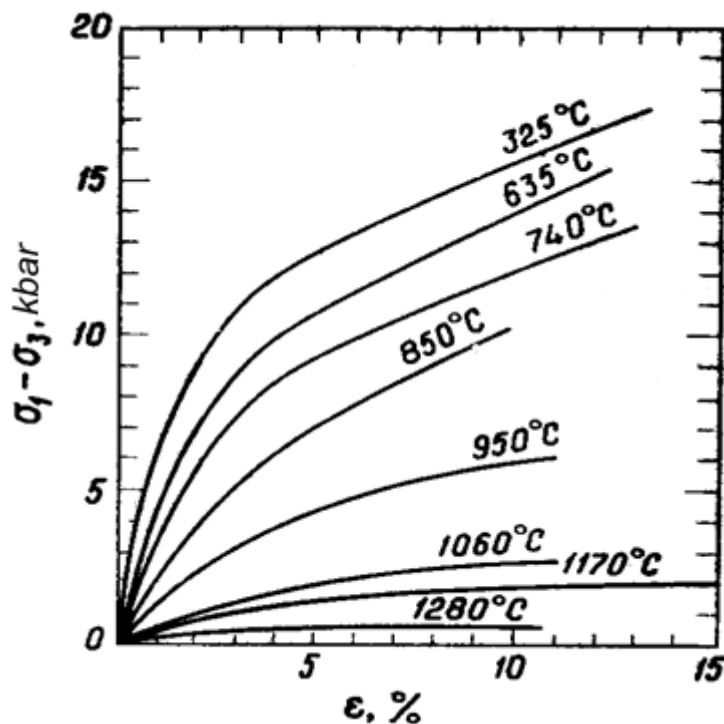


Fig. 3. Deformation of lherzolite (ϵ) at 10 – 20 kbar hydrostatic compression as function of temperature and strain [10].

For better visualization of the difference between free convection in liquid and deformation of solid material we shall consider the main peculiarities of structure of liquid. There are some models of liquid state. Accordingly these

models liquids are represented as disordered crystalline framework or as crystalline framework fragments, or as fragments having the ordered structure, which are divided by cavities with gas-like structure [1,5]. The main peculiarity of any structural model for liquid is the presence of free volume in liquid. The free volume quantity is enough to deformation of liquid and its form changing is accounted for by its weight.

We will now look the mechanism of liquid current at free convection condition. There is the most simple and illustrative variant if the liquid layer is between two infinity plaits, which have a constant temperature on its surface, Fig. 4. The border layer, which has free volume larger and density lower than cold liquid is formed in the contact with heated lower plait. The density fluctuations in the border layer gives birth the Reley-Taylor's irregularities, which transform to ascending streams of heated liquid. The fundamental differences these streams from any directional transfers in solid material implies that liquid transforms by streams but not by atoms or ions jumping from one point to another.

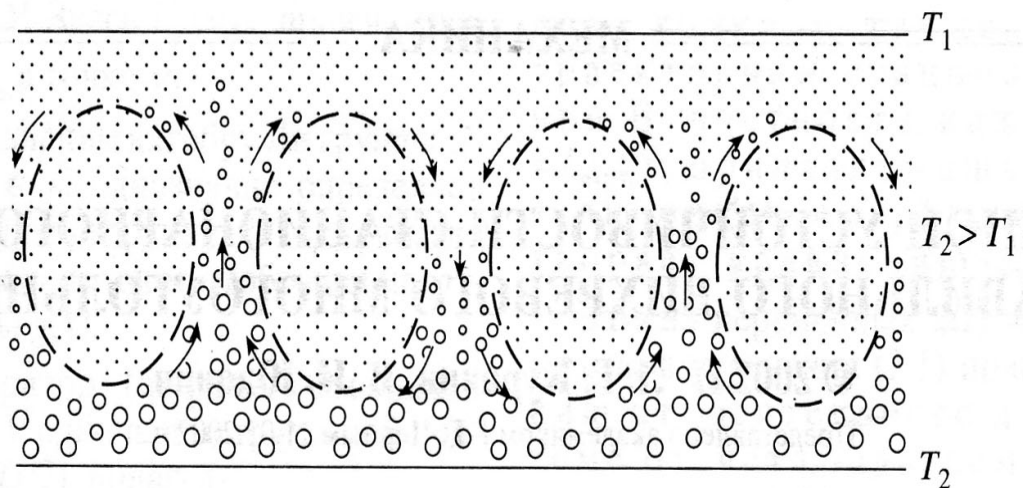


Fig. 4. **Heat-gravitational convection in liquid.** Amounts of free volume is shown by size of light circles. Area of the stable structure of liquid is shown by hatching. T_1 and T_2 - temperature on upper and low plaits.

The heat moving of atoms or ions in a solid body take make up from the next components: 1) oscillations of atoms; 2) dissociation of bonded atoms; 3) jumping of dissociated atoms interposed between framework points; 4) association of dissociated atoms; 5) free framework points (holes) translations [16]. The quantity of dissociated atoms is a function of temperature [16]:

$$n = N \cdot \exp\left(\frac{-U}{2kT}\right)$$

N – common number of atoms; U – energy of dissociation; k – Boltzman's constant; T – temperature. There are two contrary flows: holes moves to low

temperature direction and atoms to opposite ones. There is no free volume in solid material and Rayleigh-Taylor's irregularities unable to appear. Consequently the free convection can not come into existence because physical similarity between solid and liquid is absent. Violations of similarity laws, which have been noted above are enough to be certain that the base of plate tectonic is not correct. Nevertheless we will consider some additional problems which have the plate tectonic.

The heat convection begins from the boundary layers formation: hot on the low boundary and cold on the upper one, Fig. 5. As was counted by Zarkov [9] if vertical size of the convective cell, is equal 700 km then the boundary layer thickness must be 63 km and the thermal gradient in this layer must be near 8°C/km. If it is granted that the horizontal cell size is equal 7000 km [9] this gradient must be in the mantle on the area $5 \cdot 10^7 \text{ km}^2$. This brings up two questions: 1. Where such gigantic heat source was appeared in mantle? 2. How can this source keep constant temperature and thermal gradient on the gigantic area on the constant depth from the earth surface. We can propose that there is a double-level convection in the mantle and heat for the upper level transfers from the low one. The horizontal boundary, which is open for heat, but shut for material must be in the mantle in this case.

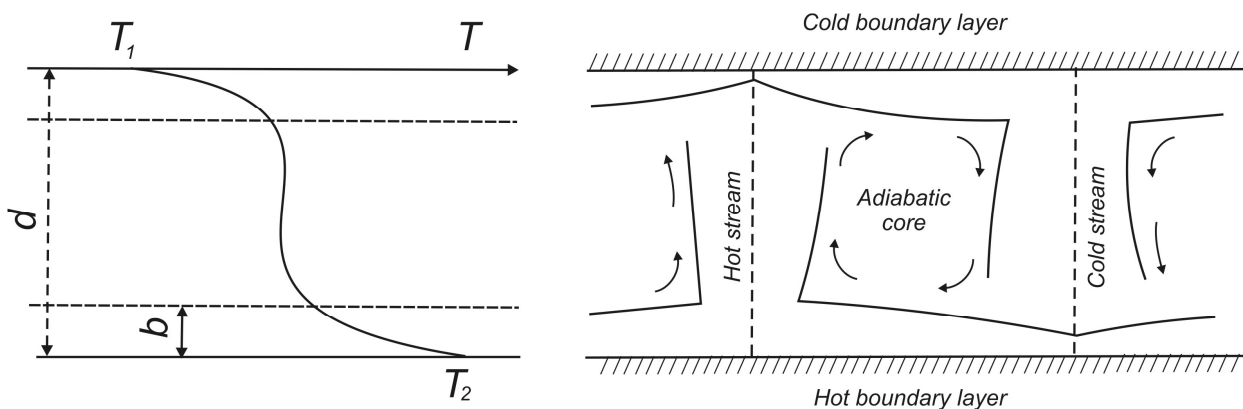


Fig. 5. Distribution of temperature in convective cell (a) and diagram of heat convection with boundary layers [9].

There are some boundaries in the upper mantle, Fig. 1. Thermal condition on these boundaries depends from the sign of derivative dP/dT of the phase transition. Three variants are possible: $dP/dT > 0$, $dP/dT < 0$ and $dP/dT = 0$. The increasing of temperature in the transition layer leads to going down of boundary, which divides mantle regions with different density in the first variant. The horizontal flow of the lower convective cell, which must produce temperature gradient in the lower boundary layer of the upper cell transforms to vertical one owing that. Because that conditions for boundary layer producing will be disrupted. The second variant leads to producing of layer with high density. The

boundary layer can not appear in this condition. The transitional zone is permeable for heat and material in the third variant and boundary layer can not appear either. By this means conditions for double-level convection forming in the Earth mantle are absent.

We will now consider the problem of compatibility mantle convection and plumes. Let us suppose that the base of the convective cell is on the 1000km depth. As soon as the vertical stream achieves 800 km the mantle material density decreases on 0.1 g/cm^3 and this material will move up more rapidly. The next discrete increasing of these parameters will be on the 700, 530 and 400 km, Fig. 1. Eventually the vertical plum will be formed rather than circular convective flow [2].

CONCLUSION

1. The equations for calculation of heat convection parameters in homogeneous liquid are unsuitable for crystalline mantle.

2. The presence of the transition zones in mantle is favorable to form long living plumes.

REFERENCES

1. **Anfilogov V.N., Bobylev I.B., Anfilogova G.I., Ziuzeva. N.A.** Structure and features of silicate-halogen melts. Moscow. Nauka. 1979. 109 p. (Russian)
2. **Anfilogov V.N., Khachay U.V.** Hydro-extrusion – the possible mechanism of diaper, domes and mantle plumes // *Geochemistry International*. 2006. N 8.
3. **Artushkov E.V.** Geodynamics. Moscow. Nauka. 1979. 327 p. (Russian)
4. **Barsukov V.L., Urusov V.S.** Phase transformations in transition mantle zone and possible variations of the Earth radius // *Geochimia*. 1982. N 12. P. 1729-1743. (Russian)
5. **Blum G., Bokris J.O.M.** Structure of ionic liquids // *Structure of melted salts*. Moscow. Mir. 1966. P. 7-75. (Russian)
6. **Volarovich M.P., Baiuk E.I., Levikin A.I., Tomishevskaya I.S.** Physic-mechanic features of rocks and minerals at high pressure. Moscow. Nauka. 1974. 223 p. (Russian)
7. **Dins G.J.** Mechanical features and defects in crystals // *Reology. Theory and applications*. Moscow. Inostrannaia literature. 1962. P. 159-180 (Russian)
8. **Dobretsov N.L., Kirdiashkin N.L., Kirdiashkin A.A.** Deepseated geo-dynamics. Novosibirsk. Nauka. 2001. 408 p.
9. **Zarkov V.N.** Internal structure of the Earth and planets. (Russian)
10. **Yoder H.S.** Generation of basaltic magma. Washington. National Academy of Sciences. 1976.
11. **Kutateladze C.C.** Analysis of similarity and physical models. Novosibirsk. Nauka. 1986. 295 p. (Russian)
12. **Landau L.D., Lifshits E.M.** Mechanics of continuous mediums. Moscow. Technical literature. 1953. 788 p. (Russian)
13. **Landau L.D., Lifshits E.M.** Theory of elasticity. Moscow. Nauka. 1965. 204 p. (Russian)
14. **Ringwood A.E.** Origin of the Earth and Moon. Springer-Verlag. New York. 1979.
15. **Tareev V.M., Matveev G.A., Grigoriev C.N.** Heat technics. Moscow. 1951. 716 p.
16. **Frenkel Y.I.** *Sobranie izbrannykh trudov*. Academy of sciences USSR
17. **Френкель Я.И.** *Собрание избранных трудов, том II*. М.: Изд-во АН СССР, 1958. 600 с.

18. Хаин В.Е., Ломизе М.Г. Геотектоника с основами геодинамики. М.: Издательство МГУ, 1995. 476 с.

UDK 552.33+550.42

Oceanic Potassic Magmas: An Example of the Atlantic Ocean

Kogarko L. N. and Asavin A. M.

*Vernadsky Institute of Geochemistry and Analytical Chemistry, Russian Academy of Sciences, ul. Kosygina 19, Moscow, 119991 Russia;
e-mail: kogarko@geokhi.ru*

ABSTRACT

Statistical study of volcanic rocks from oceanic islands and seamounts in the Atlantic Ocean based on approximately 6000 analyses (data from the authors' databank) makes it possible to recognize rocks close to the parental melts (approximately 2000 analyses). This set is demonstrated to include a unique group of high-potassium ($K_2O/Na_2O > 1$) rocks, whose K_2O/Na_2O ratio is several times higher than in the mantle and calls for the explanation of the mechanism that increased the K_2O concentration during the melting of the mantle and for the identification of an additional K_2O source in the mantle and a process responsible for K and Na differentiation. A new model is proposed to account for the genesis of high-potassium melts-fluids, whose ascent brings about extensive mantle metasomatism. The genesis of high-potassium fluid is related to solid-state reactions at deep mantle levels.

INTRODUCTION

The diversity of oceanic primary magmas is explained, first of all, by the heterogeneity of their mantle sources. Gast [1] was the first to demonstrate that no variations in the degree of mantle melting can result in the observable contrasting differences between the composition of seafloor tholeiites and alkaline basalts of oceanic islands.

Recently obtained factual materials on the petrology and trace-elements and isotopic geochemistry of basalts from oceanic islands and seamounts made it possible to geochemically classify the primary magmas of the Atlantic Ocean and to recognize distinct petrochemical provinces of intra-plate magmatism [2]. The analysis of our databank allowed us to discover a significant shift in the K/Na ratio in intra-plate magmatic rocks of the Atlantic Ocean relative to the mantle value [3] and to distinguish a unique rock group in which K dominates over Na. This research was centered on a detailed study of the geochemical specifics of potassic rocks from oceanic islands and seamounts with reference to the Atlantic Ocean.

INFORMATION RESOURCES

This research was conducted based on our database GIM on the geochemistry of within-plate oceanic magmatism [4], which now includes data on the composition of more than 30000 volcanic and plutonic rocks from oceanic islands and seamounts. The data were compiled from 400 publications on 500 occurrences

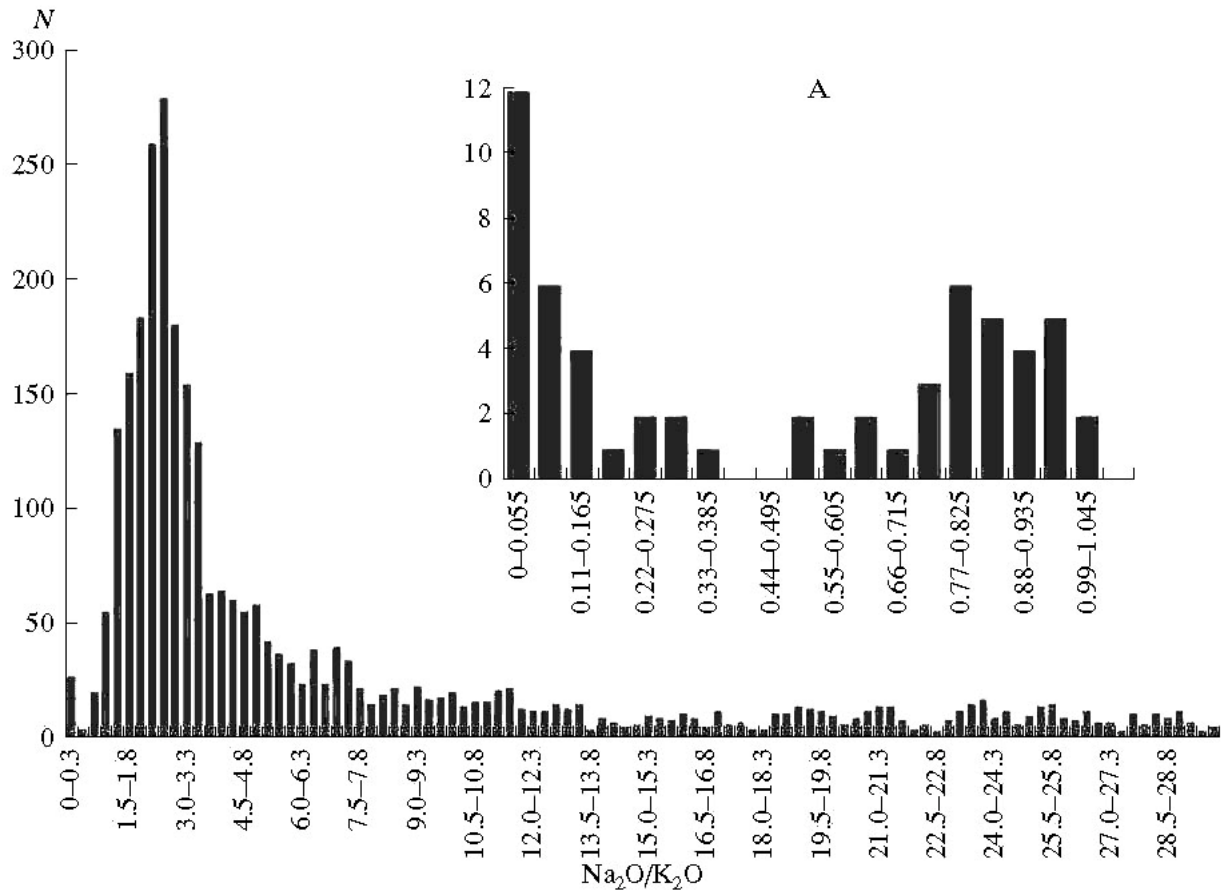


Fig. 1. Histogram of the Na₂O/K₂O ratio in high-Mg rocks close to the primary melts (MgO > 7 wt %) at oceanic islands and seamounts in the Atlantic Ocean (the total selection includes 3343 analyses). Inset A shows the selection of rock analyses with Na₂O/K₂O ≤ 1 (59 analyses).

of intra-plate magmatic rocks in the Atlantic and Indian oceans. In addition to this information, we also used data available via the internet (Petros, IGBA, GeoRock, DSDP, and others).

It should be emphasized that the authors continuously monitor current publications and append the database with newly published and preexisting information. The annual increment of the information resources thus amounts to 5–10% of the total data volume. This relatively insignificant increment testifies that the data set is representative and encompasses a broad circle of geochemical information on intra-plate magmatism in the Atlantic Ocean. Selections from the database are compiled using a flexible set of search criteria, such as concentrations

of major components (with possible constraints imposed onto certain concentrations ranges) or geographical and any other geological–structural features. After the selected data are put out in the form of DBASE or ASCII files, the data points are plotted on a map by the Arc/Info v. 8.0 computer program package. This program package is now widely applied in geoinformation studies [5], and hence, there is no need to describe in detail its data visualization capability.

In order to study tendencies in the variations of the structural–compositional characteristics of intra-plate volcanic complexes of the ocean, a geoinformation project was launched that encompasses electronic geochemical maps for intra-plate magmatism in the Atlantic [2].

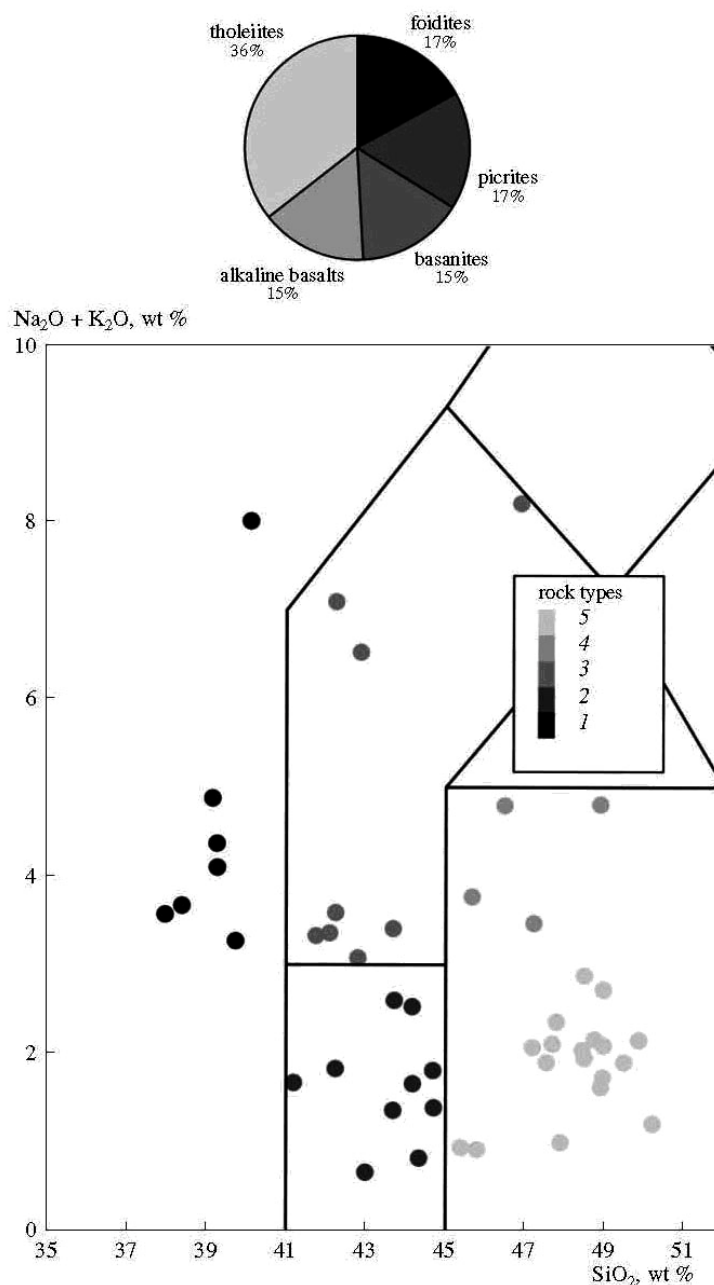


Fig. 2. Classification of K-rich rocks in the SiO₂–(Na₂O + K₂O) diagram [12, 13]. Symbols: (1) foidites, (2) picrites, (3) basanites, (4) alkaline olivine basalts, and (5) tholeiites.

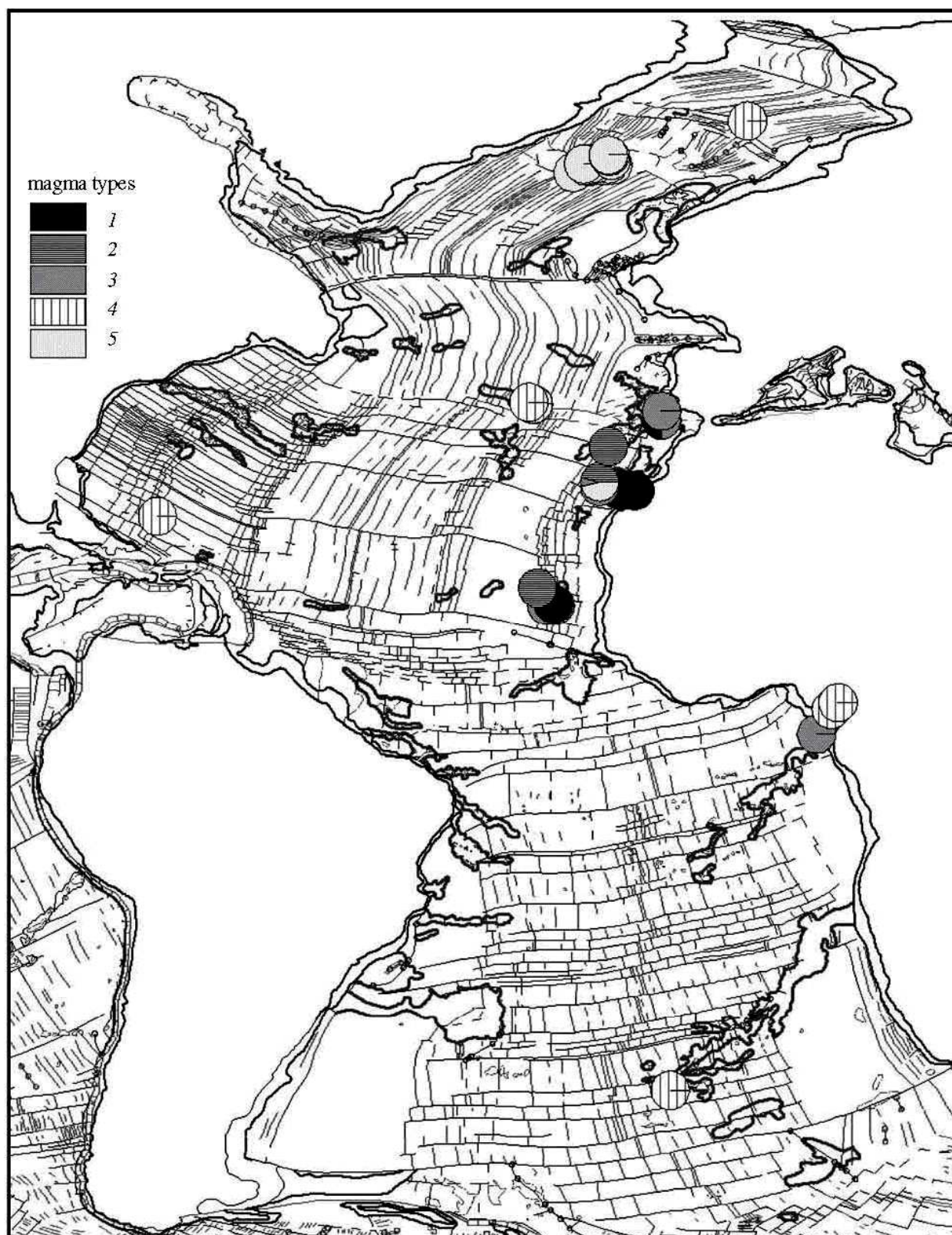


Fig. 3. Map showing the distribution of alkaline melts in islands of the Atlantic Ocean.

Pie diagrams display the quantitative proportions of rocks: (1) foidites, (2) picrites, (3) basanites, (4) alkaline olivine basalts, and (5) tholeiites.

Table 1.

Average compositions and ranges of major-component concentrations (wt %) of the recognized types of primary K-rich magmas.

Parameter	SiO ₂	TiO ₂	Al ₂ O ₃	FeO*	MgO	CaO	Na ₂ O	K ₂ O
Foidites (n=10)								
Average	35.57	4.26	11.34	13.56	8.63	12.33	1.44	2.28
Min	24	1.53	7.9	10.08	7	5.21	0.63	0.75
Max	40.11	8.5	13.91	21.52	11.59	17.41	2.24	6.49
Δ±	6.35	2.40	1.71	3.96	1.60	3.64	0.55	1.61
Picrites (n=10)								
Average	43.60	2.57	9.66	10.75	14.67	13.84	0.60	1.03
Min	41.2	1.1	6.24	8.02	11.44	9.45	0.01	0.38
Max	44.72	3.82	14.3	12.28	19.71	22.12	1.19	1.5
Δ±	1.14	0.79	2.27	1.44	2.70	3.99	0.40	0.33
Basanites–nephelinites (n = 9)								
Average	43.15	2.53	13.56	9.24	10.19	9.15	1.46	3.20
Min	41.76	1.08	10.56	3.65	7.61	1.93	0.84	1.56
Max	46.9	3.38	18.9	11.46	12.89	12.96	2.29	7.2
Δ±	1.56	0.83	3.27	3.01	2.01	4.34	0.42	2.16
Alkaline basalts (n = 9)								
Average	46.97	2.33	13.20	11.62	9.75	8.44	2.14	2.48
Min	45.68	0.83	8.9	9.9	7	1.07	1.46	2
Max	48.9	4	18.82	12.88	13.92	12.63	3	3.19
Δ±	1.08	1.02	3.13	1.23	2.60	3.92	0.54	0.43
Tholeiites (n=21)								
Average	48.46	1.18	14.78	9.13	10.22	13.72	0.13	1.70
Min	45.4	0.23	6.07	3.98	7.5	11.06	0.01	0.68
Max	50.21	3.18	21.14	11.74	20.03	20.71	0.42	2.61
Δ±	1.26	0.75	3.27	2.01	3.24	2.52	0.10	0.50

Note: all Fe is given in the form of FeO.

COMPOSITION, CLASSIFICATION, AND DISTRIBUTION OF POTASSIC MAGMAS

Some researchers believe that the group of potassic varieties should include rocks with Na₂O/K₂O < 1 [6–8]. As is known, the K₂O/Na₂O ratio continuously increases during the differentiation of many magmatic series because of the early fractionation of Na-bearing clinopyroxene and an increase in the albite concentration in the cumulus plagioclase during the intermediate stages of this process. It was demonstrated in our earlier paper [2] that magmatic rocks in the Atlantic are dominated by differentiated series produced by crystallization differentiation. According to our evaluations, primary magmas in the Atlantic

account for approximately 21%, with the remaining 79% falling onto derivative rocks.

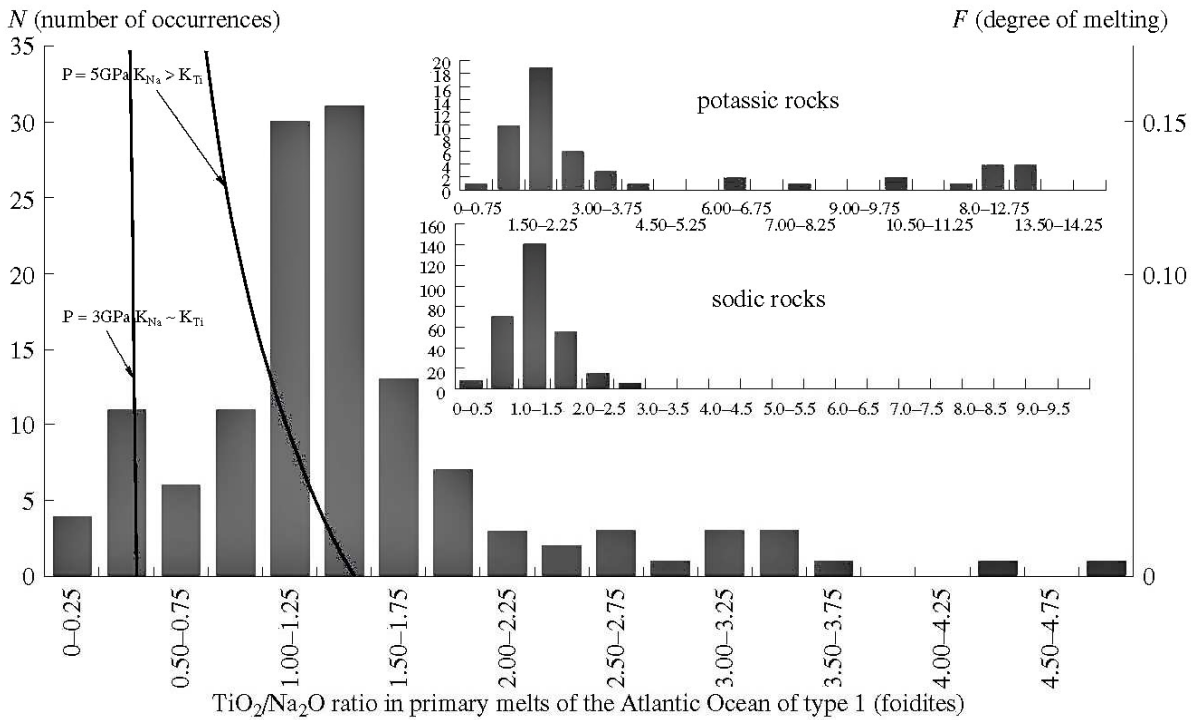


Fig. 4. $\text{TiO}_2/\text{Na}_2\text{O}$ diagram and a histogram of the distribution of the $\text{TiO}_2/\text{Na}_2\text{O}$ ratio in primary melts of the Atlantic Ocean [2].

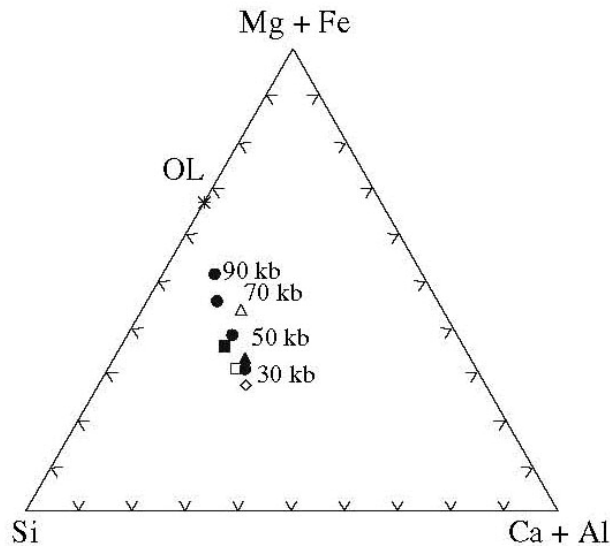


Fig. 5. **Triangular Si–(Mg+ Fe)–(Ca + Al) diagram for K-rich rocks.**

Rock types: open triangles are basanites, open squares are picrites; solid triangles are basanites, solid squares are alkaline olivine basalts, and diamonds are tholeiites. Pressure values

corresponded to data on cotectics from [19].

We tried to minimize the effect of crystallization and considered only weakly differentiated volcanic rocks. The primary melts are characterized by high $Mg\# = Mg/(Mg + Fe) = 0.7\text{--}0.8$ and high Ni concentrations and are liquids that were in equilibrium with olivine in the mantle at high temperatures and pressures [9]. For our research, we selected only highly magnesian compositions of rocks from oceanic islands and seamounts with MgO ranging from 6.5 to 25%, which were cotectic liquids saturated usually only with respect to olivine. The selection of the material was justified by our statistical studies [2]. The initial volume of the selection for melts approaching primary magmas from the Atlantic Ocean was approximately 3000 analyses. This selection of data was used for the provisional evaluation of the Na/K ratio of the rocks from oceanic islands and seamounts (Fig. 1). The selection of high-K primary melts ($Na_2O/K_2O < 1$) consisted of 59 compositions (Fig. 1, inset A). These rocks occur at 14 localities of intra-plate magmatism in the Atlantic Ocean. As is known, rocks of the kimberlite and lamproite series have never been found in the ocean. However, our database includes two compositions containing $>6\%$ K_2O and approximately 40% SiO_2 and thus having SiO_2 and K_2O proportions analogous to those of lamproites in Australia and western Kimberley [7, 8]. These ultrapotassic magmas were described at Maio Island, Cape Verde Archipelago, and São Tomé Island [10, 11].

Previously, we accomplished a petrochemical classification of all primary melts of the Atlantic [2] and recognized five petrochemical types of rocks produced by primary magmas of oceanic intra-plate magmatism: foidites, picrites–ankaramites, basanites–nephelinites, alkaline olivine basalts, and high-Mg tholeiites. Figure 2 shows the classification of high-K rocks in the $SiO_2\text{--}(Na_2O + K_2O)$ diagram [12–13]. The pie plot in this figure displays the percentages of various rock types in our selection. All varieties of potassic rocks are equally represented in this selection, with the only exception for tholeiites, whose percentage is twice as high. Figure 3 presents a map with the distribution of high-K rocks. It can be seen that these rocks occur mostly in the marginal portions of the Atlantic Ocean, which have an ancient oceanic crust and the thickest oceanic lithosphere. The calculated average compositions of our selection are listed in the table.

PHYSICOCHEMICAL CONDITIONS UNDER WHICH THE PRIMARY POTASSIC MAGMAS WERE GENERATED

The absence of a continental crust beneath the ocean definitely indicates that the genesis of oceanic magmatism is related to processes of mantle differentiation. The K_2O concentration in the mantle is very low: 250 ppm in the primitive mantle and 2100 ppm in the enriched mantle (EMORB) [3]. Such mantle source material

could hardly be the source of high-K primary magmas. Very low degrees of melting can produce liquids with high K₂O concentrations. However, taking into account the fact that the Na₂O concentration is one order of magnitude higher than that of K₂O (the Na₂O/K₂O ratio of the mantle is 12 [3]), the Na₂O concentrations in the derived magmas should have been unrealistically high (dozens of percent). Hence, the generation of potassic magmas via mantle melting seems to be hardly probable. However, data on the distribution of alkaline elements in primary intra-plate magmas unambiguously testify to significant K fractionation relative to Na. This led us to conclude that K more actively than Na passes into melts derived from the mantle. This suggests that the melt/residue partition coefficient for Na should be fairly high during the partial melting of the mantle beneath the Atlantic Ocean, whereas K actively enriches the melts because of its low partition coefficient (<1). Na is significantly dissolved in mantle clinopyroxenes at high pressures in the form of the jadeite end member NaAlSi₂O₆, and its concentrations in deep-seated clinopyroxene may reach a few percent. Experimental data indicate that the Na partition coefficient for clinopyroxene notably increases, from 0.1 at atmospheric pressure to 0.8 at 5 GPa, and this tendency continues to at least 8 GPa (with $K_{Na} \sim 1.3$).

The Ti/Na ratio can serve as an efficient barometer of magma-generating processes in the mantle [14–16]. A significant increase in the Na partition coefficient between clinopyroxene and melt with increasing pressure and a simultaneous decrease in the Ti partition coefficient (because K_{Ti} decreases with increasing pressure [17] and an increasing mole fraction of the enstatite end member in pyroxene [18]) should result in an increase in the Ti/Na ratio in the melts with increasing pressure (i.e., with the depth at which the mantle source material is melted). The bulk partition coefficients of Na and Ti at 3 GPa during the melting of a mantle source are practically identical and approximately equal to 0.1. Under these conditions, the TiO₂/Na₂O ratios are roughly equal to that in the source (0.4–0.6 for MORB pyrolite) at any degrees of melting [17]. The behavior of these elements at 5 GPa is more contrasting: while \bar{a}_{Ti} decreases to approximately 0.07, K_{Na} , conversely, increases to 0.22. In this situation, the TiO₂/Na₂O ratio can increase to 1.3 at very low degrees of melting and to 0.7 at 15% melting. Magmas with even higher TiO₂/Na₂O ratios can be generated at higher pressures, because an increase in \bar{a}_{Na} continues to at least 7.5 GPa.

The comparison of experimental data with the TiO₂/Na₂O ratios of primary K-rich magmas in the Atlantic Ocean (Fig. 4) shows that these magmas were undoubtedly generated at significant depths (the TiO₂/Na₂O ratio varies from 1.75 to 14). It should be mentioned that the TiO₂ concentrations in some potassic rocks are much higher than the upper limit for the pyrolite solidus. According to experimental data, this is close to 3% [19] and thus rules out such melts as direct

derivatives from peridotite material.

We also attempted to evaluate the depths of magma generation for various rocks of a potassic series by comparing the composition of the magmas with those of experimental melts derived at various degrees of peridotite (pyrolite) melting under variable pressures. For this purpose we employed data from [19] on the melting of natural lherzolite. The natural and experimental compositions were compared in projections onto a triangle plot of cation fractions for Si, Mg, Fe, Ca, and Al (Fig. 5). The (Mg + Fe) and (Ca + Al) sums were combined as single components. Compositions were plotted onto this projection using the method for normalizing the compositions of primary melts: the initial melt compositions were recalculated into compositions in equilibrium with mantle olivine (the assumed olivine composition in the mantle was $F_{0.90}$). It was also assumed that, upon the separation of the melt from the mantle source and ascent to the surface, the melt actively crystallized, olivine settled in it, and the composition of the system changed. This process was counterbalanced by the theoretical addition of a certain olivine portion to the initial compositions.

As can be seen in Fig. 5, a pressure increase induces an increase in the concentrations of normative nepheline in the partial melts derived from pyrolite. It can be seen from these data that each group of initial potassic magma displays a certain scatter of compositions along the olivine–pyroxene side of the triangle. These broad ranges testify to significant variations in pressure in the magma-generating sources. A notable feature is a certain systematic arrangement of composition points of potassic rocks in Fig. 5, with this feature most clearly pronounced for the foidites, tholeiites, and picrites with elevated K_2O concentrations. This likely reflects olivine control during partial melting in the ascending protolith. A comparison of the data (Fig. 5) demonstrates that the deepest seating potassic rocks of the Atlantic Ocean are foidites and alkaline basalts (whose average compositions fall into the field of melts derived at pressures of 7–5 GPa, i.e., from depths of 210–150 km). Potassium basanites and picrites were generated at lower pressures of 4–3 GPa corresponding to depths of about 120–90 km. The shallowest rocks are potassic tholeiites, whose average concentrations plot within the region of pressures <3 GPa (depths of 75–60 km), which coincides with, for example, the generation field of Hawaiian tholeiites. The comparison of the depths at which sodic and potassic magmas were derived demonstrates that all potassic melts other than tholeiites were derived at greater depths. An unexpected result is the shallower depths at which potassic tholeiites that occur only in Iceland and Jan Mayen were generated. It cannot be ruled out that the genesis of these rocks is related to certain regional features of the source or to assimilation processes. It should also be mentioned that potassic tholeiites have not been described among either basalts from mid-oceanic ridges or basalts from oceanic islands and seamounts in the Atlantic Ocean.

THE ROLE OF MANTLE METASOMATISM IN THE GENERATION OF INITIAL POTASSIC MAGMAS

Mantle metasomatism is one of the most important processes responsible for the chemical differentiation of the mantle [20]. Global material transfer is controlled by the partial melting of mantle sources, a process generating extremely mobile melts–fluids (at very low degrees of melting), which can actively react with the mantle matrix. This gives rise to minerals containing volatile components: amphiboles, micas, apatite, minerals of the lindsleyite–mathiasite group, etc.

These melts–fluids are characterized by a significant enrichment in alkalis, mostly K, and incompatible elements (because these elements have extremely low partition coefficients and enrich melts).

Experimental studies of phase diagrams with minerals concentrating K (first of all, leucite) have shown that phlogopite and amphibole appear in these compositions at high temperatures and pressures in the presence of water and carbon dioxide [21]. For instance, the melting of leucite basanite [22] at a pressure of 0.5 GPa and temperature of 850°C leads to the crystallization of clinopyroxene, amphibole, phlogopite, and magnetite. When leucite-bearing nephelinite melts at high pressures (up to 3 GPa), the liquidus phases are clinopyroxene, K-richterite, and phlogopite [21]. During the melting of K-rich lamproites [8] at high pressures (2.5–3.5 GPa) and a temperature of 800°C the crystallisation of olivine, phlogopite, orthopyroxene, apatite, and carbonate is proceeding.

Experimental data indicate that high-K melts were in equilibrium with such metasomatic minerals as phlogopite, richterite, and apatite when these melts were derived from the mantle, i.e., their genesis was significantly affected by metasomatic processes.

As was mentioned previously, many K-rich magmas are significantly enriched in Ti, and this element can not be accumulated in such amounts during the partial melting of pyrolite containing 2000 ppm TiO₂ [3]. Ti supply from deep zones of magma generation is most probably related (similar to the supply of K) to mantle metasomatism. It was demonstrated in numerous publications that Ti can be actively transported by metasomatic melts, which mostly have an alkaline silicate composition. Such Ti-concentrating mantle minerals as rutile, armalcolite, ilmenite, and minerals of the lindsleyite group are often thought to be major mantle metasomatic phases [23].

High-K continental rocks (lamproites, leucite alkaline basaltoids, and others) are regarded by most researchers as melting products of extensively metasomatized phlogopite-bearing mantle [24]. Data on microinclusions in diamonds [25] and mineral assemblages of metasomatized mantle nodules testify that carbonate and silicate melt-fluids rich in alkalis (particularly K) can occur at significant depths. For example, microinclusions in diamonds from Botswana contain a fluid phase

with 18.1–21.4% K_2O and as little as 2.2–3% Na_2O [26]. Mantle clinopyroxene with up to 4.67% K_2O definitely prove that melts–fluids can occur in nature.

Based on the analysis of the composition of microinclusions in olivine, clinopyroxene, diamond, and other minerals, many researchers distinguish the following three main metasomatic agents:

- (1) melts enriched in H_2O , SiO_2 , Al_2O_3 , and K_2O ;
- (2) carbonatite melts–fluids enriched in MgO , CaO , Na_2O , Fe , and K_2O ; and
- (3) aqueous–salt melts with high concentrations of Na and K chlorides.

According to Schiano [27], microinclusions in many minerals from spinel lherzolites sampled at various areas worldwide contain K-bearing phases and K-rich glasses, and the compositions of inclusions in distinct minerals are similar. This suggests that there are no genetic links between the inclusions and their host minerals. Thus, the mantle at relatively shallow depths of 25–60 km can contain complex K-bearing melts–fluids that are rich in LREE and volatile component [27].

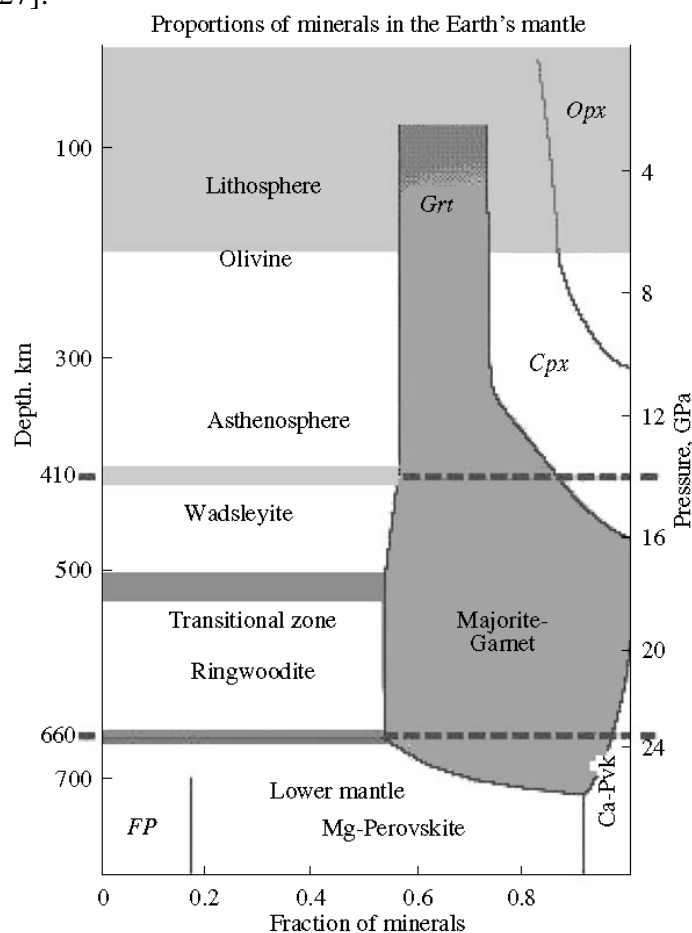


Fig. 6. Diagram for the relative contents of minerals in the Earth's mantle [36].

Mineral symbols: *FP* is ferropericlase, *Grt* is garnet, *Cpx* is clinopyroxene, *Opx* is orthopyroxene, *Ca-Pvsk* is Ca-perovskite.

A unique opportunity to estimate metasomatizing fluids at significant depths

is offered by studying microinclusions in diamonds. Diamonds usually abound in inclusions, whose size varies from a few micrometers to 1 mm. These inclusions bear silicates, sulfides, carbonates, and phosphates, along with water and carbon dioxide. These data led to the idea that diamonds crystallize in equilibrium with fluids but not with silicate melts [28]. Data on fluid inclusions in diamonds [26] indicate that all inclusions are enriched in K_2O and incompatible elements. These data also suggest that inclusions containing salt melts–fluids are significantly enriched in K_2O (even more significantly than in Na_2O , and their $K/Na > 1$), whereas carbonatite inclusions bear more Na than K.

Hence, the source of alkaline potassic rocks is most likely mantle material that was metasomatized by potassic salt melt–fluid but not by carbonatite fluids. It should be mentioned that there seem to be transitions between three types of metasomatic fluids: silicate–carbonate and salt (mostly chloride). Microinclusions in diamonds display a direct correlation between the K and Cl concentrations. A correlation between K and Cl is well known in Yakutian, African, and Canadian diamonds that were analyzed on a proton microprobe or by neutron activation and stepwise heating techniques [29–30]. According to [31], the average composition of inclusions in diamonds from the Koffiefontein and Diavik pipes corresponds to a high-K brine. The infiltration of K-rich fluids containing Cl and F is a significant metasomatic process in upper mantle blocks, whose partial melting generates alkaline potassic magmas in the ocean and continental rift zones, as well as kimberlites and lamproites.

It is interesting to discuss the genesis of K-rich fluids. Some scientists believe that alkaline ultrapotassic liquids can be produced by the long-lasting differentiation of kimberlite magmas. However, results of extensive petrologic–geochemical, isotopic, and experimental studies are consistent with the hypothesis of an autonomous flux of ultrapotassic chloride–carbonate melts–fluids, whose relics were found in microinclusions in olivine, clinopyroxene, diamond, and other mantle minerals. The genesis of kimberlites and lamproites is thought to be related to the metasomatic interaction of potassic fluids and mantle material. This is in good agreement with the age values obtained for the salt component of kimberlites, which indicate that the influx of carbonate–salt melts–fluids predated the generation of kimberlites. Now it is widely acknowledged that the genesis of mantle magmas is significantly contributed by recycling processes.

Another hypothesis proposed for the genesis of alkaline potassic fluids is underlain mostly by isotopic data. Extensive data on the isotopic systems of kimberlites (Rb–Sr, Sm–Nd, U–Th–Pb, and Lu–Hf systems) suggest that kimberlites of group 1 have mantle signatures. Data on the isotopic systematics of noble gases (He, Ar, and Xe) and proportions of halogens (Cl, F, Br, and I) in microinclusions of melts–salts in coated and fibrous diamonds show that the Ar^{40}/Cl , Br/Cl , I/Cl , Ar^{40}/Ar^{36} , Ar^{38}/Ar^{36} , Xe^{136}/Xe^{130} , and Ar^{38}/Ar^{36} ratios in the

extracts are analogous to those in MORB [29, 30]. This hypothesis is consistent with materials on the C isotopic composition of diamonds containing numerous microinclusions of potassic brines. According to Galimov [32], δC^{13} of diamonds vary from -4 to -8 , i.e., the diamonds have mantle signatures. Deviations from these values are explained as resulting from carbon fractionation in diamond–fluid equilibria or by the participation of recycling processes in the genesis of kimberlites. Both mechanisms seem to take part in the generation of high-K rocks. The former hypothesis is undoubtedly valid for potassic magmas in island-arc environments, whereas potassic oceanic magmas, which show no Nb, Ta and Ti minima, were likely formed by the differentiation of mantle source material.

Most geochemists now admit the chondritic model for the composition of the Earth and its upper and lower mantle. According to this model, the K_2O content in the Earth's primitive mantle is very low: 250 ppm [3]. All K in the uppermost mantle blocks is contained in plagioclase. This mineral disappears with increasing depth (and pressure), after which the budget of K is controlled by clinopyroxene and, to a lesser degree, garnet, whose partition coefficients for K are approximately 0.04–0.12 for clinopyroxene and 0.038 for garnet [33], with the K partition coefficient increasing in pyroxene–melt equilibria with increasing depth and pressure [34]. The main mineral concentrating Na at these depths is clinopyroxene, for which the Na distribution coefficient is 0.8. A further pressure increase results in a reaction between pyroxene and garnet that produces majorite, whose partition coefficient is 0.015 for K and 0.39 for Na [33]. At these depths (410–660 km), majorite occurs in association with wadsleyite (410–500 km) and ringwoodite (500–660 km), with none of them containing either K or Na. At still greater depths in the mantle (below 660 km), the majorite–ringwoodite association gives rise to the ferripericlase + Mg-perovskite + Ca-perovskite assemblage (Fig. 6). In this mantle zone perovskite contains close to 8% Ca. The K partition coefficient for Ca-perovskite is relatively high (0.39), and this value for Na is even higher (2) [35], so that practically all K and Na in the upper mantle zone are contained in Ca-perovskite. As a mantle diapir ascends at depths of approximately 660 km, Ca-perovskite becomes unstable, and its reaction with Mg-perovskite yields majorite, ringwoodite, and (as the pressure further decreases) wadsleyite. In this process, K only partly passes into majorite, because the K partition coefficient for Ca-perovskite is 26 times higher than the analogous value for majorite [35]. The rest of K is likely not contained in the crystal structures of any minerals composing this zone of the mantle. The relations between the K partition coefficients for Ca-perovskite and majorite definitely indicate that the thermodynamic activity of K_2O in the system increases by more than one order of magnitude with the transition from the association of Mg- and Ca-perovskite with ferripericlase to the majorite–ringwoodite assemblage. This provides favorable conditions for K transfer into melt or fluid at the boundary of the upper mantle (close to 660 km). The released

fluids should migrate to higher structural levels and metasomatize the host rocks. This should, in turn, result in a decrease in the solidus temperature of mantle peridotite and the derivation of kimberlite melts. The occurrence of majorite garnet in kimberlites and microinclusions in diamonds containing K-rich liquids validates our model for the genesis of K-rich mantle fluxes and kimberlites.

CONCLUSIONS

The genesis of K-rich oceanic magmas (at least in the Atlantic) is likely controlled by three major factors.

1. Active processes of mantle metasomatic introduction of material into magma-generating zones, which results in geochemical heterogeneities with high K and Ti concentrations.

2. Deep-seated melting of mantle protoliths (at depths of 90–270 km) in the thickened lithosphere. Manifestations of potassic magmatism are prone to be restricted to the flank zones of the ancient crust of the Atlantic Ocean.

3. Generation of large plumes beneath the Atlantic Ocean (Cape Verde, Canaries, Iceland, and Tristan da Cunha plumes).

REFERENCES

1. **P. W. Gast.** “Trace Element Fractionation and the Origin of Tholeiitic and Alkaline Magma Types,” *Geochim. Cosmochim. Acta* 32, 1057–1086 (1968).
2. **L. N. Kogarko and A. M. Asavin.** “Regional Features of Primary Alkaline Magmas of the Atlantic Ocean,” *Geokhimiya*, No. 9, 915–932 (2007) [*Geochem. Int.* 45, 841–856 (2007)].
3. **W. F. McDonough and S. Sun.** “The Composition of the Earth,” *Chem. Geol.* **120**, 223–253 (1995).
4. <http://earth.jscc.ru/gim>
5. **K. Asch.** “The Geological Map: The Visual Language of Geologists (with Too Many Dialects for Even the Most Sophisticated Computers),” in *Extended Abstracts of Conference GIS-in Geology (Moscow, 2002)*, p. 15.
6. **J. B. Gill.** *Orogenic Andesites and Plate Tectonics* (Springer, Berlin, 1981).
7. **S. F. Foley, G. Venturell, D. H. Green, and L. Toscani.** “The Ultrapotassic Rocks: Characteristics, Classification and Constraints for Petrogenetic Models,” *Earth-Sci. Rev.* 24, 81–134 (1987).
8. **A. K. Gupta and W. S. Fyfe.** *The Young Potassic Rocks* (Ane Books, New Delhi, 2003).
9. **D. H. Green and A. E. Ringwood.** “The Genesis of Basaltic Magmas,” *Contrib. Mineral. Petrol.* 15, 103–190 (1967).
10. **R. C. Mitchell-Thome.** *Geology of the South Atlantic Islands* (Berlin, 1970).
11. **P. de Paepe, J. Klerkx, J. Hertogen, and P. Plinke.** “Oceanic Tholeiites on the Cape Verde Islands: Petrochemical and Geochemical Evidence,” *Earth Planet. Sci. Lett.* 22, 347–354 (1974).
12. *Igneous Rocks. A Classification and Glossary* Sciences Subcommittee on the Systematic of Igneous Rocks, Ed. by R. W. Le Maitre, (University Press, Cambridge, 2002).

13. **M. J. Le Bas and A. L. Streckeisen.** The IUGS Systematics of Igneous Rocks, *J. Geol. Soc. London*, 148, 825–833 (1991),.
14. **K. Putirka.** “Clinopyroxene + Liquid Equilibria to 100 Kbar and 2450 K,” *Contrib. Mineral. Petrol.* 135, 151–163 (1999).
15. **K. Putirka.** “Garnet + Liquid Equilibrium,” *Contrib. Mineral. Petrol.* 11, 27–288 (1998).
16. **I. D. Ryabchikov, T. Ntaflos, A. Büchl, and I. P. Solovova.** “Subalkaline Picrobasalts and Plateau Basalts from the Putorana Plateau (Siberian Continental Flood Basalt Province). I. Mineral Compositions and Geochemistry of Major and Trace Elements,” *Geokhimiya* 39 (5), 467–483 (2001) [*Geochem. Int.* 39, 415–431 (2001)].
17. **J. Adam and T. H. Green.** “The Effects of Pressure and Temperature on the Partitioning of Ti, Sr and REE between Amphibole, Clinopyroxene and Basanitic Melts,” *Chem. Geol.* 117, 219–233 (1994).
18. **W. E. Gallahan and R. L. Nielsen.** “The Partitioning of Sc, Y, and the Rare Earth Elements between High-Ca Pyroxene and Natural Mafic to Intermediate Lavas at 1 Atmosphere,” *Geochim. Cosmochim. Acta* 56, 2387–2404 (1992).
19. **M. J. Walter.** “Melting of Garnet Peridotite and the Origin of Komatiite and Depleted Lithosphere,” *J. Petrol.* 39 (1), 29–60 (1998).
20. **L. N. Kogarko.** “Role of Deep-Seated Fluids in the Genesis of Mantle Heterogeneity and Alkali Magmatism,” *Geol. Geofiz.* 46 (12), 1234–1245 (2005).
21. **A. K. Gupta, K. Yagi, Y. Hariya, and K. Onuma.** “Experimental Investigation of Some Synthetic Leucite-Rocks under Water Vapor Pressure,” *Proc. Jap. Acad. Sci.* 52, 469–472 (1976).
22. **M. Arima and A. Edgar.** “High Pressure Experimental Studies on a Katangite and Their Bearing on the Genesis of Some Potassium-Rich Magmas of the West Fracture of the African Rift,” *J. Petrol.* 24, 166–187 (1983).
23. *Mantle Metasomatism.* Ed. by M. A. Menzies and Hawkesworth (Academic, London, 1987).
24. **S. F. Foley.** “Vein-Plus-Wall-Rock Melting Mechanism in the Lithosphere and the Origin of Potassic Alkaline Magmas,” *Lithos* 28, 425–453 (1992).
25. **N. V. Sobolev and V. S. Shatsky.** “Diamond Inclusions in Garnets from Metamorphic Rocks: A New Environment for Diamond Formation,” *Nature* 4, 742–746 (1990).
26. **O. Navon and E. S. Izraeli.** “Cl- and K-Rich Micro-Inclusions in Cloudy Diamonds,” *EOS, Trans. Am. Geophys. Union* 80, F1128 (1999).
27. **P. Schiano and B. Bourdon.** “On the Preservation of Mantle Information in Ultramafic Nodules: Glass Inclusions within Minerals versus Interstitial Glasses,” *Earth Planet. Sci. Lett.* 169, 173–188 (1999).
28. **L. A. Taylor, H. J. Milledge, G. P. Bulanova, et al.** “Metasomatic Eclogitic Diamond Growth: Evidence from Multiple Diamond Inclusions,” *Int. Geol. Rev.* 40 (8), 663–676 (1998).
29. **G. Turner, R. Burgess, M. Laurenzi, et al.** “Ar⁴⁰–Ar³⁹ Laser Probe Dating of Individual Inclusion in Diamonds,” *Chem. Geol.* 70 (1988).
30. **R. Burgess, E. Layzelle, G. Turner, and J. W. Harris.** “Constraints on the Age and Halogen Composition of Mantle Fluids in Siberian Coated Diamonds,” *Earth Planet. Sci. Lett.* 197 (2002).

31. **E. S. Izraeli, J. W. Harris, and O. Navon.** “Brine Inclusions in Diamonds: A New Upper Mantle Fluid,” *Earth Planet. Sci. Lett.* 187, 323–332 (2001).
32. **E. M. Galimov.** “Isotope Fractionation Related to Kimberlite Magmatism and Diamond Formation,” *Geochim. Cosmochim. Acta* 55, 1697-1708 (1991).
33. **A. Corgne and B. J. Wood.** “Trace Element Partitioning between Majoritic Garnet and Silicate Melt at 25 GPa,” *Phys. Earth Planet. Int.* 143–144, 407–419 (2004).
34. **O. G. Safonov, L. L. Perchuk, and Yu. A. Litvin.** “Effect of Carbonates on Crystallization and Composition of Potassium-Bearing Clinopyroxene at High Pressures,” *Dokl. Akad. Nauk* 408, 580–585 (2006) [*Dokl. Earth Sci.* 408, (2006)].
35. **A. Corgne, C. Liebske, B. J. Wood, et al.** “Silicate Perovskite–Melt Partitioning of Trace Elements and Geochemical Signature of a Deep Perovskitic Reservoir,” *Geochim. Cosmochim. Acta* 69 (2), 485–496 (2005). 36. **A. E. Ringwood, S. E. Kesson, W. Hibberson, and N. Ware.** “Origin of Kimberlites and Related Magmas,” *Earth Planet. Sci. Lett.* 113, 521–538 (1992).

Average Compositions of Magmas and Mantle Sources of Mid-Ocean Ridges and Intraplate Oceanic and Continental Settings Estimated from the Data on Melt Inclusions and Quenched Glasses of Basalts

Kovalenko V. I.¹, Naumov V. B.², Giris A. V.¹, Dorofeeva V. A.², and Yarmolyuk V. V.¹

¹*Institute of Geology of Ore Deposits, Petrography, Mineralogy, and Geochemistry (IGEM), Russian Academy of Sciences, Staromonetnyi per. 35, Moscow, 119017 Russia, e-mail: vik@igem.ru*

²*Vernadsky Institute of Geochemistry and Analytical Chemistry, Russian Academy of Sciences, ul. Kosygina 19, Moscow, 119991 Russia, e-mail: naumov@geokhi.ru*

ABSTRACT

Based on the generalization of the compositions of melt inclusions and quenched glasses from basaltic rocks, the average compositions of magmas were estimated for mid-ocean ridges (MOR), intraplate continental environments (CR), and ocean islands and plateaus (OI). These compositions were used to constrain the average contents of trace and volatile elements in mantle sources. A procedure was developed for the estimation of the average contents of incompatible elements, including volatiles (H₂O, Cl, F, and S), in the mantle. A comparison of the obtained average contents for the depleted mantle (DM) with the available published estimates showed that the contents of most incompatible trace elements (H₂O, Cl, F, Be, B, Rb, Sr, Zr, Ba, La, Ce, Nd, Sm, Eu, Hf, Ta, Th, and U) can be reliably estimated from the ratio of K to the desired trace element in the MOR magmas and the average content of K in the DM. For Nb, Ti, P, S, Li, Y, and heavy REE, we used the ratios of their contents to an element with a similar degree of incompatibility in MOR magmas (U for Nb and Dy for the other elements). This approach was used to determine the average contents of incompatible elements in oceanic plume mantle (OPM) and the subcontinental mantle of intraplate settings or continental plume mantle (CPM). It was shown that the average composition of both suboceanic and subcontinental mantle plumes is moderately enriched compared with the DM in the most incompatible elements (K, U, Ba, and La) and volatile components (H₂O, Cl, and F). The extent of volatile component enrichment in the plume mantle (500–1500 ppm H₂O) is insufficient for a significant depression of the mantle solidus. Therefore, mantle plumes must be hotter than the ambient depleted mantle. The average contents of incompatible trace elements in the OPM are similar to those of the primitive mantle, which could be related either to the retention of primitive mantle material in the regions of plume generation or to DM fertilization at the expense of the deep mantle recycling of crustal materials. In the latter case, the negative anomaly of water in the trace-element distribution patterns of the OPM is explained by the participation of dehydrated crust in its formation. Variations in the compositions of magmas and their sources were considered for various geodynamic settings, and it was shown that the sources are heterogeneous with respect to trace

and volatile components. The chemical heterogeneity of the magma sources and gradual transitions between them suggest that the mantle reservoirs interact with each other. Chemical variations in continental and oceanic plume magmas can be attributed to the existence of several interacting sources, including one depleted and at least two enriched reservoirs with different contents of volatiles. These variations are in agreement with the zoned structure of mantle plumes, which consist of a hot and relatively dry core, a colder outer shell with high contents of volatile components, and a zone of interaction between the plume and depleted mantle.

INTRODUCTION

Several reservoirs are distinguished in the modern mantle: the depleted mantle (DM) producing midocean ridge (MOR) basalts, oceanic plume mantle (OPM) producing the magmas of ocean islands and plateaus, continental plume mantle (continental rifts, hot spots, etc., CPM), and mantle of island arcs and continental margins. The goal of the present study was to estimate the average compositions and interrelations between the former three types of mantle materials and magmas derived from them. The OPM and CPM would probably be better referred to as the mantle of intraplate geodynamic settings, because many recent publications have strongly modified the classical concept of mantle plumes and sometimes even rejected this concept. In this paper, we use the terms “plume” and “intra-plate” geodynamic settings as synonyms. The average composition of the depleted mantle was estimated by several authors [28, 42, 46, 48]. The abundances of a number of elements were estimated for particular regions related to the mantle of oceanic plumes [7] and the first estimates of their average composition appeared only recently [22,23,40]. The average compositions of magma sources for continental plumes have practically been never studied, and there are only estimates of the composition of the subcontinental lithospheric mantle [27].

The composition of the Earth’s mantle, which is the main source of basic magmas, can be estimated from the proportions of incompatible elements in these magmas [19]. Such estimates require the solution of at least two problems: (1) how the composition of magma can be determined from the samples of rocks formed from this magma, and (2) how the influence of different degrees of incompatibility of chemical elements on their ratios in magmas can be eliminated at different degrees of differentiation and melting (or how element ratios in sources can be obtained from the ratios in magmas).

One promising approach to the former problem is the investigation of melt inclusions in minerals of igneous rocks and glasses formed during the quenching of melts at elevated pressures, for instance at the ocean floor. Nowadays, this is probably the most robust way to estimate the compositions and physicochemical parameters of magmas. It has become especially efficient since the advent of local methods of quantitative chemical analysis (electron and ion microprobe, laser ablation, local IR spectroscopy, etc.). These methods provide an opportunity to determine the contents of both major components and volatile and trace elements

in melt inclusions. Our database [32] includes the analyses of more than 23000 compositionally diverse melt inclusions and quenched glasses from various geodynamic settings. Many of these analyses were used in this study.

The second problem has no general solution. Some authors (e.g., [20]) argued that only the ratios of elements with similar incompatibilities, which remain practically invariant within the whole range of differentiation and melting (e.g., Ta/Nb and Nb/U), can be used for the estimation of mantle composition. Unfortunately, there are only a few such stable ratios, and they can be used to constrain a limited number of reference ratios and concentrations in model mantle compositions.

Another obvious approach involves modeling the processes of magma formation and differentiation. As a first step, the composition of magma segregated from the mantle has to be determined. Such estimates can be made on the basis of the analysis of melt inclusions in olivine of the mantle composition (Sobolev, 1993), containing no less than 90% of the forsterite end-member. Using a certain model of formation of such a melt, it can be added to the supposed mantle residue to obtain the initial composition of the source material. Although this approach is feasible, it results in the loss of a tremendous amount of factual data on evolved melts encapsulated in minerals.

In our previous studies [22, 23], we used a somewhat different approach not separating the processes of primary magma formation by mantle melting and its subsequent crystallization differentiation. If only mafic melts are considered, the mineral composition of the mantle residue is similar to the associations of crystallizing minerals. Then, the minerals crystallizing in crustal chambers can be added to the mantle residue, and relations can be considered between the melt evolved to a varying degree and the combined crystal residue. In such a case, the problem is reduced to the search for a dependency of the ratios of incompatible elements in melt on the respective ratios in the source. In our previous study [23], we considered the behavior of two incompatible elements, 1 and 2, whose bulk partition coefficients are D_1 and D_2 , depending on the mass fractions of melt and residue and the difference between D_1 and D_2 (it was assumed that element 2 is extremely incompatible, having $D_2 = 10^{-5}$). The concentration ratio of incompatible elements in the magma (C_1/C_2) can be strongly different from that in the source (mantle) at low degrees of melting (<5%) and (or) high partition coefficients of the more compatible element (1). The C_1/C_2 ratio of the magma is identical to that of the source if $D_2 - D_1 = 0$ or the degree of melting is 1 [19]. [23] showed that up to the value $(D_1 - D_2) \sim 0.03$ (this interval includes K, Ce, H₂O, Cl, F, P, Ti, and many other trace elements of interest), the C_1/C_2 ratio of magma differs from the same ratio in the source by no more than 10–20%, which is comparable with the analytical uncertainty for many elements. The effect of incompatible element fractionation can be more significant for alkaline rocks, which are formed at low degrees of melting, and ratios of elements with similar D values should be used for

them. The elements addressed in this paper have low D values, but there are some differences. The lowest partition coefficients between mantle mineral assemblages and basaltic magmas are characteristic of K and Cl ($D < 0.01$). Water is probably slightly more compatible ($D \sim 0.01$ – 0.02 ; [7, 17, 29]) and is similar in this respect to Ce. More compatible are F ($D = 0.036$; [29, 43]) and P ($D = 0.075$; [5]). Thus, it is reasonable to suggest that the ratios of K/Cl, H₂O/Ce, and P/F in basaltic magmas approach the respective mantle values. Taking into account the uncertainties in the estimation of partition coefficients and relatively high degrees of melting during the formation of basaltic magmas, it can be stated that the ratios of elements whose D values differ by 0.02 are also not strongly different from the respective ratios in the mantle sources (e.g., K₂O/H₂O, F/Cl, etc.).

The compositions of basaltic glasses and melt inclusions evidently represent melts evolved to a different degree. However, the removal of up to 50% of Mg-rich olivine ($F_{0.88-0.90}$) exerts a negligible influence on incompatible element ratios, even for the elements whose D values differ by 0.03–0.05.

Two conclusions can be drawn from this analysis: (1) differences in the degree of incompatibility of elements have a minor effect on the majority of ratios considered in this paper compared with their natural variations (K₂O/H₂O, K₂O/F, etc.); and (2) the concentration ratio of incompatible elements in magmas can be recalculated to the respective ratio in the source at any difference between the D values of the elements using the equations of fractional melting and crystallization ([39]; Shaw, 1970).

AVERAGE COMPOSITIONS OF BASIC MAGMAS FROM MID-OCEAN RIDGES, OCEAN ISLANDS, AND INTRAPLATE CONTINENTAL SETTINGS

In order to estimate the abundances of elements in the mantle, the compositions of respective basaltic magmas have to be determined. Table 1 gives the average compositions of basaltic magmas from mid-ocean ridges (MOR), ocean islands (OI), and intraplate continental settings (continental rifts, hot spots, etc.; CR) calculated on the basis of the compositions of primary melt inclusions in minerals and quenched glasses from basalts. Since the average compositions of the basic magmas of MOR and OI were published elsewhere [22, 23, 32], they are not described here in detail, and their compositions are used for comparison with the compositions of the basic magmas of CR.

Similar to the magmas of MOR and OI, geometric means were calculated for incompatible trace element contents in the CR magmas, because their distribution is approximately lognormal (Fig. 1 for volatile components and K₂O). The estimation of the average composition of CR magmas raised the problem of the representativeness of the available analytical data. In principle, the average composition of magmas from intraplate continental settings must be close to the

composition of magmas from continental flood basalt provinces, because such rocks are obviously overwhelmingly dominant. However, flood basalts represent

Table 1. Average contents of major, volatile, and trace elements in the basic magmatic melts (40–54 wt % SiO₂) of mid-ocean ridges, ocean islands, and continental intraplate settings

Component	Average melt composition								
	mid-ocean ridges			ocean islands			continental intraplate settings		
	<i>n</i>	arithm	geom	<i>n</i>	arithm	geom	<i>n</i>	arithm	geom
SiO ₂	3869	50.22 0.93	50.22 0.96–0.94	4227	50.26 2.14	50.25 2.22–2.12	1549	48.51 3.52	48.55 3.76–3.49
TiO ₂	2695	1.35 0.61	1.24 0.53–0.37	4040	2.44 0.85	2.09 0.91–0.64	1536	1.46 1.22	1.33 1.33–0.66
Al ₂ O ₃	2624	15.57 1.20	15.56 1.24–1.15	3967	13.83 1.44	13.83 1.57–1.41	1539	15.26 4.14	15.20 6.22–4.41
FeO	2693	9.25 1.64	9.24 1.68–1.42	4003	10.63 2.03	10.58 2.38–1.94	1549	8.16 4.01	8.15 4.64–2.96
MnO	1557	0.16 0.04	0.16 0.06–0.04	2861	0.16 0.06	0.16 0.06–0.05	1002	0.15 0.11	0.15 0.17–0.08
MgO	2925	7.82 1.41	7.81 1.55–1.30	4086	7.47 2.24	7.47 2.80–2.04	1539	5.72 3.31	5.27 4.62–2.46
CaO	2624	11.54 1.09	11.54 1.21–1.09	3967	11.11 1.48	11.13 1.79–1.54	1541	9.68 3.55	9.53 5.19–3.36
Na ₂ O	2675	2.67 0.57	2.67 0.63–0.51	3952	2.34 0.65	2.30 0.61–0.48	1549	3.08 2.06	2.80 2.94–1.43
K ₂ O	3561	0.19 0.27	0.14 0.30–0.10	4090	0.52 0.53	0.57 0.53–0.27	1549	2.94 3.22	2.01 3.64–1.29
P ₂ O ₅	2341	0.15 0.11	0.14 0.15–0.07	3630	0.28 0.22	0.29 0.26–0.13	1126	0.66 0.61	0.63 1.07–0.40
H ₂ O	1086	0.29 0.41	0.30 0.65–0.29	969	0.43 1.47	0.52 1.88–0.88	269	1.96 1.47	1.66 1.88–0.88
Cl	1151	180 260	130 450–100	1673	470 680	300 680–210	788	2650 2950	2480 7470–1860
F	341	180 170	160 210–90	938	700 760	680 1240–440	250	2170 2390	2060 4930–1450
S	557	1010 420	990 480–320	2583	750 800	590 1280–410	647	1060 950	1060 2000–690
CO ₂	455	190 210	150 120–70	706	150 270	100 250–70	129	1780 1160	1780 2110–970
Total <i>T</i> , °C	504	99.37 1227 42	99.17 1227 43–42	870	99.69 1194 65	99.36 1194 66–62	770	98.36 1199 71	96.03 1200 77–72
Li	329	6.37 2.17	6.21 1.81–1.40	126	6.26 2.26	6.44 3.12–2.10	118	19.7 35.0	11.3 25.8–7.9
Be	330	0.64 0.43	0.63 0.38–0.24	61	0.78 0.26	0.74 0.48–0.29	103	5.94 7.19	3.50 9.10–2.53
B	193	1.86 1.18	1.61 1.00–0.62	207	2.48 1.89	1.84 1.85–0.92	105	30.4 43.6	15.5 91.9–13.2
Sc	610	38.5 5.2	38.5 5.7–5.0	112	31.9 8.6	32.6 11.9–8.7	99	34.2 12.6	33.9 19.2–12.3
V	582	271 65	270 78–60	341	277 99	275 132–89	72	288 65	287 80–63
Cr	894	300 196	295 233–130	966	503 559	417 616–249	367	749 1108	516 1467–382
Co	252	44.2 5.1	44.2 5.2–4.7	76	51.5 9.9	51.3 12.1–9.8	40	99.0 129	74.1 162–50.8
Ni	462	99.4 47.1	99.1 54.5–35.2	350	229 221	179 274–108	144	1073 2230	517 1930–408
Rb	536	3.83 6.68	1.43 3.31–1.00	419	15.7 17.8	12.0 21.0–7.6	151	92.7 121	73.6 296–59.0

Table 1. (Contd.)

Component	Average melt composition								
	mid-ocean ridges			ocean islands			continental intraplate settings		
	<i>n</i>	arithm	geom	<i>n</i>	arithm	geom	<i>n</i>	arithm	geom
Sr	839	134	129	805	321	298	326	1220	944
		63	60–41		297	438–177		1460	1610–595
Y	810	28.2	28.2	680	23.1	22.7	177	20.9	21.4
		13.1	12.7–8.7		11.2	14.6–8.9		7.7	9.9–6.8
Zr	943	94.1	90.9	795	115	124	248	309	175
		52.9	74.1–40.8		111	209–78		526	393–121
Nb	799	4.74	2.39	643	22.5	15.5	174	30.2	20.6
		6.62	4.25–1.53		32.5	32.5–10.5		51.8	34.8–12.9
Ba	690	29.6	16.1	676	119	98	358	3040	1880
		51.2	53.0–12.3		163	254–71		5770	10200–1580
La	1079	5.51	4.40	841	12.7	5.7	164	46.3	26.8
		5.95	5.69–2.48		20.5	16.8–4.2		90	92.7–20.8
Ce	1189	12.5	11.3	725	30.1	19.9	215	98.4	69.9
		10.8	13.3–6.1		45.9	86.8–16.2		171	131–45.6
Pr	195	2.15	1.76	270	3.19	2.75	24	7.79	5.61
		1.66	1.36–0.77		2.13	2.31–1.25		10.2	8.68–3.41
Nd	888	10.6	10.4	725	16.5	14.3	152	27.8	27.3
		5.9	7.0–4.2		20.2	41.3–10.6		27.5	38.2–15.9
Sm	966	3.57	3.46	741	4.11	3.76	199	7.41	6.41
		1.84	1.85–1.21		3.89	6.59–2.40		6.85	8.32–3.62
Eu	807	1.28	1.21	703	1.66	1.20	131	2.08	1.63
		0.61	0.51–0.36		1.51	1.34–0.63		2.09	1.46–0.77
Gd	561	4.44	4.38	457	5.97	6.22	100	5.93	5.28
		1.46	1.56–1.15		3.23	3.76–2.34		4.49	4.92–2.55
Tb	260	0.75	0.79	182	0.78	0.84	31	1.16	0.79
		0.27	0.26–0.20		0.24	0.24–0.18		1.54	0.71–0.37
Dy	793	4.84	4.76	723	4.22	4.30	134	4.35	4.33
		2.05	2.02–1.42		2.41	3.17–1.83		2.03	2.09–1.41
Ho	184	1.03	1.00	268	0.88	0.94	8	1.15	1.20
		0.35	0.37–0.27		0.30	0.27–0.21		0.70	0.49–0.35
Er	651	3.06	3.02	626	2.13	2.07	94	2.13	2.05
		1.23	1.13–0.82		1.04	1.10–0.72		0.84	0.76–0.56
Tm	187	0.42	0.41	182	0.34	0.34	–	–	–
		0.14	0.15–0.11		0.13	0.15–0.10		–	–
Yb	831	2.99	2.91	835	1.94	1.90	172	2.27	2.16
		1.36	1.25–0.88		0.84	0.85–0.59		1.27	1.30–0.81
Lu	469	0.45	0.43	224	0.29	0.30	78	0.31	0.31
		0.20	0.15–0.11		0.09	0.11–0.08		0.12	0.14–0.10
Hf	434	2.45	2.38	349	3.96	3.90	82	3.90	2.95
		1.05	1.18–0.79		2.13	2.45–1.50		3.97	3.87–1.67
Ta	406	0.30	0.28	223	0.82	0.83	61	1.45	0.61
		0.39	0.50–0.18		0.35	0.53–0.32		2.99	2.07–0.47
Pb	362	0.70	0.71	245	0.86	0.82	65	4.04	1.32
		0.50	0.38–0.25		0.65	0.56–0.33		8.28	5.52–1.06
Th	561	0.44	0.36	334	1.53	1.07	172	6.32	2.15
		0.70	0.73–0.24		2.63	2.52–0.75		8.79	6.88–1.64
U	433	0.16	0.09	315	0.44	0.41	153	2.08	1.37
		0.25	0.18–0.06		0.62	0.59–0.24		3.19	4.42–1.05

Note: Here and in Table 2, the contents of major components and water are given in wt %, and other elements are in ppm; *n* is the number of determinations; "arithm" is the arithmetic mean with standard deviations beneath the values; "geom" is the geometric mean with standard deviations beneath the values (first number shows the positive deviation, and the second number is the negative deviation). The contents of elements are calculated as arithmetic and geometric means, and the maximum deviation of an individual measurement from the average value is no higher than 2σ with a probability of 95%. *T*, °C is the temperature of melt.

only a very minor part of the total number of published compositions, whereas the analyses of alkaline rocks are most numerous, although their real fraction is very small. The data set on basic magmas from CR (Table 1) includes many analyses of the potassium-rich basaltoid magmas of Vesuvius Volcano from 24 publications

[6, 11, 12, 25, 26, 37, 47 and others]. This results in that the estimate of the average composition of CR basic magmas (Table 1) is biased toward alkaline (especially, potassic) compositions. Furthermore, the tectonic setting of Vesuvius is a topic of debate. Some authors supposed that the magma source region includes both intraplate mantle material and a subduction component related to the Ionian subduction zone [2, 35]. Because of this, the average composition of Vesuvius magmas was calculated separately and compared with the data for other complexes.

Thus, the calculated composition is the sample average and cannot be considered as an unbiased estimate of the average composition of magmas produced by subcontinental mantle plumes. However, since our goal was to estimate the composition of magma sources on the basis of element ratios, this limitation is not crucial. However, it should be kept in mind that, if some evidence for source heterogeneity will be revealed, our approach will provide no information on the relative sizes of different reservoirs.

The average composition of CR magmas differs from the average compositions of magmas from MOR and OI in lower Fe, Mg, and Ca and higher K and P contents (Table 1) at similar $Mg/(MgO + FeO)$ values of 0.39–0.46. The average composition of CR magmas is significantly enriched compared with the magmas of MOR and OI in all volatile components and trace elements, including both incompatible (Be, B, LREE, Zr, Nb, Pb, U, and Th) and compatible elements (Ni, Cr, V, and Sc). The only exceptions are HREE, Hf, and Ta, whose contents in the CR magmas are similar to those of the magmas of MOR basalts. Table 2 also gives the average composition of basic magmas from Vesuvius Volcano, which is enriched compared with the average compositions of CR magmas in Ca, K, Cl, F, S, Li, Be, B, Rb, and Nb. Note that the average composition of Vesuvius magmas does not show any significant depletion of Nb relative to Ba or La, which suggests a subordinate contribution of the subduction component to the magma source.

Figure 2 presents spidergrams for the average compositions of basic magmas. Among the common features of magmas related to oceanic and continental plumes are the depletion of H_2O relative to K_2O , La, Ce, and Sr, and positive anomalies of F, Sr, Nb, and Ta. A salient feature of the average composition of CR magmas is a negative Pb anomaly and a positive Cl anomaly. Also noteworthy is the considerable enrichment of highly incompatible elements compared with the magmas of OI. The abundances of moderately incompatible elements (Ti, Dy, S, Y, and HREE) are similar in the magmas of all the environments. A comparison of the magmas with the compositions of the continental and oceanic crust (Fig. 2) suggests that crustal contamination have in general no significant effect on the average compositions of magmas, although its influence may be considerable in some complexes.

In particular, the average composition of CR magmas does not show a relative enrichment in Pb, which is an indicator of magma contamination with continental crustal rocks. The Pb/Nb ratio is 0.05 for both oceanic and continental plume

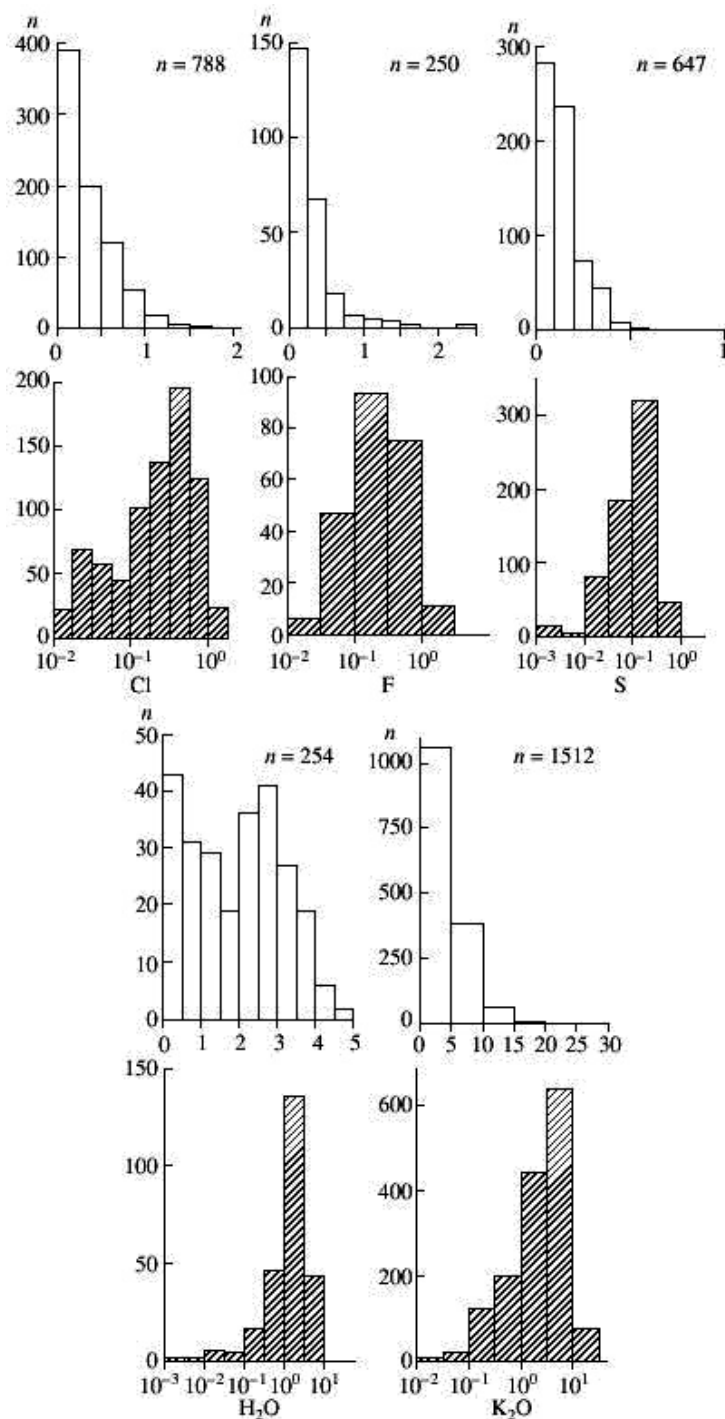


Fig. 1. Histograms showing the distribution of chlorine, fluorine, sulfur, water, and potassium oxide contents in the basic melts of continental intraplate settings (CR). The unshaded and shaded histograms are drawn on linear and logarithmic scales to test the hypotheses of normal and lognormal distribution, respectively, n is the number of analyses of melt inclusions and glass samples.

Table 2. Average contents of major elements, water (wt %), volatile components, and trace elements (ppm) in the magmatic melts of Vesuvius Volcano

Component	Average melt composition of Vesuvius			Component	Average melt composition of Vesuvius		
	<i>n</i>	arithm	geom		<i>n</i>	arithm	geom
SiO ₂	356	48.35	48.34	V	28	276	276
		2.50	2.59–2.46			59	71–57
TiO ₂	354	1.02	1.01	Cr	43	195	194
		0.27	0.43–0.30			139	163–88
Al ₂ O ₃	356	15.61	15.76	Rb	73	162	156
		2.96	2.90–2.45			77	118–67
FeO	356	7.10	7.10	Sr	77	862	856
		1.62	2.07–1.60			277	332–239
MnO	281	0.15	0.16	Y	73	22.6	23.0
		0.06	0.12–0.07			9.1	12.1–7.9
MgO	354	5.25	4.40	Zr	73	180	183
		2.65	3.64–1.99			67	82–57
CaO	356	10.01	9.85	Nb	73	29.4	28.1
		2.89	3.89–2.79			14.0	14.3–9.5
Na ₂ O	356	2.72	2.47	Ba	42	1630	1670
		1.71	1.87–1.07			518	798–540
K ₂ O	356	5.55	5.53	La	28	55.9	55.2
		1.41	1.64–1.26			21.2	24.2–16.8
P ₂ O ₅	288	0.83	0.80	Ce	73	101.0	99.6
		0.27	0.48–0.30			43.2	60.0–37.4
H ₂ O	163	2.20	1.79	Nd	33	53.9	55.6
		1.15	1.36–0.77			25.8	28.1–18.7
Cl	278	5690	5840	Sm	71	10.90	10.97
		2350	3220–2070			6.87	8.43–4.77
F	73	2640	2420	Eu	24	2.75	2.79
		1560	4850–1610			1.03	1.09–0.78
S	206	1330	1210	Gd	25	8.30	8.67
		830	1630–690			2.69	2.81–2.12
CO ₂	85	2030	1950	Dy	44	4.89	4.90
		670	3360–1130			1.50	2.05–1.44
Total		99.95	98.35	Yb	60	2.56	2.58
<i>T</i> , °C	152	1152	1148			1.55	1.64–1.00
		77	87–81	Pb	18	29.4	29.7
Li	62	21.1	19.4			6.3	8.5–6.6
		18.6	24.0–10.7	Th	60	13.8	13.6
Be	58	8.8	8.6			5.2	7.2–4.7
		4.7	7.3–4.0	U	58	3.9	3.8
B	62	40.8	39.8			2.4	3.2–1.7
		24.4	39.7–19.9				

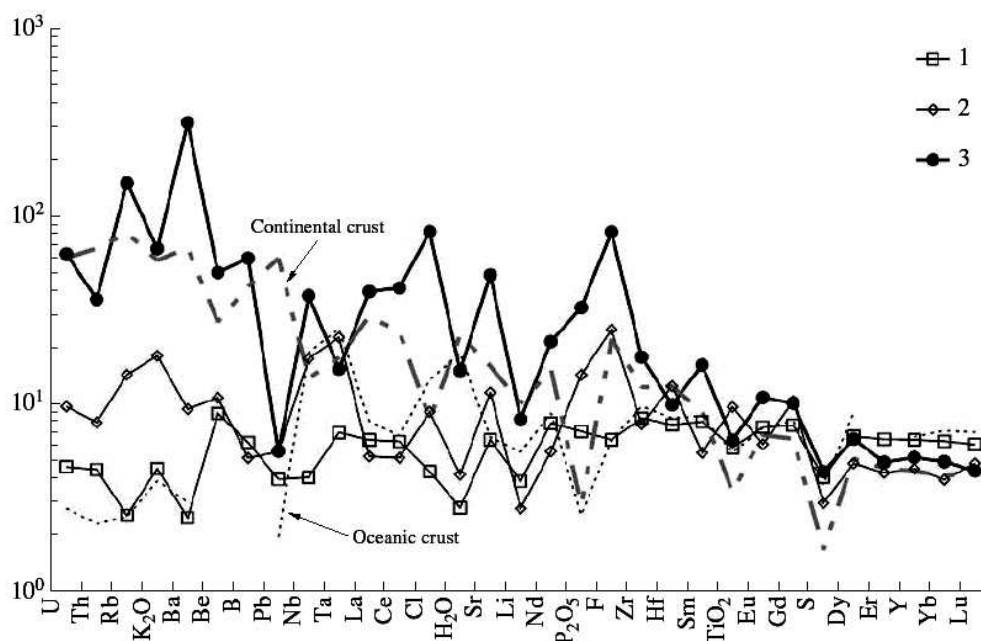


Fig. 2. Spidergrams for the average compositions of basic magmas of (1) mid-ocean ridges, (2) ocean islands, and (3) continental intraplate settings. Also shown are the average composition of the oceanic (Wedepohl and Hartmann, 1994) and continental (Rudnick and Gao, 2003) crust. Here and in Figs. 3, 4, 17, contents are normalized to primitive mantle (Palme, O'Neill, 2003).

magmas. The Pb/Nd ratios of the average compositions of the continental [38] and oceanic crust (Wedepohl and Hartmann, 1994) are very different (0.55 and 0.03, respectively), and even small degrees of contamination change this ratio in magmas (e.g., [1]).

ESTIMATION OF THE AVERAGE CONTENTS OF TRACE ELEMENTS IN MANTLE SOURCES

Average Contents of Volatile Components and K_2O in the Sources of Basic Magmas.

Table 3 shows the average ratios of K_2O to volatile components and some trace elements, as well as the ratios of trace elements with similar degrees of incompatibility, H_2O/Ce , P_2O_5/F , S/Dy , $HREE/Dy$, TiO_2/Dy , P_2O_5/Dy , Li/Dy , and Nb/U (Workman and Hart, 2005) in the basic magmas of various settings. These data are used as a basis for the estimation of the average contents of elements in the respective mantle reservoirs. Such estimates were previously made by us for volatile components in the mantle of MOR [22] and OI [23]. Similar to the OI mantle, the composition of the CR mantle was calculated using two models, isochemical (I in Table 4) and moderately enriched (II in Table 4). We first consider the ratios of volatile components to K_2O and, then, estimate the concentration ratios of other incompatible components.

The isochemical model (I in Table 4) assumes that the whole mantle in the region of basic magma formation has approximately uniform chemistry approaching the composition of the depleted mantle, and the specific features of intraplate magmas are of a thermal origin. Similar to our previous studies, our

Table 3. Concentration ratios of K₂O to other components and some other ratios (H₂O/Ce, P₂O₅/F, S/Dy, HREE/Dy, TiO₂/Dy, P₂O₅/Dy, and Li/Dy) in the magmatic melts of mid-ocean ridges, ocean islands, and continental intraplate settings

Component ratios	Ratio of average contents					
	<i>n</i>	mid-ocean ridges	<i>n</i>	ocean islands	<i>n</i>	continental settings
K ₂ O/H ₂ O	1086	0.5 (1.0–0.3)	969	1.1 (1.4–0.5)	269	1.2 (2.2–0.8)
K ₂ O/Cl	1143	11 (40–8)	1658	19 (41–9)	788	8.1 (24.4–5.2)
K ₂ O/F	341	9.0 (19–6)	938	8.4 (15–4.0)	250	9.7 (23.3–6.3)
K ₂ O/S	557	1.4 (3.0–1.0)	2568	9.6 (20–4.6)	647	19 (36–12)
K ₂ O/CO ₂	447	9.1 (19–6.2)	706	58 (150–28)	129	11 (20–7)
K ₂ O/TiO ₂	2695	0.11 (0.24–0.08)	4040	0.27 (0.25–0.13)	1536	1.5 (2.7–1.0)
K ₂ O/P ₂ O ₅	2341	0.98 (2.1–0.66)	3630	2.0 (1.8–1.0)	1126	3.2 (5.8–2.1)
K ₂ O/Li	329	230 (480–150)	126	880 (820–430)	118	1800 (4000–1100)
K ₂ O/Be	330	2200 (4700–1500)	61	7700 (7200–3700)	103	5700 (15000–3700)
K ₂ O/B	193	870 (1800–590)	207	3100 (3100–1500)	105	1300 (7700–840)
K ₂ O/Rb	536	980 (2300–670)	419	470 (830–230)	151	270 (1100–180)
K ₂ O/Sr	839	11 (23–7)	805	19 (28–9)	326	21 (38–14)
K ₂ O/Y	810	50 (100–33)	680	250 (230–120)	177	940 (1700–600)
K ₂ O/Zr	943	15 (33–10)	795	46 (77–22)	248	110 (260–74)
K ₂ O/Nb	799	580 (1200–400)	643	370 (770–180)	174	970 (1800–630)
K ₂ O/Ba	690	87 (290–59)	676	58 (150–28)	358	11 (58–7)
K ₂ O/La	1079	320 (670–220)	841	1000 (3000–480)	164	750 (2600–480)
K ₂ O/Ce	1189	120 (260–84)	725	290 (1200–140)	215	290 (540–180)
K ₂ O/Nd	888	130 (280–90)	725	400 (1200–190)	152	730 (1300–470)
K ₂ O/Sm	966	400 (850–270)	741	1500 (2600–730)	199	3100 (5700–2000)
K ₂ O/Eu	807	1100 (2400–780)	703	4700 (5300–2300)	131	12000 (22000–8000)
K ₂ O/Gd	561	320 (670–220)	457	910 (850–440)	100	3800 (6900–2400)
K ₂ O/Dy	793	290 (620–200)	723	1300 (1200–640)	134	4600 (8400–3000)
K ₂ O/Er	651	460 (980–310)	626	2700 (2600–1300)	94	9800 (18000–6300)
K ₂ O/Yb	831	480 (1000–330)	835	3000 (2800–1400)	172	9300 (17000–6000)
K ₂ O/Lu	469	3300 (6900–2200)	224	19000 (18000–9300)	78	66000 (120000–42000)
K ₂ O/Hf	434	590 (1200–400)	349	1500 (1400–700)	82	6800 (12000–4400)
K ₂ O/Ta	406	5100 (11000–3400)	223	6900 (6400–3300)	61	33000 (110000–21000)
K ₂ O/Pb	362	2000 (4100–1300)	245	6900 (6500–3300)	65	15000 (64000–9800)
K ₂ O/Th	561	3900 (8300–2700)	334	5300 (12000–2600)	172	6900 (23000–4500)
K ₂ O/U	433	15000 (13200–10000)	315	14000 (20000–6700)	153	14000 (46000–9400)
H ₂ O/Ce	540	190 (80–60)	196	120 (120–60)	70	180 (720–140)
P ₂ O ₅ /F	266	7.9 (5.6–3.3)	931	5.3 (3.5–2.1)	229	3.3 (7.5–2.3)
S/Dy	169	230 (66–51)	392	130 (230–84)	65	255 (350–150)
TiO ₂ /Dy	793	2800 (890–680)	717	4100 (2200–1400)	134	2600 (1500–940)
P ₂ O ₅ /Dy	746	270 (250–130)	580	550 (490–260)	120	1100 (1900–700)
Gd/Dy	532	0.88 (0.08–0.08)	457	1.1 (0.2–0.2)	78	1.1 (0.3–0.2)
Er/Dy	650	0.61 (0.05–0.04)	626	0.55 (0.13–0.10)	94	0.52 (0.13–0.10)
Yb/Dy	697	0.60 (0.06–0.06)	722	0.48 (0.18–0.13)	134	0.48 (0.22–0.15)
Lu/Dy	381	0.087 (0.011–0.010)	224	0.058 (0.011–0.009)	42	0.071 (0.050–0.029)
Nb/U	374	41.9 (10.1–8.2)	311	49.9 (13.8–10.8)	130	17.5 (48.9–12.9)
Li/Dy	307	1.21 (0.19–0.16)	113	0.97 (0.18–0.16)	83	2.62 (5.91–1.81)

Note: Geometric mean values are given with one standard deviation in parentheses (first number shows the positive deviation, and the second number is the negative deviation).

estimates are based on the data of Table 3 and the assumption that the concentration of K₂O in the mantle is equal to that in the DM, 72 ppm [42]. Then, the CR mantle contains, on average, 60 ppm H₂O, 9.0 ppm Cl, and 7.4 ppm F.

Table 4. Average contents of elements (ppm) in the magma sources of mid-ocean ridges, ocean islands, and continental intraplate settings calculated on the basis of (I) the thermal model and (II) the model of an enriched source

Component	Mid-ocean ridges		Ocean islands			Continental intraplate settings		
	<i>n</i>	I	<i>n</i>	I	II	<i>n</i>	I	II
K ₂ O		72		72	510		72	510
H ₂ O	1086	150 330–100	969	65 82–32	460 580–220	269	60 100–38	420 770–270
Cl	1151	6.5 23–4.4	1673	3.8 8.2–1.8	27 58–13	788	9.0 27–5.7	63 190–41
F	341	8.0 17–5.5	938	8.6 15.7–4.2	61 110–29	250	7.4 18–4.8	52 120–34
S	557	51 110–35	2583	7.5 16.0–3.6	53 110–26	647	3.8 7.2–2.4	27 51–17
S*	157	123 35–28	392	71 120–45	71 120–45	65	135 184–78	135 184–78
CO ₂	447	7.9 17–5.4	706	1.2 3.2–0.6	8.5 22.7–4.2	129	6.4 12–4.1	45 82–29
TiO ₂	2695	640 1350–430	4040	270 250–130	1900 1750–900	1536	48 86–31	340 610–220
TiO ₂ *	793	1500 470–360	717		2180 1170–760	134		1370 790–500
P ₂ O ₅	2341	74 160–50	3630	36 34–18	260 240–120	1126	23 41–15	160 290–100
P ₂ O ₅ *	746	146 132–69	577		294 263–138	120		590 1010–370
Li	329	0.32 0.67–0.22	126	0.082 0.076–0.039	0.58 0.54–0.28	118	0.041 0.093–0.026	0.29 0.66–0.18
Li*	307	0.64 0.10–0.08	113		0.52 0.10–0.08	83		1.39 3.14–0.96
Be	330	0.032 0.068–0.022	61	0.0093 0.0087–0.0045	0.066 0.061–0.032	103	0.013 0.033–0.008	0.089 0.230–0.057
B	193	0.083 0.175–0.056	207	0.023 0.023–0.011	0.17 0.17–0.08	105	0.055 0.33–0.036	0.39 2.30–0.25
Rb	536	0.073 0.170–0.050	419	0.15 0.26–0.07	1.1 1.9–0.5	151	0.26 1.06–0.17	1.9 7.5–1.2
Sr	839	6.6 14.0–4.5	805	3.8 5.5–1.8	27 39–13	326	3.4 6.1–2.2	24 44–15
Y	810	1.5 3.1–1.0	680	0.29 0.27–0.14	2.0 1.9–1.0	177	0.077 0.14–0.050	0.55 0.99–0.35
Y*	678	3.1 0.4–0.3	652		2.8 0.6–0.5	132		2.66 0.61–0.50
Zr	943	4.7 9.9–3.2	795	1.6 2.6–0.8	11 19–5	248	0.63 1.41–0.40	4.5 10.0–2.9
Nb	799	0.12 0.26–0.08	643	0.20 0.41–0.09	1.4 2.9–0.7	174	0.074 0.13–0.048	0.52 0.95–0.34

Table 4. (Contd.)

Component	Mid-ocean ridges		Ocean islands			Continental intraplate settings		
	<i>n</i>	I	<i>n</i>	I	II	<i>n</i>	I	II
Ba	690	0.83 2.7–0.6	676	1.2 3.2–0.6	8.8 22.8–4.2	358	6.7 37–4.3	48 260–31
La	1079	0.23 0.48–0.15	841	0.072 0.213–0.035	0.51 1.51–0.24	164	0.10 0.33–0.06	0.68 2.4–0.44
Ce	1189	0.58 1.23–0.39	725	0.25 1.10–0.12	1.8 7.8–0.9	215	0.25 0.47–0.16	1.8 3.3–1.1
Nd	888	0.54 1.13–0.36	725	0.18 0.52–0.09	1.3 3.7–0.6	152	0.10 0.18–0.06	0.69 1.3–0.45
Sm	966	0.18 0.38–0.12	741	0.048 0.083–0.023	0.34 0.59–0.16	199	0.023 0.42–0.015	0.16 0.30–0.11
Eu	807	0.062 0.132–0.042	703	0.015 0.017–0.007	0.11 0.12–0.05	131	0.0059 0.011–0.0038	0.042 0.075–0.027
Gd	561	0.23 0.48–0.15	457	0.079 0.073–0.038	0.56 0.52–0.27	100	0.019 0.034–0.012	0.13 0.24–0.09
Gd*	532	0.47 0.05–0.04	457		0.57 0.11–0.09	78		0.59 0.16–0.13
Dy	793	0.24 0.52–0.17	723	0.054 0.051–0.026	0.39 0.36–0.18	134	0.016 0.028–0.010	0.11 0.20–0.07
Er	651	0.16 0.33–0.11	626	0.026 0.024–0.013	0.19 0.17–0.09	94	0.0074 0.013–0.0048	0.052 0.095–0.034
Er*	650	0.34 0.03–0.02	626		0.29 0.07–0.06	94		0.28 0.07–0.05
Yb	831	0.15 0.32–0.10	835	0.024 0.022–0.012	0.17 0.16–0.08	172	0.0077 0.014–0.0050	0.055 0.099–0.035
Yb*	697	0.32 0.03–0.03	722		0.25 0.09–0.07	134		0.25 0.11–0.08
Lu	469	0.022 0.047–0.015	224	0.0037 0.0035–0.0018	0.026 0.025–0.013	78	0.0011 0.0020–0.0007	0.0078 0.014–0.0050
Lu*	381	0.046 0.006–0.005	224		0.031 0.006–0.005	42		0.037 0.026–0.015
Hf	434	0.12 0.26–0.08	349	0.049 0.046–0.024	0.35 0.32–0.17	82	0.011 0.019–0.007	0.075 0.140–0.048
Ta	406	0.014 0.030–0.010	223	0.010 0.010–0.005	0.074 0.069–0.036	61	0.0022 0.0074–0.0014	0.015 0.053–0.010
Pb	362	0.037 0.077–0.025	245	0.010 0.010–0.005	0.073 0.068–0.035	65	0.0047 0.020–0.0030	0.033 0.140–0.022
Th	561	0.018 0.039–0.012	334	0.014 0.032–0.006	0.096 0.226–0.046	172	0.0077 0.034–0.0067	0.055 0.240–0.047
U	433	0.0047 0.010–0.003	315	0.0051 0.0074–0.0025	0.036 0.053–0.018	153	0.0049 0.016–0.0032	0.035 0.110–0.022

Note: *n* is the number of determinations. The contents of elements are calculated as geometric means, and the maximum deviation of an individual measurement from the average value is no higher than 2σ with a probability of 95%. Standard deviations are shown beneath the values (first number shows the positive deviation, and the second number is the negative deviation).

* Contents of elements were calculated on the basis of their ratio to Dy, assuming that the average Dy content of the mantle is 0.531 ppm.

Assuming that the average content of Dy in the mantle is 0.531 ppm [42], and the average S/Dy value in the CR mantle is 255 (Table 3), the average content of S in

the CR mantle is estimated as 135 ppm. The similarity between the mafic magmas of MOR and CR in the average K_2O/Cl , K_2O/F , and S/Dy ratios (Table 3) implies similar average contents of Cl, F, and S in the MOR and CR mantle (Table 4): 6.5 and 9.0 ppm Cl, 8.0 and 7.4 ppm F, and 123 and 135 ppm S, respectively. In contrast to these elements, the content of H_2O in the mantle of thermal plumes is 2.5 times lower than that in the MOR mantle (60 and 150 ppm, respectively).

Let us estimate the cumulative degree of melting and differentiation of magmas (hereafter, referred to as the degree of total fractionation) for the model of a thermal plume. For the processes of fractional melting and fractional crystallization of basic magmas, the degree of total fractionation for a highly incompatible element ($D \sim 0$) is $(1 - M) = C_0/C$, where C_0 is the element content in the source (mantle) and C is the element content in the magma. For the thermal model, the contents of K_2O in the mantle and magma (Tables 1, 4) yield $(1 - M) = 0.0034$, i.e., the fraction of melt in the bulk mass of melt, solid residue, and minerals removed during crystallization is only about 0.3%. Even assuming that up to 50% of crystal phases could be eliminated in magma chambers and the degree of source melting could be twice as high, the segregation of such an amount of melt from the mantle is questionable. We conclude therefore that the purely thermal model of mantle plumes is improbable (cf. [22, 23]).

In the model of moderately enriched mantle (II in Table 4), the K_2O content in the mantle of intraplate settings or plumes (oceanic and continental) is estimated as 510 ppm [23]. In accordance with Table 4, the CPM contains 420 ppm H_2O , 63 ppm Cl, and 52 ppm F. If the Dy content of this material is similar to that of the DM (0.531 ppm), its S content will also be similar to that in the DM and, consequently, in the thermal model (135 ppm). This supposition is supported by the similarity of basic magmas from all the geodynamic environments in Dy and S contents (Fig. 2). If the moderately enriched mantle of plumes contains 0.92 ppm Dy [23], its S content is 212 ppm. With respect to the C_0/C ratio for K_2O , the average degree of total fractionation of CR magmas is about 2.5%. This value appears realistic for alkaline mantle magmas. However, such low degrees of total fractionation of mantle magmas could result in that the ratios of incompatible elements in the magma will be significantly different from those in the source (mantle); therefore, it is desirable to use the ratios of elements with similar partition coefficients between solid and liquid phases. Such ratios (e.g., K_2O/Cl , H_2O/Ce , and P_2O_5/F) are termed canonical [48]. If the Ce content of the plume mantle is 3.9 ppm [23], the H_2O/Ce ratio of magmas (Table 3) yields a mantle H_2O content of 850 ppm. This is comparable with the H_2O content of the OPM (460 ppm). The contents of Cl and S in the CR mantle remain to be the same. The average content of F in the CR mantle calculated from the P_2O_5/F ratio is about 100 ppm. This value is twice that obtained above from the K_2O/F ratio and the average content of F in the mantle of suboceanic plumes [23]. Variations in the

degree of melting within 0.01–0.03 exert a minor influence on these ratios. Calculations by the equation $(C^1/C^2)/(C_0^1/C_0^2) = (1 - M)$ show that at $D_1 - D_2 = 0.03$ and $(1 - M) = 0.01-0.03$, the ratio of incompatible elements will decrease by no more than 10% compared with the mantle value, which is lower than the variance of such ratios in natural rocks. The effects of differences in the degree of incompatibility are considered below in more detail for other incompatible elements.

Average Contents of Other Incompatible Trace Elements in the Mantle. Let us estimate the average contents of trace elements in the mantle of mid-ocean ridges (DM), suboceanic plumes (OPM), and subcontinental plumes (CPM) from the available compositions of basic magmas. The composition of DM is used as a check on the validity of our method, because there are published estimates for the DM composition, which can be compared with our results. The average contents of trace elements in the mantle are first estimated from their ratios to K_2O content. The calculated values for the DM [22], OPM [23] and CPM are given in Table 4 for the models of isochemical (I) and moderately enriched (II) compositions of OPM and CPM. In the ensuing discussion, the model of the moderately enriched composition of plume material is considered, because the purely thermal model leads to controversies [23]. Note that the average composition of the OPM in Table 4 is somewhat different from that reported by [23] because during the time between the preparation of these papers, our database expanded and the method of calculation was modified.

Our results are compared with the estimates of other authors in Table 5. For many elements, the difference is no higher than the 2σ values of our average contents. The discrepancy in Cl was discussed by [22] who explained it by the overestimated role of shallow-level assimilation of Cl by magmas and the involvement of Cl in deep mantle recycling. Figures 3 and 4 and Table 4 show that the estimated average contents of moderately incompatible elements in the OPM and CPM are significantly lower than those of the DM. The possible reason is the difference in the degree of incompatibility between the moderately incompatible elements and K_2O .

In order to account for variations in the degree of trace element incompatibility relative to K_2O , we used the relation $(C^1/C^2)/(C_0^1/C_0^2) = (1 - M)^{D_1 - D_2}$, where D_1 and D_2 are the bulk partition coefficients of K_2O and any of the trace elements between the solid phases and magma [48]. The higher the absolute value of $D_1 - D_2$, the greater the difference between (C_0^1/C_0^2) and (C^1/C^2) . For instance, the values D_1 and D_2 are the bulk partition coefficients of K_2O and any of the trace elements between the solid phases and magma [48]. The higher the absolute value of $D_1 - D_2$, the greater the difference between (C_0^1/C_0^2) and (C^1/C^2) . For instance, the values $C_0^1/C_0^2 = 0.475$ and $(C^{K_2O}/C^{H_2O}) = 0.5$ in the DM are similar, and there is no need to apply a correction for the difference between the incompatibilities of K_2O and H_2O . In contrast, a more significant correction is needed for K_2O and Y:

$(C_0^{K2O}/C_0^Y) = 40$ and $C^{K2O}/C^Y = 50$. Even with these corrections, the average contents of HREE in the OPM appeared to be slightly higher than those of the DM, but the average contents of moderately incompatible elements were still too low. What could be the reason for this discrepancy?

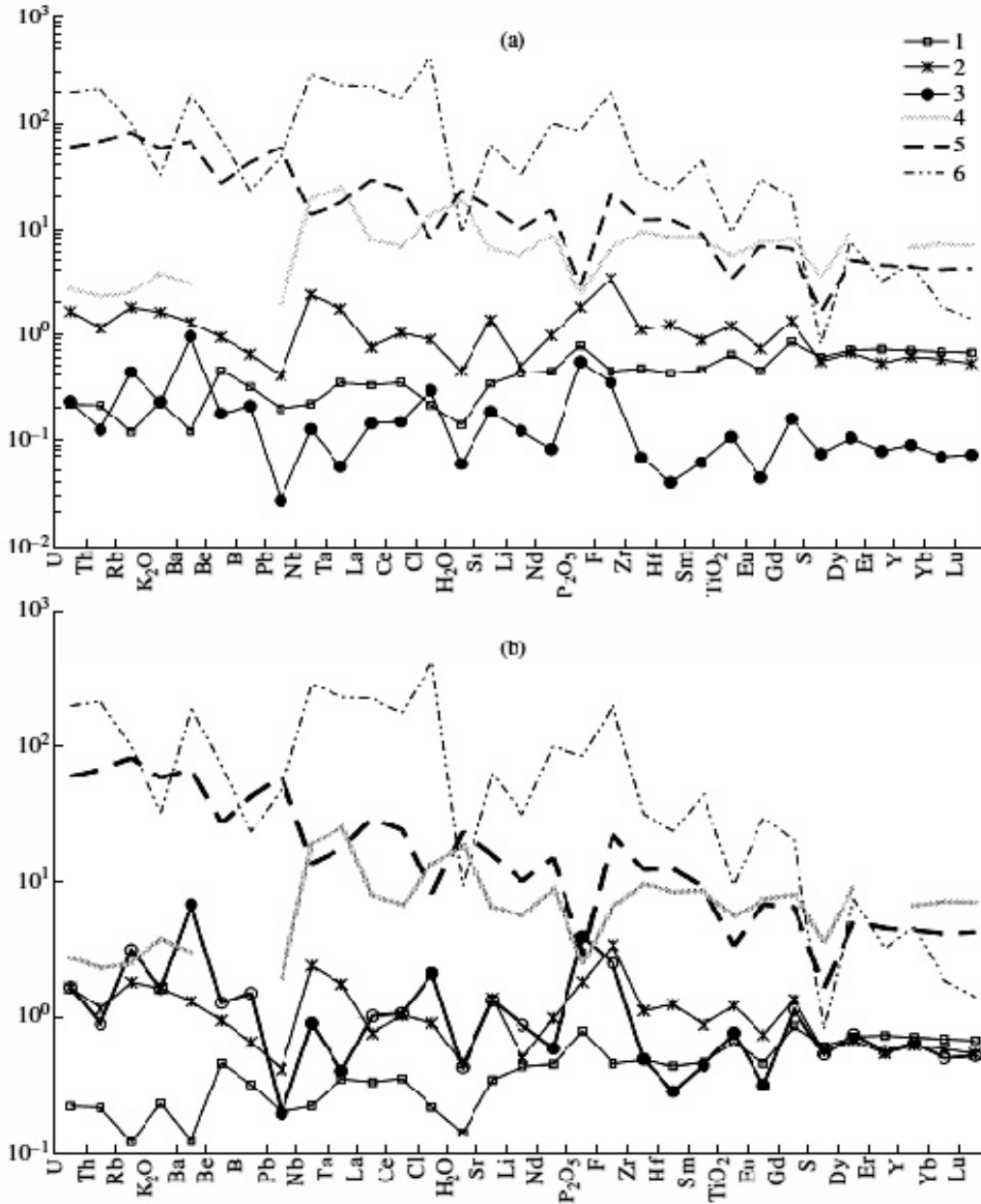


Fig. 3. Spidergrams of the average compositions of the (1) depleted mantle, (2) mantle of oceanic plumes, and (3) mantle of continental plumes calculated from the concentration ratios of K_2O and incompatible trace elements in magmas on the basis of the (a) thermal and (b) moderately enriched models (Table 4). See text for explanation. Also shown are the average compositions of the (4) oceanic crust (Wedepohl and Hartmann, 1994), (5) oceanic crust (Rudnick and Gao, 2003), and (6) group I kimberlites (Le Roex et al., 2003).

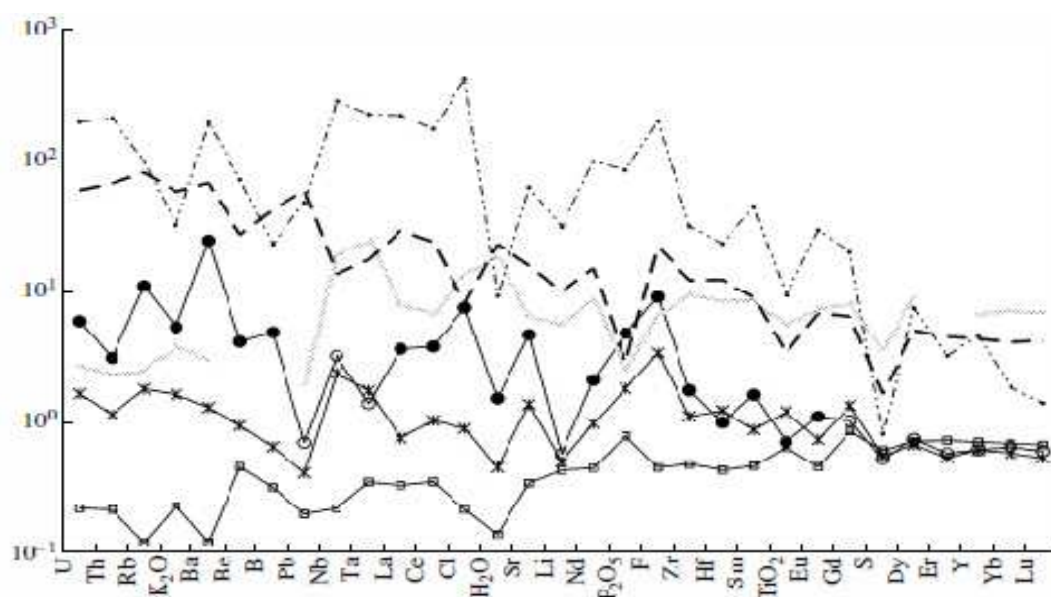


Fig. 4. Spidergrams for the average compositions of the DM, OPM, and CPM calculated from the ratios of the average contents of K_2O and incompatible trace elements with corrections for the difference in the degree of incompatibility between K_2O and trace elements in magmas (Table 5). The average contents of moderately incompatible trace elements ($Th, U, P_2O_5, HREE, Li, and S$) were calculated from their ratios to Dy, assuming that the average content of Dy in the OPM, CPM-2, and DM is 0.531 ppm. The average contents of incompatible elements in the CPM-2 were calculated assuming similar degrees of melting (0.08) for the OPM and CPM. Symbols are the same as in Fig. 3.

The estimates of incompatible trace element contents in the mantle rely heavily on the accepted K_2O content. The average contents of K_2O in the DM and OPM are well constrained, and K_2O variations in the basic magmas of MOR and OI are relatively low. The average content of K_2O in the CPM was taken to be equal to that of the OPM, because mantle plumes are deep structures, and their composition should not be strongly dependent on the presence or absence of continental crust above them. Nonetheless, the suggestion that the CPM is richer in K_2O than the OPM cannot be ruled out. In order to determine the K_2O content of the CPM, it is necessary to estimate the content of any other incompatible element or the total degree of magma fractionation. It can be supposed that the total degrees of fractionation of magmas formed in the CPM and OPM are similar and close to 0.08. Then, the content of K_2O in the CPM will be 1600 ppm. Furthermore, it can be supposed that all the mantle sources are similar in HREE contents. This suggestion is based on the similarity in the behavior of these elements in the magmas of MOR, OI, and CR (Table 1, Fig. 2) and the low sensitivity of moderately incompatible elements to the migration of small portion of melts and fluids in the mantle. The contents of HREE in the DM are rather tightly constrained. Therefore, we accepted that the Dy content in the CPM is identical to that of the DM (0.531 ppm; Salters and Stracke, 2004). Given the refined value $K_2O^0/Dy^0 = 3443$, 1828 ppm K_2O is obtained for the CPM. The obtained K_2O estimates for the CPM are similar under both these assumptions. Since their plausibility cannot yet be rigorously demonstrated, two variants of average trace element contents in the CPM can be considered (Table 5): (1) estimated from an

Table 5. Average contents of elements (ppm) in the depleted mantle, mantle of suboceanic and subcontinental plumes, mantle of Vesuvius, and primitive mantle

Elements and their ratios	Depleted mantle			Oceanic plume mantle (OPM)	Continental plume mantle (CPM)		Vesuvius mantle	Primitive mantle (Palme and O'Neill, 2003)
	our data	Workman and Hart, 2005	Salters and Stracke, 2004		CPM-1	CPM-2		
K ₂ O	72		72	510	1600	4400	315	
H ₂ O	160	110	116	490	1400	1500	1080	
Cl	340-110*	50-40**	±58**	610-230*	2600-910*	1200-630*		
	6.5	0.38	0.51	27	200	470	30	
F	23-4.4	±0.25	±0.09	58-13	600-130	260-170		
	11.2	-	11.0	85	230	270	25	
S	24-7.7	-	±4.5	150-41	530-160	550-180		
	123 (61)	-	119	71 (64)	135 (100)	130 (120)	200	
	35-28	-	±30	120-45	180-80	130-60		
TiO ₂	1500 (700)***	1196	1330	2180 (2100)	1370 (1160)	1250 (890)	2140	
	470-360	1113-1263	±160	1170-760	790-500	790-490		
P ₂ O ₅	150 (100)	190	270	294 (360)	590 (690)	1050 (900)	197	
	132-69	-	±70	263-138	1010-370	560-360		
Li	0.64 (0.32)	-	0.70	0.52 (0.58)	1.39 (0.29)	2.0 (1.55)	1.6	
	0.10-0.08	-	±0.06	0.10-0.08	3.14-0.96	5.2-1.4		
Be	0.032	-	0.025	0.066	0.089	0.69	0.07	
	0.068-0.022	-	±0.025	0.061-0.032	0.230-0.057	0.58-0.32		
B	0.083	-	0.06	0.17	0.39	3.18	0.26	
	0.175-0.056	-	±0.05	0.17-0.08	2.30-0.25	3.18-1.59		
Rb	0.073	0.050	0.088	1.1	1.9	12.5	0.605	
	0.170-0.050	0.023-0.079	±0.022	1.9-0.5	7.5-1.2	9.4-5.4		
Sr	7.3	7.664	9.8	30	26	75	20.3	
	15.0-5.0	6.462-8.709	±1.9	43-14	48-16	29-21		
Y	3.1 (1.8)	3.328	4.07	2.8 (2.4)	2.66 (0.66)	2.4 (2.2)	4.37	
	0.4-0.3	3.179-3.445	±0.49	0.6-0.5	0.61-0.50	0.5-0.4		
Zr	5.2	5.082	7.94	12	5.0	17	10.81	
	10.9-3.5	4.465-5.601	±1.75	21-6	11.0-3.2	8-6		
Nb	0.20	0.1485	0.21	1.8	0.61	2.2	0.588	
	0.26-0.08	0.1277-0.1671	±0.07	2.9-0.7	0.95-0.34	1.1-0.8		
Ba	0.83	0.563	1.20	8.8	48	130	6.75	
	2.7-0.6	0.256-0.896	±0.59	22.8-4.2	260-31	64-43		
La	0.23	0.192	0.234	0.51	0.68	4.4	0.686	
	0.48-0.15	0.157-0.222	±0.033	1.51-0.24	2.4-0.44	1.9-1.3		
Ce	0.61	0.550	0.772	1.9	1.9	8.0	1.786	
	1.30-0.41	0.451-0.639	±0.116	8.2-0.9	3.5-1.2	5.0-3.1		

Table 5. (Contd.)

Elements and their ratios	Depleted mantle			Oceanic plume mantle (OPM)	Continental plume mantle (CPM)		Vesuvius mantle	Primitive mantle (Palme and O'Neill, 2003)
	our data	Workman and Hart, 2005	Salters and Stracke, 2004		CPM-1	CPM-2		
Nd	0.57 1.19-0.38	0.581 0.507-0.644	0.713 ±0.050	1.4 3.9-0.6	0.72 1.36-0.47	2.2 4.1-1.4	4.6 2.3-1.6	1.327
Sm	0.20 0.42-0.13	0.239 0.217-0.256	0.270 ±0.027	0.37 0.65-0.18	0.18 0.33-0.12	0.56 1.04-0.38	0.97 0.74-0.42	0.431
Eu	0.068 0.145-0.046	0.096 0.088-0.102	0.107 ±0.011	0.12 0.13-0.06	0.046 0.082-0.030	0.144 0.26-0.09	0.24 0.10-0.07	0.162
Gd	0.47 (0.26) 0.05-0.04	0.358 0.332-0.379	0.395 ±0.039	0.57 (0.64) 0.11-0.09	0.59 (0.15) 0.16-0.13	0.59 (0.47) 0.16-0.13	0.73 (0.80) 0.26-0.19	0.571
Dy	0.531 (0.29)	0.505 0.480-0.525	0.531 ±0.053	0.531 (0.47)	0.531 (0.13)	0.531 (0.41)	0.531 (0.47)	0.711
Er	0.34 (0.21) 0.03-0.02	0.348 0.334-0.359	0.371 ±0.037	0.29 (0.25) 0.07-0.06	0.28 (0.06) 0.07-0.05	0.28 (0.19) 0.07-0.05	0.25 (0.17) 0.04-0.04	0.465
Yb	0.32 (0.20) 0.03-0.03	0.365 0.353-0.374	0.401 ±0.028	0.25 (0.22) 0.16-0.08	0.25 (0.07) 0.11-0.08	0.25 (0.22) 0.11-0.08	0.26 (0.27) 0.13-0.08	0.462
Lu	0.046 (0.031) 0.006-0.005	0.058 0.056-0.059	0.063 ±0.006	0.031 (0.036) 0.006-0.005	0.037 (0.011) 0.026-0.015	0.037 (0.034) 0.026-0.015	— —	0.0711
Hf	0.13 0.29-0.09	0.157 0.142-0.170	0.199 ±0.016	0.38 0.35-0.19	0.082 0.154-0.053	0.26 0.48-0.17	— —	0.3
Ta	0.014 0.030-0.010	0.0096 0.0082-0.0108	0.0138 ±0.0045	0.074 0.069-0.036	0.015 0.053-0.010	0.047 0.166-0.031	— —	0.04
Pb	0.026 0.079-0.026	0.018 0.015-0.021	0.0232 ±0.0070	0.059 0.070-0.036	0.17 0.14-0.02	0.53 0.45-0.07	1.7 0.7-0.5	0.185
Th	0.018 0.039-0.012	0.0079 0.0068-0.0089	0.0137 ±0.0041	0.096 0.226-0.046	0.055 0.240-0.047	0.17 0.75-0.15	1.1 0.6-0.4	0.0834
U	0.0047 0.010-0.003	0.0032 0.0027-0.0036	0.0047 ±0.0014	0.036 0.053-0.018	0.035 0.110-0.022	0.11 0.34-0.07	0.3 0.2-0.1	0.0218
Nb/Ta	14.3	15.5	15.2	24.3	40.7	40.7	—	14.7
Nb/U	42.6	46.4	44.7	50.0	17.4	17.4	7.3	27.0
Ba/Rb	11.4	11.3	13.6	8.0	25.3	25.3	10.4	11.2
Ce/Pb	23.5	30.5	33.3	32.2	11.2	11.2	4.6	9.7
H ₂ O/Ce	260	200	150	260	240	240	190	605

* Standard deviations are shown beneath the geometric mean values (first number shows the positive deviation, and the second number is the negative deviation).

** Range of variations is shown beneath the arithmetic mean content.

*** Values without parentheses show the geometric mean contents of elements corrected for the incompatibilities of elements and calculated from the ratios of elements to Dy and an average Dy content of 0.531 ppm, and values in parentheses are the average contents of elements calculated from their ratios to K₂O. The average contents of Nb were calculated from the Nb/U ratio, and the average contents of Pb were calculated from the Pb/Ce ratio.

average K_2O content of 510 ppm (CPM-1 in Table 5) and (2) estimated on the basis of $(1 - M) = 0.08$ and $Dy_0 = 0.531$ ppm, which implies an average K_2O content of 1600 ppm (CPM-2 in Table 5).

The contents of HREE and other geochemically similar elements (Li, Y, Ti, and P) in the DM can be refined using Dy as a reference element (Salters and Stracke, 2004). The concentration ratios of elements to Dy (Table 1) yield the following contents for the DM (ppm): 123 S, 0.47 Gd, 3.1 Y, 0.34 Er, 0.32 Yb, 0.046 Lu, 1500 TiO_2 , 150 P_2O_5 , and 0.64 Li. These estimates (Table 5) are in adequate agreement with the values reported by [42] and [48].

The same procedure was used for the calculation of average element contents from their ratios to K_2O (values in parentheses in Table 5) and Dy (values without parentheses in Table 5) in the OPM and CPM. Similarly, the contents of selected trace elements were calculated for the mantle source of Vesuvius Volcano (Table 5).

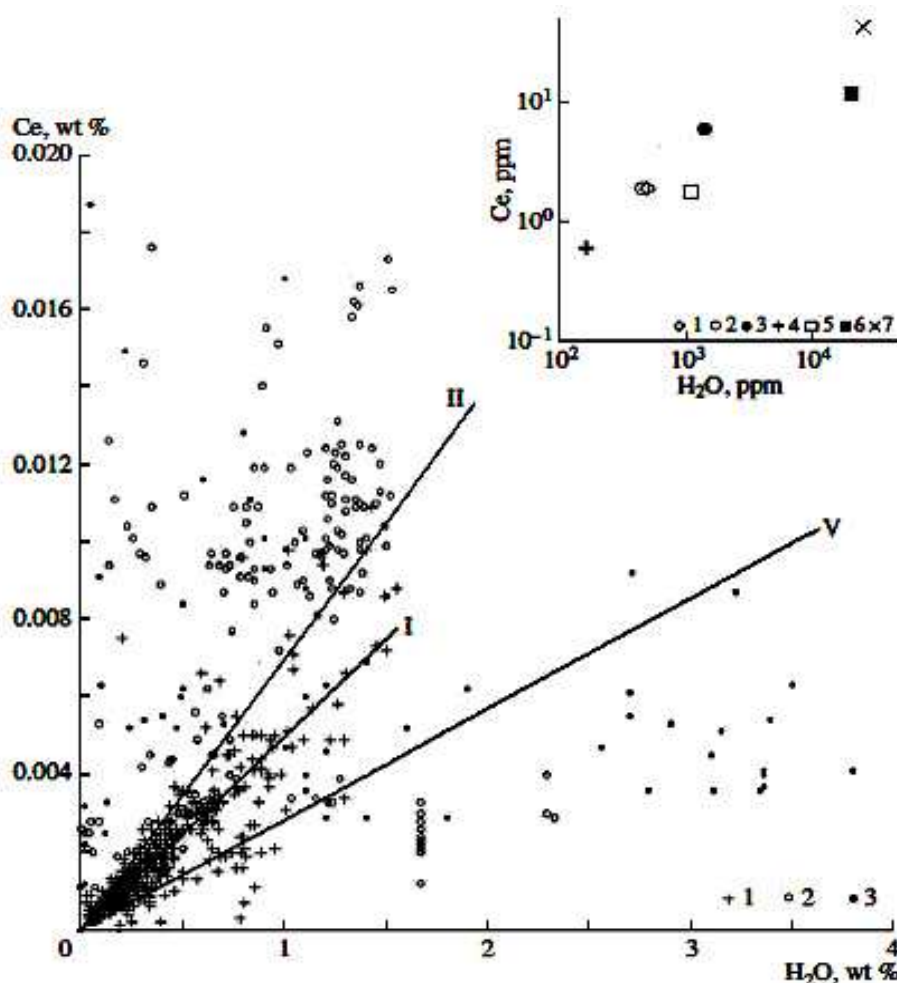


Fig. 5. Variations in cerium and water contents in the basic magmas of (1) mid-ocean ridges, (2) ocean islands, and (3) continental intraplate settings. The inset shows the average compositions of the sources of basic magmas: (1) OPM, (2) CPM-1, and (3) CPM-2; (4) the average composition of the DM; (5) the average composition of the primitive mantle (Palme and O'Neill, 2003); (6) the average composition of the oceanic crust (Wedepohl and Hartmann, 1994); and (7) the average composition of the continental crust (Rudnick and Gao, 2003). The regression lines drawn through the origin have the following correlation coefficients: (I) $R = 0.88$ (number of analyses $n = 540$) for MOR magmas and DM, (II) $R = 0.70$ ($n = 192$) for OI magmas and OPM, and (V) $R = 0.49$ ($n = 66$) for CR magmas and CPM.

[48] distinguished several canonical ratios, whose values are fairly uniform in the majority of basic magmas from MOR and OI: $H_2O/Ce = 200$, $Nb/Ta = 15.5$,

$Nb/U = 46.4$, $Ba/Rb = 11.3$, $Ce/Pb = 30.5$, and $F/P = 0.27$. According to these authors, the very small variations in these ratios are related to the very close values of their bulk partition coefficients between solid phases and melt. In such a case, these ratios in magmas must be identical to those in their sources. Figure 5 shows the contents of H_2O and Ce in basic magmas. The H_2O/Ce ratio of MOR magmas is 200. In contrast, we obtained $H_2O/Ce = 260$ for the DM (Table 5). The difference is related to the different sets of analyses: the ratio H_2O/Ce in Table 5 was determined using the estimates of average H_2O and Ce contents in all samples, whereas Fig. 5 shows only those samples in which both H_2O and Ce were analyzed (which are much fewer in number). The same problem is relevant to other canonical ratios. In this paper, we estimated the average ratios of incompatible element contents using all the available analytical data rather than only those samples in which both elements were analyzed (Table 5).

We can now consider in more detail the obtained average trace element contents in various mantle reservoirs (Table 5; Figs. 3, 4). As was previously suggested [23] the thermal model is unlikely (Fig. 3a), because it implies that the CPM is more depleted in incompatible elements than the DM. The moderately enriched model of the OPM and CPM (Fig. 3b) appears more realistic with respect to the most incompatible elements, whose contents in the OPM and CPM are higher than in the DM. The contents of many incompatible trace elements in the OPM and CPM reach or even exceed the primitive mantle level. However, this model with a K_2O content of 510 ppm fails to explain the low contents of moderately incompatible elements in the CPM (Table 5). Accepting the higher K_2O content that was discussed above, we obtain more realistic distributions of trace elements in the OPM and CPM (Fig. 4).

The distribution patterns of trace elements are generally similar in all the mantle reservoirs (Figs. 3, 4). The DM exhibits negative anomalies of Rb, Ba, Pb, Nb, Cl, and H_2O and a general increase in normalized contents from highly incompatible to moderately incompatible elements. The OPM shows positive anomalies of Rb, K_2O , Be, Nb, Ta, and F and negative anomalies of B, Pb, H_2O , and S. All these variations in the normalized average contents of elements in the OPM are not far from the composition of the primitive mantle. The CPM shows negative anomalies of Th, K_2O , Pb, and Ta, positive anomalies of Ba, Cl, F, and a slight depletion in Ti, Li, and S. In contrast to the DM composition, there is a general decrease in normalized contents from the highly to moderately incompatible elements. Although the general shape of the CPM-1 spidergram is similar to that of the OPM, the former displays more significant variations in highly incompatible elements and lower contents of moderately incompatible elements. This distinction vanishes in the CPM-2 composition. The mantle magma source of Vesuvius Volcano (Table 5) exhibits almost all the compositional characteristics of the CPM-2, except for the higher normalized contents of strongly incompatible elements.

RATIOS OF AVERAGE INCOMPATIBLE ELEMENT CONTENTS IN THE SOURCES AND BASIC MAGMAS (C^0/C)

The C^0/C ratios of incompatible components are important characteristics of mantle melting. For the most incompatible elements, when the degree of melting

(F) is much higher than the bulk partition coefficient between solid phases and melt (D), the C^0/C value approaches F . If $F \leq D$ (very low degrees of melting), C^0/C characterizes the value of D for the given element. These relations are independent of the mechanism of melt segregation from the crystal matrix (fractional or batch melting).

Basaltic magmas are formed at relatively high degrees of mantle melting (5–15%), and the C^0/C values of mantle sources (Table 5) and average magma compositions (Table 1) correspond to the average degrees of melting. This ratio averages 0.076 in the DM, 0.106 in the OPM, and 0.107 in the CPM. The obtained values illustrate two important features. On the one hand, the higher values for the plume settings compared with the DM are in agreement with the suggestion on the high temperatures of mantle plumes. On the other hand, the identical values for subcontinental and suboceanic plumes are indicative of their similar compositions and structures.

As was noted above, under certain conditions, the C^0/C ratio (Table 1, 5) characterizes the bulk partition coefficients of elements between the source and the magma (Table 6), provided that the basic magmas (Table 1) were in equilibrium with their sources (DM, OPM, and CPM). In fact, such estimates require the compositions of primary magmas, i.e., basic melts in equilibrium with the mineral assemblages of the DM, OPM, or CPM and unaffected by crystallization or other

Table 6. Bulk partition coefficients of elements between source material and magma

Element	Bulk partition coefficient		
	D_{DM}	D_{OPM}	D_{CMP-2}
K ₂ O	0.051	0.089	0.083
H ₂ O	0.050	0.094	0.099
Cl	0.050	0.090	0.090
F	0.071	0.125	0.111
S	0.152	0.232	0.122
TiO ₂	0.112	0.123	0.114
P ₂ O ₅	0.111	0.117	0.150
Li	0.111	0.124	0.081
Be	0.051	0.089	0.083
B	0.052	0.092	0.082
Rb	0.051	0.091	0.091
Sr	0.054	0.094	0.100
Y	0.110	0.119	0.126
Zr	0.057	0.097	0.109
Nb	0.054	0.090	0.092
Ba	0.051	0.090	0.088
La	0.052	0.091	0.093
Ce	0.056	0.093	0.097
Nd	0.057	0.091	0.103
Sm	0.058	0.101	0.109
Eu	0.061	0.100	0.110
Gd	0.112	0.124	0.112
Dy	0.112	0.112	0.123
Er	0.113	0.121	0.132
Yb	0.110	0.112	0.139
Lu	0.112	0.127	0.139
Hf	0.055	0.095	0.102
Ta	0.050	0.084	0.092
Pb	0.052	0.093	0.098
Th	0.050	0.090	0.121
U	0.053	0.088	0.095

differentiation events after magma segregation from the source. The compositions of primary magmas must be poorer in incompatible trace elements than the compositions shown in Table 1, and, correspondingly, the obtained values constrain in fact the minimum bulk partition coefficients of trace elements. For instance, the geometric mean K_2O content in the magmas of the CPM with $MgO > 8$ wt %, which is closer to the K_2O content of primary magmas than the value in Table 1, is 1.31 wt %, and the bulk partition coefficient of K_2O between the CPM-2 and a near-primary melt is 0.128. This is much higher than the value in Table 6. A similar situation was obtained for other incompatible elements. Since there are few data for highly magnesian magmas, the values given in Table 6 were used as minimum estimates.

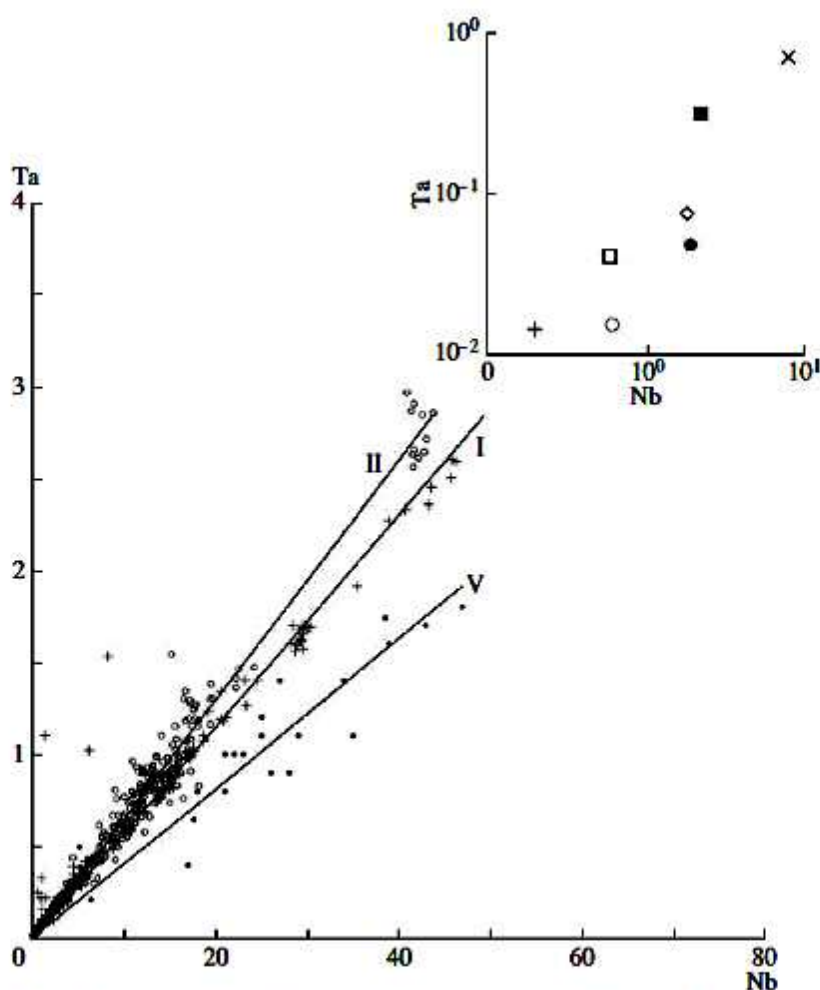


Fig. 6. Variations in Nb and Ta contents (ppm) in the basic magmas of MOR, OI, and CR and average ratios of these elements in the magmas and their sources, DM, OPM, and CPM (shown by lines corresponding to the respective regression equations). Symbols are the same as in Fig. 5. The regression lines have the following correlation coefficients: (I) $R = 0.98$ ($n = 380$) for MOR magmas and DM, (II) $R = 0.99$ ($n = 223$) for OI magmas and OPM, and (V) $R = 0.98$ ($n = 45$) for CR magmas and CPM.

The bulk partition coefficients obtained for the DM and MOR basic magmas derived from this source range from 0.05 to 0.152 (Table 6). All the values can be divided into two groups: (1) $D = 0.050$ – 0.071 for the highly incompatible elements K, H_2O , Cl, F, Be, B, Rb, Sr, Zr, Hf, Nb, Ta, Ba, LREE, Pb, Th, and U; and (2) $D = 0.110$ – 0.152 for the moderately incompatible elements Ti, P, S, Li, Y,

and HREE. These estimates of the bulk partition coefficients of incompatible trace elements for the DM are not consistent with the values reported by [48]. For instance, our D values for Rb, Ba, Nb, Ta, U, Th, and LREE are close to 0.05–0.06, whereas [48] reported values of 0.0001, 0.00012, 0.0034, 0.0034, 0.0011, 0.001, and 0.01–0.05, respectively. It is evident that even the use of primitive magma compositions does not provide

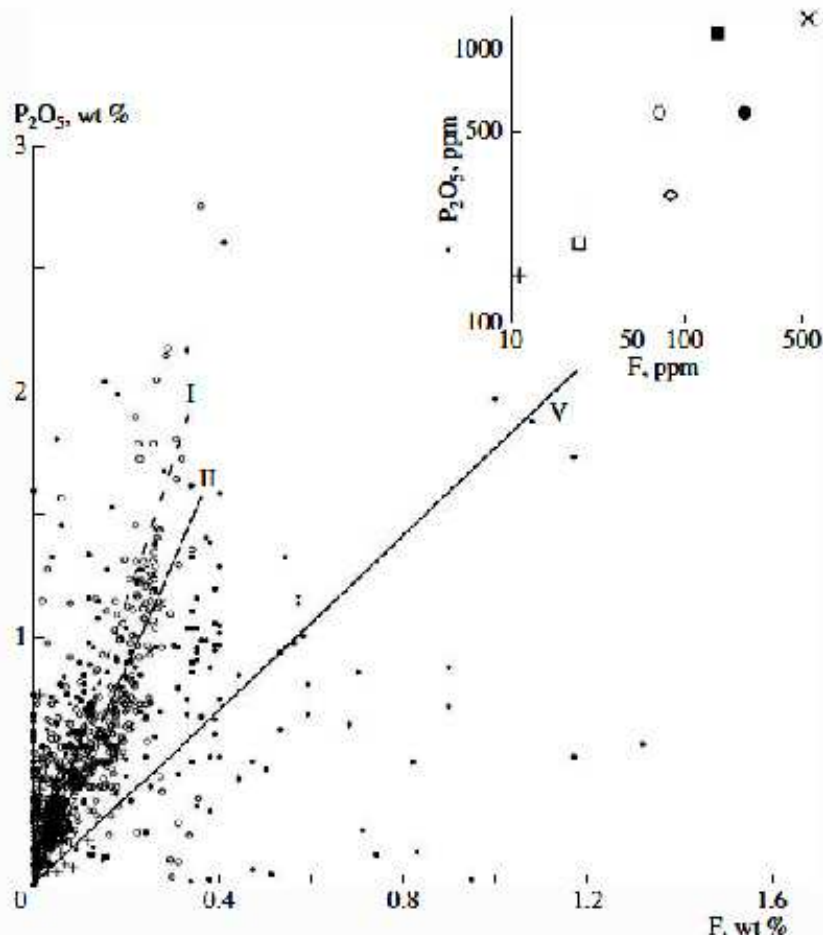


Fig. 7. Variations in the contents of P_2O_5 and F in the basic magmas of MOR, OI, and CR and average ratios of these components in the magmas and their sources, DM, OPM, and CPM (shown by lines corresponding to regression equations). Symbols are the same as in Fig. 5. The regression lines have the following correlation coefficients: (I) $R = 0.71$ ($n = 256$) for MOR magmas and DM, (II) $R = 0.83$ ($n = 931$) for OI magmas and OPM, and (V) $R = 0.53$ ($n = 221$) for CR magmas and CPM.

agreement with the published estimates of the bulk partition coefficients of incompatible elements. The only way to approach these values is to use the compositions of melts derived at very low degrees of melting, i.e., alkaline magmas with the highest contents of incompatible elements. Approximate estimates can be obtained using the average contents of elements plus 2σ (Table 1). The C_0/C ratios for such compositions and the CPM-2 composition (Table 6) vary from ~ 0.01 for the most incompatible elements (K, Cl, Rb, B, Ba, La, Pb, Th, U, etc.) to 0.07–0.08 for moderately incompatible Y and HREE. It should be noted that the condition $F \leq D$ may not hold for the most incompatible elements, and the real D values can be somewhat lower. The low D values for K and Ba indicate that micas and amphiboles did not play a significant role during magma generation and

differentiation. The relatively low D values for HREE suggest a low average content of garnet in the solid residue. Indeed, given a garnet–melt partition coefficient of Yb of 5 (Irving and Frey, 1978), the bulk partition coefficient of Yb between the mantle assemblage and melt will be lower than 0.1, only if the content of garnet is no higher than 2%.

VARIATIONS IN THE CONTENTS AND RATIOS OF INCOMPATIBLE COMPONENTS IN BASIC MAGMAS AND MANTLE SOURCES

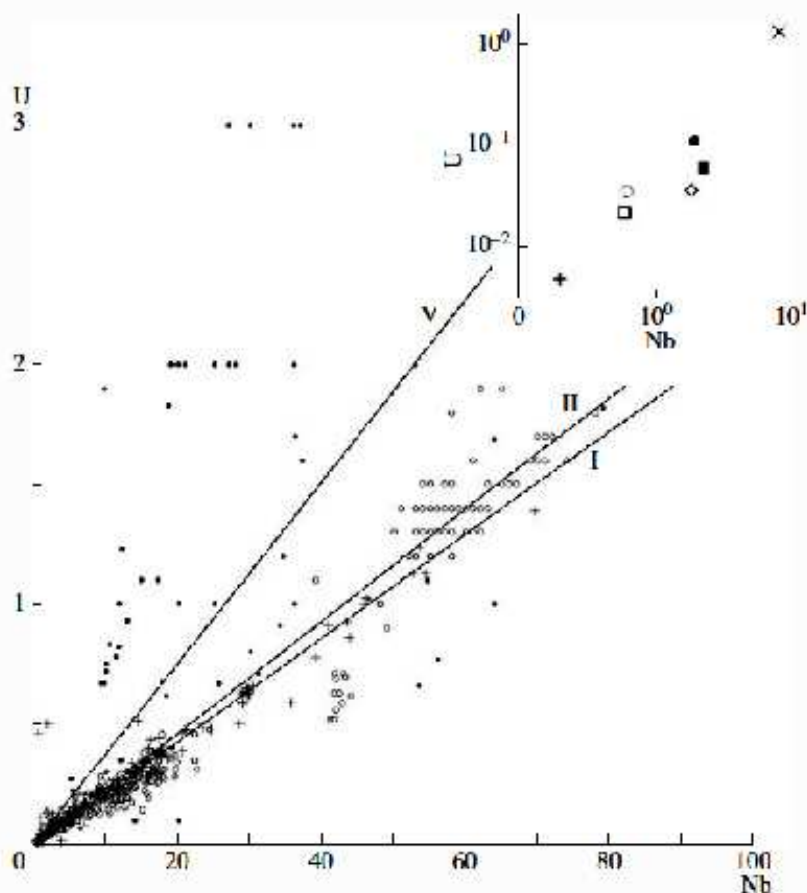


Fig. 8. Variations in the contents of U and Nb (ppm) in the basic magmas of MOR, OI, and CR and average ratios of these components in the magmas and their sources. DM, OPM, and CPM (shown by lines corresponding to regression equations). Symbols are the same as in Fig. 5. The regression lines have the following correlation coefficients: (I) $R = 0.98$ ($n = 373$) for MOR magmas and DM, (II) $R = 0.98$ ($n = 311$) for OI magmas and OPM, and (V) $R = 0.65$ ($n = 65$) for CR magmas and CPM.

The estimated average contents of many elements in the three sources are statistically different with a probability of more than 99%. However, the standard deviations of these values indicate considerable variations in the compositions of magmas and their sources for the geodynamic settings considered here. Consider these variations in more detail.

Consider first the trace elements that are involved in the canonical ratios (Figs. 5–10). As can be seen in Fig. 5, despite the difference in the average H_2O/Ce values of the DM, OPM, and CPM, the fields of these ratios overlap to a considerable extent. It can also be noted that the variance of magma compositions

increases from MOR through OI to CR. The average compositions of the oceanic and continental crust (Fig. 5, inset) plot at high H₂O/Ce values, but their H₂O and Ce contents are significantly lower than the highest contents in the respective magmas.

Other canonical ratios are shown in Figs. 6–10. The Nb/Ta ratios (Fig. 6) of the MOR and OI magmas are similar, and the maximum compositional variations were observed for the CR magmas and CPM sources. The average P₂O₅/F values (Fig. 7) of the MOR and OI magmas are similar to each other but are significantly lower than that of the CR magmas, which show the highest variations in this ratio. The average Nb/U (Fig. 8) of the MOR and OI magmas are also similar and lower than those of the CR magmas. The average Ba/Rb ratios (Fig. 9) are similar for all the magmas, and the magmas of OI and, especially, CR show considerable variations.

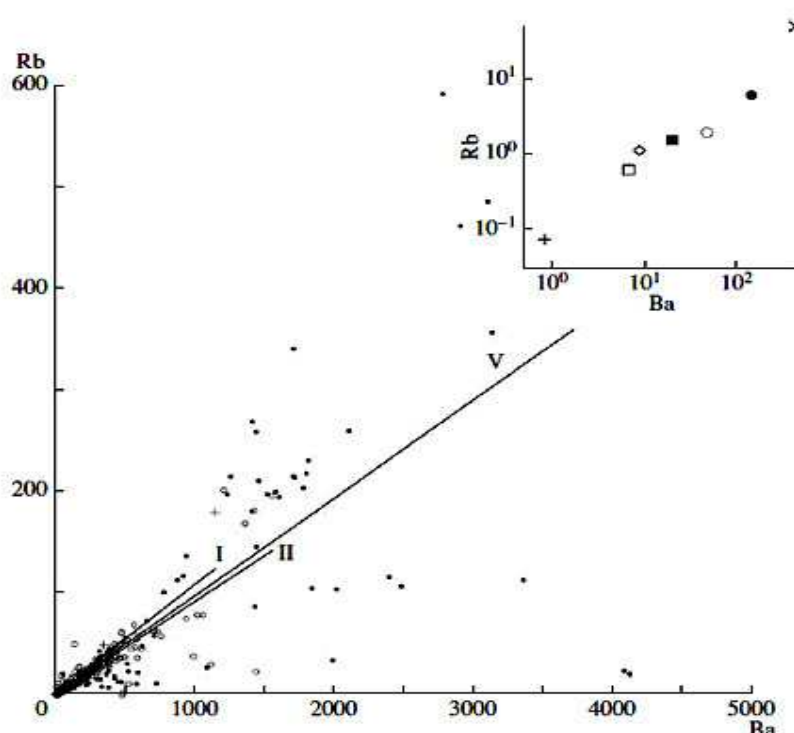


Fig. 9. Variations in the contents of Rb and Ba (ppm) in the basic magmas of MOR, OI, and CR and average ratios of these components in the magmas and their sources, DM, OPM, and CPM (shown by lines corresponding to regression equations). Symbols are the same as in Fig. 5. The regression lines have the following correlation coefficients: (I) $R = 0.92$ ($n = 478$) for MOR magmas and DM, (II) $R = 0.87$ ($n = 390$) for OI magmas and OPM, and (V) $R = 0.71$ ($n = 98$) for CR magmas and CPM.

The average Ce/Pb values (Fig. 10) of the MOR and OI magmas are identical, whereas the CR magmas show much lower Ce/Pb values and considerable variations in Ce and Pb contents. The fields of all these ratios in the magmas of various geodynamic settings overlap with each other, and there are gradual transitions between them.

Figure 11 shows the contents of volatile components and K₂O in basic magmas. This diagram also exhibits overlaps between the fields of the three geodynamic settings. The compositions of the basaltic magmas of MOR with the highest K₂O and H₂O contents coincide with the compositions of H₂O-rich OI

magmas and CR magmas with the lowest K_2O and H_2O contents (Fig. 11). Similar overlaps can be observed between the compositional fields of basic magmas in the coordinates K_2O –Cl, F–Cl, K_2O –F, F– H_2O , and Cl– H_2O . As can be inferred from Figs. 5–11, there are no distinct compositions of magma sources for MOR, OI, and CR, but there are all transitions between them.

The aforementioned types of mantle magmas from different geodynamic settings show distinctive chemical variations. For instance, the compositions of MOR basic magmas show a clear positive correlation between K_2O and H_2O contents [23], whereas the majority of magma compositions from OI vary considerably in H_2O but have almost constant K_2O (Fig. 11). Based

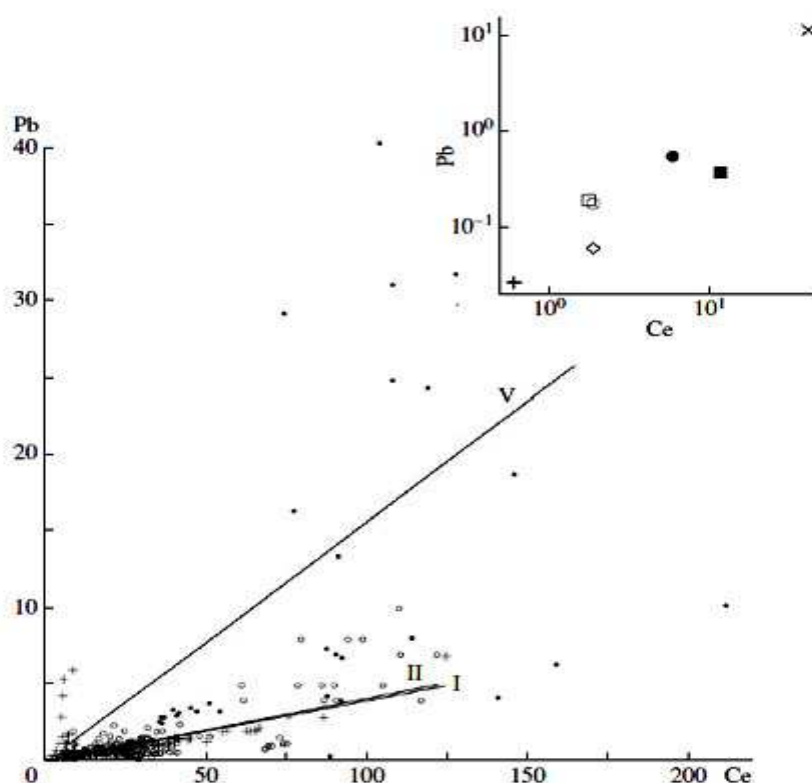


Fig. 10. Variations in the contents of Pb and Ce (ppm) in the basic magmas of MOR, OI, and CR and average ratios of these components in the magmas and their sources, DM, OPM, and CPM (shown by lines corresponding to regression equations). Symbols are the same as in Fig. 5. The regression lines have the following correlation coefficients: (I) $R = 0.71$ ($n = 324$) for MOR magmas and DM, (II) $R = 0.75$ ($n = 243$) for OI magmas and OPM, and (V) $R = 0.75$ ($n = 64$) for CR magmas and CPM.

on H_2O and K_2O variations in the OPM, we distinguished three types of mantle plume sources, M1, M2, and M3 [23]. The composition of M1 is similar to the MOR mantle, and the compositions of M2 and M3 are moderately enriched in incompatible elements and differ from one another in H_2O content (higher in M3). The difference between M2 and M3 in terms of H_2O content at almost constant K_2O is illustrated by Fig. 11. The compositions of CR magmas (and, especially, Vesuvius magmas) lie closer to the OI field than to the MOR field (Fig. 11). The average compositions of MOR, OI, and CR magmas (Table 1) plot along a common trend in Fig. 11. The compositions of basic magmas from all the geodynamic settings form common fields with positive correlations in the K_2O –Cl, K_2O –F, and Cl– H_2O diagrams (Fig. 11).

As was noted above, the compositions of magma sources from various geodynamic settings (DM, OPM, and CPM) differ primarily in incompatible element ratios (Figs. 12, 13). Figure 12a illustrates a positive correlation in the $K_2O/F-Cl/F$ diagram. In Fig. 12b, linear trends in the compositions of magmas from various geodynamic settings and their sources are less pronounced (except for the magmas of the CPM). The K_2O/H_2O and H_2O/F ratios of all the compositions of magmas and their sources are negatively correlated (Fig. 12c). In Fig. 12d, the compositions

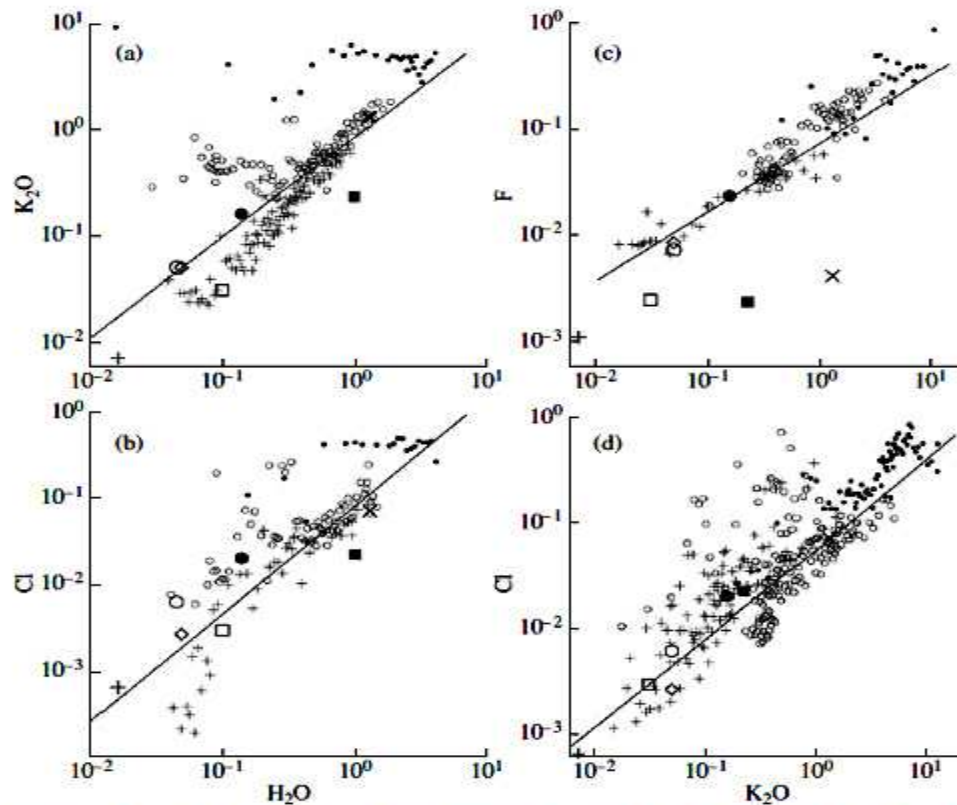


Fig. 11. Distribution of K_2O , H_2O , Cl , and F contents (wt %) in the basic magmas of MOR, OI, and CR. Symbols are the same as in Fig. 5. For a better visualization, the number of points was decreased by a factor of 10 for each geodynamic setting in the following way. The data were ranged in one of the parameters and divided into several groups. Average parameters were calculated for each group and plotted on the diagram. Correlation parameters were calculated using all the available analyses. The total numbers of analyses are the following: (a) $n = 1057, 786,$ and 252 for the magmas of MOR, OI, and CR, respectively; (b) $n = 209, 436,$ and 658 ; (c) $n = 250, 932,$ and 266 ; and (d) $n = 788, 1091,$ and 1667 . The magmas of all the geodynamic settings show the following correlation coefficients: (a) $R = 0.88,$ (b) $R = 0.51,$ (c) $R = 0.46,$ and (d) $R = 0.54$.

of MOR and OI magmas form a tight cluster at high H_2O/Cl and low K_2O/H_2O values.

Figure 13 shows some canonical incompatible element ratios. The Nb/U ratio (Fig. 13a) is almost constant for almost all the compositions of MOR and OI magmas and DM and OPM reservoirs. On the other hand, the H_2O/Ce value in the average composition of DM is higher than that of the OPM, although there are gradual transitions between them. The CR magmas show a considerable scatter in Nb/U with excursions to the compositions of the continental oceanic crust. Variations in the H_2O/Ce values of CR magmas are no higher than the compositional variations of MOR magmas. Similar relationships were observed for P_2O_5/F and Nb/U variations (Fig. 13b). Like in Fig. 13a, a stable Nb/U value is

accompanied by a complete overlap between the compositional fields of the DM and OPM in terms of P_2O_5/F . The compositions of the CPM magmas are strongly variable and extend toward the composition of the continental crust. Figures 13c and 13d show

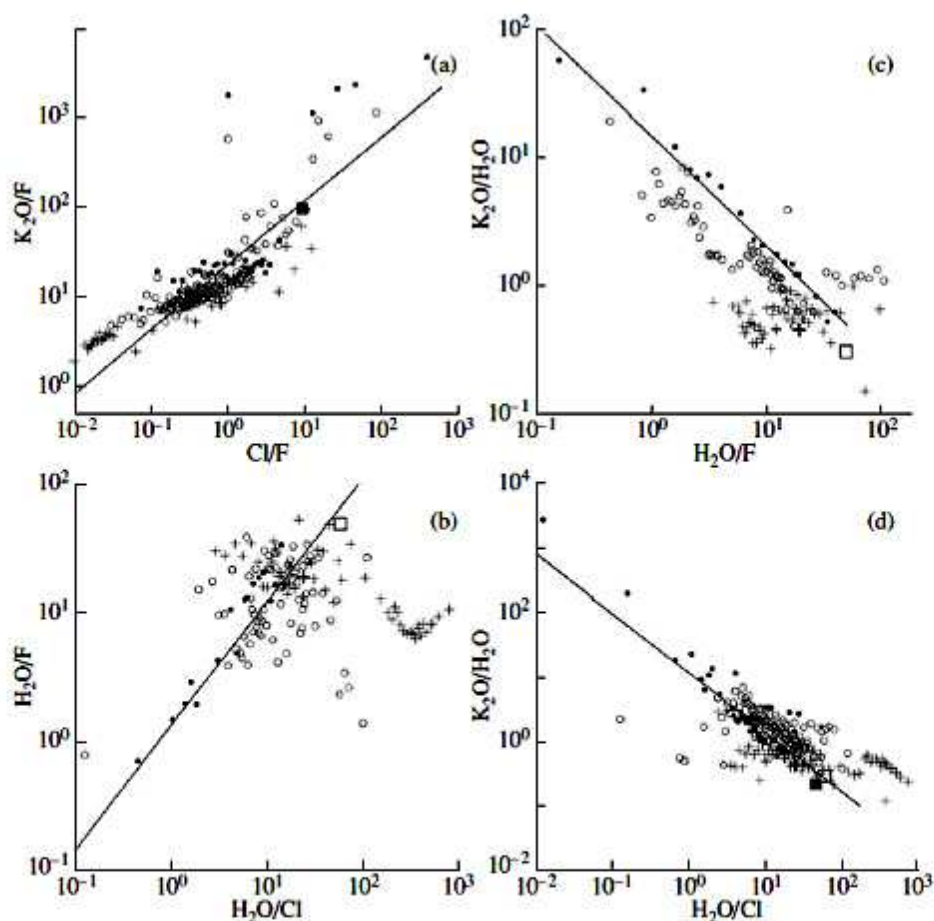


Fig. 12. Concentration ratios of volatile components and K_2O in the basic magmas of MOR, OI, and CR and in their sources, DM, OPM, and CPM. Symbols are the same as in Fig. 5. For a better visualization, the number of points was decreased for each geodynamic setting by a factor of 5. The total numbers of analyses are the following: (a) $n = 266, 920,$ and 210 for the magmas of MOR, OI, and CR, respectively; (b) $n = 276, 352,$ and 91 ; (c) $n = 252, 351,$ and 91 ; and (d) $n = 412, 491,$ and 209 . The magmas of intraplate continental settings show the following correlation coefficients (straight lines in the diagrams): (a) $R = 0.60,$ (b) $R = 0.62,$ (c) $R = 0.92,$ and (d) $R = 0.79$.

variations in the K_2O/Cl and P_2O_5/F ratios, respectively, as functions of H_2O/Ce . All the compositions fall within the range of H_2O/Ce values from 80 to 400 (Fig. 13c). The derivatives of the DM tend to cluster in two regions: (1) at high K_2O/Cl values (>100), where peculiar Cl-poor magmas described by [41] fall, and (2) at moderate K_2O/Cl values of about 10, where the compositions of magmas from other geodynamic settings are located. These compositional clusters are also extended in agreement with the considerable variations in H_2O/Ce values. There are almost no transitional compositions between the clusters. In Fig. 13d, the compositions of DM-related magmas show a negative correlation, and the compositions of OPM- and most of CPM-related magmas have low P_2O_5/F values. The compositions of CPM magmas show higher H_2O/Ce values compared with the OPM magmas, but there exist all transitional compositions between the DM, OPM, and CPM fields.

A question arises as to the nature of variations in the composition of basic magmas. Since the elements considered are incompatible, an increase in their content can be related to the crystallization differentiation of basic magmas. This is

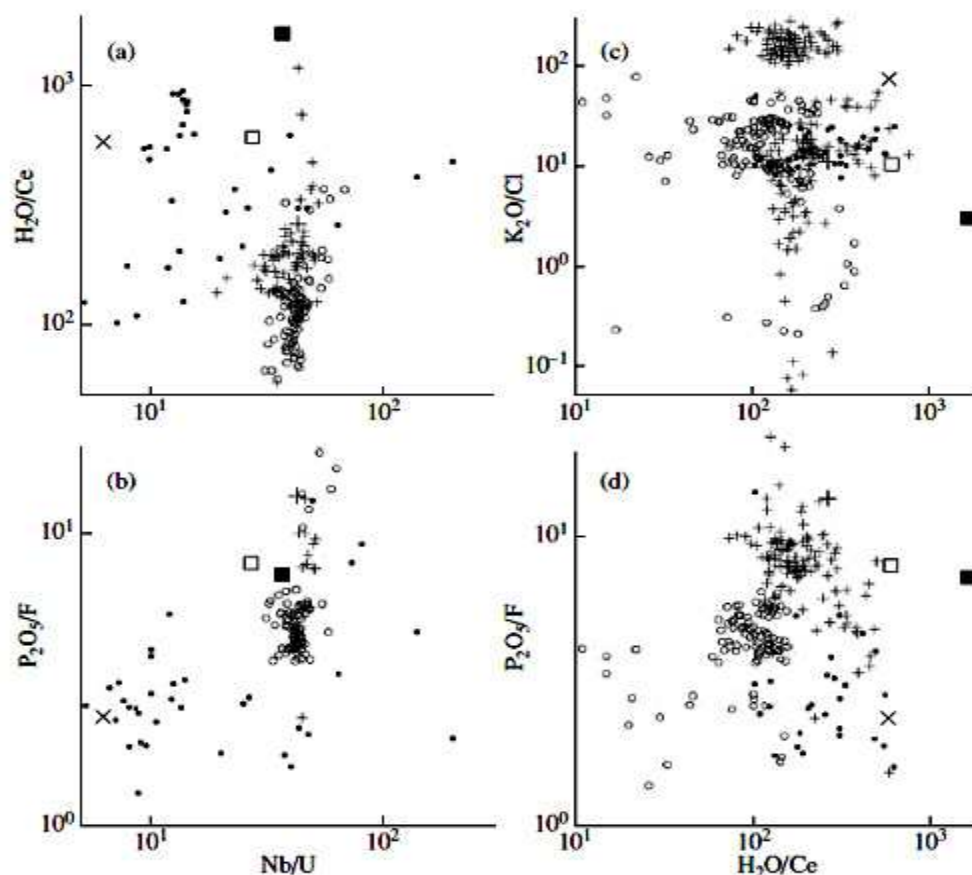


Fig. 13. Concentration ratios of volatile components and canonical ratios in the basic magmas of MOR, OI, and CR and their sources, DM, OPM, and CPM. Symbols are the same as in Fig. 5. Numbers of analyses of the MOR, OI and CR magmas, respectively: (a) $n = 63, 100,$ and 47 ; (b) $n = 12, 95,$ and 35 ; (c) $n = 206, 150,$ and 52 ; and (d) $n = 127, 116,$ and 51 .

consistent with the negative correlation of K_2O , Cl, F, and H_2O with MgO (Fig. 14). However, the slope of crystallization differentiation trends for these components is much less steep than the observed extension of the compositional fields (Fig. 14). In particular, the slope of the crystallization differentiation trend for K_2O (Fig. 14a) is similar to the slope of the K_2O –MgO dependency of Vesuvius magmas and apparently intersects the general trend of all the geodynamic settings. Perhaps, the elongation of the compositional fields of basic magmas in the diagrams of components versus MgO reflects a combined effect of crystallization differentiation and mixing of sources or magmas with different contents of K_2O , H_2O , F, and Cl. The basic magmas of various geodynamic settings show similar variations in S content.

Figures 15 and 16 show variations in the concentration ratios of incompatible elements versus MgO content in magmas. Only the Nb/U ratio (Fig. 16) is

independent of MgO in the basic magmas of MOR and OI, which was repeatedly shown by A. Hofmann in the above-cited publications. The CR magmas show con

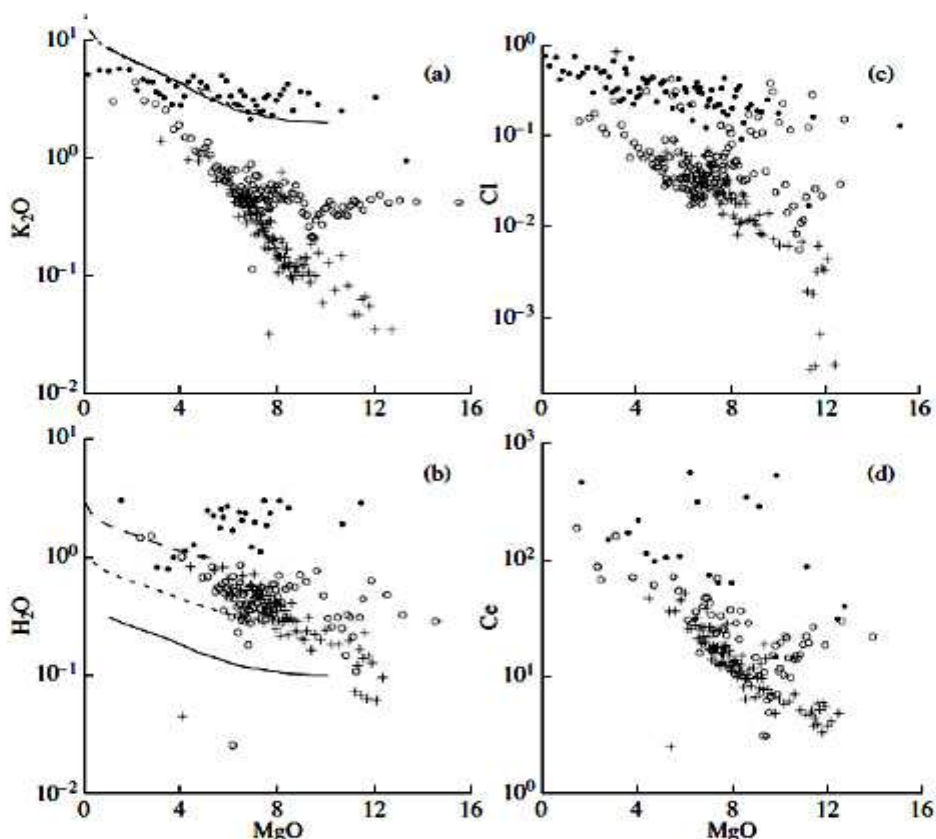


Fig. 14. Contents of (a) K_2O , (b) H_2O , (c) Cl, and (d) Ce as functions of MgO (wt %) in the basic magmas of MOR, OI, and CR. Thin lines show crystallization differentiation trends for various compositions of primary magmas. Symbols are the same as in Fig. 5. The numbers of points on the diagrams were decreased by a factor of (a) 30 or (b)–(d) 10. Numbers of analyses of MOR, OI and CR magmas, respectively: (a) $n = 2866, 4002, \text{ and } 1539$; (b) $n = 813, 864, \text{ and } 269$; (c) $n = 670, 1579, \text{ and } 786$; and (d) $n = 1014, 631, \text{ and } 207$.

siderable variations in this ratio at any MgO content. A comparison of Figs. 12 and 15 suggests that the trend formed by the compositions of MOR and OI magmas (Fig. 16) with a slight increase in K_2O/F and Cl/F can be related to crystallization differentiation. This is accompanied by minor variations in the K_2O/F ratio, and this effect was accounted for through the degree of total fractionation of magmas and the difference in the degree of incompatibility of elements (see above). On the other hand, the general extension of the compositional fields of the MOR and OI magmas is accompanied by minor variations in MgO and cannot be attributed to crystallization differentiation only.

The chemical variations in the MOR magmas (Figs. 12, 15) could be related to crystallization differentiation. However, this is not the case for the magmas of OI and CR. This is most clearly demonstrated by variations in the H_2O/F and H_2O/Cl ratios of CR magmas. Consequently, the increase in H_2O/Cl and MgO content in magmas from the CPM through OPM to the DM source (Fig. 16) cannot be related to crystallization differentiation only.

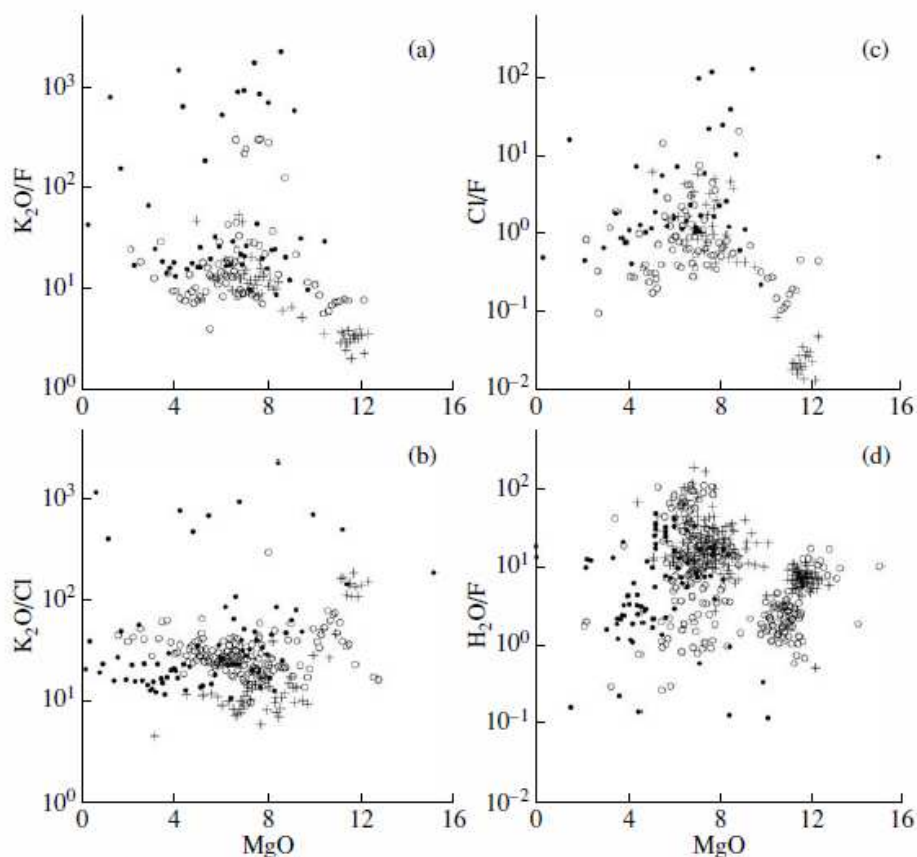


Fig. 15. Ratios of (a) K_2O/F , (b) K_2O/Cl , (c) Cl/F , and (d) H_2O/F as functions of MgO (wt %) in the basic magmas of MOR, OI, and CR. Symbols are the same as in Fig. 5. The numbers of points were decreased by a factor of 5 for MOR and CR magmas and 10 for OI magmas in panels (a) and (c) and by a factor of 10 for all settings in panel (b). Numbers of analyses of MOR, OI and CR magmas, respectively: (a) $n = 266, 844, \text{ and } 250$; (b) $n = 650, 1579, \text{ and } 786$; (c) $n = 286, 832, \text{ and } 210$; and (d) $n = 272, 263, \text{ and } 91$.

Like in the case of variations in element contents, it can be concluded that the general trends of incompatible trace element ratios in basic magmas as functions of MgO content reflect a combined effect of crystallization differentiation and mixing of sources or magmas.

DISCUSSION

In the following discussion of the obtained results, we address the character of differences between the compositions of the DM, OPM, and CPM, reasons for the considerable chemical variations, and interaction between mantle sources in the framework of the models of global and regional convection.

Average Contents of Incompatible Trace Elements in Mantle Sources. The estimated average contents of incompatible trace elements in the magma sources are given in Table 5 and Figs. 3 and 4. A comparison of our estimates for the DM with the values reported by [42] and [48] showed that the average contents of the most incompatible elements (H_2O , Cl , F , Be , B , Rb , Sr , Zr , Nb , Ba , La , Ce , Nd , Sm , Eu , Hf , Ta , Th , and U) can be adequately estimated from their ratios to K_2O and the average content of K_2O in the DM. Ratios of elements with similar incompatibilities should be used for other elements. The ratios of TiO_2 , P_2O_5 , S , Li , Y , and HREE to Dy were used for such estimates. This method was initially

developed for the determination of the average contents of incompatible trace elements in the DM and then applied to the compositions of the OPM, CPM, and the source of Vesuvius magmas.

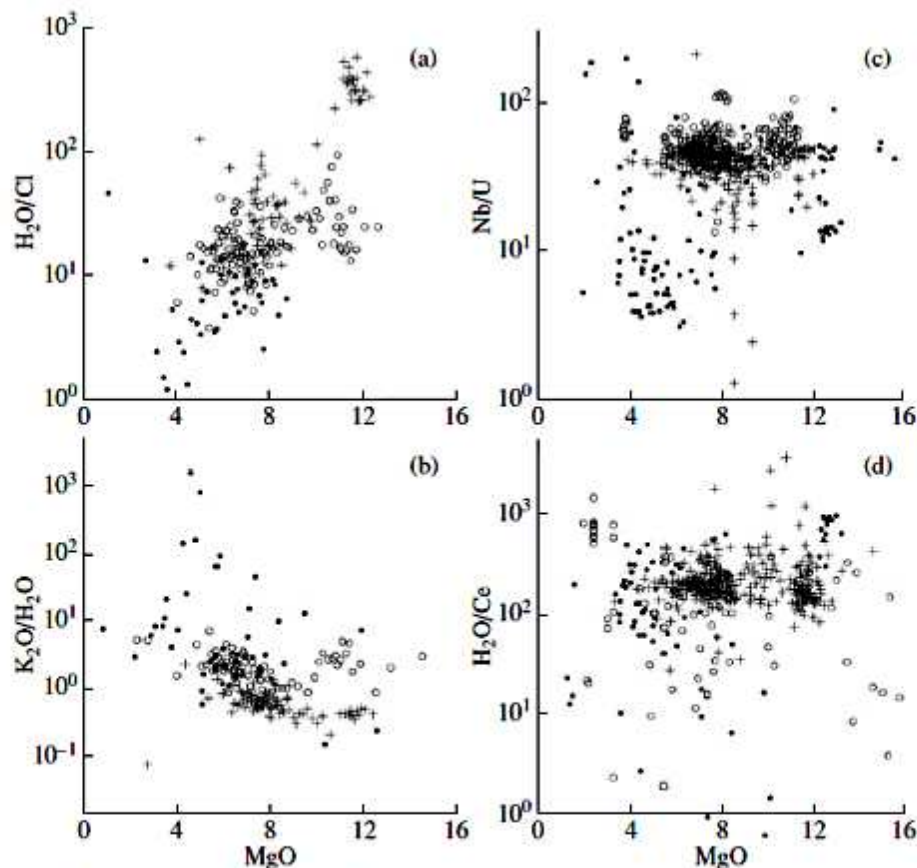


Fig. 16. Ratios of (a) H_2O/Cl , (b) K_2O/H_2O , (c) Nb/U , and (d) H_2O/Ce as functions of MgO (wt %) in the basic magmas of MOR, OI, and CR. Symbols are the same as in Fig. 5. The numbers of points were decreased in panel (a) by a factor of 5 for all settings and in panel (b) by a factor of 10 for MOR and OI magmas and by a factor of 5 for CR magmas. Numbers of analyses of MOR, OI and CR magmas, respectively: (a) $n = 392, 564, \text{ and } 209$; (b) $n = 782, 864, \text{ and } 269$; (c) $n = 374, 221, \text{ and } 130$; and (d) $n = 361, 109, \text{ and } 71$.

It should be noted that our estimates rely heavily on the accepted geodynamic model. Of prime importance is the model of mantle plumes ascending from the deep mantle (although not necessarily from the core–mantle boundary) through a more depleted mantle zone beneath the lithosphere. It is believed that the mantle plumes may be of a purely thermal (hot spots) or compositional (enrichment in volatile components, primarily in water, wet spots) nature. We assumed that in the model of thermal plumes, the content of nonvolatile K_2O in the OPM must be similar to that in the DM. Our calculations revealed controversies in such a model, because the depleted mantle appeared to be richer in many incompatible elements than the plume mantle generating basaltic magmas with high contents of these elements. Therefore, we favored a model of moderately enriched and hot plume material. In the accepted model, the CPM composition is moderately enriched in incompatible elements, including K, relative to the DM. Then the problem arose on the estimation of the average content of K_2O or any other incompatible element. To this end, we used an assumption on the similar degrees of mantle melting

during the formation of basaltic magmas in the DM and OPM. This assumption is not obvious, because the thermal regimes of the DM and OPM are different. However, the analysis of the compositions of primary mantle magmas [14] suggested that an increase in mantle temperature affects primarily the depth of magma segregation, whereas the average degree of melting shows minor variations. Therefore, the assumption on the similar degrees of melting in the DM and OPM seems reasonable, at least for the estimation of average compositions. Highly alkaline basic magmas are generated at low degrees of melting in the relatively cold marginal zones of plumes, whereas the central hot parts produce tholeiitic basalts and ultramafic magmas, which require high-degree melting. In general, this model is in adequate agreement with the assumption on the similar contents of moderately incompatible elements (in particular, Dy) in all the mantle reservoirs considered (DM, OPM, and CPM) and basic magmas generated from them (Tables 1, 5).

What are the general characteristics and nature of the distribution of average contents of trace elements in the DM, OPM, and CPM? This problem was previously considered for the DM by [22] and many other authors. The most probable distribution of incompatible trace elements in the DM, including volatile components, is shown in Fig. 4. The average contents of incompatible elements in the DM show a saw-tooth pattern with negative anomalies of Rb, Ba, Pb, Cl, and H₂O and a general increase in normalized contents from strongly to moderately incompatible elements. The elements in spidergrams are arranged in the order of decreasing incompatibility, and Fig. 4 presents one of the most widely used sequences. However, this sequence can be modified using our estimates of bulk partition coefficients (Table 6). In particular, the partition coefficients of H₂O, Cl, Th, Ta, K₂O, Be, Rb, Ba, B, La, Pb, and U are close to 0.01, and these elements can be arranged in the order of increasing average normalized content, assuming a correlation between the incompatibility and normalized content of elements. The moderately incompatible elements also show a narrow range of bulk partition coefficients (0.03–0.08), and it is convenient to arrange them in the order of increasing normalized contents. Sulfur appears at the right end of the spidergram. Such a sequence results in a rather smooth distribution pattern for the average incompatible element contents of the DM (Fig. 17a). Figure 17b shows a spidergram without volatile components with the element sequence accepted by [42]. It also displays a smooth incompatible trace element distribution pattern in the DM with a monotonous increase from highly to moderately incompatible elements. On the other hand, Figs. 17a and 17b reveal stepwise patterns in the distribution of incompatible trace elements. An increase in the normalized contents of these elements from left to right occur in steps, while the normalized contents of elements between the steps are almost identical. It is possible that each segment between the steps includes elements with similar degrees of incompatibility. The following groups of elements can be distinguished (from higher to lower

incompatibility): (1) Rb, Ba, and H₂O; (2) Cl, Th, Pb, U, K₂O, and Nb; (3) B, Ta, La, Sr, Ce, and Hf; (4) Be, Zr, Nd, Sm, Eu, F, and Li; and (5) TiO₂, P₂O₅, S, Y, and HREE.

Many authors discussed the complementary compositions of the DM and continental crust (e.g., [18] and reference therein). This observation provided a basis for the hypothesis of DM formation as a residue after continental crust extraction from the mantle during the early stages of Earth evolution (e.g., Galer and Goldstein, 1991). Such a complementariness is clearly seen in Fig. 17b, but it is disturbed by the negative anomalies of Nb, Ta, and Ti in the average composition of the continental crust, which are not reflected in the DM composition. This is most likely related to the complex mechanism of continental crust formation, which included, in addition to the direct melting of the primitive mantle, island-arc magmatic processes favorable for the formation of negative anomalies of Nb, Ta, and Ti. The negative anomalies of H₂O and Cl compared with Ce in the DM (Fig. 4) were explained by [22] by the separation of the hydrosphere during the early stages of Earth evolution and the deep recycling of crust into the mantle, which must be accompanied by its dehydration.

As was noted above, the spidergrams of the OPM composition show positive anomalies of Rb, K₂O, Nb, Ta, and F and negative anomalies of B, Pb, and H₂O (Fig. 4). All these variations occur near the composition of the primitive mantle (Fig. 17b). This poses the question as to the preservation of primitive mantle domains at great depths and their role in the formation of mantle plumes. However, recent isotopic and geochemical data did not support this suggestion [3, 20]. Another possible explanation for the specific features of the average OPM composition is related to the concept of DM formation by the extraction of the early continental crust from the primitive mantle. If this hypothesis is correct, the opposite process of DM fertilization is possible at the expense of the deep recycling of the early continental crust. In such a case, the negative anomaly of H₂O in the OPM can be attributed to the dehydration of the crust contributing to the formation of this mantle reservoir. In addition, noteworthy is a distinct resemblance between the trace element distribution patterns of the OPM and the oceanic crust (Figs. 4, 17). It can be supposed that the OPM could be produced by mixing the DM with a certain amount of eclogitic material formed by the recycling of the oceanic crust into the mantle [3]. Remember also that the oceanic plume mantle is heterogeneous and includes three main compositions [23], one of which is similar to the MOR mantle and the other two are moderately enriched in K, Ti, P, F, and incompatible trace elements but depleted in Cl and H₂O. In our opinion [23], the plume mantle was primarily formed through the mixing of the ultradepleted mantle, moderately enriched dry (poor in H₂O, Cl, and S) mantle, and moderately enriched hydrous mantle. In addition to these three main components of the OPM, materials enriched in Cl and depleted in F could exist. In our opinion, they participate in the plume mantle through the recycling into the deep mantle of

the components of the oceanic and continental crust. This model is in agreement with the zonal structure of a mantle plume, which includes a hot central part depleted in H₂O, Cl, and S but enriched in incompatible nonvolatile elements; a colder periphery enriched in volatile and nonvolatile incompatible elements; and the ambient DM.

We noted above that the general decrease from highly to moderately incompatible elements in the composition of the CPM-1 is accompanied by negative anomalies of Th, K₂O, Pb, Ta, Ti, Li, and S and positive anomalies of Ba, Cl, and F (Fig. 4). The trace element distribution pattern of the CPM-1 resembles that of the OPM but differs from it in higher variations in strongly incompatible elements. Remember that the CPM-1 is the average composition of the mantle of intracontinental settings under the condition that the K₂O contents of the suboceanic and subcontinental plumes are identical (510 ppm). In order to evaluate the statistical similarity of the average contents of other incompatible nonvolatile elements in the OPM and CPM-1 or in the OPM and CPM-2, open and filled circles in Figs. 3b and 4 show elements whose average contents in the OPM and CPM-1 are statistically undistinguishable and significantly different, respectively. The test criterion for the significance of difference is

$$Z = \frac{\bar{X} - \bar{Y}}{\sqrt{D(X)/n_X + D(Y)/n_Y}},$$

where \bar{X} and \bar{Y} are the average values for the two sets (in our case, average contents in the OPM and CPM-1), $D(X)$ and $D(Y)$ are the respective variances, and n_X and n_Y are the numbers of determinations in the two sets. The critical Z value for the comparison of averages of two large sets is 2.58 for a confidence level of 99% (e.g., [15]). The average contents of H₂O, Sr, Y, La, Ce, Er, Lu, Th, and U appeared to be statistically undistinguishable in the OPM and CPM-1, whereas the average contents of Cl, Ti, P, Ba, Hf, Nb, and Ta show very large differences ($Z > 10$). Some elements (F, Cl, Li, Be, B, Nd, Gd, Yb, and Pb) are characterized by intermediate Z values of 3–5. The difference between the concentrations of these elements in the mantle sources is, perhaps, insignificant, taking into account the different character of melt evolution and systematic errors (for instance, analytical

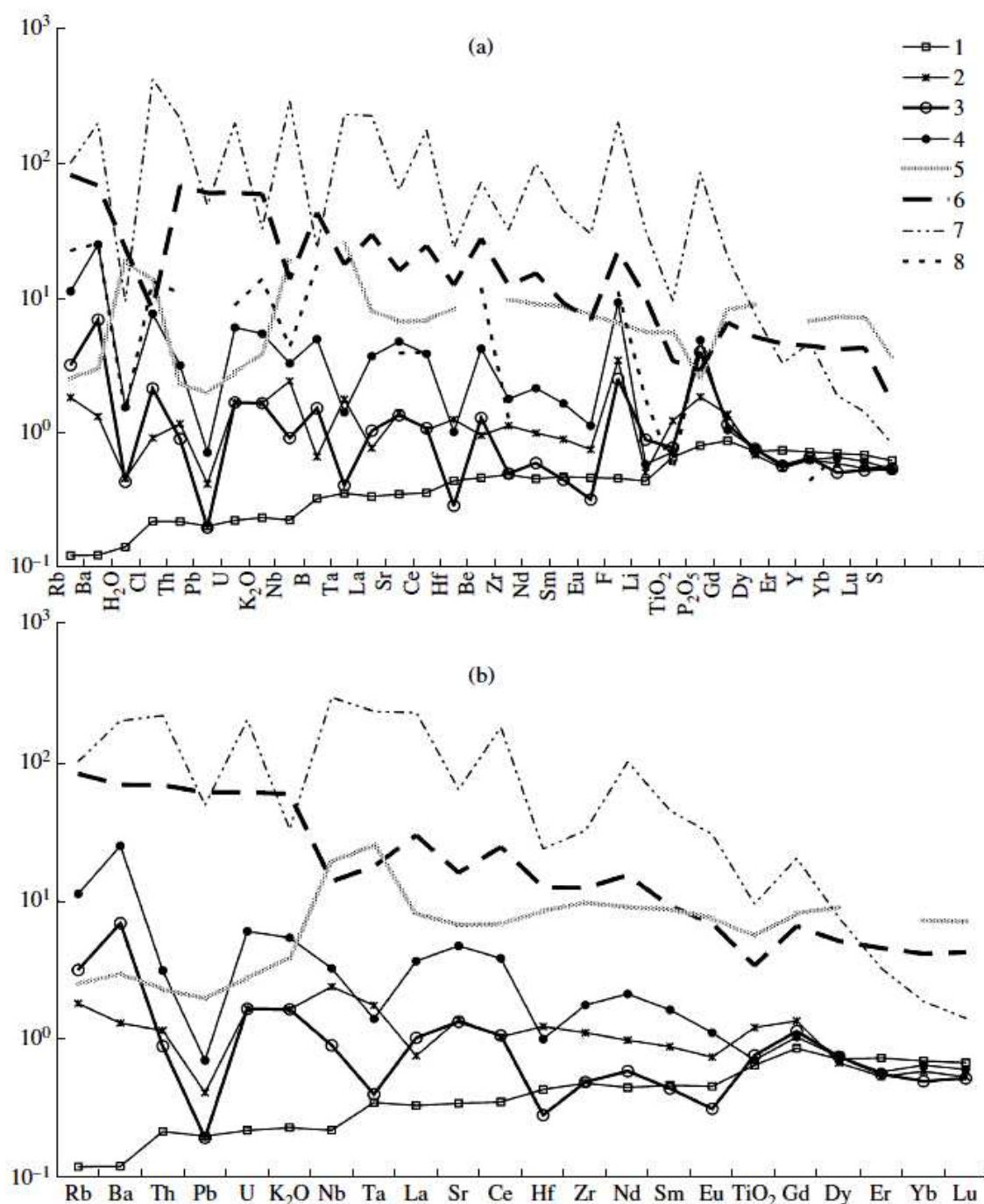


Fig. 17. Spidergrams for the average contents of incompatible elements in the (1) DM, (2) OPM, (3) CPM-1, and (4) CPM-2 obtained from our estimates of bulk partition coefficients and normalized average contents of highly and moderately incompatible elements, (a) with and (b) without volatile components. Also shown are the average compositions of (5) the continental crust (Wedepohl and Hartmann, 1994), (6) the continental crust (Rudnick and Gao, 2003), (7) group I kimberlites (Le Roex et al., 2003), and (8) the Vesuvius mantle.

errors). The distribution patterns of incompatible elements in the average composition of the CPM-2 and the mantle source of Vesuvius Volcano are similar to those of the CPM-1, but the average contents of strongly incompatible elements are higher, especially in the Vesuvius magma source.

The origin of the sources of potassium-rich alkaline magmas, which compose a significant portion of our CR database, is still the subject of heated debate. In

particular, the formation of the potassic alkaline magmas of the Roman province was discussed by [21]. Such rocks are usually subdivided into orogenic (island-arc) and anorogenic. As was shown in many publications, the potassium alkalinity of rocks from both orogenic and anorogenic associations could be related to the influence of fluids released from subducted continental sediments (mantle metasomatism). This results in the formation of phlogopite-bearing mantle rocks, the melting of which in rift zones or under the influence of mantle hot spots produces potassium-rich magmas (Nelson, 1992). This model is in agreement with the available geochemical data on the potassium-rich alkaline rocks of the Aldan shield [4, 30].

However, the presence of phlogopite in the mantle is not a necessary prerequisite for the formation of potassium-rich magmas. High contents of potassium and other incompatible elements can be provided by the very low degrees of melting of mantle materials with moderate contents of these elements. In the absence of potassium phases (phlogopite, potassium feldspar, or amphibole), clinopyroxene is the principal host of potassium in mantle peridotites. The bulk content of K_2O in the CPM-2 was estimated as about 0.16 wt %, which corresponds to a clinopyroxene K_2O content of 0.75–1.5 wt %, if the abundance of this phase in mantle peridotite is 10–20%. Clinopyroxenes with such K_2O contents were described in natural mantle assemblages and were obtained in experiments at pressures of higher than 70 kbar [36]. Therefore, the moderately enriched composition of mantle plumes does not require a change in the phase composition of the mantle at great depths. A pressure decrease results in that clinopyroxene with 1 wt % K_2O becomes unstable, which must lead to the formation of potassium-rich minerals (phlogopite or potassium feldspar). The appearance of a new phase in the mantle assemblage decreases solidus temperature, and this process is therefore favorable for the formation of deep-seated potassium-rich magmas.

On the other hand, the question arises as to why the material of deep mantle plumes beneath the continents is chemically different from the mantle of suboceanic plumes. A certain contribution to this difference is likely from the assimilation of continental and oceanic crust by the magmas. However, as was noted above, this contribution was probably not significant for the average compositions, which is supported by small variations in some indicator ratios (e.g., Pb/Nd) in the magmas of suboceanic and subcontinental plumes. Another viable explanation is related to the models of plume–lithosphere interaction (e.g., [10, 45]). The most incompatible elements can be enriched at the expense of the participation in magma generation of melts produced by the low-degree melting of deep portions of the continental lithosphere. This produces strongly enriched melts similar to kimberlites and lamproites, the addition of which to asthenospheric magmas results in the formation of enriched magmas. Indeed, there is an apparent similarity between the average compositions of the calculated potassium-rich

mantle source and kimberlites [24] (Fig. 4). In particular, the considerable enrichment of Ba, Cl, and F in the continental magmas can be attributed to the influence of the lithospheric mantle. Such a suggestion allows us to minimize the difference between the sources of oceanic and continental plume magmas. On the other hand, some differences cannot be accounted for in this model. In particular, the relatively low contents of Ta, Nb, and Ti in the CPM are noteworthy (Fig. 4). This feature suggests some peculiarities in the composition of subcontinental plumes or an increased stability of oxide phases (rutile and ilmenite) in continental settings.

The average composition of the EM2 mantle component was recently estimated by [49]. Although this type of mantle does not represent the average composition of all plume mantle reservoirs, it is instructive to compare this composition with our data for the OPM (Table 5). There is a good agreement for Sr, Y, Zr, Nb, La, Ce, Nd, Sm, Eu, Gd, Dy, Ta, and U. The contents of other elements differ by no more than a factor of two, which is comparable with the estimated confidence interval for average contents.

Interaction of Mantle Sources

It was shown above that the contents and ratios of incompatible trace elements in basic magmas from various settings show wide variations, and their fields overlap significantly in almost all diagrams. Such relationships were noted for the magmas of MOR [23] and OI [23]. One general feature of variations in the contents of incompatible elements in basic magmas and their sources is an increase in variance from the DM to OPM and CPM. Correlations between incompatible element ratios shown in Figs. 12 and 13 are especially important for the assessment of variations in the compositions of sources of basic magmas. It can be seen in these diagrams that the K_2O/F and K_2O/H_2O ratios increase, whereas H_2O/F and H_2O/Cl decrease in the sequence DM–OPM–CPM, which may indicate interactions between the main mantle reservoirs. The interaction between the DM and OPM reservoirs is clearly illustrated by variations in the H_2O/Ce , P_2O_5/F , and K_2O/Cl ratios at constant Nb/U (Fig.13).

The suggestion on the interaction between mantle reservoirs requires discussion. This phenomenon was revealed by the analysis of variations in volatile components in the DM [22] and OPM [23]. These studies showed that the chemical variability of the DM is related to the mixing of two main components: ultradepleted mantle and enriched mantle of the OPM type. If this suggestion is correct, it should be admitted that there is a link between the DM and OPM, although global geodynamic models [50] and seismic tomography data [31] suggest that these reservoirs are located at different depths and probably connected with different convection systems. However, some processes can lead to the interaction between the DM and OPM. In particular, the possibility of significant lateral migration of plume material was advocated by [44]

It cannot be excluded that the current stage of Earth evolution is characterized by single-cell mantle convection (e.g., [9]). Then, the interaction of the DM with the enriched and deeper OPM reservoir becomes a natural outcome: mantle plumes continuously supply the depleted source formed by the extraction of the early continental crust from the primitive mantle.

The interaction of the OPM and DM in the regions of basic magma generation beneath OI seems also natural [23]. It is supported by the fact that main components of the OPM include not only the composition similar to the DM but also all the transitional varieties from the DM to the water-rich OPM component. The zonal structure of plumes owes its origin to the interaction of suboceanic plumes with the ambient DM: a hot dry and moderately enriched core is changed by a colder moderately enriched periphery and, then, by the zone of OPM–DM interaction. The latter zone must not consist of mantle rocks with transitional chemical characteristics. It is important that the ascent of plume material entrains considerable amounts of the enclosing mantle [16]. Decompression leads to the melting of both the plume material and the ascending portions of the DM. Mixing of these melts produces transitional compositions from the typical products of DM melting to plume-related magmas.

The character of interaction between mantle reservoirs is not yet fully understood, primarily because of the paucity of data on the magmas of continental flood basalt provinces. It was shown that the OPM and CPM-1 are similar in terms of average contents of many highly incompatible elements but different in average contents of more compatible elements. The canonical ratios indicate interactions only between the DM and OPM. The role of the lithospheric mantle and continental crust in the formation of CR magmas is also not clear. There are still more questions than answers.

CONCLUSIONS

1. Using the available database on the compositions of melt inclusions and quenched glasses, the average compositions of basic magmas from MOR, OI, and CR were calculated.

2. A method was developed for the estimation of the average contents of incompatible elements in the DM, OPM, and CPM. A comparison of our results for the DM with published estimates showed that the average contents of the most incompatible trace elements (H₂O, Cl, F, Be, B, Rb, Sr, Zr, Ba, La, Ce, Nd, Sm, Eu, Hf, Ta, Th, and U) can be reliably estimated from their ratios to K₂O and the average content of K₂O in the DM. The average contents of Nb, Ti, P, S, Li, Y, and HREE should be determined from their ratios to elements with similar incompatibilities (U for Nb and Dy for the other elements). This procedure was used for the estimation of the average contents of incompatible elements in the OPM, CPM, and the magma source of Vesuvius Volcano.

3. The average contents of incompatible trace elements in the mantle depend on the accepted geodynamical model of the mantle. Our estimates of the average contents of incompatible elements in the OPM rely on the model of a moderately enriched hot plume. The composition of the OPM must be moderately enriched in incompatible elements, including K_2O , compared with the DM; its average contents of moderately incompatible elements (e.g., Dy) must be similar to those of the DM; and the degree of melting during the formation of basaltic magmas must be similar for the DM and OPM.

4. The distribution pattern of the average contents of incompatible elements in the DM lies below the primitive mantle level. The DM composition shows a saw-tooth pattern with negative anomalies of Rb, Ba, Pb, Cl, H_2O , S, and TiO_2 and a general increase in the average normalized contents from highly to moderately incompatible elements.

5. The distribution pattern of the average contents of incompatible trace elements in the OPM displays positive anomalies of Rb, K_2O , Be, Nb, and Ta and negative anomalies of B, Pb, and F. The average contents are in general close to the primitive mantle composition. This could be related either to the preservation of primitive mantle material at the birthplace of plumes or DM fertilization at the expense of the deep recycling of crustal materials. The negative anomaly of H_2O and the positive anomaly of F in the distribution of trace elements in the OPM can be attributed to a contribution from the dehydrated crust.

6. The distribution pattern of the average contents of incompatible trace elements in the CPM shows negative anomalies of Th, K_2O , Pb, and Ta, positive anomalies of Ba, F, and Cl, and weak negative anomalies of Ti, Li, and S. The shape of spidergram for the CPM is similar in many respects to that of the OPM but differs from the latter in higher variations in the contents of strongly incompatible elements.

7. Chemical variations in the magmas of MOR, OI, and CR suggest the existence of gradual transitions between the compositions of their sources and possible interaction between the sources. The interaction of the OPM with the DM occurs through the thermal and chemical fluxes between the hot and moderately enriched plumes and the enclosing cold DM. The influence of the OPM on the DM implies either a single-cell convection in the Earth's interiors or a connection between the OPM and DM through both vertical and lateral flows.

ACKNOWLEDGMENTS

The authors thank E.V. Sharkov (Institute of Geology of Ore Deposits, Petrography, Mineralogy, and Geochemistry, Russian Academy of Sciences) for his helpful comments and discussion of the results of our study. This work was financially supported by the Russian Foundation for Basic Research, project nos. 05-05-64056, 04-05-65123, 05-05-64175, and 07-05-00497; Program for the Support of Leading Scientific Schools, grant no. 2006-RI-112.0/01/008; and

research programs of the Earth Science Department, Russian Academy of Sciences.

REFERENCES

1. **Baker J. A., Menzies M. A., Thirlwall M. F., and Macpherson C. G.**, “Petrogenesis of Quaternary Intraplate Volcanism, Sana’a, Yemen: Implications for Plume–Lithosphere Interaction and Polybaric Melt Hybridization,” *J. Petrol.* 38, 1359–1390 (1997).
2. **Beccaluva L., Di Girolamo P., and Serri G.**, “Petrogenesis and Tectonic Setting of the Roman Volcanic Province, Italy,” *Lithos* 26, 191–221 (1991).
3. **Blichert-Toft J. and Albarede F.**, “The Lu–Hf Isotope Geochemistry of Chondrites and the Evolution of the Mantle–Crust System,” *Earth Planet. Sci. Lett.* 148, 243–258 (1997).
4. **Bogatikov O. A., Kononova V. A., Pervov V. A., and Zhuravlev D. Z.**, “Petrogenesis of Mesozoic Potassic Magmatism of the Central Aldan: A Sr–Nd Isotopic and Geodynamical Model,” *Int. Geol. Rev.* 36, 629–644 (1994).
5. **Brunet F. and Chazot G.**, “Partitioning of Phosphorus between Olivine, Clinopyroxene and Silicate Glass in a Spinel Lherzolite Xenolith from Yemen,” *Chem. Geol.* 176, 51–72 (2001).
6. **Cioni R., Marianelli P., and Santacroce R.**, “Thermal and Compositional Evolution of the Shallow Magma Chambers of Vesuvius: Evidence from Pyroxene Phenocrysts and Melt Inclusions,” *J. Geophys. Res.* 103, 18277–18294 (1998).
7. **Dixon J. E., Stolper E. M., and Delaney J. R.**, “Infrared Spectroscopic Measurements of CO₂ and H₂O Glasses in the Juan De Fuca Ridge Basaltic Glasses,” *Earth Planet. Sci. Lett.* 90, 87–104 (1988).
8. **Dixon J. E., Leist L., Langmuir C., and Schilling J.-G.**, “Recycled Dehydrated Lithosphere Observed in Plume-Influenced Mid-Ocean-Ridge Basalt,” *Nature* 420 (6914), 485–489 (2002).
9. **Dobretsov N. L., Kirdyashkin A. G., and Kirdyashkin A. A.**, *Deep Geodynamics* (SO RAN, Novosibirsk, 2001) [in Russian].
10. **Ellam R. M. and Cox K. G.**, “An Interpretation of Karoo Picrite Basalts in Terms of Interaction between Asthenospheric Magmas and the Mantle Lithosphere,” *Earth Planet. Sci. Lett.* 105, 330–342 (1991).
11. **Fulignati P., Marianelli P., and Sbrana A.**, “Glass-Bearing Felsic Nodules from the Crystallizing Sidewalls of the 1944 Vesuvius Magma Chamber,” *Mineral. Mag.* 64, 481–496 (2000).
12. **Fulignati P., Marianelli P., Santacroce R., and Sbrana A.**, “Probing the Vesuvius Magma Chamber–Host Rock Interface through Xenoliths,” *Geol. Mag.* 141, 417–428 (2004).
13. **Galer S. J. G. and Goldstein S. L.**, “Early Mantle Differentiation and Its Thermal Consequences,” *Geochim. Cosmochim. Acta* 55, 227–239 (1991).
14. **Girnis A. V.**, “Olivine–Orthopyroxene–Melt Equilibrium as a Thermobarometer for Mantle-Derived Magmas,” *Petrologiya* 11, 115–127 (2003) [*Petrology* 11, 101–113 (2003)].
15. **Gmurman V. E.**, *Fundamentals of Probability Theory and Mathematical Statistics* (Black Oak Books, Berkeley, 1976; Vysshaya Shkola, Moscow, 2001).
16. **Hauri E. H., Whitehead J. A., and Hart S. R.**, “Fluid Dynamic and Geochemical Aspects of Entrainment in Mantle Plumes,” *J. Geophys. Res.* 99, 24275–24300 (1994).
17. **Hirth G. and Kohlstedt D. L.**, “Water in the Oceanic Upper Mantle: Implications for Rheology, Melt Extraction and the Evolution of the Lithosphere,” *Earth Planet. Sci. Lett.* 144, 93–108 (1996).

18. **Hofmann A. W.**, “Chemical Differentiation of the Earth: the Relationship between Mantle, Continental Crust and Oceanic Crust,” *Earth Planet. Sci. Lett.* 90, 297–314 (1988).
19. **Hofmann A. W.**, “Mantle Geochemistry: The Message from Oceanic Volcanism,” *Nature* 385, 219–229 (1997).
20. **Hofmann A. W.**, “Sampling Mantle Heterogeneity through Oceanic Basalts: Isotopes and Trace Elements,” in *Treatise on Geochemistry* (Elsevier, Amsterdam, 2003), Vol. 2, pp. 61–101.
21. **Kovalenko V. I., Yarmolyuk V. V., Vladykin N. V.**, et al., “Epochs of Formation, Geodynamic Setting, and Sources of Rare-Metal Magmatism in Central Asia,” *Petrologiya* 10, 227–253 (2002) [*Petrology* 10, 199–221 (2002)].
22. **Kovalenko V. I., Naumov V. B., Girnits A. V.**, et al., “Estimation of the Average Contents of H₂O, Cl, F, and S in the Depleted Mantle on the Basis of the Compositions of Melt Inclusions and Quenched Glasses of Mid-Ocean Ridge Basalts” *Geokhimiya*, No. 3, 243–266 (2006a) [*Geochem. Int.* 44, 209–231 (2006a)].
23. **Kovalenko V. I., Naumov V. B., Girnits A. V.**, et al., “Composition and Chemical Structure of Oceanic Mantle Plumes,” *Petrologiya* 14, 482–507 (2006b) [*Petrology* 14, 424–451 (2006b)].
24. **Le Roex A. P., Bell D. R., and Davis P.**, “Petrogenesis of Group I Kimberlites from Kimberley, South Africa: Evidence from Bulk-Rock Geochemistry,” *J. Petrol.* 44, 2261–2286 (2003).
25. **Marianelli P., Metrich N., Santacroce R., and Sbrana A.**, “Mafic Magma Batches at Vesuvius: A Glass Inclusion Approach to the Modalities of Feeding Stratovolcanoes,” *Contrib. Mineral. Petrol.* 120, 159–169 (1995).
26. **Marianelli P., Metrich N., and Sbrana A.**, “Shallow and Deep Reservoirs Involved in Magma Supply of the 1944 Eruption of Vesuvius,” *Bull. Volcanol.* 61, 48–63 (1999).
27. **McDonough W. F.**, “Constraints on the Composition of the Continental Lithospheric Mantle,” *Earth Planet. Sci. Lett.* 101, 1–18 (1990).
28. **McKenzie D. and O’Nions R. K.**, “Partial Melt Distributions from Inversion of Rare Earth Element Concentrations,” *J. Petrol.* 32, 1021–1091 (1991).
29. **Michael P.**, “Regionally Distinctive Sources of Depleted MORB: Evidence from Trace Elements and H₂O,” *Earth Planet. Sci. Lett.* 131, 301–320 (1995).
30. **Morikiyo T., Miyazaki T., Kagami H.**, et al., “Sr, Nd, C, and O Isotope Characteristics of Siberian Carbonatites,” in *Alkaline Magmatism and the Problems of Mantle Sources* (Irkutsk, 2001), pp. 69–84.
31. **Nataf H.-C.**, “Seismic Imaging of Mantle Plumes,” *Annu. Rev. Earth Planet. Sci.* 28, 391–417 (2000).
32. **Naumov V. B., Kovalenko V. I., Dorofeeva V. A., and Yarmolyuk V. V.**, “Average Concentrations of Major, Volatile, and Trace Elements in Magmas of Various Geodynamic Settings,” *Geokhimiya*, No. 10, 1113–1124 (2004) [*Geochem. Int.* 42, 977–987 (2004)].
33. **Nelson D. R.**, “Isotopic Characteristics of Potassic Rocks: Evidence for the Involvement of Subducted Sediments in Magma Genesis,” *Lithos* 28, 403–420 (1992).
34. **Palme H. and O’Neill H. St. C.**, “Cosmochemical Estimates of Mantle Composition,” in *Treatise on Geochemistry* (Elsevier, Amsterdam, 2003), Vol. 2, pp. 1–38.
35. **Peccerillo A.**, “Geochemical Similarities between the Vesuvius, Phlegraean Fields and Stromboli Volcanoes: Petrogenetic, Geodynamic and Volcanological Implications,” *Mineral. Petrol.* 73, 93–105 (2001).
36. **Perchuk L. L., Safonov O. G., Yapaskurt V. O., and Barton J. M., Jr.**, “Crystal–Melt Equilibria Involving Potassium-Bearing Clinopyroxene As Indicator of Mantle-Derived Ultrahigh-Potassic Liquids: An Analytical Review,” *Lithos* 60, 89–111 (2002).

37. **Pettke T., Halter W. E., Webster J. D., et al.**, “Accurate Quantification of Melt Inclusion Chemistry by ICP-MS: A Comparison with EMP and SIMS and Advantages and Possible Limitations of These Methods,” *Lithos* 78, 333–361 (2004).
38. **Rudnick R. L. and Gao S.**, “Composition of the Continental Crust,” in *Treatise on Geochemistry* (Elsevier, Amsterdam, 2003), Vol. 3, pp. 1–64.
39. **Ryabchikov I. D.**, *Thermodynamic Analysis of the Behavior of Trace Elements during Crystallization of Silicate Melts* (Nauka, Moscow, 1965) [in Russian].
40. **Ryabchikov I. D.**, “Main Components of Geochemical Reservoirs of the Silicate Earth,” *Geokhimiya*, No. 1, 14–22 (2006) [*Geochem. Int.* 44, 11–18 (2006)].
41. **Saal A. E., Hauri E. H., Langmuir C. H., and Perfit M. R.**, “Vapour Undersaturation in Primitive Mid-Oceanic-Ridge Basalt and the Volatile Content of Earth’s Upper Mantle,” *Nature* 419, 451–455 (2002).
42. **Salters V. J. M. and Stracke A.**, “The Composition of the Depleted Mantle,” *Geochem. Geophys. Geosyst.* 5 (5), 1–27 (2004).
43. **Schilling J.-G., Bergeron M. B., and Evans R.**, “Halogens in the Mantle beneath the North Atlantic,” *Philos. Trans. R. Soc. London A297*, 147–178 (1980).
44. **Sleep N. H.**, “Lateral Flow and Ponding of Starting Plume Material,” *J. Geophys. Res.* 102, 10001–10012 (1997).
45. **Spath A., Le Roex A. P., Opiyo-Akech N.**, “Plume–Lithosphere Interaction and the Origin of Continental Rift-Related Alkaline Volcanism—the Chyulu Hills Volcanic Province, Southern Kenya,” *J. Petrol.* 42, 765–787 (2001).
46. **Sun S. S. and McDonough W. F.**, “Chemical and Isotopic Systematics of Oceanic Basalts: Implication for Mantle Composition and Processes,” in *Magmatism in the Ocean Basins*, Ed. by A. D. Saunders and M. J. Norry, *Geol. Soc. Lond. Spec. Publ.* 42, 313–345 (1989).
47. **Webster J. D., Raia F., De Vivo B., and Rolandi G.**, “The Behavior of Chlorine and Sulfur during Differentiation of the Mt. Somma–Vesuvius Magmatic System,” *Mineral. Petrol.* 73, 177–200 (2001).
48. **Workman R. K. and Hart S. R.**, “Major and Trace Element Composition of the Depleted MORB Mantle (DMM),” *Earth Planet. Sci. Lett.* 231, 53–72 (2005).
49. **Workman R. K., Hart S. R., Jackson M., et al.**, “Recycled Metasomatized Lithosphere as the Origin of the Enriched Mantle II (EM2) End-Member: Evidence from the Samoan Volcanic Chain,” *Geochem. Geophys. Geosyst.* 5 (4), 1–44 (2004).
50. **Zindler A. and Hart S.**, “Chemical Geodynamics,” *Annu. Rev. Earth Planet. Sci.* 14, 493–571 (1986).

Regime of Volatile Components in the Zones of Diamond Formation

Ryabchikov I. D.

*Institute of Geology of Ore Deposits, Petrography, Mineralogy, and Geochemistry
Russian Academy of Sciences, Moscow*

The leading forms of carbon in natural magmas and fluids are either oxidized (CO₂, CO, and carbonates) or reduced (mainly methane and other hydrocarbons) compounds. The formation of crystalline forms of elementary carbon (graphite or diamond) in endogenous processes may proceed through either reduction of CO₂ or carbonates or partial oxidation of hydrocarbons. Thermodynamic analysis of mineral equilibria in carbon-bearing systems allowing us to choose between these two alternatives is carried out in this study. Most mineral inclusions in diamonds have a composition practically identical to the minerals of rocks from the mantle lithosphere, namely peridotite and eclogite.

Estimations of temperatures and pressures for mineral assemblages of these inclusions are very similar to the geotherm estimated for xenoliths in kimberlites and correlate with the value of heat flow for the stable Precambrian, in which the majority of kimberlitic fields are located. Contacting mineral inclusions in diamonds provide an average temperature of 1079°C and a pressure of 5.4 GPa. At the same time, isolated mineral inclusions provide an average temperature of 1197°C and a pressure of 6.3 GPa [1]. These parameters are significantly lower than the solidus of volatile-free mantle lherzolite, but close to the solidus of carbonated peridotite [2].

Undeniably, carbonates may play an important role in diamond-forming media. Quantitative estimation of the water content seems to be more problematic. Unaltered depleted harzburgite, being a predominant material in the subcratonic lithosphere, must be characterized by low concentrations of all incoherent elements including water. With allowance made for the similar behavior of water and cerium in magmatic processes, the expected water content at a cerium content of ~5 ppb (Fig. 1) and H₂O/Ce ~200 would be only ~1 ppm [3]. Such low water concentrations were reported for some olivines from mantle peridotites [4].

A comparison of these results with experimental data on water solubility in olivine at high pressures [5] provides an H₂O activity of ~10⁻³. Lower values of water activity were obtained in analysis of amphibole equilibria in mantle peridotites [6]. However, in most cases the water contents in olivines from kimberlite and mantle peridotite exceed this value: the average value for olivines in kimberlite is ~120 ppm [7], but in this case the value of water activity will be

~0.1. An increase in the water content above several ppm is probably controlled by mantle metasomatism resulting from the ascent of silicate and carbonate melts or supercritical water-rich fluids from

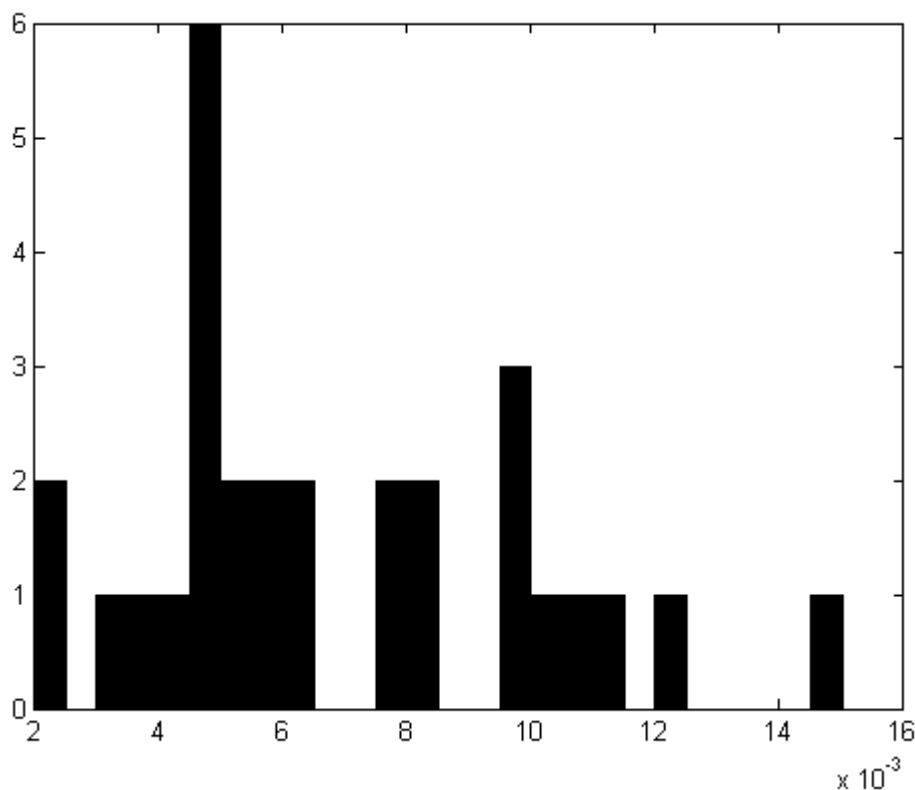
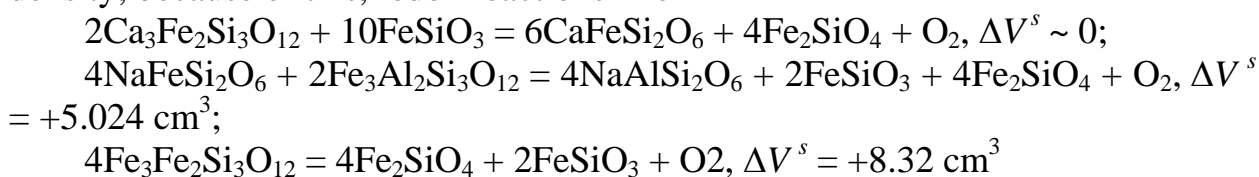


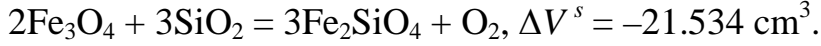
Fig. 1. **Histogram of cerium concentrations (Ce < 15 ppb) in nonmetasomatized mantle harzburgites.** This figure is plotted using the GEOROC database. Ce contents of ~5 ppb are the most common.

the underlying convecting mantle or ascending plume to the lithosphere. High rates of water diffusion in lattices of rock forming minerals and especially intergranular diffusion result in rapid water migration from initially water-rich fluids/melts to wall rocks leading to dehydration of mobile phases. In this connection in most cases the processes of diamond formation probably proceed at a low water activity of ~0.1 or even lower values.

The lower parts of the subcratonic lithosphere, where the majority of diamonds are probably formed, are characterized by strongly reduced conditions. This is caused by a decrease in the oxygen fugacity in mantle rocks resulting from pressure increase with depth [8]. The explanation is that the components of upper mantle minerals (garnets, clinopyroxenes) containing Fe^{3+} have a high density; because of this, redox reactions like



are characterized by higher values of volume effect than those typical for normal oxygen buffers, such as quartz–fayalite–magnetite



Estimations of oxygen fugacity for mantle peridotites from South Africa using garnet–olivine–orthopyroxene oxybarometer demonstrate that values decrease with depth relative to the quartz–fayalite–magnetite buffer (Fig. 2); at a pressure of ~6.5 GPa these values are close to -4 [9, 10]. Such values of the redox potential are deep in the field of diamonds, but not of carbonate stability.

Let us apply the estimations of oxygen fugacity presented above for evaluation of the role of hydrocarbons f_{O_2} in the diamond formation. We consider this problem for the reaction

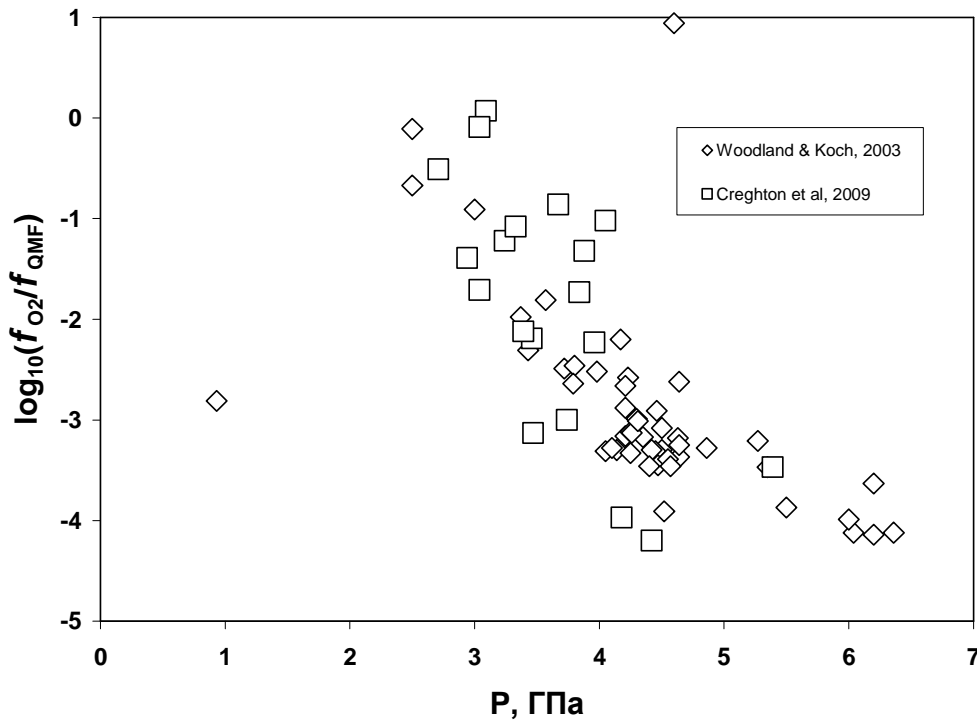


Fig. 2. Correlation between oxygen fugacity logarithm normalized on quartz–fayalite–magnetite (QFM) buffer and pressure. (1) Data by [9]; (2) data by [10].

Methane activity in the system is controlled by the reaction equilibrium

$$\text{constant } (K) \text{ as } a_{\text{CH}_4} = K \cdot \frac{a_{\text{H}_2\text{O}}^2 \cdot (f_{\text{H}_2\text{O}}^0)^2}{f_{\text{O}_2} \cdot f_{\text{CH}_4}^0}$$

where a is the activity of components; f^0 are the fugacities of pure components at the given temperature and pressure.

The upper limit of H₂O activity for kimberlite is estimated as ~0.1 (see above). For 5 GPa and 1500 K (typical conditions of diamond formation) and an oxygen fugacity lower than the quartz–fayalite–magnetite buffer by three orders of magnitude (such values were obtained for mantle garnet peridotite, in which the pressure of mineral equilibria is close to 5 GPa), the calculated methane activity is 0.001 (Fig. 3) or lower; i.e., the system is far from saturation with methane. Hence, it follows that diamond formation most likely occurs through reduction of carbonate components, but not partial oxidation of hydrocarbons.

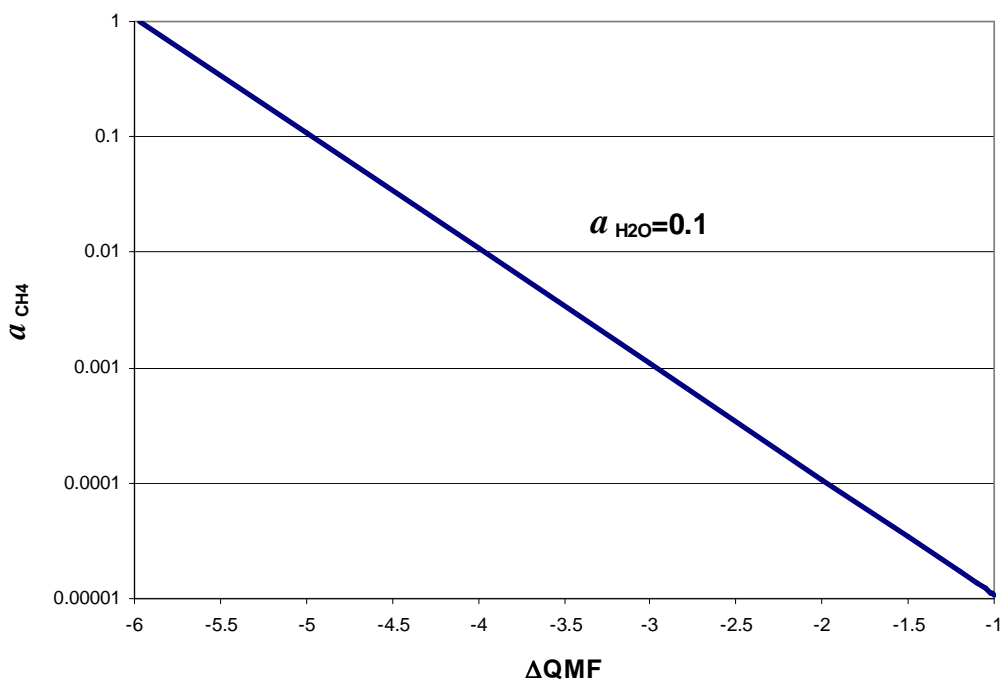


Fig. 3. Correlation between methane activity in diamond-bearing paragenesis and oxygen fugacity logarithm normalized on a quartz–fayalite–magnetite (QFM) buffer at a constant water activity = 0.1. Pressure 5 GPa; temperature 1500 K.

This conclusion is in agreement with the studies on volatile-rich components of microinclusions in natural diamonds. Water, carbonates, and halides, but not hydrocarbons, prevail in their composition [11]. The idea that oxidized carbon represented by carbonate components of the melt or supercritical fluid ascended to the subcratonic lithosphere from the underlying asthenosphere or uprising mantle plume makes sense.

Estimations of f_{O_2} for midocean ridge basalts with the asthenosphere mantle as a source range from the QFM buffer to values lower by approximately one logarithmic unit [12]. These values are higher than the boundary values for carbonate–graphite (or carbonate–diamond) buffer reactions of the EMOD (enstatite–magnesite–olivine–diamond) type. Consequently, carbon under such conditions must occur in an oxidized form. This is proved by the prevalence of CO₂ in the gaseous phase of oceanic tholeiite. Typical derivatives of plume magmas,

such as basalt of intraplate oceanic islands, are characterized by higher values relative to mid-ocean ridge basalts [13]. Derivates from plume matter resulting in the formation of Siberian Trap Province (meimechite) [14] and subalkaline basalt of the Putorana Plateau [15] are more oxidized.

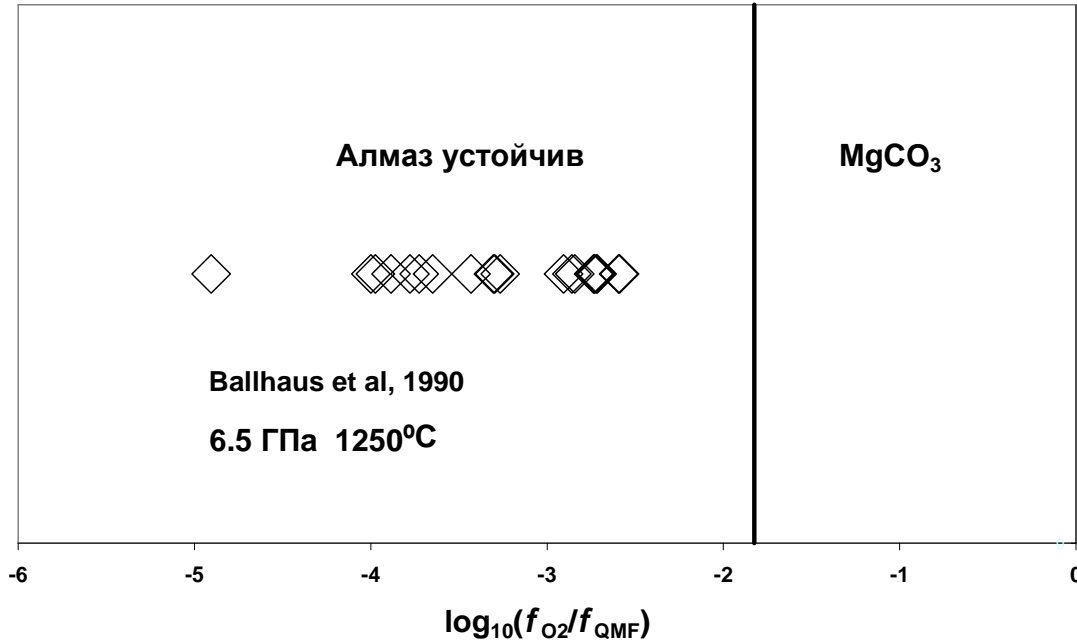


Fig. 4. Variations of oxygen fugacity values estimated from the data on the compositions of chrome spinel inclusions in diamonds. Oxygen fugacity is normalized on a quartz–fayalite–magnetite (QFM) buffer. Pressure 6.5 GPa; temperature 1250°C.

Most likely relative oxidation of plume magmas may result from disproportionation of divalent iron in deep zones with participation of high-pressure phases. In the lower mantle, trivalent iron is strongly stabilized in metasilicate of perovskite structure when this mineral contains a high aluminum concentration. This occurs at a depth of >700 km after garnet is removed from the mineral association of mantle peridotite and the Al_2O_3 concentration increases to a maximum. The intense incorporation of trivalent iron by silicate perovskite requires a parallel reduction of part of the divalent iron according to the scheme $3\text{Fe}^{2+} = \text{Fe}^0 + 2\text{Fe}^{3+}$. This must result in the appearance of approximately 1% of metallic iron in the rock with an average composition of mantle peridotite. For the lower mantle pressures eutectic with metallic iron in the Fe–S system is characterized by significantly lower temperatures than those estimated for the lower mantle (> 1600°C). Because of this, an essential portion of metallic iron, which appeared during disproportionation reaction, is dissolved in the low-sulfurous sulfide melt.

During the ascent of lower mantle material in mantle plumes, heavy sulfide–metallic melt will be removed to lower parts of the uprising column. As a result, anatexis of the upper part of the plume beginning because of decompression during

the ascent to the base of the lithosphere will proceed with participation of matter with high $\text{Fe}^{3+}/\text{Fe}^{2+}$ ratios. Magmas appearing under such conditions will have a relatively oxidized nature. Furthermore, it is not inconceivable that redox differentiation may result from diffusive migration of hydroxyl in mantle zones, which differ by water content in nominally anhydrous minerals. If such migration occurs at least partially in the form of elementary H_2 , diffusive dehydration will be accompanied by oxidation. Under such relatively oxidized conditions, near-solidus magmas generated in the plume beneath the lithospheric mantle will be represented by carbonate or silicate–carbonate melts. Their intrusion into the lower parts of the lithosphere will lead to reduction of carbonate components of the melt with the formation of diamond as a result of interaction with strongly reduced peridotite.

The described mechanism of diamond formation in the course of reduction of carbonate components in melts/fluids intruding into the subcratonic lithosphere from the underlying convecting mantle is consistent with the observed links between diamonds and processes of mantle metasomatism. This mechanism is also proved by the signs of mantle matter oxidation in metasomatically modified samples, in particular, the increase of the $\text{Fe}^{3+}/\text{Fe}^{2+}$ ratios in the outer parts of zoned garnet crystals from mantle peridotites, which demonstrate the influence of mantle metasomatism [10]. Estimations of oxygen fugacity based on the data on compositions of chrome spinel inclusions in diamonds (Fig. 4) demonstrate a range from values typical for the subcratonic lithosphere (Fig. 2) to boundary conditions of diamond equilibrium with carbonates. These variations are consistent with the mechanism of interaction of relatively oxidized melts from the ascending mantle plume with reduced material of the lower part of the lithosphere. In conclusion, it may be said that low water activity in the lower part of the subcratonic lithosphere prevents the formation of hydrocarbons even in the presence of elementary carbon and at a low oxygen fugacity.

The most likely mechanism of diamond formation is the reduction of carbonate components in near-solidus melts intruding into the lithosphere from ascending mantle plumes. The intrusion of diamond-forming melts into the overlying cool horizons of the lithosphere results in their partial crystallization; residual aqueous–halide phases participate in the formation of polycrystalline diamond aggregates or fibrous grains with inclusions of aqueous–carbonate–chloride brines.

ACKNOWLEDGMENTS

This work was supported by the Russian Foundation for Basic Research (project no. 08-05-00356), the International Association for the Promotion of Cooperation with Scientists from the Independent States of the Former Soviet Union (project no. 05-1000008-7938), the Division of the Earth Sciences, Russian

Academy of Sciences (program no. 9), and the Presidium of the Russian Academy of Sciences (program no. P12).

REFERENCES

1. **Phillips D., Harris J. W., and Viljoen K. S.**, *Lithos* 77, 155–179 (2004).
2. **Brey G. P., Bulatov V. K., Girs A. V., et al.**, *J. Petrol.* 49 (4), 797–821 (2008).
3. **Dixon J. E., Leist L., Langmuir C., et al.**, *Nature* 420 (6914), 385–389 (2002).
4. **Peslier A. H., Woodland A. B., and J. A. Wolff**, *Geochim. Cosmochim. Acta* 72 (11), 2711–2722 (2008).
5. **Kohlstedt D. L., Keppler H., and Rubie D. C.**, *Contrib. Mineral. Petrol.* 123, 345–357 (1996).
6. **Lamb W. M. and Popp R. K.**, *Am. Mineral.* 94 (1), 41–52 (2009).
7. **Matveev S. and Stachel T.**, *Geochim. Cosmochim. Acta* 71 (22), 5528–5543 (2007).
8. **Ryabchikov I. D.**, *Dokl. Akad. Nauk* 268 (3), 703–706 (1983).
9. **Woodland A. B. and Koch M.**, *Earth Planet. Sci. Lett.* 214, 295–310 (2003).
10. **Creighton S., Matveev S., Höfer H., et al.**, *Contrib. Mineral. Petrol.* 157, 491–504 (2009).
11. **Klein Ben David, Izraeli E. S., Hauri E., et al.**, *Geochim. Cosmochim. Acta* 71, 723–744 (2007).
12. **Bezos A. and Humler E.**, *Geochim. Cosmochim. Acta* 69 (3), 711–725 (2005).
13. **Ryabchikov I. D. and Kogarko L. N.**, *Intern. Geol. Rev* 36, 173–183 (1994).
14. **Ryabchikov I. D., Solovova I. P., Kogarko L. N., et al.**, *Geochem. Int.* 40 (11), 1031–1043 (2002) [*Geokhimiya*, No. 11, 1139–1150 (2002)].
15. **Ryabchikov I. D., Ntaflos T., Solovova I. P., et al.**, *Geochem. Int.* 39 (5), 415–433 (2001) [*Geokhimiya*, No. 5, 467–483 (2001)].

Evolution aspects of geochemical heterogeneity of the lithosphere

Balashov Yu.A.

*Geological Institute of the Kola Science Centre, RAS, Apatity, e-mail:
balashov@geoksc.apatity.ru*

ABSTRACT

The lithosphere heterogeneity of the Earth is the result of a complex multi-stage action of physical (astronomical), geodynamic and chemical factors. These factors embrace virtually the whole interval (≈ 4.56 Ga) from the early stages of the protoplanetary cloud condensation and accretion to the interplanetary multi-stage differentiation and homogenization. These processes reflect the evolution of magma generation and secondary transformation under the effect of mantle metasomatism or mixing in subduction conditions and other processes [1 etc.].

In this paper the results of isotope-geochemical investigations of rare elements for the continental lithosphere are compared with those for the oceanic lithosphere. To reveal isotope-geochemical heterogeneities in the vertical section of the mantle continental lithosphere we chose variations of the REE contents, Sm/Nd and $\epsilon\text{Nd}(0)$ values in peridotite xenoliths. This section covers all variations in peridotite mineral composition with the lithosphere depth from the upper plagioclase-spinel (Pl-Sp) and spinel (Sp) facies to the lower high-temperature garnet (Gt2) facies in a depth range of ≈ 15 -250 km. In all diagrams the data for peridotites are compared with the reference average estimations of the primitive (PM) and oceanic (OM) mantle composition.

VERTICAL ZONING OF MODERN LITHOSPHERE

The change in the Sm/Nd ratio and $\epsilon\text{Nd}(0)$ values in peridotites from different depths correlate well. This correlation reflects a successive transition from “primary oceanic” with Sm/Nd > 0.3247 (average for the primitive mantle) and $\epsilon\text{Nd}(0) \gg \text{CHUR}=0$ to the values that reflect the influence of the mantle metasomatism and other secondary factors. The influence is registered by Sm/Nd $\ll 0.3247$ and the appearance of $\epsilon\text{Nd}(0) < \text{CHUR}$ negative values (Fig. 1). For the spinel facies we added the data on clinopyroxene (Cpx) which is the main concentrator of the peridotite REE since the isotope parameters and REE contents in them are close or identical with those observed in the initial rocks. In the vertical section of the modern continental lithosphere (Fig. 1) the uppermost and lowermost peridotite zones are distinctly more homogeneous than the middle (Sp + Sp-Gt + Gt1) lithosphere. Nevertheless, it should be noted that the presented diagram is a rather rough generalization since it cannot reflect the $\epsilon\text{Nd}(T)$ changes in time that are important for the Precambrian. These changes are distorted when we convert them to $\epsilon\text{Nd}(0)$ values measured today. But this is a forced method since age characteristics for the majority of xenoliths are not available. For

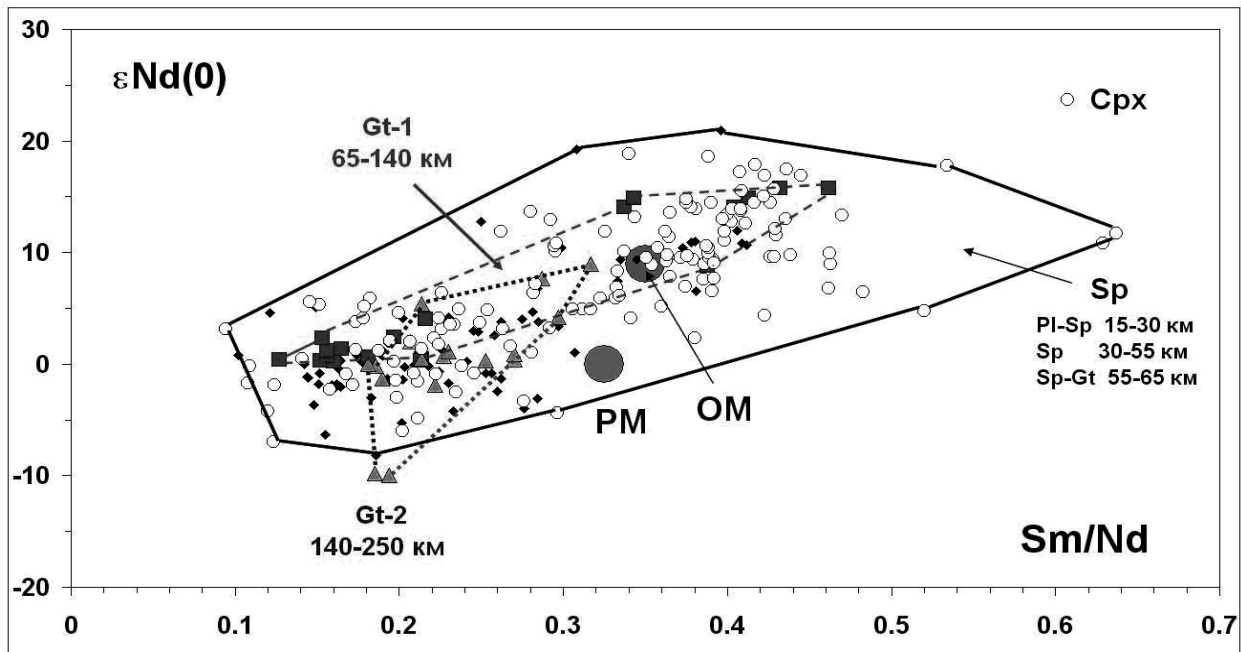


Fig. 1. Variations of $\epsilon\text{Nd}(0)$ and Sm/Nd in peridotite xenoliths of all depth facies in the modern continental lithosphere.

The field contours: 1) *Sp* – includes spinel and transition spinel-plagioclase [2] and spinel-garnet facies; 2) *Gt 1* – low-temperature garnet facies ($< 1200^\circ\text{C}$) [3]; *Gt 2* – high-temperature garnet facies. PM – primitive mantle; OM – oceanic mantle. The data for Precambrian peridotite differences are excluded since the majority of the oldest peridotites are distinctly displaced to negative $\epsilon\text{Nd}(0)$ values.

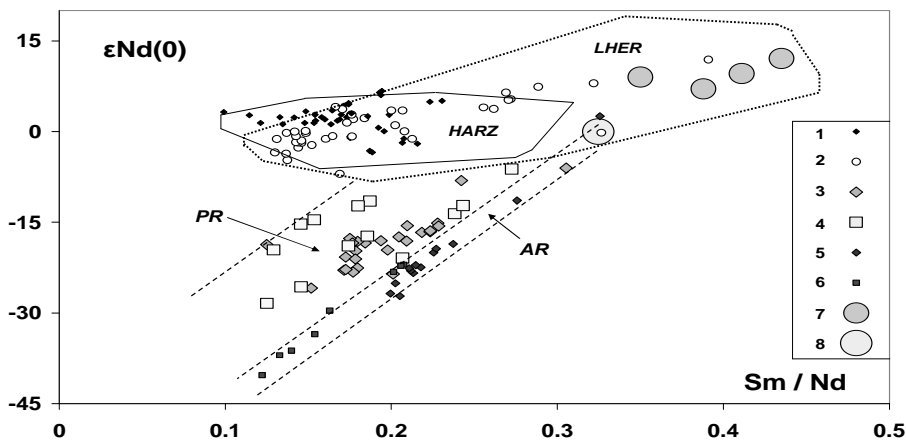


Fig. 2. The influence of the endogenic events age on Sm/Nd and $\epsilon\text{Nd}(0)$ relations in peridotite xenoliths of spinel facies and mantle magmas [5]:

1 – alkaline volcanites, intrusions and carbonatites (0.1-130 Ma); 2 – the same for 239-404 Ma; 3 – alkaline intrusions (1160-1884 Ma); 4 – carbonatites (1299-1872 Ma); 5 – Archaean volcanites of greenstone belts (2575-2681 Ma); 6 – Archaean carbonatites (2661-2677 Ma); 7 – average for the oceanic mantle depleted to a different degree; 8 – average for the primitive mantle. HARZ and LHER are modern fields of harzburgite and lherzolite xenoliths of the lithosphere.

instance, for the low-temperature garnet xenolith from South Africa (Premier) dated at 1150 ± 41 Ma, we obtained the value of $\epsilon\text{Nd}(T) = +0.7$, while for spinel

harzburgite from the Khibiny massif (Kola Peninsula) dated at 2054 ± 79 the value of $\epsilon\text{Nd}(T) = +17.9$ [3, 4].

A wide range of Sm/Nd variations in peridotites reflects essential geochemical heterogeneity independent of time. Therefore Sm/Nd distinctions can be used for stricter geochemical constructions. For instance, distinctions between initial lherzolites and harzburgites were observed. In most cases harzburgites (and dunites) are considered as restites of melting mantle magmas from lherzolites. This in its turn allows one to compare their isotope-geochemical characteristics with those observed in the Phanerozoic mantle magmas with a high degree of reliability since the influence of the time factor is excluded for Phanerozoic rock differences. As shown in Fig.2, late Phanerozoic alkaline magmas are fully confined to harzburgite-lherzolite fields. All other magma types generated in the Precambrian greatly deviate from the modern field of spinel facies peridotite. This is indirect evidence of their older generation. The calculated values of $\epsilon\text{Nd}(0)$ are sharply decreased.

Differentiation is registered along the lithosphere vertical for different elements of the mantle xenoliths (Table 1, Fig. 3). Two trends were distinguished

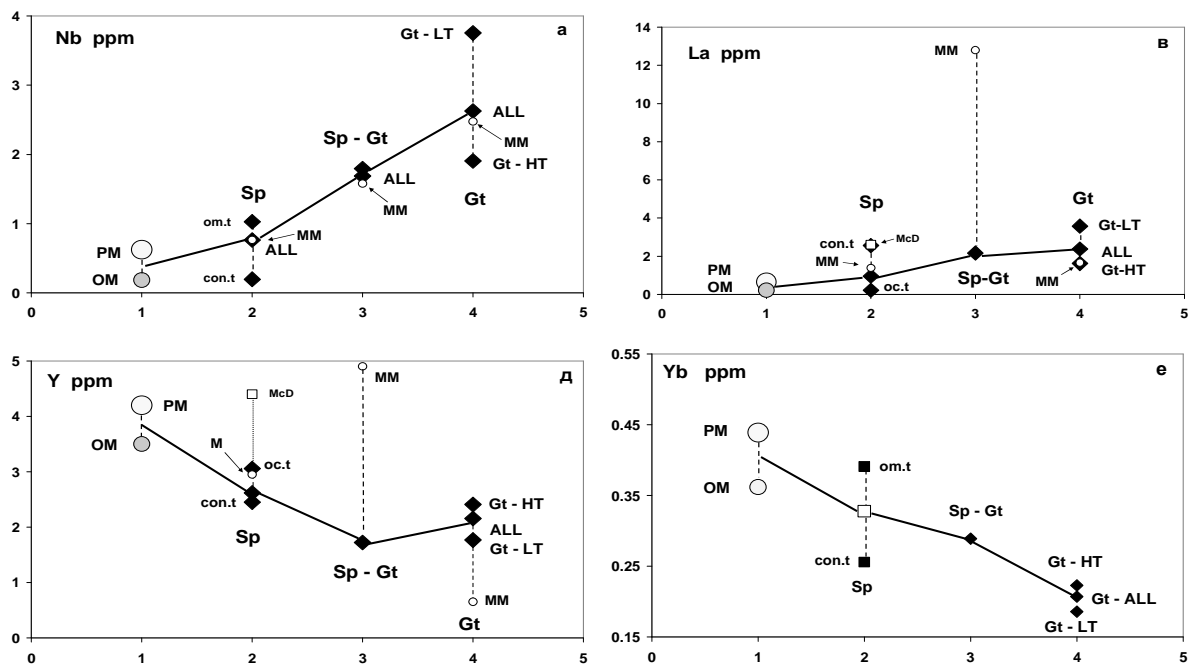


Fig. 3. Vertical zoning of the rare element distribution in the lithosphere: increase of the average content from the spinel facies to garnet ones (a, b) and decrease (d, e). PM and OM – the average for the primitive (chondrite) and oceanic mantle; Sp, Sp-Gt, Gt-LT, Gt-HT – spinel, spinel-garnet, low- and high-temperature garnet facies; MM – metamorphosed differences (mantle metasomatism); oc.t and con.t. –oceanic and continental differences of the spinel facies.

Table 1

**The average content (ppm) of rare elements in harzburgite and lherzolite xenoliths
in the vertical section of the continental lithosphere.**

Facies	nn	Nb	nn	Th	nn	La	nn	Zr	nn	Y	Nn	Yb
PM≈BSE	3	0.625	3	.081	3	0.649	3	10.34	3	4.203	3	0.439
OC-M	3	0.186	3	0.013	3	0.219	3	6.07	3	3.499	3	0.362
Sp-H	14	2.022	14	0.25	28	2.471	26	3.806	23	0.76	28	0.078
Sp-H MM	7	1.531	7	0.307	9	2.219	7	7.881	6	1.167	10	0.117
Sp-H ALL	21	1.858	21	0.269	37	2.41	33	4.671	29	0.844	38	0.087
Sp-Gt -H (MM)	5	5.208	5	0.366	6	2.583	6	3.173	6	0.257	6	0.0817
Gt-H LT	4	2.633	5	0.246	4	2.907	5	5.08	3	1.42	4	0.0119
Gt-H HT	3	1.213	3	0.142	3	0.991	3	3.68	3	0.813	3	0.0657
Gt-H ALL	7	2.024	8	0.207	7	2.086	8	4.555	7	1.16	7	0.096
Sp-L-oc. type	15	1.026	14	0.141	46	0.212	7	5.554	7	3.056	46	0.391
Sp-L-con. type	7	0.196	16	0.288	21	2.559	16	4.99	18	2.449	21	0.256
Sp-L MM	26	0.764	26	0.278	37	1.382	28	9.719	21	2.95	37	0.292
Sp-L ALL	48	0.763	56	0.247	104	1.102	51	7.664	46	2.77	104	0.328
Sp-Gt-L	5	1.794	3	0.153	5	2.16	3	6.273	4	1.722	5	0.2
Sp-Gt-L MM	5	1.578	5	0.219	5	12.8	5	11.01	3	4.9	5	0.378
Sp-Gt-L ALL	10	1.686	8	0.194	10	7.5	8	9.235	7	3.084	10	0.289
Gt-L LT	9	3.752	9	0.429	9	3.572	9	5.369	9	1.767	9	0.186
GtL LT-MM	5	2.474	4	0.267	5	1.658	4	5.15	3	0.653	5	0.198
Gt-L HT	13	1.905	13	.183	14	1.614	13	8.468	14	2.407	14	0.223
Gt-L ALL	27	2.626	26	0.281	28	2.251	26	6.885	26	1.983	28	0.207

Note: nn – a number of determinations; PM≈BSE –average for the primitive mantle (the Earth’s silicate composition); OC-M – the same for the oceanic mantle; Sp-H and Sp-L spinel facies of harzburgites and lherzolites; Sp-Gt spinel-garnet facies; Gt- garnet facies; LT and HT- low-temperature and high-temperature; MM – altered peridotite differences; Sp-oc. and Sp-con. – lherzolites with geochemical parameters of oceans and continents.

that reflect a directional increase or decrease of rare elements and their anomalous build-up under superposition of secondary processes (mantle metasomatism – MM and others). An optimal enrichment in La and Zr for peridotites of Sp-Gt facies is definitely related to MM. Mineralogical features of MM are displayed in the appearance of accessory minerals (apatite, monazite etc.), amphibole and mica and REE spectrum distortion [6 etc.]. It is not improbable that oceanic lherzolite enrichment in Y and Yb reflects an additional impact of the early moving away of light lanthanides during formation of the oceanic reservoir in combination with MM.

The presence of mantle metasomatism signs in the lithosphere section allows one to distinguish the most drastic changes in the element concentration due to this process. For instance, one can see a sharp accumulation of the most mobile among REE – La as compared with Yb in peridotite xenoliths (Fig.4) that reaches the level of the “primary» mantle magmas – pyroxenites in peridotite xenoliths. This indicates potential “ore presence” of peridotites which experienced the maximum impact of the mantle metasomatism [5, 7].

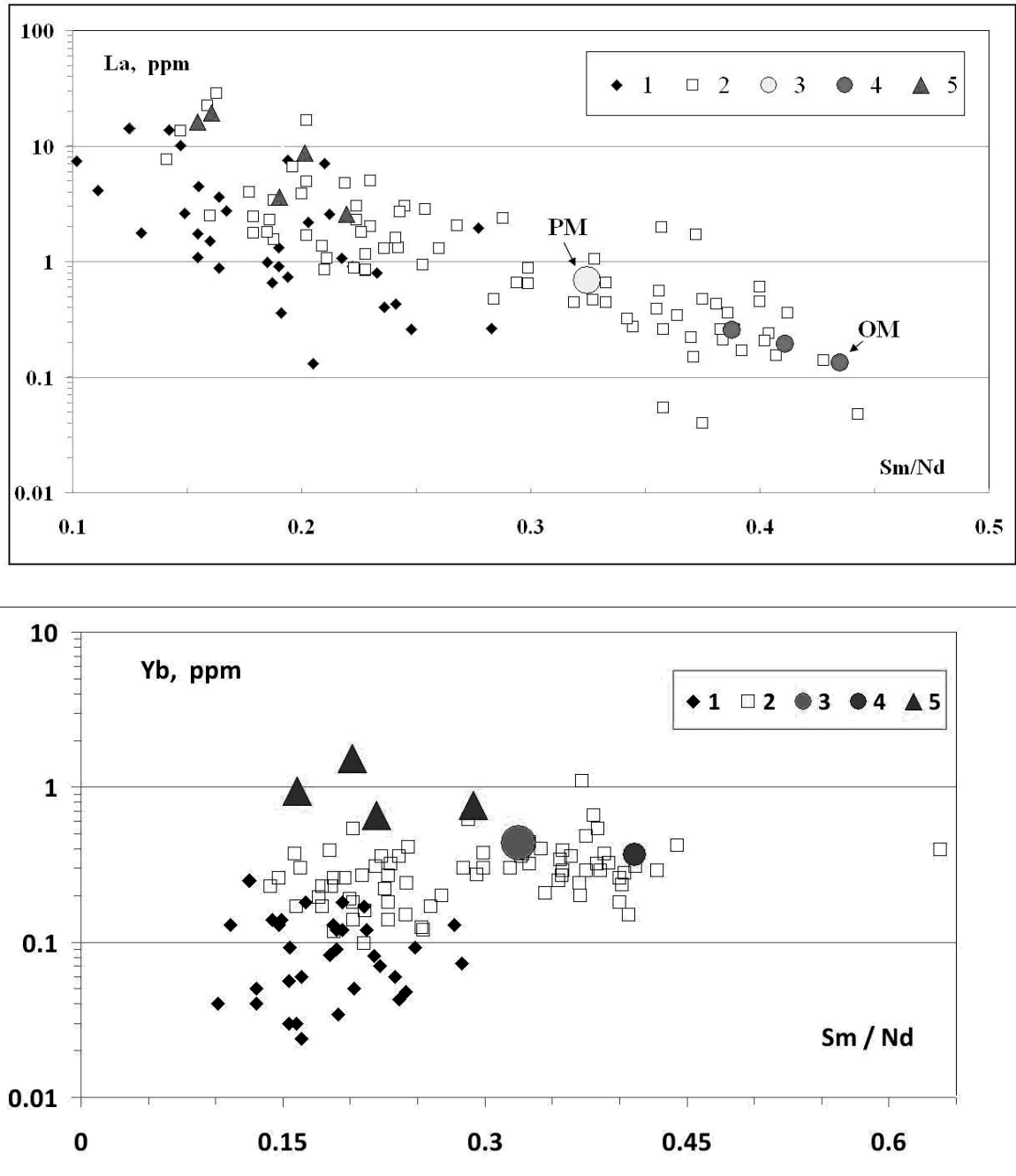


Fig. 4. Enrichment in La and Yb of harzburgites (1), lherzolites (2) and pyroxenites (5). 3 and 4 – average for the primitive and oceanic mantle.

GEOCHEMICAL CONTRAST IN LHERZOLITES AND HARZBURGITES

A rather strict Yb distribution along the lithosphere section allows one to trace in more details the concentration contrast for individual elements between lherzolites and harzburgites along the lithosphere vertical section (Figs. 5 and 6). The variations mentioned reflect the total variability for a number of rare and trace elements in the continental and oceanic lithosphere segments separately. This is

true for the entire available age interval of the lithosphere restricted by the differentiation line (EM-DM) of lherzolites in Hadean [1].

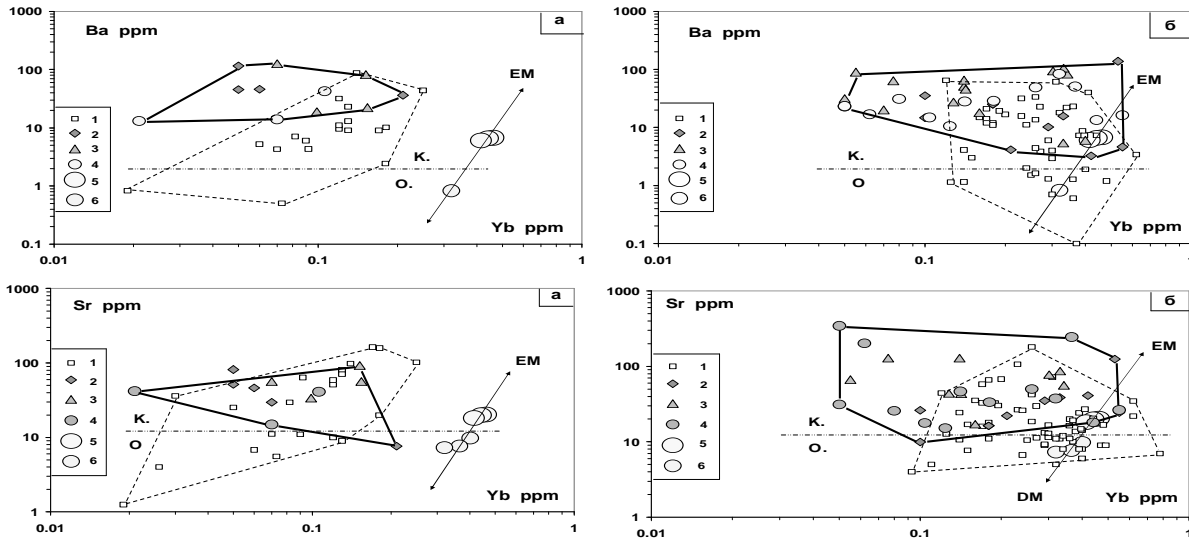


Fig. 5. The relation between alkaline-earth elements and Yb in harzburgite (a) and lherzolite (b) xenoliths.

1 – spinel; 2 – spinel-garnet; 3 – low-T garnet; 4 – high-T garnet; 5 – average for the primitive mantle; 6 – average for the oceanic mantle. EM-DM – tentative variation field for the relation between Yb and rare elements in lherzolites in Hadean [1]. K and O – tentative division of the subcontinental and suboceanic segments of the lithosphere.

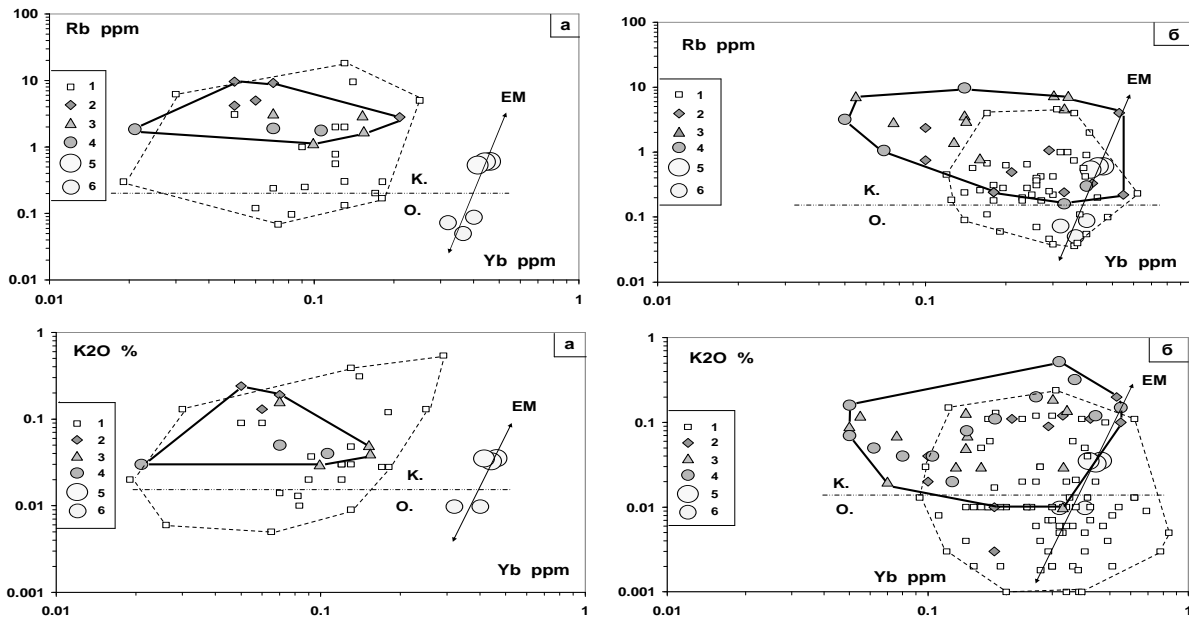


Fig. 6. Relation between alkaline elements and Yb in harzburgites (a) and lherzolites (b) xenoliths. (Symbols as in fig.5).

GEOCHEMICAL RELATIONSHIP BETWEEN THE LITHOSPHERE COMPOSITION AND GENERATED MAGMAS

An Figures 1 – 6 show the difference in the relations Sm/Nd and $\epsilon\text{Nd}(0)$ and rare elements to Yb for peridotites of the “primitive” and “oceanic” mantle. This suggests that peridotites and generated magmas in both lithosphere segments inherited these contrasts. We can check this by REE examples. As Figs 7 and 8

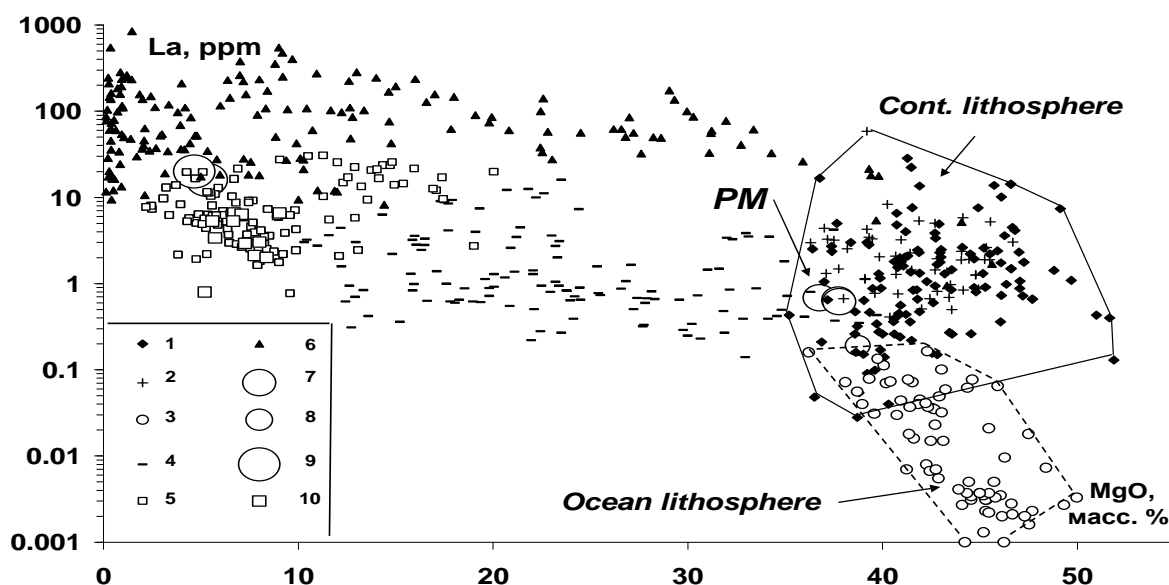


Fig. 7. La distribution trends in the peridotite lithosphere – mantle magmatism series.

1 – 2: spinel and garnet facies of the continental peridotites; 3 – oceanic peridotites; 4 – komatiites; 5 – continental basalts; 6 – alkaline magmas; 7 - average for the primitive mantle; 8 – average for the oceanic mantle; 9 – average for the crust; 10 – oceanic basalts.

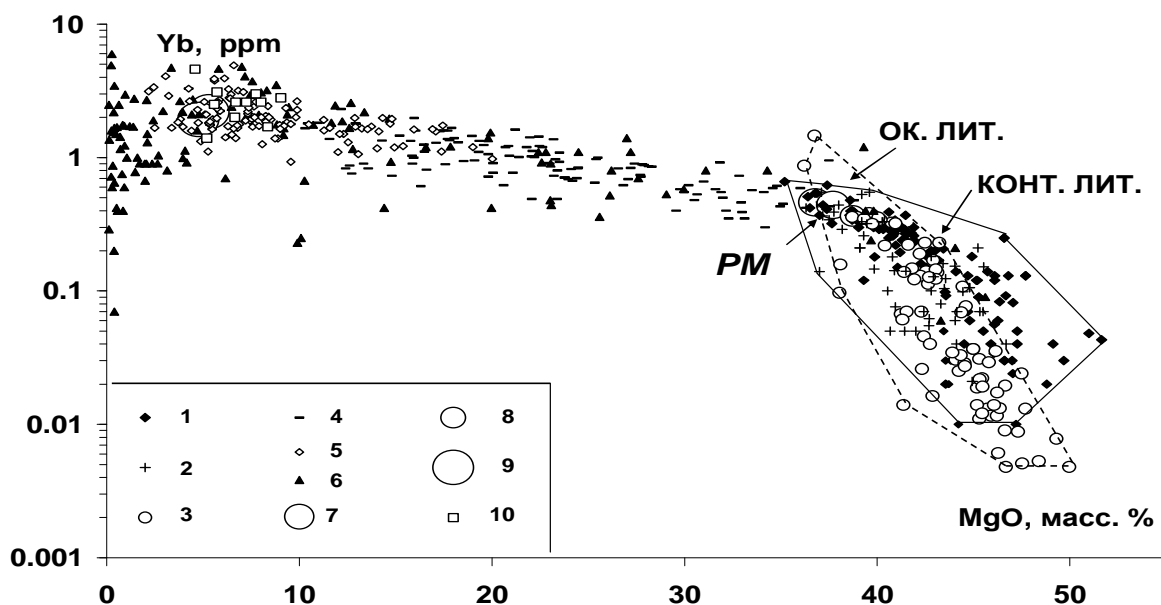


Fig. 8. Yb distribution trends in the peridotite lithosphere – mantle magmatism series. (Symbols as in Fig 7).

suggest, the data set for La and Yb in peridotites and generated mantle magmas greatly differ in the Earth's segments – optimally for La and minimally for Yb. Since these contrasts are traced through the whole age interval of the mantle magmas, one may state that geochemical differences optimally for La and minimally for Yb. Since these contrasts are traced through the whole age interval of the mantle magmas, one may state that geochemical differences between both lithosphere segments were laid at the early stages of the planet geospheres formation [1 etc.]

Thus, a generalized picture of the lithosphere geochemical heterogeneity includes contrast between xenoliths of different composition constantly observed, registers effects of repeated superposition of secondary processes and the presence of alternative trends for vertical differentiation. All these phenomena reflect the impact of geochemical and isotope heterogeneity generation in the lithosphere. It is an easy matter to see from Figs. 7 and 8 that the Earth's lithosphere registers the difference between the continental and oceanic segments that is likely to arise at the earliest stages of the geospheres formation.

THE RELATION BETWEEN LITHOSPHERIC PROCESSES OF DIFFERENTIATION AND HOMOGENIZATION

Much more complicated problems concern an interpretation of variations of geochemical relations in mantle rocks in attempting to trace their changes in geological time.

It is not improbable that the primary heterogeneity of the initial meteoritic matter of all types in the solar system was inherited since the primary homogenization of the initial meteoritic matter is unknown. The meteoritic matter participated in the accretion at the Earth (and other planets of the Earth group) formation. This issue has not been discussed in press so far. Meteorites are mainly composed of chondrite that is considered to be a formation source of the Earth silicate shell – its mantle. If we compare the initial geochemical heterogeneity of meteorites with the Archaean lithosphere heterogeneity, we shall find out that the degrees of the Sm/Nd variations in the oldest rocks of the Earth and in meteorites are similar (Fig. 9). Furthermore, if we use the REE data for the mantle magmas dominating in the Archaean that are represented by komatiite and basalt of the greenstone belts, we shall see the directed decrease in the geochemical heterogeneity degree in the series from the Archaean to Proterozoic complexes. This allows the existence of continuous processes of homogenization in the Earth's mantle in the range of 3.9 to ≈ 2.0 Ga. There is an alternative interpretation of such regularity – probable working by secondary processes and repeated superposition of contamination. These processes are well displayed in the oldest rocks, for instance, in the complex of mantle and crust rocks in Greenland [10 – 12 etc.]. At the same time, it is in these oldest rocks in Greenland that the signs of the

preserved positive anomaly for $\epsilon^{142}\text{Nd}$ were discovered. The anomaly was inherited from the Earth accretion stage [22-24 etc.] and suggests the initial depleted composition of the Earth's mantle.

This is evidence of the limited homogenization of the silicate shell in the oldest rocks and allows one to support the idea about large-scale homogenization at the successive stages of the mantle existence.

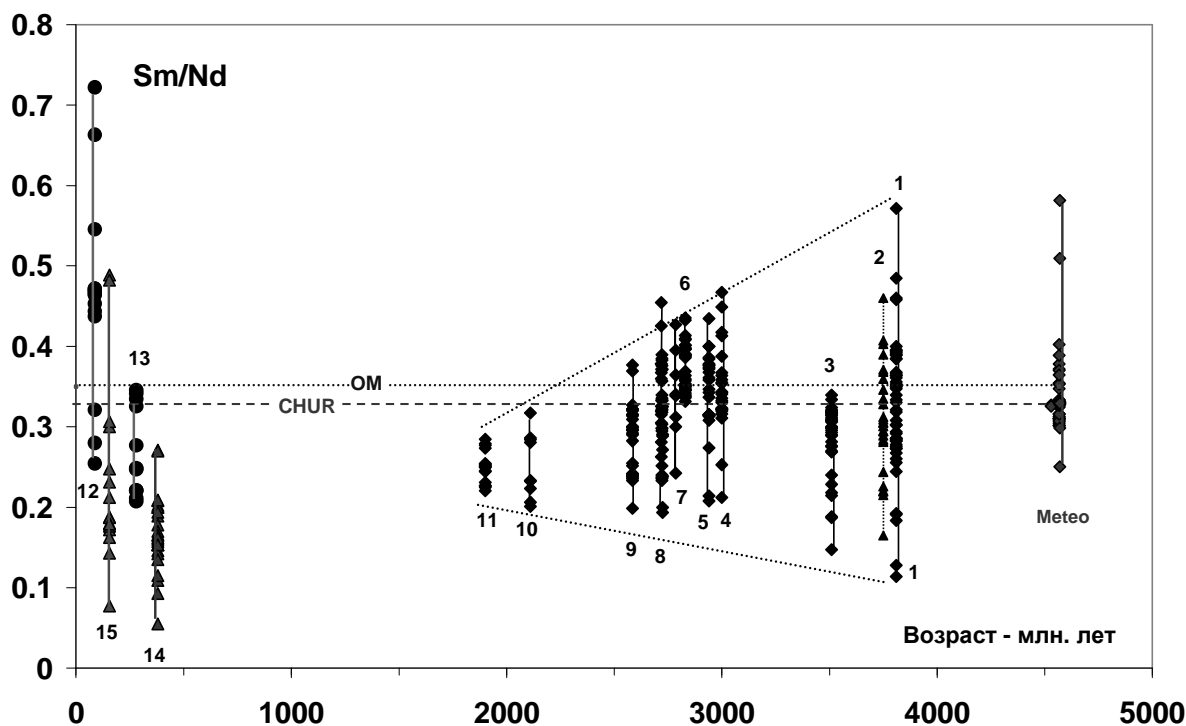


Fig. 9. Two development trends of the lithosphere heterogeneity on evidence from variations of the Sm/Nd ratio for peridotite xenoliths and mantle magmas.

Meteo – chondrite, eucrite, chondre and its minerals, silicate inclusions in iron meteorites [8, 9], 1-12 komatiite-basalt complexes of the greenstone belts and zones: 1 – SW Greenland, Isua (3810 Ma), 2 – SW Greenland, Isua (3750 Ma), 3 – South Africa, Onverwacht (3510 Ma), 4 – Canada, Lumdy Lake and Uchi, Balmer (≈ 3000 Ma), 5 – Karelia: Koikara, Palaselga, Sovdozero and Hautavaara structures (≈ 2940 Ma), 6 – Karelia, Kostomuksha structure (2830 Ma), 7 – Canada, Vizien (2786 Ma), 8 – Canada, Abitibi (2718 Ma), Vizien (2724 Ma), Australia, Kambalda (2722 Ma), Australia, Yilgarn, Kalgoorlie (2585 Ma), 10 – French Guiana, Dachine (2110 Ma), 11 – South China, Northern Guangxi Province (1900 Ma), 12 – Colombia, Gorgona Island (88 Ma) [10-19 etc.], 13 – Australia, New South Wales (280 Ma), [8-14 etc.], 14 – apaitic alkaline complexes, ultrabasic xenoliths and magmas of the Kola Paleozoic province (380 Ma) [20], 15 – xenoliths of spinel peridotites in oceanic basalts (Kerguelen, Saint Paul Island, Zabargat) (155 Ma) [21 etc.].

For the younger lithosphere this effect is changed by appearance and increase in the heterogeneity degree during the last 2.0 Ga. Within the Phanerozoic very high fractionation in terms of Sm/Nd was found in mantle xenoliths and magmas of different composition. As a result gigantic modern lithospheric heterogeneity

was formed. It is recorded in peridotites and accompanying mantle magmas (Fig. 10).

Thus, cosmic heterogeneity of the chondrite-like material is only the primary heterogeneity that affected geochemical relations in the early Earth's mantle and in its upper zone – lithosphere.

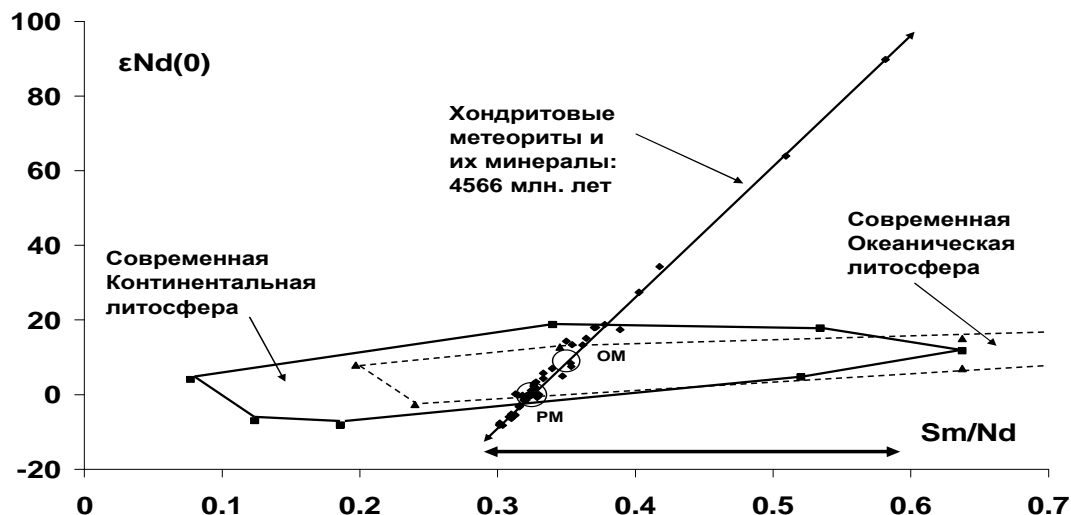


Fig.10. Contrast of the Sm/Nd variation range between chondrites and modern lithosphere (about double increase for the lithosphere).

The discovery of a two-stage evolution of the lithosphere heterogeneity allows specific corrections to be introduced in the ideas about the history of formation and interaction between the Earth's geospheres. The discovery also promotes new understanding of other adjacent geological, geodynamic and geochemical problems.

The work was done according to NIR plan №4-2009- 2102 and was financially supported by the Russian Foundation for Basic Research, grant №07-05-00572-a.

REFERENCES

1. **Balashov Yu.A.** Development of the lithosphere heterogeneity: geochemical grounds // Petrology. 2009. V. 17. № 1. P. 97-107.
2. **Ionov D.A., O'Reilly S.Y., Ashchepkov I.V.** Feldspar-bearing lherzolite xenoliths in alkali basalts from Hamar-Daban, southern Baikal region, Russia // Contrib. Mineral. Petrol. 1995. V. 122. P. 174-190.
3. **Pearson D.G., Carlson R.W., Shirey S.B., Boyd F.R., Nixon P.N.** Stabilisation of Archaean lithospheric mantle: A Re-Os isotope study of peridotite xenoliths from the Kaapvaal craton // Earth and Planet. Sci. Lett. 1995. V.134. P. 341-357.
4. **Arzamastsev A.A., Glaznev V.N.** Plume-lithospheric interaction under conditions of the ancient sublithospheric mantle keel by the example of the Kola alkaline province // Proc. of Acad. Sciences. 2008. V. 419. № 4. P. 515-518.

5. **Balashov Yu.A.** Correlation between modern heterogeneous lithosphere and Phanerozoic alkaline magmatism // "Geochemistry of magmatic rocks". XXVI International conference. School. "Geochemistry of alkaline rocks". Moscow, Russia, May 11-15, 2009. P. 21-23.
6. **Carlson R.W., Irving A.J.** Depletion and enrichment history of subcontinental lithospheric mantle: An Os, Sr, Nd and Pb isotopic study of ultramafic xenoliths from the north-western Wyoming Craton // *Earth and Planet. Sci. Lett.* 1994. V. 126. P. 457-472.
7. **Balashov Yu.A., Glaznev V.N.** Cycles of alkaline magmatism // *Geochemistry*. 2006. № 3. P. 1-14.
8. **Amelin Yu., Rotenberg E.** Sm-Nd systematics of chondrites // *Earth Planet Sci. Lett.* 2004. V. 223. P. 267-282.
9. **Stewart B., Papanastassiou D.A., Wasserburg G.J.** Sm-Nd systematics of a silicate inclusion in the Caddo IAB iron meteorite // *Earth Planet Sci. Lett.* 1996. V. 143. P. 1-12.
10. **Frey R., Jensen B.K.** Re-Os, Sm-Nd isotope- and REE systematics on ultramafic rocks and pillow basalts from the Earth's oldest oceanic crustal fragments (Isua Supracrustal Belt and Ujaragssuit nunât area, W Greenland) // *Chem. Geol.* 2003. V. 196. P. 163-191.
11. **Bennett V.C., Nutman A.P., McCulloch M.T.** Nd isotope evidence for transient, highly depleted mantle reservoirs in the early history of the Earth // *Earth Planet Sci. Lett.* 1993. V. 119. P. 299-317.
12. **Polat A., Hofmann A.W., Münker C., Regelous M., Appel P.W.** Contrasting geochemical patterns in the 3.7-3.8 Ga pillow basalt cores and rims, Isua greenstone belt, Southwest Greenland: Implications for postmagmatic alteration processes // *Geochim. Cosmochim. Acta.* 2003. V. 67. P. 441-457.
13. **Jochum K.P., Arndt N.T., Hofmann A.W.** Nb-Th-La in komatiites and basalts: constraints on komatiite petrogenesis and mantle evolution // *Earth Planet Sci. Lett.* 1991. V. 107. P. 272-289.
14. **Hollings P., Wyman D., Kerrich R.** Komatiite-basalt-rhyolite volcanic associations in Northern Superior Province greenstone belts: significance of plume-arc interaction in the generation of the proto continental Superior Province // *Lithos.* 1999. V. 46. P. 137-161.
15. **Svetov S.A.** Magmatic systems of the ocean-continent transition zone in the Archaean eastern Fennoscandinavian shield. Petrozavodsk. 2005. 230 pp.
16. **Puchtel I.S., Hofmann A.W., Mezger K., Jochum K.P., Shchipansky A.A., Samsonov A.V.** Oceanic plateau model for continental crustal growth in the Archaean: A case study from the Kostomuksha greenstone belt, NW Baltic Shield // *Earth Planet Sci. Lett.* 1998. V. 155. P. 57-74.
17. **Arndt N.T., Kerr A., Tarney J.** Dynamic melting in plume heads: the formation of Gorgona komatiites and basalts // *Earth and Planet. Sci. Lett.* 1997. V. 146. P. 289-301.
18. **Capdevilla R., Arndt N., Letendre J., Sauvage J.-F.** Diamonds in volcanoclastic komatiite from French Guiana // *Nature.* 1999. V.399. P. 456-458.
19. **Zhou M.-F., Zhao T.-P., Malpas J., Sun M.** Crustal-contaminated komatiitic basalts in Southern China: products of a Proterozoic mantle plume beneath the Yangtze Block // *Precambrian Res.* 2000. V. 103. P. 175-189.
20. **Arzamastsev A.A., Bea F., Belyatsky B.V., Glaznev V.N., Arzamastseva L.V., Travin A.V., Montero P.** Paleozoic processes of a plume-lithospheric interaction in the NE Baltic Shield: duration, volumes and conditions of magmogenesis // *Geology and mineral resources of the Kola Peninsula. V. 2. Mineral resources, mineralogy, petrology, geophysics. Apatity.* 2002. P. 104-145.
21. **Mattielli N., Weis D., Gregoire M., Mennessier J.P., Cottin J.Y., Giret A.** Kerguelen basic and ultrabasic xenoliths: Evidence for long-lived Kerguelen hotspot activity // *Lithos.* 1996. V. 37. P. 261-280.

22. **McCulloch M.T., Bennett V.C.** Evolution of the early Earth: constraints from ^{143}Nd - ^{142}Nd isotopic systematics // *Lithos*. 1993. V. 30. P. 237-255.
23. **Caro G., Bourdon B., Birck J.-L., Moorbath S.** ^{146}Sm - ^{142}Nd evidence from Isua metamorphosed sediments for early differentiation of the Earth's mantle // *Nature*. 2003. V. 423. P. 428-432.
24. **Boyet M., Carlson R.W.** A new geochemical model for the Earth's mantle inferred from ^{146}Sm - ^{142}Nd systematics // *Earth and Planet. Sci. Lett.* 2006. V. 250. P. 254-268.

Application of the monomineral thermobarometers for the reconstruction of the mantle lithosphere structure.

Ashchepkov I.V.¹, Vladykin N.V.³, Pokhilenko N.P., Logvinova A.M.¹, Kuligin S.S.¹, Pokhilenko L.N.¹, Malygina L.V.¹, Alymova N.V.³, Mityukhin S.I.², M.Kopylova⁴.

¹ *Institute of Geology and Mineralogy, SD RAS Novosibirsk 630090, Russia;*

² *Central Science and Research Geology And Prospecting Institute Of The Stock Company "ALROSA", Chernyshevsky Str, 7, Mirny, 678170 Russian Federation;*

³ *Institute of Geochemistry SD RAS, Favorsky str. 1a, Irkutsk, 66403*

⁴ *University British Columbia, 6339 Stores Rd EOS Dept V6T 1Z4 Vancouver, Canada;*

ABSTRACT

System of the original monomineral thermobarometers [3] in modified variant allow to reconstruct the structure of the mantle lithosphere beneath the Siberian craton (60 pipes) using original data, and Africa (30 pipes), North America (20 pipes) using data from literature and public domains. Original monomineral thermobarometers for mantle peridotites for clinopyroxene, garnet, chromite and ilmenites for the mantle peridotites were statistically calibrated on the TP estimates for mantle peridotites were tested using the mineral phases obtained in high pressure experiments with the natural peridotites (380 runs) and eclogites (240 runs). Clinopyroxene barometer give the correlation ($k \sim 1$) with experimental pressure to 100 kbar ($R \sim 0.93$) for peridotites and to 80 kbar ($R \sim 0.77$) for eclogites. Fe#Ol determined according to the regression equations found from the compositions of the minerals from xenoliths (>900) allow to receive very good coincidence with the monomineral versions.

For the reconstruction of the equilibrium of the peridotite minerals and details of the structure of mantle columns the calculated with the regressions the Fe#Ol coexisting with each minerals and series of the TPF diagrams was used. The layered structure of the mantle suggested by the geophysical models is proved by the TP estimates. The influence of the plume melts is shown by the rising of the Fe# of the minerals and temperatures which are coinciding on TP diagrams with the position of the HT eclogites and HT diamond inclusions and TP trajectories of the ilmenite trends leaved by the protokimberlite melts. In mantle sections it is possible to determine several geotherms starting from the subduction (<35 mwtm-2) to conductive (35-40 mwtm-2) and HT ones (>45 mwtm-2) associated with plume melt rising. The deeper part of the mantle column beneath the Udachnaya show the presence of the subadiabatic HT branch traced by HT pyroxenites and deformed peridotites 65 to 40 kbar, which coinciding with the TP trajectories of the ilmenites and deformed peridotites. High scattering of the temperatures was followed by the melting of peridotites and eclogites due to the polybaric interaction with the plume melts melt percolation and mantle diapirism. Presence of the several branches of the geotherms evidences about the several stages of the melt percolation.

Similar regularities were determined for the mantle columns beneath the Mesozoic pipes of Canada and South Africa. Due to the difference in the diffusion rates for the minerals they are tracing different stages of the thermal history of the peridotites rocks. Garnet gives the more deep seated conditions and clinopyroxenes marks all the stages including most low temperature. Eclogites TP also mark quite different thermal conditions.

Eclogite inclusions in diamonds reflect as a rule more HT conditions. Different cratons reveal their typical features of the TPXF diagrams of the mantle sections beneath the kimberlite pipe. The thicker the lithospheric keel the colder are the geothermal gradients. Of craton kimberlites and rifting zones as well as the youngest pipes demonstrate most shallow and heated conditions of the mantle sections. Hot PT paths are associated with the evolution of the protokimberlite melts. Internal layering of the mantle keel is the controlling factor of the protokimberlite

Keywords. Mantle, craton, monomineral thermobarometry, garnet, pyroxene, ilmenite, chromite, lithosphere, kimberlite.

INTRODUCTION

Thermobarometric mantle reconstruction of the mantle of South Africa [9, , 10, 13, 15, 31, 46, 60, 61, 70], North America [6, 8, 16, 20, 22, 24, 26, 33- 35, 43, 57, 67], Baltica [38, 54] and Siberia [3, 5, 7, 12, 23, 29, 30, 55-57, 62- 64] using common methods of polymineral thermobarometry) and monomineral garnet thermobarometry [19, 59] allow us to produce models of the composition and structure of mantle keels beneath the continents which often correlate with the seismic tomography and sounding [1, 2, 48, 49, 51].

Recent studies have shown a layered structure of the lithospheric mantle [3, 8, 20, 22, 24, 37]. It is divided into 3-7 major units according to garnet thermobarometry [19, 58], but a combination of several methods [3,7] yields more detailed layering consisting of 9-12 units for mantle beneath Udachanaya and other pipes. The common model for subcontinental mantle lithosphere (SCML) growth invokes the underplating of oceanic and probably continental lithosphere beneath the continental keel of a craton which, according to Re/Os ages of the sulfides, was formed in Archaean times [[9, 21, 28, 29, 30, 52, 53]. According to these models, only the craton cores were created in Archaean time [49] and the outer parts were formed in the Proterozoic and later time. Sharp layering determined by pyroxene thermobarometry for the mantle column beneath Udachnaya [5, 7] supports the common subduction model for mantle layering beneath Siberia at least for one Daldyn kimberlite field. Zircon ages from eclogites and lower crustal xenoliths suggest that plume events were recorded during underplating of melts which probably affected also the peridotites in the mantle column [52]. Recent data show a more extended time of formation during Proterozoic and Phanerozoic time [51, 52] and a complex structure modified by melt percolation [21, 48].

ORIGINAL MONOMINERAL THERMOBAROMETERS

For mantle peridotites for clinopyroxene, garnet, chromite and ilmenites for the mantle peridotites were statistically calibrated on the TP estimates for mantle peridotites [3] were tested using the mineral phases obtained in high pressure experiments with the natural peridotites (380 runs) and eclogites (240 runs). The precision of the Cpx barometer for peridotites is a bit lower than P.Nimis and W.

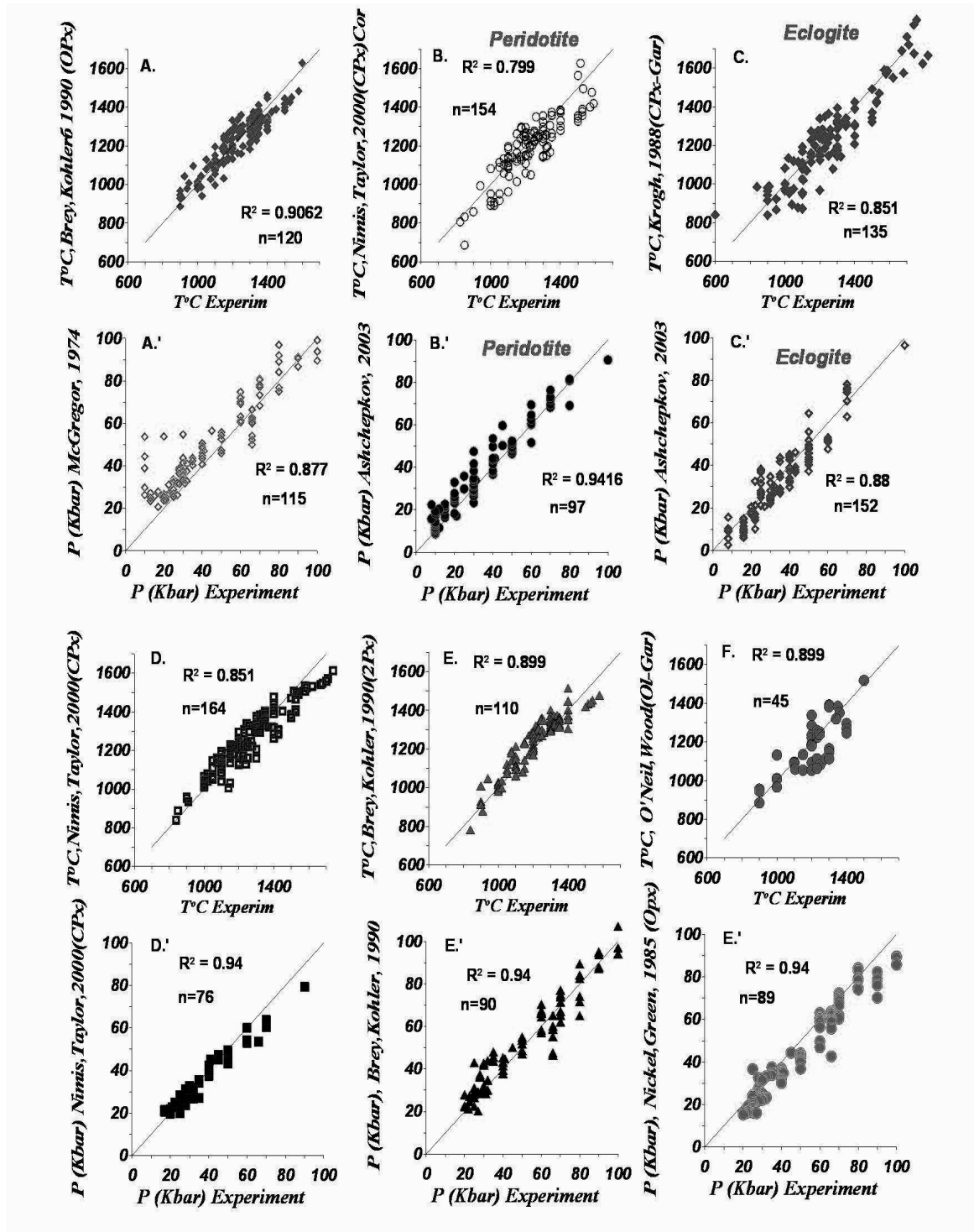


Fig.1. Correlations between the determined pressures and temperatures with barometers [3-7, 44, 45, 47] and thermometers [3, 7, 14, 36, 45, 47, 48, 69] and experimental conditions.

Taylor [44] barometer. But it allow to use it for the wide spectrum of the mantle rocks: peridotites , pyroxenites, eclogites together. This may be applicated for the reconstruction of the mantle sections using concentrates of the heavy fractions

from the kimberlites. The other monomineral barometric methods [4] give very similar results though the amount of the experimental data do not allow statistical experimental test for garnets ilmenites and chromites.. In new version of the TP program compiling together >45 thermometers 40 barometers [14, 35, 43, 44, 46, 47, 58, 65] and modified monomineral barometric equations [3-5] are used with the best thermometers for the mantle peridotites. In this version we calculate Fe#Olg the regressions with Fe#Ol_{xen} obtained by the correlations from the large data set (~2000) xenoliths from the kimberlites. It allows us to use the Gar-Cpx [36] and Gar-Ol [47] thermometers for garnet. The later have modifications more strongly accounting for Ca-Cr variations which produce the coincidence with the OPx methods [14]. For the chromites and ilmenites we used the monomineral variants of the equations from the W. Taylor and colleagues [69]. And for the clinopyroxenes the regression with the G. Brey [14, 42] and colleagues orthopyroxene barometer was used to obtain the TP estimates which are very close to those received by the orthopyroxenes and other minerals. Addition correlation was added for the high Al –Na pyroxenes from eclogites which give a good correlation for the Fe-Mg exchange Gar –Cpx thermometer.

The following equations are used for the calculation of the monomineral thermobarometry

GARNET

Three variants of barometer give similar results. The first is published [3, 5]. The second is calculating the Al₂O₃ from Garnet for Orthopyroxene according to procedure:

$$x_{CrOpx} = Cr_2O_3 / CaO / FeO / MgO / 500$$

$$x_{AlOpx} = 1 / (3875 * (\exp(Cr_2O_3^{0.5} / CaO - 0.3) * CaO / 1000 + 16) - x_{CrOpx})$$

$$x_{AlOpx} = x_{AlOpx} * 24.64 / (x_{(5,4)}^{0.5} * x_{(5,8)}^{0.2/3} + x_{(5,5)} * (ToK - 500) / 900)$$

$$x_{val} = x_{val} / ((ToK - 550) / 850) - 2.25 * \ln(MgO - 1.5)$$

$$IF(CaO.LE.4.or. Cr_2O_3.ge.7) \quad x_{Al_2O_3} = (x_{val} / \log((ToK - 550) * 2000 - 2.25 * \ln(MgO - 1.5))) * 1.07$$

And then it suppose using of the calculated xAl₂O₃ in Opx barometer [43].

The third variant is transformation of the G. Grutter [25] method by introducing of the influence of temperature.

$$P = 40 + (Cr_2O_3 - 4.5) * 10 / 3 -$$

$$20 / 7 * CaO + (ToC) * 0.0000751 * MgO * CaO + 2.45 * Cr_2O_3 * (7 - x_{(5,8)}) - Fe * 0.5$$

$$\text{with the correction for } P > 55: P = 55 + (P - 55) * 55 / (1 + 0.9 * P)$$

T temperature is estimated according to Gar-Cpx thermometer [36] where

$$T = (-6173.Ca^2 + 6731.Ca + 1879. + 10.P) / (\ln(KD) + 1.393)$$

$$KD = Fe_{Gar} / Mg_{Gar} (1 - Fe\#_{Cpx}) / Fe\#_{Cpx}$$

$$Fe\#_{Ga} = Fe / (Fe + Mg)$$

$$Fe_{Cpx} = Fe\#_{Ga} / 2 + (T^{\circ}K - 1420) 0.0001 + (P - 30) 0.000015 + 0.012 Cr / Ca + 0.013$$

$$\text{Fe\#Ol} = \text{Fe\#}_{\text{Gar}}/2 + (\text{T(K)} - 1325) * 0.000075 + (\text{P} - 35) * 0.000375 + 0.00370 * \text{XCr/XCa}^{0.75} + 0.0004 * \text{XTi} * (\text{P} - 25)$$

Ilmenite

$P = ((\text{TiO}_2 - 23.) * 2.15 - (\text{T} - 973) / 20 * \text{MgO} * \text{Cr}_2\text{O}_3)$ and next $P = (60 - P) / 6.1 + P$
 T°K is determined according to [69].

$$\text{Fe\#Ol}_{\text{Chr}} = (\text{Fe} / (\text{Fe} + \text{Mg})_{\text{ilm}} - 0.35) / 2.252 - 0.0000351 * (\text{T(K)} - 973)$$

Chromite

The equations for PT estimates with chromite compositions

$$P = \text{Cr} / (\text{Cr} + \text{Al}) * \text{T(K)} / 14. + \text{Ti} * 0.10 \text{ with the next iteration}$$

$$P = -0.0053 * P^2 + 1.1292 * P + 5.8059 + 0.00135 * \text{T(K)} * \text{Ti} * 410 - 8.2$$

$$\text{For } P > 60 \quad P = P + (P - 57) * 2.75$$

Temperature estimates are according to the [63].

The Fe#Ol values are estimated according to three iterations

$$\text{Fe\#Ol}_{\text{Chr}} = (\text{Fe} / \text{Fe} + \text{Mg}) / 4.5 - (\text{P} - 32) * 0.00115 - 0.03$$

$$\text{Fe\#Ol}_{\text{Chr}} = (\text{Fe\#Ol} - 0.074) * 0.45 + 0.086$$

$$\text{Fe\#Ol}_{\text{Chr}} = \text{Fe\#Ol} - (\text{Fe\#Ol} - 0.06) * (\text{T(K)} - 1300) * 0.000115 + 0.01$$

Clinopyroxene

$$\text{Pash2009} = 0.32 * (1 - 0.2 * \text{Na} / \text{Al} + 0.012 * \text{Fe} / \text{Na}) * \text{Kd}^{0.75} * \text{T}^\circ\text{K} / (1 + \text{Fe}) - 35 * \ln(1273 / \text{T}^\circ\text{K}) * (\text{Al} + \text{Ti} + 2.5\text{Na} + 1.5\text{Fe}^{3+}) + (0.9 - \text{CaO}) * 10 + \text{Na}_2\text{O} / \text{Al}_2\text{O}_3 * \text{T}^\circ\text{K} / 200$$

with the second iteration

$$P = (0.0000002 * P^4 + 0.000002 * P^3 - 0.0027 * P^2 + 1.2241 * P)$$

Clinopyroxene barometer [3,4] give the correlation ($k \sim 1$) with experimental pressure to 100 kbar ($R \sim 0.93$) for peridotites and to 80 kbar ($R \sim 0.77$) for eclogites. Garnet barometer reveal the correlation 80 kbar for low Cr (< 4) compositions ($R \sim 0.54$) and much better ($R \sim 0.76$) for high Cr garnet compositions determined from the minerals (40 runs). Chromite barometer also reveal a good correlation (~ 0.87). In thermometers for garnets [46] for ilmenite [69] and chromite [48] Fe#Ol determined according to the regression equations found from the compositions of the minerals from xenoliths (> 900) allow to receive very good coincidence with the monomineral versions.

DATA AND RESULTS OF TP CALCULATIONS

Using the data set for the ~ 30 kimberlite pipes from Africa [9, 10, 13, 15, 31, 46, 60, 61, 70], ~ 20 from N. America [6, 8, 16, 20, 22, 24, 26, 33- 35, 43, 57, 67] and ~ 15 from Baltica [38, 54] and 60 from Siberia [3, 5, 7, 12, 23, 29, 30, 55-57, 62- 64] we obtained the TP-X-FO2 diagrams. Here we represent the most typical sections of the mantle sections with the most large publish data set. The other can be found in WWW\igc.igm.nsc.ru.ash.htm.

For Siberan craton we reported the TP diagrams or the 7 regions from Siberan craton [3,5,7]. They all show mostly similar thermal structure despite in the different structures for the separate regions and even pipes. The common

feature is relatively low geothermal gradient (35 mvm-2), presence of several TP paths and much hopper one for TiO₂(HFSE) enriched associations and sharp layering to 9-12 horizons or 5-6 layer units. This is more clearly seen on the PTX plot for the Udachnaya pipe [3, 5, 7, 12, 23, 29, 30, 55-57, 62- 64] (Fig.10). The most depleted in Al Ca content peridotites occurs mainly in the lower part of the mantle sections where they compile 5 layers with the growth of Ca content upward. A similar arrays of the Fe increase with the decreasing pressure are possibly a result of the primary mantle layering. While in the upper part of the mantle section (<40 kbar) the trend of the P-CaO is divided on to two part. Those with the pyroxenitic values is decreasing which means that the pyroxenites are saturating in MgO upward possibly are reacting with the lherzolites or differentiation. Eclogites are forming two branches. Most of them are giving conditions from 40 to 55 kbars but there many relatively low pressure varieties also. Those containing diamonds [29, 30] are more high temperature and are close in TP conditions to the ilmenites and chromite diamond inclusions.

Ilmenite TP conditions are tracing convective branch within 45-65 kbar interval . They are close in Fe#Ol to the low Cr clinopyroxenes.

Diamond bearing peridotites and diamond garnet inclusions [40, 62, 64, 65] are mainly relatively low temperature giving in TP estimates near conductive cold geotherms with the deviations in HT conditions in 60-65 and 70-75 kbar intervals. The chromite diamond inclusions of reflect the conditions of the hot convective branch at the lithosphere base.

Bulk rock of peridotites from the Eastern part of the Siberian craton in Markha block refer commonly to the very depleted compositions. But they are subjected to the pervasive metasomatism with the high Na-Cr Al compositions of the pyroxenes probably due to the hybridization with the eclogites. While in the Daldyn block contain peridotites from fertile to the depleted lherzolites- harzburgites which are very close to the oceanic peridotites. [12]. The most depleted peridotites were detected in the Anabar block where many xenoliths are close to the dunites containing the nests of the garnets with the pyroxene rims. The eclogites in the Botuobinsky regions were found starting from 20 kbars. They are most frequent there near the Diamond-Graphite boundary. But in Daldyn block the higher amount of the eclogites was determined near 50 -55 kbar where they are forming the lens relatively pure in peridotites. Most of them coincides in the tP conditions determined for the ilmenites which reflect the TP path of the protokimberlite melts.

For South Africa there several kimberlite pipes which were studied more detail than the others, for example Jagersfontain , Kimberly, and others from

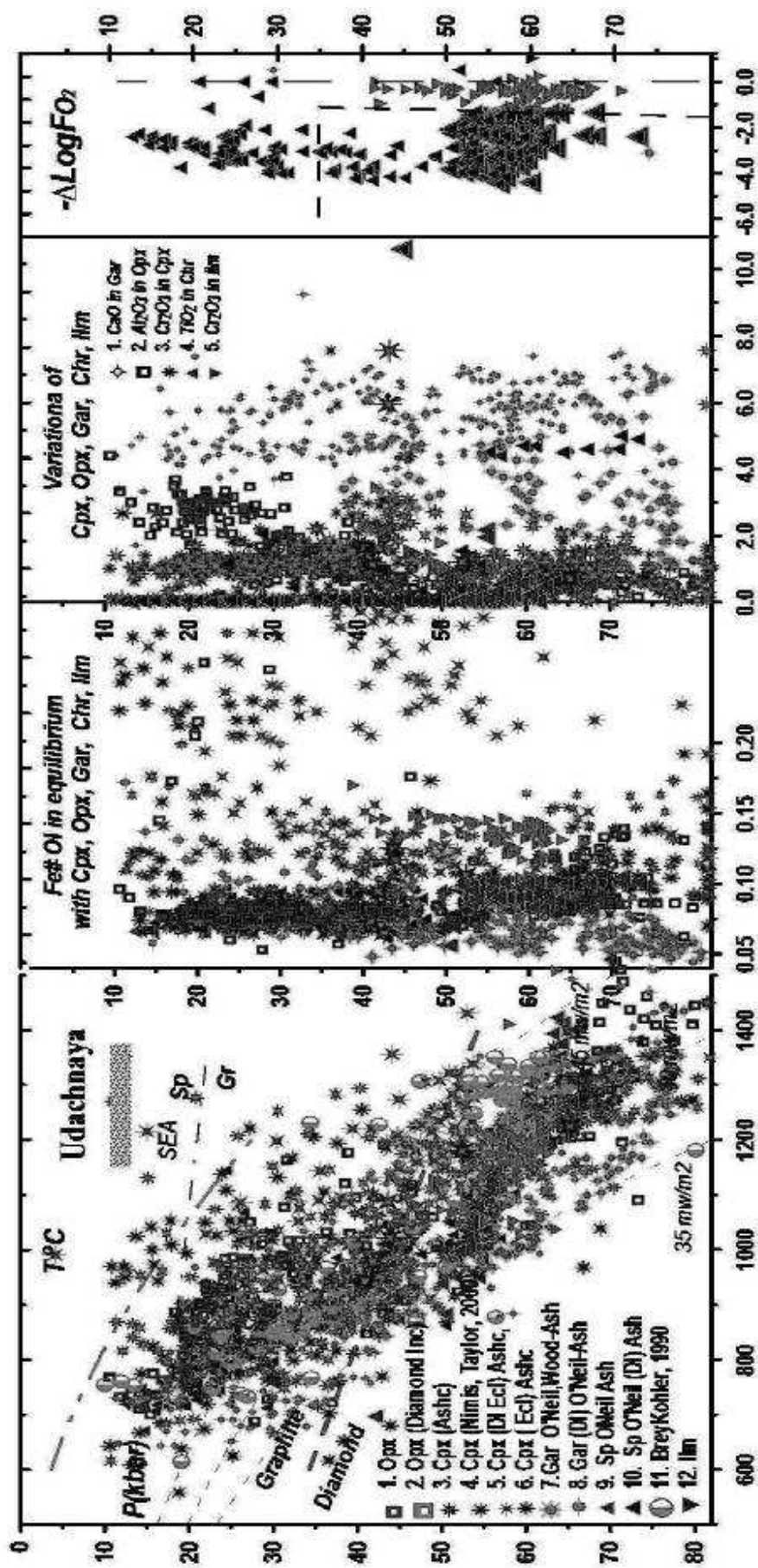


Рис. 2. TFX диаграммы для мантийных перидотитов по тр. Удачная по опубликованным данным ксенотитов [12, 27, 28, 60] и диссергационных работ С.С.Кулигина [37], Е.В.Мальгиной [41], Л.Н.Похиленко [56] и Н.В.Альмовой [2], а также по концентрации. **Примечания:** ТР оценки по минералам: 1. Ортопироксен (Opx) T°C[14]- P(kbar) [42], 2. То же для включений в алмазах, 3. Клинопироксен (Cpx) T°C [42]- P(kbar) [4]; 4. TP [42]- P(kbar) [4] для эклогитов; 5. - T°C [42]- P(kbar) [4] для включений в алмазах; 7. Гранат (Gar) (моно)- T°C [47]- P(kbar) [3], 8. - То же для включений в алмазах; 9. Хромит (Chr) ToC [45]- P(kbar) [3]; 10. То же для включений в алмазах; 11. T°C[14]- P(kbar); [39] Ильменит (Ilm) [69]- P(kbar) [3], 12.

Kaapvaal craton [9, 10, 13, 15, 31, 46, 60, 61, 70]. For some pipes mostly eclogitic xenoliths were studied such as Roberts Victor, Zero Kofifintain [10,13,46].

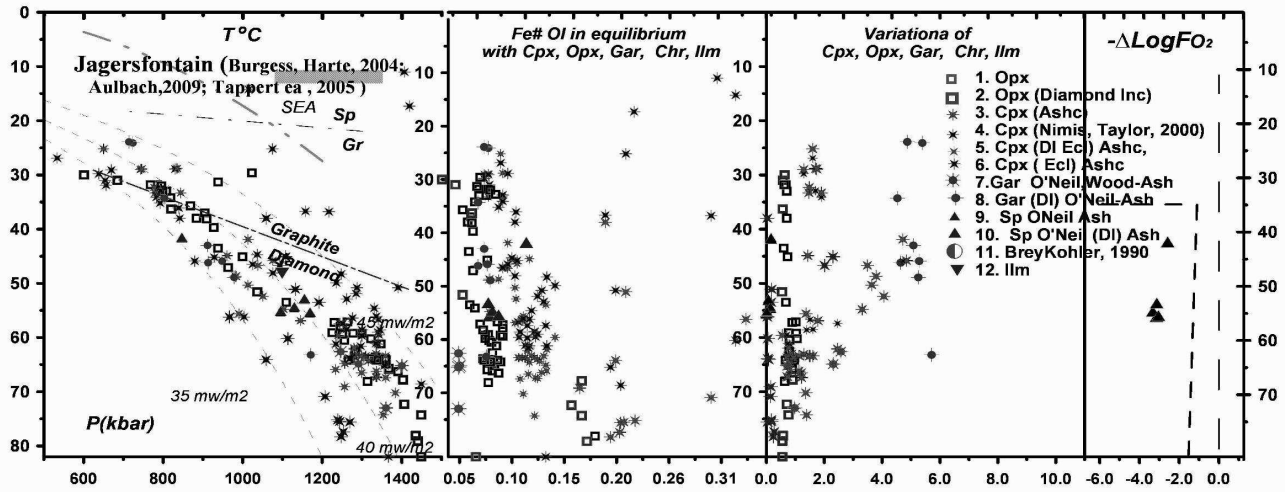


Fig. 3. TPXF diagram for the mantle beneath the Jagersfontain pipe, S.Africa [9,58,68].

Reported geotherms for the Kaapvaal craton based on the xenoliths from Mesozoic pipes are mostly tracing the 40 mvm-2 gradients [10, 46, 60, 61]. The same were detected for mantle the more ancient pipes like Premier [66]. All the authors reported very smooth or straight line geotherms with the inflections only near the 60 Kbars. These PT plots were obtained mostly by the pyroxene methods with the estimation of the pressures by orthopyroxene I.D.McGregor [43] barometer. Our monomineral barometers were all calibrated on this method. Nevertheless the thermobarometry of G Brey and P.Kohler [14] and coauthors shows similar but more inflected geotherms possibly due to the complex mantle

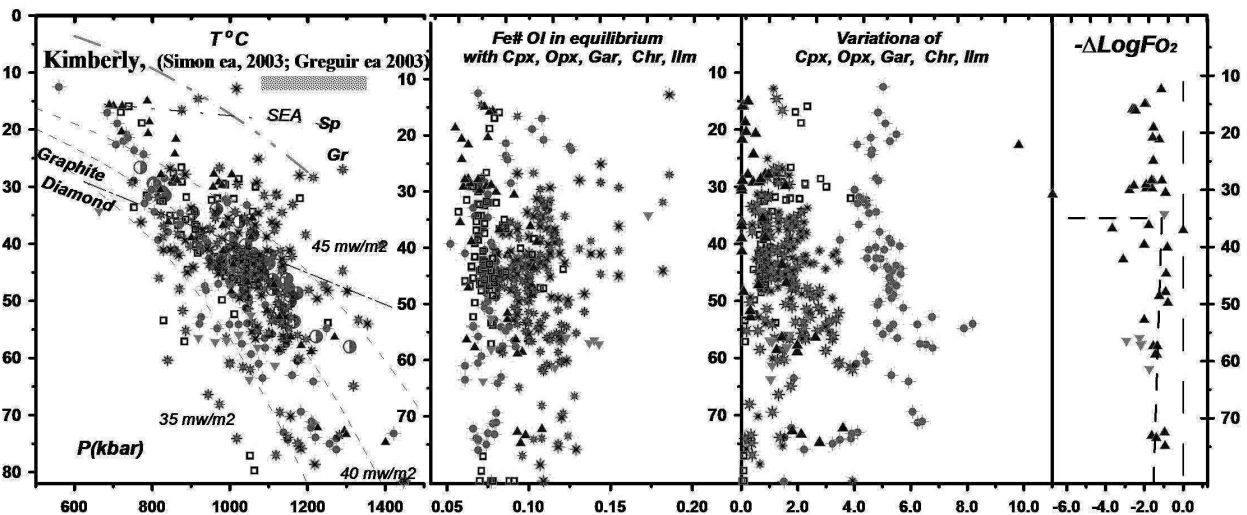


Fig. 4. TPXF diagram for the mantle beneath the Kimberly pipe S.Africa [46].

layering. Combining together the TP plots based on the monomineral methods for all 5 the minerals and plotting together the PTX diagram. It easy to estimate the

separate units of the mantle structures. Inflections of the Fe#Ol determined for all the minerals show that there are the clusters. W.Griffin and his coauthors [21] reported the gradual decrease of the Fe#Ol obtained by the Gaul's method [18]

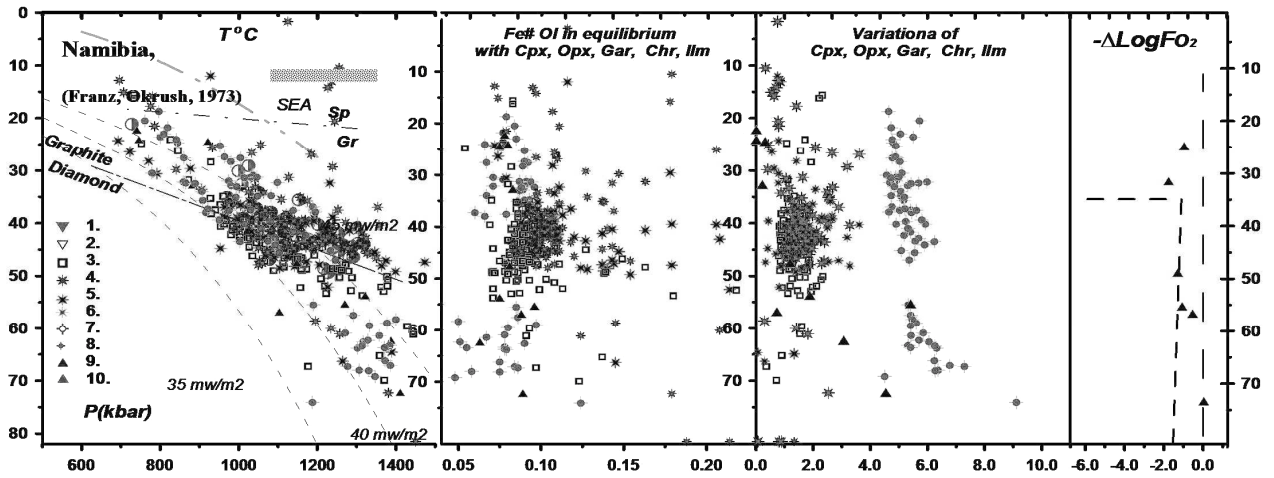


Fig. 5. TPXF diagram for the mantle beneath the Namibia, W Africa [17,39].

from the garnet compositions to the bottom of the lithosphere. This may be predicted because the pressures are determined in this method by the projections of the Ni temperatures on the geotherms and temperatures are using for the calculations of Fe#.

We also detected such a decrease but more complex consisting some time from separate several lines. Usually Fe# is coinciding for the orthopyroxenes and garnets but for the clinopyroxenes it is much higher. This was suggested to be the result of the fertilization [15,70]. Our estimates give more higher pressure conditions than 60 kbars as were reported in most works before. But this is supported by the seismic data [49] detecting the deep roots of the lithosphere to 300 km for Kaapwaal and even to 400 km for the Congo Kasai craton. For the Kaapwaal the gentle gradients as were detected for the Jagersfontain [9, 31, 46, 61] is not a result of the single event but is a different heating degree of the separate units which are underlain by the hot layers heated by the melts forming the polybaric or polyasthenospheric system. Presence of the melts is evident by the sharp increase of Fe# and TiO₂. The polybaric nature of the sheared peridotites [31] are likely prove this suggestion. The lower parts of lithosphere very often show the low heating degree to 35 mvm² or heterogeneous heating which may be interpreted as the presence of the cold depleted rocks and Magma feeders and rocks heated by the interaction with the melts. TP estimates for the eclogites also show quite different TP gradients and conditions.

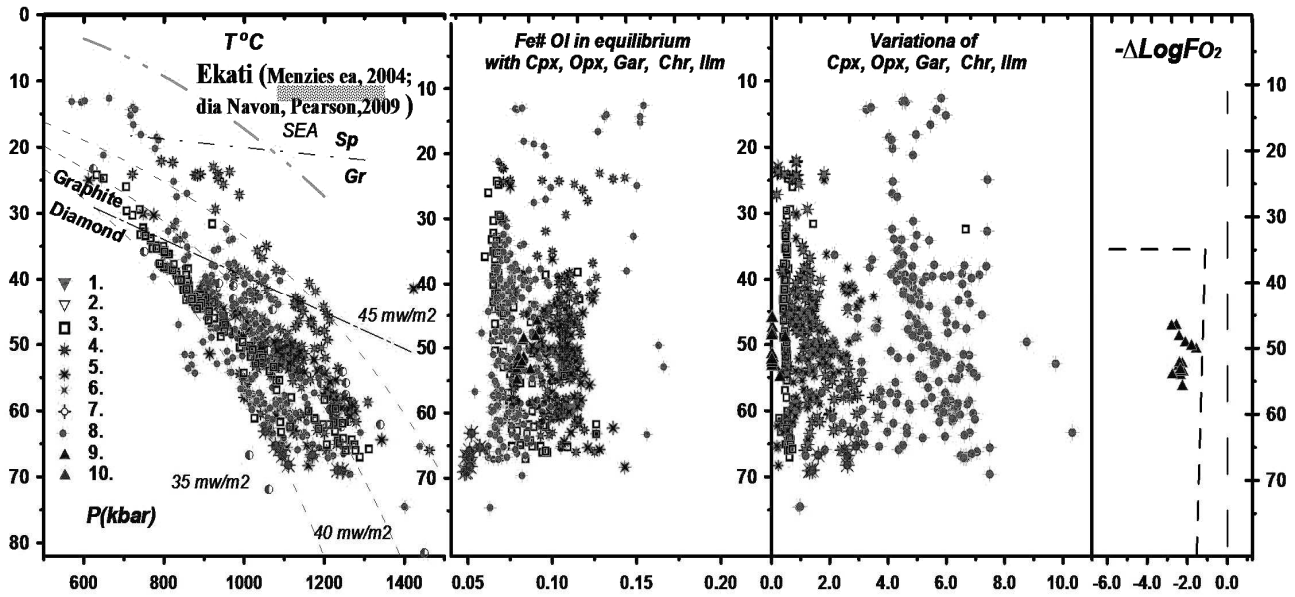


Fig. 6. TPXF diagram for the mantle beneath the Ekati diamond mine, Slave craton, Lac De Gras area [42].

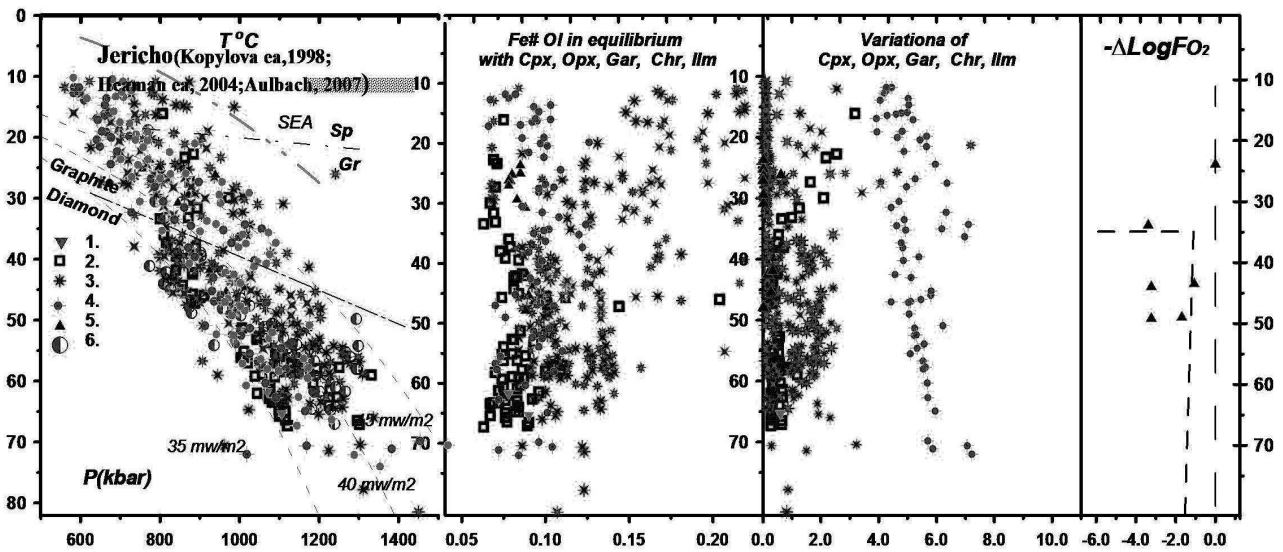


Fig. 7. TPXF diagram for the mantle beneath the Jericho pipe, Slave craton, [26,33,34].

Most of them also trace 40 mW/m² gradients. Rare are close to the 35 and some especially diamondiferous are close to 45 or adiabatic TP path coinciding with the ilmenite TP estimates.

For the most pipes from the Namibia and especially those placed in of craton environment the most Pt estimated are grouping near the Graphite –Diamond

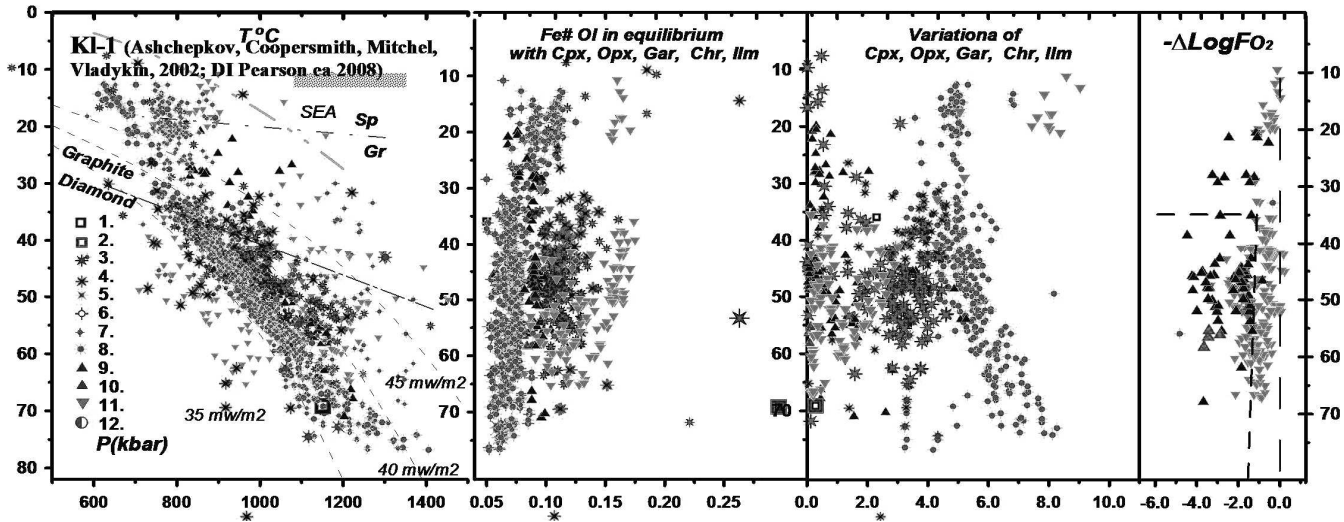


Fig. 8. TPXF diagram for the mantle beneath the Kelsey Lake pipe, Wyoming craton, State Line field. [6, 16, 66].

boundary and show the heating up to 1400 or more. The rare PT estimates may be found as deep as 220 km (65 kbars or more). They are tracing the adiabatic TP gradient which was found recently not only for the Kaapvaal and for Siberian and other cratons.

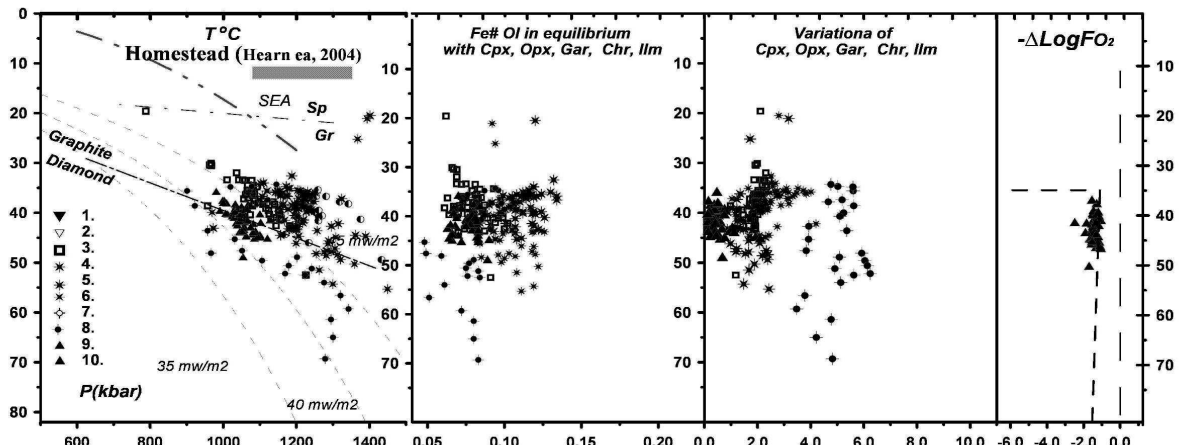


Fig. 9. TPXF diagram for the mantle beneath the Homestead kimberlite pipe, Montana [27].

TP Plots for the North America are varying and in a high degree. Despite on the reported PT plots tracing all the graphite diamond transition we found most of the lithospheric sequences beneath the kimberlites are very deep especially in the Slave craton [8, 20, 26, 34, 35, 43, 57] which coincides with the TP estimates with the polymineral and orthopyroxene methods from xenoliths [6, 8, 16, 20, 26, 27, 33, 34, 42] despite on the previous TP estimates with pyropes of W.Griffin [22] giving pressure values grouping near 40 kbar graphite-diamond boundary [32].

The large data set for the xenoliths from Ekati diamond [43] mine in the SE part of the Slave craton allow to calculate the dense PT plot showing mostly the

cold (35 mvm-2) geotherm branch from the top of the mantle to bottom according to OPx PT estimates. The complex twice kinked at 50 and 60 kbars branches is determined according to both Opx and Brey & Kohler [14, 42] barometers as well as the clinopyroxene and garnet. The clinopyroxene, garnets and more rare Opx estimates also mark the advective hot TP path. An opposite garnet diamond inclusions give mostly cold and deepest TP estimates though some of them are located near the 40 mvm² geotherm.

Well studied peridotite, pyroxenite and eclogite xenoliths from the Jericho pipe from the northern part of the Slave craton [24, 26, 34, 35] also show a bit more complex geotherms and layering. We determined two geothermal kinks in 60 and 70 kbars which may be regarded as the interaction with the plume melts. But a cold geotherm to 35 mvm-2 and less was detected to 70 kbar and more. In the upper part of the geotherm the Fe-enriched peridotites give the TP path more hot than the common conductive gradients.

The TP estimates for the lower Paleozoic kimberlites from Montana like Kelsey Lake 1 [6, 16, 66] also give the TP path splitting into convecting and conductive branches. The heated conditions were detected also between 50 and 60 kbars and even near 40 kbar. But the colder part of the geotherms is determined up to 75 kbar with the deviation to the heated conditions. The garnet diamond inclusions [61] refer to the lower part of mantle column there. This did not support the seismic evidence for the absence of the more deep roots of the lithosphere as 60 (180 km) kbar found for modern time [39]. Possibly in Paleozoic time it was strengthening lower to 300 km or more.

The Mesozoic pipes in Montana [27] show the thermal structure of the lithosphere similar to that of craton in Africa [11, 17, 39]. Most of the TP estimates are concentrating within 45-35 kbar interval revealing the irregular heating. More deeper part are represented by the relic cold lithosphere or by the heated and Fe-rich peridotites.

In Baltica there are data for the Upper –Paleozoic pipes from Finland and [38, 53] for the Archangelsk province. Combining together the data for the studied xenoliths and mantle xenocrysts from the we determined the thermal regime and layering in the mantle lithosphere. Peridotites give the geotherm which is close to the 38 mvm² but with the deviations to the 45 mvm-2 geotherm. The heating is higher in the lower part of mantle section. There are at least four levels of the joint increase of Fe# and temperatures to 1200 °C at 40 kbars and to 1400 °C at 70 kbars but the highest is detected between 60 and 65 kbars. One can determine about 9 different levels in the mantle lithosphere of the Finland [35, 51] and similar structure was found for the Arkhangelsk province. The eclogites are determined according to the TP estimates at the lower part of the mantle sequence. The diamondiferous are close to the 40-45 mvm-2 geotherm.

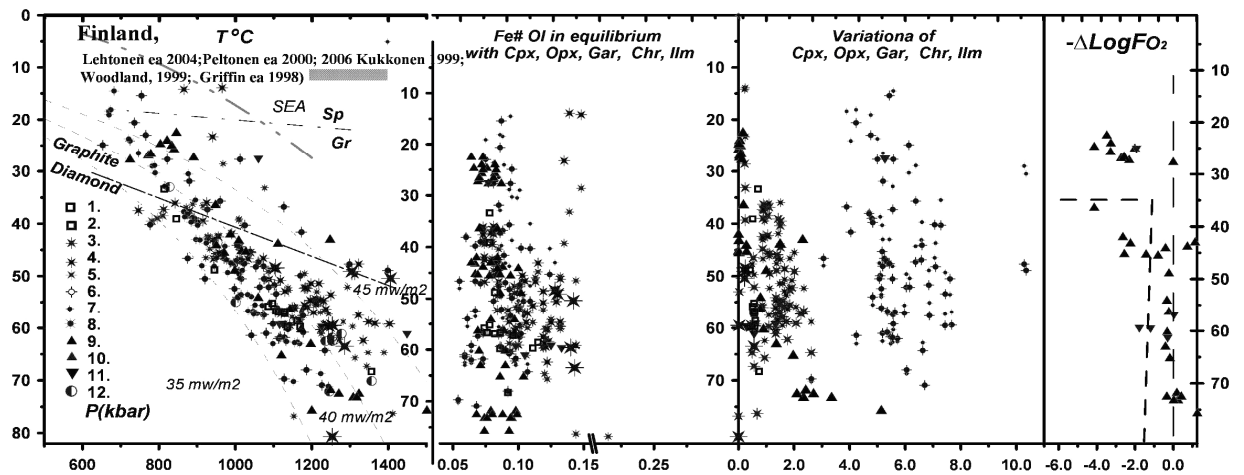


Fig. 10. TPXF diagram for the mantle beneath Fennoscandia [38, 54].

DISCUSSION.

Regularities for the PT diagrams for the mantle beneath the kimberlite pipes from different regions.

The combined PT, P-Fe#Ol and P – X_{min} (compositions of minerals) diagrams were used to detect variations of thermal conditions and layering of the mantle columns beneath the kimberlite pipes (Fig.2-10). In our interpretation we have used the common division between depleted and enriched rocks according to the CaO and Cr₂O₃ contents in garnets [67]. Enriched Fe#Ol and TiO₂ are regarded as signs of melt metasomatized associations [3, 64] or the megacrystalline series [33]. Al-Na content in clinopyroxenes is used to divide rocks into eclogites, peridotites and pyroxenites [8, 56, 63]. Simultaneous rise of Cr and Fe# for ilmenites results from polybaric AFC detected for many pipes from North America [65], while Cr-free varieties are formed by uncontaminated protokimberlites [67, 71]. Cr-rise and Fe# decrease is typical for metasomatic trends. Similar Ti-rich chromites are formed due to interaction with melts and most Mg-rich chromites are from dunites and other diamond-bearing rocks [60].

In general there are several types of the mantle structure in the mantle columns of the kimberlite pipes which reflect the primary layering and the interaction with the different melts of the subduction, and plume nature including basalts, and kimberlites and possibly komatiates, Most simple geotherms with one inflection at the base of the craton were detected for the some kimberlites from Lesotho [46]. But some pipes reveal more complex thermal structure with several inflections. But it seems that the lower and the colder part of the lithosphere is also represented by the xenocrysts sometimes mainly by the diamond inclusions. The 40 mvm-2 geotherms [10] referred to the high heat flow for the South Africa was found starting from the Proterozoic times for the Premier pipe [70]. The thick lithospheric roots [45,46] like beneath the Slave [24, 30, 39, 53], Congo Kasai

craton [60] and Siberia corresponds to the colder geotherm [3, 11]. But even here the kimberlite rifting zones and so cold of craton [17, 26, 39] area show the heated geotherm started from the 40 kbar usually. But the colder and deeper relics are determined in each case. Monomineral thermobarometry in this case mark the advective branches formed likely by the diapiric upwelling or by the interaction with the plume melts.

The vast perturbations in the mantle column structures were made during the interaction with the protokimberlites during the developing of the magmatic channels before the eruptions.

Less inclined (P/T) geotherms like those determined for mantle column beneath the Jagersfontein pipe in Lesotho Kirkland Lake [24] pipe in Canada are possibly a result of the stepped heating from the bottom. Sometimes the middle parts of the geotherm are more heated like in mantle beneath the Udachnaya pipe where two horizons near 40 kbars are traced by the TP estimates from heated pyroxenites [37, 56] and ~ 50 kbar [3] by the eclogites subjected by the heating from protokimberlites. Presence of the heating near the 60-65 kbar found in the most mantle columns is not a result of the intrusion of convective asthenosphere [46] but a result of the melt intrusion in this level. The stress and the shearing of mantle peridotites [51] is accompanied the melt intrusion. Presence of the polybaric shearing zones in the mantle columns [31] may be result if the magmatic fracturing or an opposite penetration of the melts in to deformed zones in the mantle.

CONCLUSIONS

Different cratons reveal their typical features of the TPXF diagrams of the mantle sections beneath the kimberlite pipe. The thicker the lithospheric keel the colder are the geotherms gradients,

Of craton kimberlites and rifting zones as well as the youngest pipes demonstrate most shallow and heated conditions of the mantle sections.

Hot PT paths are associated with the evolution of the protokimberlite melts. Internal layering of the mantle keel is the controlling factor of the protokimberlite movements and interaction with the peridotites.

Grant RBRF 09-05-00116, 09-05-90002.

REFERENCES

1. **Artemieva I M.** The continental lithosphere: Reconciling thermal, seismic, and petrologic data. //Lithos (in press).
2. **Alymova N.A.** 2006. Peculiarities of ilmenites and ilmenite – bearing association from kimberlites of Yakutian province. PHD dissertation thesis. Irkutsk. Institute of Geochemistry SB RAS. 175.
3. **Ashchepkov I. V., Pokhilenko N. P., Vladykin N.V., Rotman A.Y., Afanasiev V.P., Logvinova A.M., Kostrovitsky S.I., Pokhilenko L.N., Karpenko M.A., Kuligin S.S., Malygina E.V., Stegnitsky Y.B., Alymova N.A., Khmelnikova**

- O.S.** Reconstruction of mantle sections beneath Yakutian kimberlite pipes using monomineral thermobarometry. // Geological Society, London, Special Publications, 2008. v.293. P.335 – 352.
4. **Ashchepkov I.V.** More precise equation of the Jd-Di Barometer.// Herald of the Earth department RAS. 2003. № 1. P. 45-46.
 5. **Ashchepkov I.V., Vladykin N.V., Logvinova A.M., Kuligin S.S., Malygina L.V., Pokhilenko L.N., Alymova N.V., Mityukhin S.I.** Using of the monomineral thermobarometers for the reconstruction of the mantle lithosphere structure. //Vestn. Otd.nauk o Zemle RAN. № 1(27)'2009.
 6. **Ashchepkov I.V., Vladykin N.V., Mitchell R.H., Coopersmith H., Garanin V.G., Saprykin A.I., Khmelnikova O.S., Anoshin G.N.** Geochemical features of the minerals from the heavy concentrate from KL-1 (Kelsey Lake) kimberlite pipe, State Line, Colorado: petrologic reconstruction Deep-seated magmatism, magmatic sources and the problem of plumes: Vladivostok, Dalnauka, 2002. P.174-184.
 7. **Ashchepkov I. V., Pokhilenko N. P., Vladykin N. V., Logvinova A. M., Afanasiev V. P., Pokhilenko L. N., Kostrovitsky S.I., Kuligin S.S., Stegnitsky Y.B., Rotman A.Y., Karpenko M.A., Mityukhin S.I., Vishnyakova E.V.** 2008. Geochemical evidence for mantle lithosphere heterogeneity of Siberian craton. //9th International Kimberlite Conference Long Abstract. 9IKC-A-00386. 123.
 8. **Aulbach S., Pearson N.J., O'Reilly S.Y. Doyle. J.** Origins of Xenolithic Eclogites and Pyroxenites from the Central Slave Craton, Canada.// J. Petrology, October 2007; 48: p. 1843 - 1873.
 9. **Aulbach S., Shirey S.B., Stachel T., Creighton S., Muehlenbachs K., Harris J. W.** Diamond formation episodes at the southern margin of the Kaapvaal Craton: Re–Os systematics of sulphide inclusions from the Jagersfontein Mine.// Contrib Mineral Petrol 2009. 157: p.525–540.
 10. **Bell D.R., Schmitz M.D., Janney P.E.** Mesozoic thermal evolution of the southern African mantle lithosphere. //Lithos. 2003. 71. P. 273-287. *
 11. **Boyd F.R., Pearson D.G., Hoal K.O., Hoal B.G., Nixon P.H., Kingston M.J., Mertzman S.A.** Garnet lherzolites from Louwrensia, Namibia: bulk composition and P/T relations.// Lithos. 2004. Vol. 77. Iss. 1-4.
 12. **Boyd F.R., Pokhilenko N.P., Pearson D.G., Mertzman S.A., Sobolev N.V.& Finger L.W.,** Composition of the Siberian cratonic mantle: evidence from Udachnaya peridotite xenoliths. //Contrib. Mineral. Petrol. 1997. 128. P. 228-246.
 13. **Boyd F.R., Nixon P.H.** . Ultramafic nodules from the Kimberley pipes, South Africa. Geochim. Cosmochim. 1978. Acta 42. P.367–1382.*
 14. **Brey G.P., Kohler T.** Geothermobarometry in four phase lherzolites II: new thermo-barometers and practical assessment of using thermobarometers. //J.Petrol., 1990. 31. P.1353-1378.
 15. **Burgess S.R., Harte B.** Tracing lithosphere evolution through the analysis of heterogeneous G9-G10 garnets in peridotite xenoliths, II: REE chemistry. //J. Petrol. 2004. V. 45. Iss. 3. P. 609-634.
 16. **Coopersmith H. G., Mitchell R.H., Hausel W. D.** Kimberlites And Lamproites Of Colorado And Wyoming, Usa. Guidebook for the VIIIth International

- Kimberlite Conference, Colorado and Wyoming Field Trip. 2003. P.32.*
17. **Franz L., Brey G., Okrusch M.** Steady state geotherm, thermal disturbances and tectonic development of the lower lithosphere underneath the Gibeon Kimberlite Province, Namibia.// *Contrib.Mineral. Petrol.*1996 . 126., P.181–198.
 18. **Gaul O.F., Griffin W.L., O'Reilly S.Y., Pearson N.J.** Mapping olivine composition in the lithospheric mantle.// *Earth Planet. Sci. Lett.* 2000 .182. P. 223–235.
 19. **Griffin W.L., Cousens D.R., Ryan C.G., Suter G.F.** Ni in chrome garnet: a new geothermometer.// *Contrib. Mineral. Petrol.* 1989. 103. P. 199–202.
 20. **Griffin W.L., Doyle B.J., Ryan C.G., Pearson N.J., O'Reilly S. Y., Davies R., Kivi K., Van Achtebergh E., Natapov L.M.** Layered mantle lithosphere in the Lac de Gras area, Slave craton: Composition, structure and origin . *J. Petrol.* 1999. Vol. 40. N 5. P. 705-727.
 21. **Griffin W.L., O'Reilly S.Y., Abe N., Aulbach S., Davies R.M., Pearson N.J., Doyle B.J., Kivi K.** The origin and evolution of Archean lithospheric mantle.// *Prec.Res.* 2003. 127 . P. 19 –41.
 22. **Griffin, W.L., O'Reilly, S.Y., Doyle, B.J., Pearson, N.J., Coopersmith, H., Kivi, K., Malkovets, V., Pokhilenko, N.** Lithosphere mapping beneath the North American plate.// *Lithos.*2004. 77. P. 873– 922.
 23. **Griffin W.L., Ryan C.G., Kaminsky F.V., O'Reilly S.Y., Natapov L.M., Win T.T., Kinny P.D., Ilupin I.P.** The Siberian lithosphere traverse: Mantle terranes and the assembly of the Siberian Craton. *Tectonophysics*, 1999. v.310. P.1–35.
 24. **Grütter H.S.** Pyroxene xenocryst geotherms: Techniques and application.// *Lithos.* 2009 (in press).
 25. **Grütter H.S., Latti D., Menzies A.** Cr-saturation arrays in concentrate garnet compositions from kimberlite and their use in mantle barometry. // *Journal of Petrology.* 2006. 47. P.801–820.
 26. **Heaman L., Creaser R.A., Cookenboo H., Chacko T.** Multi-stage modification of the Northern Slave mantle lithosphere: evidence from zircon- and diamond-bearing eclogite xenoliths entrained in Jericho kimberlite, Canada. // *J. Petrol.* 2006 .47 (4). P. 821–858.
 27. **Hearn C.** The Homestead kimberlite, central Montana, USA: mineralogy, xenocrysts, and upper-mantle xenoliths. // *Lithos.* 2004. v. 77. P. 473– 491.
 28. **Horodyskyj U.N., Lee C.-T. A., Ducea M.N.** Similarities between Archean high MgO eclogites and Phanerozoic arc-eclogite cumulates and the role of arcs in Archean continent formation. // *Earth and Planetary Science Letters.* 2007. 256. P.510–520.
 29. **Jacob D., Jagoutz E., Lowry D., Matthey D., Kudrjavitseva G.** Diamondiferous eclogites from Siberia: remnants of Archean oceanic crust. // *Geochim. Cosmochim.* 1994. Acta 58. P. 5191-5207.
 30. **Jagoutz E., Lowry D., Matthey D., Kudrjavitseva G.** Diamondiferous eclogites from Siberia: Remnants of Archean oceanic crust. // *Geochim. Cosmochim.* 1994. Acta 58. P. 5195-5207. *
 31. **Katayama I., Suyama Y., Ando S., Komiya T.** Mineral chemistry and P–T condition of granular and sheared peridotite xenoliths from Kimberley, South Africa: Origin of the textural variation in the cratonic mantle. *Lithos* . 2008 (in

- press).
32. **Kennedy S.C., Kennedy G.C.** The equilibrium boundary between graphite and diamond. // *J Geophys Res* 1976. 81: p. 2467-2470
 33. **Kopylova M.G., Nowell G.M., Pearson D.G., Markovic G.** Crystallization of megacrysts 1 from protokimberlitic fluids: geochemical evidence from high-Cr megacrysts in the Jericho kimberlite. // *Lithos*. 2009 (in press).
 34. **Kopylova M.G., Caro G.** Mantle xenoliths from the Southeastern Slave craton: Evidence for chemical zonation in a thick, cold lithosphere. // *J. Petrol.* 2004. Vol. 45. Iss. 5. P. 1045-1067.
 35. **Kopylova M.G., Russell J.K., Cookenboo H.** Petrology of peridotite and pyroxenite xenoliths from the Jericho kimberlite: Implications for the thermal state of the mantle beneath the Slave craton, northern Canada. // *J. Petrol.* 1999. 40. P. 79-104.
 36. **Krogh, E. J.** The garnet-clinopyroxene Fe-Mg geothermometer a reinterpretation of existing experimental data. // *Contrib. Mineral. Petrol.* 1988. V.99. P.44-48.
 37. **Kuligin S. S., Malkovets V. G., Pokhilenko N. P., Vavilov M. A., Griffin W. L., O'Reilly S. Y.** Mineralogical and Geochemical Characteristics of a Unique Mantle Xenolith from the Udachnaya Kimberlite Pipe. // *Extended Abstracts of the 8th International Kimberlite Conference, 2003. FLA_0114.*
 38. **Lehtonen M.L.; O'Brien H.E.; Peltonen P.; Johanson B.S.; Pakkanen L.K.** Layered mantle at the Karelian Craton margin: P-T of mantle xenocrysts and xenoliths from the Kaavi-Kuopio kimberlites, Finland // *Lithos*. 2004. Vol. 77. Iss. 1-4. P.593-608.
 39. **Leost I., Stachel T., Brey G.P., Harris J.W., Ryabchikov I.D.** Diamond formation and source carbonation: mineral associations in diamonds from Namibia // *Contrib. Mineral. Petrol.* 2003. V. 145. P.12-24.
 40. **Logvinova A.M., Taylor L.A., Floss C., Sobolev N.V.** Geochemistry of multiple diamond inclusions of harzburgitic garnets as examined in situ. // *Int Geol Rev.* 2005. 47. P. 1223-1233.
 41. **Malygina E.V.** Xenoliths of granular mantle peridotites in Udachnaya pipe. PhD thesis, United Institute of Geology Geophysics & Mineralogy, Novosibirsk. 2000.
 42. **McGregor, I.D.** The system MgO–Al₂O₃–SiO₂: solubility of Al₂O₃ in enstatite for spinel and garnet–spinel compositions. // *Am. Mineral.* 1974. v 59: p.110–190.
 43. **Menzies A.; Westerlund K.; Grutter H.; Gurney J.; Carlson J.; Fung A.; Nowicki T.** Peridotitic mantle xenoliths from kimberlites on the Ekati Diamond Mine property, NWT, Canada: major element compositions and implications for the lithosphere beneath the central Slave craton. // *Lithos* 2004. 77 . P. 317– 335.
 44. **Nickel K.G., Green D.H.** Empirical thermobarometry for garnet peridotites and nature of lithosphere, kimberlites and diamonds. // *Earth. Planet. Sci. Lett.* 1985. 73, P.153-170.
 45. **Nimis P., Taylor W.** Single clinopyroxene thermobarometry for garnet peridotites. Part I. Calibration and testing of a Cr-in-Cpx barometer and an enstatite-in-Cpx thermometer. // *Contrib. Mineral. Petrol.* 2000. 139. P.541-554.
 46. **Nixon P.H., Boyd F.R.** Petrogenesis of the granular and sheared ultrabasic nodule suite in peridotite xenoliths. // *Ext Abstrts, 5 th IKC, 1973. Cape Town. P.*

122-126.*

47. **O'Neill H.St.C, Wood B.J.** An experimental study of Fe-Mg- partitioning between garnet and olivine and its calibration as a geothermometer. //Contrib Mineral Petrol. 1979. 70: 5970.
48. **O'Neill H. St. C. & Wall V. J.** The olivine orthopyroxene-spinel oxygen geobarometer, the nickel precipitation curve, and the oxygen fugacity of the Earth's upper mantle. // Journal of Petrology .1987. 28. P. 1169-1191.
49. **O'Reilly S.Y., Griffin W.L.** Imaging global chemical and thermal heterogeneity in the subcontinental lithospheric mantle with garnets and xenoliths: Geophysical implications.// Tectonophysics 416 (2006). P..89–309.
50. **O'Reilly S.Y., Zhang M., Griffin W.L., Begg G., Hronsky J.** Ultradeep continental roots and their oceanic remnants: A solution to the geochemical “mantle reservoir” problem?// Lithos, In Press, 2009. P. 112 .*
51. **Pasyanos M. E., Nyblade A.A.** A top to bottom lithospheric study of Africa and Arabia Tectonophysics. 2007. 444. P. 27-44.
52. **Pearson D.G., Shirey S.B., Bulanova G.P., Carlson R.W., Milledge H.J.** Re–Os isotope measurements of single sulfide inclusions in a Siberian diamond and its nitrogen aggregation systematics. //Geochimica et Cosmochimica. Acta 63, 1999. P.703–711.
53. **Pearson D.G.; Irvine G.J.; Ionov D.A.; Boyd F.R.; Dreibus G.E.** Re-Os isotope systematics and platinum group element fractionation during mantle melt extraction: a study of massif and xenolith peridotite suites. //Chem. Geol.. 2004. Vol. 208. Iss. 1-4. P. 29-59.
54. **Peltonen P., Brüggmann G.** Origin of layered continental mantle (Karelian craton, Finland): Geochemical and Re-Os isotope constraints.// Lithos . 2006. v.89. P. 405-423.
55. **Pokhilenko L.N.** Volatile composition and oxidation state of mantle xenoliths from Siberian kimberlites. PhD thesis. // United Institute of Geology Geophysics and Mineralogy. 2006. Novosibirsk. P. 225.
56. **Pokhilenko N. P., Sobolev N.V., Kuligin S. S., Shimizu N.** Peculiarities of distribution of pyroxenite paragenesis garnets in Yakutian kimberlites and some aspects of the evolution of the Siberian craton lithospheric mantle.// Proceedings of the VII International Kimberlite Conference.1999. The P.H. Nixon volume. P. 690-707.
57. **Pokhilenko N.P., Sobolev N.V., Chernyi S.D., Yanygin Yu.T.** Pyropes and chromites from kimberlites in the Nakyn field (Yakutia) and Snipe Lake district (Slave River region, Canada): evidence for anomalous structure of the lithosphere. //Dokl. Earth Sci. 2000. 372. P. 638–642.
58. **Pyle J.M., Haggerty S.E.** Eclogites and the metasomatism of eclogites from the Jagersfontein kimberlite: punctuated transport and implications for alkali magmatism.// Geochim. Cosmochim. Acta. 1998. v.62. P.1207–1231.
59. **Ryan C. G.; Griffin W. L.; Pearson N. J.** Garnet geotherms: Pressure-temperature data from Cr-pyrope garnet xenocrysts in volcanic rocks. //J. Geophys. Res. B. 1996. V. 101. N3. P. 5611-5625. *
60. **Simon N. S. C., Irvine G.J., Davies G.R., Pearson D. G., Carlson R. W.** The origin of garnet and clinopyroxene in “depleted” Kaapvaal peridotites. //Lithos,

- 71, 2003.P. 289-322.
61. **Simon N. S.C., Carlson R.W., Pearson D. G., Davies G. R.** The Origin and Evolution of the Kaapvaal Cratonic Lithospheric Mantle // *J. Petrology*, 2007; v.48. P.589 - 625.
 62. **Sobolev, N V, Logvinova, M, Zedgenizov, D. A, et al.** Mineral inclusions in microdiamonds and macrodiamonds from kimberlites of Yakutia: a comparative study.// *Lithos*, 2004. 77. P. 225–242.
 63. **Sobolev, N.V.** Deep-Seated Inclusions in Kimberlites and the Problem of the Composition of the Mantle. Amer. Geophys.Union, 1977.Washington, DC. 279 p.
 64. **Solov'eva, L.V., Lavrent'ev, Yu.G., Egorov, K.N., Kostrovitskii S.I., Korolyuk V.N., Suvorova L.F.** The genetic relationship of the deformed peridotites and garnet megacrysts from kimberlites with asthenospheric melts. // *Russian Geology and Geophysics*. 2008. 49. P.207–224.
 65. **Stachel, T., Harris, J.W.** The origin of cratonic diamonds - constraints from 700 mineral inclusions. // *Ore Geology Reviews*, 2008 . 34(1-2). P.5-32.
 66. **Schulze D.J., Coopersmit H.G., Harte Pizzolato B.L.-A.** Mineral inclusions in diamonds from the Kelsey Lake mine, Colorado, U.S.A.: depleted Archean mantle beneath the Proterozoic Yavapai province.// *Geochimica et Cosmochimica*. 2008 .
 67. **Schulze D.L., Anderson P.F.N., Hearn Jr., B.C. & Hetman C.M.** Origin and significance of ilmenite megacrysts and macrocrysts from kimberlite.// *Int. Geol. Review*, 1995. 37. P. 780-81 2.
 68. **Tappert R., Stachel., Harris J.W., Muehlenbachs K., Ludwig T., Brey G. P.** Diamonds from Jagersfontein (South Africa): messengers from the sublithospheric mantle. // *Contrib Mineral Petrol*. 2005. 150: 505–522.
 69. **Taylor W.R., Kammerman M., Hamilton R.** New thermometer and oxygen fugacity sensor calibrations for ilmenite and chromium spinel-bearing peridotitic assemblages. // 7th International Kimberlite Conference. Extended abstracts. 1998. Cape town. 891-901
 70. **Viljoen F., Dobbe R., Smith B.** Geochemical processes in peridotite xenoliths from the Premier diamond mine, South Africa: Evidence for the depletion and refertilisation of subcratonic lithosphere . // *Lithos*. 2009. 112.
 71. **Wyatt B. A., Baumgartner M., Anckar E. & Grutter H.** Compositional classification of “kimberlitic” and “non-kimberlitic” ilmenite . *Lithos*. 2004. 77. P.819–840.

Principal Physicochemical Parameters of Natural Mineral-Forming Fluids

Naumov V. B., Dorofeeva V. A., and Mironova O. F.

Vernadsky Institute of Geochemistry and Analytical Chemistry, Russian Academy of Sciences, ul. Kosygina 19, Moscow, 119991 Russia e-mail: naumov@geokhi.ru

ABSTRACT

The authors' database (which includes data from more than 17500 publications on fluid and melt inclusions in minerals) was used to generalize information on the principal physicochemical parameters of natural mineral-forming fluids (temperature, pressure, density, salinity of aqueous solutions, and the gas composition of the fluids). For 21 minerals, data are reported on the frequency of occurrence of the homogenization temperatures of fluid inclusions in various temperature ranges, which make it possible to reveal temperature ranges most favorable for the crystallization of these minerals. Data on 5260 determinations were used to evaluate the frequency of occurrence of certain temperature and pressure ranges of natural fluids within the temperature intervals of 20–1200°C and 1–12000 bar. Within these intervals, frequencies of occurrence were evaluated for water-dominated and water-poor or water-free fluid inclusions in minerals. The former are predominant at temperatures below 600°C and pressures below 4000 bar, whereas the latter dominate at temperatures of 600–1200°C and pressures of 4000–12000 bar. Illustrative examples are presented for visually discernible magmatic water that exists as an individual high-density phase in melt inclusions in minerals from various rocks sampled worldwide (in the Caucasus, Italy, Slovakia, United States, Uzbekistan, New Zealand, Chile, and others). Attention is drawn to the fact that extensive data testify to fairly high (>1000–1500 bar) pressures during hydrothermal mineral-forming processes. These pressures are much higher not only than the hydrostatic but also the lithostatic pressures of the overlying rocks. Data on more than 18000 determinations are used to evaluate the frequency of occurrence of certain temperature and salinity ranges of mineral-forming fluids within the intervals of 20–1000°C and 0–80 wt % equiv. NaCl and certain temperature and density ranges of these fluids at 20–1000°C and 0.01–1.90 g/cm³. Information is presented on the gas analysis methods most commonly applied to natural fluids in studying fluid inclusions in minerals in 1965–2007. The average composition of the gaseous phase of natural inclusions is calculated based on more than 3000 Raman spectroscopic analyses (the most frequently used method for analyzing individual inclusions).

INTRODUCTION

The problem of the composition and physical and chemical properties of natural fluids and their spatiotemporal evolution is pivoting for the theory of mineral- and ore-forming processes. One of the methods able to provide reliable quantitative information on natural fluids, crystallization processes of minerals, and conditions under which rocks and mineral deposits are formed is studying inclusions of mineral-forming media. Finding an ever growing application in geology, these techniques enable the researcher to derive necessary information

which is needed for the solution of a great diversity of problems, ranging from evaluating physicochemical parameters of mineral-forming processes (a key problem in the theory ore-forming processes) to elaborating prospecting guides for the exploration of mineral deposits. The onrush of technologies for the physical and chemical analysis of tiny Table 1 shows the clearly pronounced tendency in the inclusions (microinclusions) and the continuously enhanced possibilities for obtaining more and more reliable (and often unique) data resulted in the fact that most modern publications comprehensively covering natural mineral-forming processes necessarily report data on and microinclusions. This is coupled with the growth in the number of publications presenting data on inclusions in minerals (Table 1), a process triggered in the mid-20th century by the publication of a specialized monograph by Ermakov [1]. While the total number of papers published worldwide since 1822 (when the first experimental study of liquid inclusions in quartz samples was accomplished by H. Davy) amounts to approximately 17600, the number of papers published over the past 15 years alone was close to 5300, i.e., 30% of the total. It is worth mentioning that a significant role in the development of this new avenue of mineralogy, geochemistry, and petrology was also played by Lemlein [2, 3], Roedder [4, 5], Kalyuzhnyi [6, 7], Dolgov [8, 9], Poty [10, 11], Clocchiatti [12, 13], Bodnar [14, 15], Sobolev [16, 17], and many other researchers.

Table 1 shows the clearly pronounced tendency in the inclusions (microinclusions) and the continuously studies of inclusions in minerals: such studies in the 19th century were carried out mostly by lone researchers, and 90% of the papers

Table 1.

Number of papers presenting data on inclusions in minerals and published in various periods of time, percentage of papers with various numbers of authors of a single publication, and the number of publications in national and foreign journals

Years	Number of publications		Number of author of a single publication				Percentage of publications	
	Total during the period	Per year	1	2	3	>3	National	Foreign
1822–1900	101	~1	90%	8%	1%	1%	4	96
1901–1950	147	3	87	9	3	1	25	75
1951–1960	306	31	75	20	5	0	73	27
1961–1970	1236	124	53	32	10	5	75	25
1971–1980	3471	347	38	32	19	11	70	30
1981–1990	5530	553	29	31	22	18	30	70
1991–2000	3896	390	17	28	25	30	20	80
2001–2007	2884	412	9	18	23	50	19	81

have a single author; the latter figure systematically decreased in the 20th century to 75% in 1951–1960, 38% in 1971–1980, and 17% in 1991–2000. In the early 21st century, as little as 9% of these publications has a single author. The mushrooming of new methods in recent years resulted in that more than half of the studies were carried out by research teams (consisting of four or more persons), each of them being a professional in a certain scientific field.

The first significant review of data on the principal physicochemical parameters of mineral-forming fluids was published in 1980 [18] and was based on our database (stored on a punch card media) on fluid and melt inclusions in minerals. The database, which we started to compile in 1964, included all our results on microinclusions plus those published in 4700 papers. Each punch card usually contained information on a single mineral or a single population of minerals. Hence, one card commonly provided data on several (often even dozens) microinclusions. The database contained generalized information on the phase state of mineral-forming fluids (6670 determinations in 32 minerals), their temperatures and densities (1015 determinations), the temperatures and salinities of fluids (1124 determinations), and the temperatures and pressures of fluids (880 determinations). The most favorable formation temperatures were determined for ten most typical minerals of ore deposits.

In 1994 we began to gradually transfer this database into the Paradox for Windows PC data-entry and database management system and continued to append the base with newly obtained information. The main principle used in appending the database was as follows: if extensive data were obtained on the homogenization temperatures of inclusions or the crystallization temperatures for a single sample, and the difference between the extreme values were greater than 50°e, only the minimum and maximum values were input; if this difference was less than 50°e, an average temperature value was fed. For the salinity of aqueous solutions, we used an average value if the range was less than 5 wt % and the minimum and maximum values at ranges greater than or equal to 5 wt %. For the pressures of natural fluids, if the difference between the extreme and average values for a single sample was no higher than 10%, only the average pressure value was fed into the database, and the minimum and maximum values were recorded when this difference exceeded 10%. Data obtained by the widely used mass spectrometric, chromatographic, and Raman spectroscopic techniques were compiled from publications devoted to the analysis of gaseous components. If the same samples or fluid inclusions were examined and analyzed by various methods, all data on them were filed. For the sake of uniformity, the concentrations of volatile components were input into the database in the form of mol %. If concentrations of volatiles were expressed in other units, these values were recalculated into mol %; otherwise no data were recorded in the database.

Table 2 presents data on the number of publications and determinations of the principal physicochemical parameters of natural fluids and melts derived by

studying inclusions in minerals during various periods of time. Note that all data on the temperatures (approximately 2900 publications and more than 38700 determinations) pertain only to the homogenization temperatures of inclusions. Of these temperature values, approximately 8% are our data, and the rest are compiled from

Table 2. Number of publications and determinations of the principal physicochemical parameters of natural fluids determined in inclusions in minerals in various periods of time

Years	Number of publications	%	Number of determinations	%
<i>Temperature</i>				
1900–1949	16	1	52	0.1
1950–1959	89	3	503	1.3
1960–1969	351	12	2235	5.8
1970–1979	710	24	6824	17.6
1980–1989	713	25	8974	23.2
1990–1999	555	19	9124	23.6
2000–2007	460	16	10998	28.4
1900–2007	2894	100	38700	100.0
<i>Pressure</i>				
1953–1959	6	1	11	0.2
1960–1969	40	5	148	2.7
1970–1979	179	21	1021	18.9
1980–1989	240	28	1501	27.8
1990–2007	387	45	2724	50.4
1953–2007	852	100	5405	100.0
<i>Salinity</i>				
1960–1969	16	1	47	0.3
1970–1979	182	14	1625	8.8
1980–1989	381	29	4837	26.2
1990–1999	385	29	4837	26.2
2000–2007	361	27	7089	38.5
1960–2007	1325	100	18435	100.0
<i>Gas composition</i>				
1965–1969	5	2	5	0.1
1970–1979	12	5	85	1.6
1980–1989	57	21	838	15.8
1990–1999	111	41	2163	40.8
2000–2007	85	32	2209	41.7
1965–2007	279	100	5300	100.0

the literature. Of the 5400 determines, ~15% is our data, and ~5% of the salinity

values (of 18400 determines) is also our data. While most papers published in the 19th century quote only microscopical descriptions of fluid and melt inclusions in minerals, the 20th century was marked by the beginning of their experimental studying with the use of more and more diverse analytical techniques. This made it possible to reliably determine the principal physicochemical parameters at which certain minerals crystallize in nature. As can be seen from Table 2, initially only the homogenization temperatures of fluid inclusions were measured, and then methods were proposed for evaluating the pressures. The advent of cryometric techniques made it possible to determine the temperatures of eutectics in the aqueous solutions of fluid inclusions, to evaluate their salinity, and to identify gases (CO₂, CH₄, and N₂) contained in these inclusions. The extensive application of methods for the analysis of gaseous components of fluid inclusions was started

Table 3.

Number of determinations of the principal physicochemical parameters of natural fluids in fluid inclusions in various minerals (I is the temperature, II is the pressure, III is the salinity, and IV is the gas composition)

Mineral	Number of determinations				Mineral	Number of determinations			
	I	II	III	IV		I	II	III	IV
<i>Quartz</i>	18144	3728	10868	4232	<i>Antimonite</i>	88	2	19	2
Fluorite	3327	137	1735	64	Magnesite	74	3	64	-
Calcite	2494	80	1331	65	Disthene	54	49	-	-
Sphalerite	1983	34	1356	143	Cryolite	52	8	20	-
Barite	770	10	530	14	Celestine	46	-	7	-
Dolomite	587	16	405	23	Spodumene	45	13	3	-
Cassiterite	468	25	201	29	Halite	41	8	5	29
Pyroxenes	423	284	52	8	Amphiboles	40	16	10	3
Feldspars	376	178	89	37	Vesuvianite	38	2	25	-
Garnets	332	107	93	22	Scapolite	34	10	7	-
<i>Scheelite</i>	330	26	225	13	Rhodochrosite	33	5	12	-
Apatite	318	72	94	2	Axinite	29	4	6	6
Beryl	299	49	147	19	Realgar	27	7	8	-
Anhydrite	292	15	213	43	Orpiment	26	1	20	-
Topaz	260	55	98	7	Zircon	25	4	4	-
Olivine	234	232	-	37	Datolite	20	-	13	6
Tourmaline	173	30	65	24	Corundum	17	13	-	-
Cinnabar	152	4	12	-	Sodalite	16	5	1	3
Nepheline	132	18	4	3	Spinel	14	12	-	-
Ankerite	120	6	46	3	Sillimanite	11	11	-	-
Wolframite	118	4	63	1	Danburite	10	-	5	9
Siderite	118	9	56	-	Galena	-	-	-	7
Epidote	113	20	51	-	Gold	-	-	-	24

after 1965 (Table 2). The total number of analyses of the gas composition of fluid inclusions had doubled by the end of 2007 and exceeded 5300 (in 279 publications). The material contained in our database by the end of 2008 is generally highly representative.

Table 3 summarizes data on the total number of determinations of the principal physicochemical parameters of mineral-forming fluids (temperature, pressure, salinity, and gas composition) currently available for a great variety of minerals. The table reports such data on 46 minerals. The number of determinations in six minerals most widely spread at hydrothermal ore deposits and occurrences exceeds 1000 (36972 for quartz, 5263 for fluorite, 3970 for calcite, 3516 for sphalerite, 1324 for barite, and 1031 for dolomite). The total number of temperature measurements in fluid inclusions in 44 minerals (all minerals in Table 3 except galena and gold) is 32264, with these data characterizing more than 5000 localities worldwide. Our database contains information on the crystallization temperatures of 272 minerals. A list of these minerals and the number of measurements for each of them is given in Table 4. Note that the table does not include any data on the homogenization temperatures of silicate melt inclusions, neither does it present any information on the decrepitation temperatures of inclusions in minerals. Publications provide data on the crystallization temperatures of some minerals, many of which are opaque.

These data were usually obtained by studying fluid inclusions in transparent minerals (quartz, calcite, fluorite, barite, and others) that contain the opaque minerals as syngenetic crystalline inclusions. Progress recently achieved in the development of IR spectroscopic techniques and equipment makes it possible to observe inclusions in many opaque minerals and even conduct thermometric and cryometric experiments with them. Fluid inclusions were examined in, for example, antimonite [19–21], wolframite [22–25], hausmannite [26], hematite [26, 27], pyrite [28–31], and enargite [28, 32].

Estimates of the pressure for the mineral-forming fluids (5312 determinations) were obtained for 41 minerals from 1200 localities worldwide. The salinity of hydrothermal solutions (17963 determinations for 2410 localities worldwide) was calculated from the temperature of ice melting or from the dissolution temperatures of daughter minerals in fluid inclusions; such measurements were made for 39 minerals (Table 3). The data on the gas composition of natural fluids comprise 4878 determinations in 29 minerals from 460 localities worldwide.

Below we discuss results successively obtained on certain parameters of mineral-forming processes.

TEMPERATURES OF NATURAL MINERAL-FORMING FLUIDS

Table 5 presents data on the frequency of occurrence (in %) of certain ranges of the homogenization temperatures of fluid inclusions within the interval of 20–

Table 4. List of minerals and data on the number of temperature determinations in fluid inclusions in these minerals

Mineral	<i>n</i>	Mineral	<i>n</i>	Mineral	<i>n</i>	Mineral	<i>n</i>
Actinolite	11	Chalcostibite	1	Hackmanite	3	Pistomesite	2
Adularia	80	Chkalovite	4	Halite	41	Pitchblende	4
Aegirine	9	Chlorite	9	Halloysite	1	Plagioclase	63
Alabandite	2	Chromite	2	Hastingsite	7	Pollucite	10
Albite	89	Chrysoberyl	2	Hausmannite	2	Powellite	1
Allactite	4	Cinnabar	152	Hedenbergite	12	Prehnite	6
Almandite	2	Cleavelandite	1	Helvite	3	Proustite	1
Alunite	6	Clinohumite	4	Hematite	30	Pumpellyite	1
Amazonite	1	Clinopyroxene	96	Heulandite	1	Pyrrargyrite	5
Amblygonite	4	Clinozoisite	7	Holmquistite	1	Pyrite	66
Amethyst	13	Cobaltite	2	Hornblende	26	Pyrochlore	3
Amphibole	40	Coesite	1	Huebnerite	40	Pyroxene	423
Analcite	8	Colemanite	6	Hyperstene	5	Pyrrhotite	14
Anatase	1	Columbite	3	Ilvaite	4	Quartz	18 144
Andalusite	3	Copper	1	Inyoite	1	Ralstonite	4
Andradite	4	Corundum	17	Jadeite	1	Rammelsbergite	2
Anhydrite	292	Cosalite	1	Jamesonite	1	Realgar	27
Ankerite	120	Creedite	2	Kainite	2	Rectorite	7
Anorthite	3	Criddleite	1	Kalaverite	1	Rhodochrosite	33
Anthophyllite	1	Cryolite	52	Kaolinite	15	Rhodonite	4
Antimonite	88	Cubanite	1	K-feldspar	15	Rhoducite	1
Antimony	2	Danburite	10	Kyanite	5	Riebeckite	1
Apatite	318	Dashkesanite	3	Langbeinite	3	Roscherite	1
Apophyllite	6	Datolite	20	Laumontite	2	Rubellite	1
Aragonite	14	Desmine	3	Lazulite	3	Rutile	6
Argentite	2	Diaspore	1	Lollingite	2	Safflorite	4
Armenite	1	Dickite	15	Magnesite	74	Sarabauite	1
Arsenic	3	Diopside	73	Magnetite	1	Sarkinite	4
Arsenopyrite	10	Disthene	54	Malayaite	6	Scapolite	34
Astrakhanite	1	Dolomite	587	Manganhedenbergite	12	Scheelite	330
Augelite	3	Donbassite	1	Marcasite	4	Seinajokite	1
Axinite	29	Dumortierite	1	Melilite	1	Selenite	1
Babingtonite	1	Elpasolite	2	Mg-Fe carbonate	2	Selenium	1
Barite	770	Emplectite	1	Microcline	18	Sellaite	7
Bastnaesite	29	Enargite	33	Milarite	1	Sepiolite	2
Berlinite	1	Enstatite	1	Millerite	1	Sericite	2
Berthierite	1	Epidote	113	Mirabilite	1	Shortite	2
Bertrandite	6	Epsomite	1	Molybdenite	21	Siderite	118
Beryl	299	Eschynite	1	Monazite	7	Sideroplesite	1
Biotite	2	Euclase	2	Montebrasite	6	Sillimanite	11
Bischofite	2	Eucryptite	1	Monticellite	4	Silver	2
Bismuth	4	Fahlore	4	Montmorillonite	10	Skutterudite	3
Bismuthinite	3	Famatinite	1	Mordenite	1	Smaltite	1

Table 4. (Contd.)

Mineral	<i>n</i>	Mineral	<i>n</i>	Mineral	<i>n</i>	Mineral	<i>n</i>
Bornite	2	Fassaite	2	Muscovite	24	Smythite	2
Boulangerite	1	Feldspar	376	Nepheline	132	Sodalite	16
Breunnerite	2	Fluorite	3327	Neptunite	3	Sorensenite	1
Britholite	2	Forsterite	1	Nickeline	3	Sphalerite	1983
Bromelite	1	Gagarinite	8	Nifontovite	1	Sphene	10
Brookite	2	Gahnite	2	Nyerereite	1	Spinel	14
Bustamite	3	Galena	14	Olivine	234	Spodumene	45
Cahnite	1	Garnet	332	Omphacite	17	Stibiotantalite	1
Calcite	2494	Genthelvite	9	Opal	2	Stronalsite	1
Cancrinite	10	Gersdorffite	3	Orpiment	26	Sulfur	7
Camallite	1	Gibbsite	8	Orthite	1	Sylvite	3
Cassiterite	468	Goethite	25	Paravauxite	1	Syngenite	1
Celadonite	1	Gold	19	Parisite	1	Tantalite	2
Celestine	46	Goldfieldite	1	Petalite	1	Tantalo-columbite	2
Celestobarite	2	Glaserite	1	Phenakite	28	Tennantite	4
Cerussite	1	Grossular	6	Phlogopite	16	Tetrahedrite	2
Chalcopyrite	19	Gypsum	46	Picromerite	3	Thenardite	2
Thomsonite	2	Tugtupite	2	Wairakite	8	Wurtzite	4
Thorite	1	Ussingite	2	Wavellite	1	Xenotime	6
Tilasite	4	Valentinite	4	Whewellite	7	Yttrosynchisite	1
Tomsenolite	1	Variscite	1	Willemite	7	Zeolite	4
Topaz	260	Vauxite	1	Witherite	2	Zinkenite	1
Tourmaline	173	Vesuvianite	42	Wodginite	4	Zinnwaldite	1
Tremolite	5	Vivianite	2	Wolframite	118	Zircon	25
Triplite	9	Wagnerite	1	Wollastonite	16	Zoisite	6

1000°C. As can be seen from these data, such minerals as quartz, garnets, beryl, tourmaline, topaz, scheelite, fluorite, and calcite exhibit a broad range of possible crystallization temperatures from hydrothermal solutions. This range can be as wide as a few hundred centigrade degrees. For example, quartz, garnets, fluorite, and calcite can crystallize at both low and fairly high temperatures, which can reach 800–1000°C. At the same time, it should be mentioned that most hydrothermal minerals are formed at temperatures below 500°e.

High, higher than 400–500°e, homogenization temperatures are observed in fluid inclusions that contain one–two, up to 5–8 or, occasionally, up to ten–twelve daughter minerals at room temperature. Daughter crystalline phases often occupy up to 50% of fluid inclusions by volume. Figure 1 shows micrographs of such

inclusions in various minerals (quartz, beryl, fluorite, and scheelite) from various geological objects.

As follows from the data of Table 5, some minerals are characterized by quite similar ranges of their most favorable crystallization temperatures. The high-temperature interval of 500–300°e is typical of cassiterite (81% of the 468 determinations) and topaz (64%). Temperatures of 400–200°e are favorable for the crystallization of wolframite (95% of all measurements), scheelite (78%), beryl

Table 5. Frequency of occurrence (%) of homogenization temperatures of fluid inclusions in various minerals within various temperature ranges

Mineral	n	Temperature, °C									
		20–100	100–200	200–300	300–400	400–500	500–600	600–700	700–800	800–900	900–1000
Quartz	18087	2.6	22.1	36.8	23.5	6.4	3.4	2.3	2.0	0.7	0.2
Garnets	332	–	0.4	12.4	20.1	16.1	12.0	13.3	16.1	6.8	2.8
Beryl	299	–	5.4	29.8	43.1	12.0	6.7	2.0	1.0	–	–
Tourmaline	173	–	7.6	34.6	37.8	11.9	7.0	1.1	–	–	–
Topaz	260	–	0.4	11.2	45.6	18.5	18.8	4.2	1.3	–	–
Spodumene	45	–	–	28.9	33.3	15.6	6.7	15.5	–	–	–
Cassiterite	468	–	1.7	13.0	58.1	22.8	4.3	–	–	–	–
Scheelite	330	0.6	7.5	39.2	39.2	9.9	3.0	0.6	–	–	–
Wolframite	118	–	3.8	58.1	37.1	1.0	–	–	–	–	–
Fluorite	3327	12.6	57.5	17.2	8.6	2.4	0.5	0.6	0.3	0.2	0.1
Calcite	2494	24.9	42.2	24.3	6.9	0.8	0.3	0.4	0.1	0.1	–
Dolomite	587	26.1	54.6	15.0	2.7	0.7	–	0.7	0.2	–	–
Ankerite	120	7.5	56.7	22.5	11.7	–	–	0.8	0.8	–	–
Magnesite	74	2.7	62.1	25.7	8.1	1.4	–	–	–	–	–
Siderite	116	7.8	39.7	49.1	3.4	–	–	–	–	–	–
Anhydrite	292	12.3	18.8	38.4	27.1	2.7	0.7	–	–	–	–
Celestine	46	29.5	43.2	18.2	2.3	–	–	2.3	–	–	–
Barite	769	25.9	48.0	22.6	3.2	0.3	–	–	–	–	–
Sphalerite	1983	15.7	42.6	32.3	9.2	0.2	–	–	–	–	–
Cinnabar	152	32.0	66.7	1.3	–	–	–	–	–	–	–
Orpiment	26	19.2	61.6	19.2	–	–	–	–	–	–	–

(73%), anhydrite (66%), tourmaline (72%), and spodumene (62%). The relatively low-temperature range of 300–100°e is favorable for the crystallization of sphalerite (75% of 1983 measurements), fluorite (75%), many carbonates (88% for magnesite, 89% for siderite, 79% for ankerite, 70% for dolomite, 67% for calcite), and orpiment (81%). The lowest temperatures (<200°C) are typical of the origin of

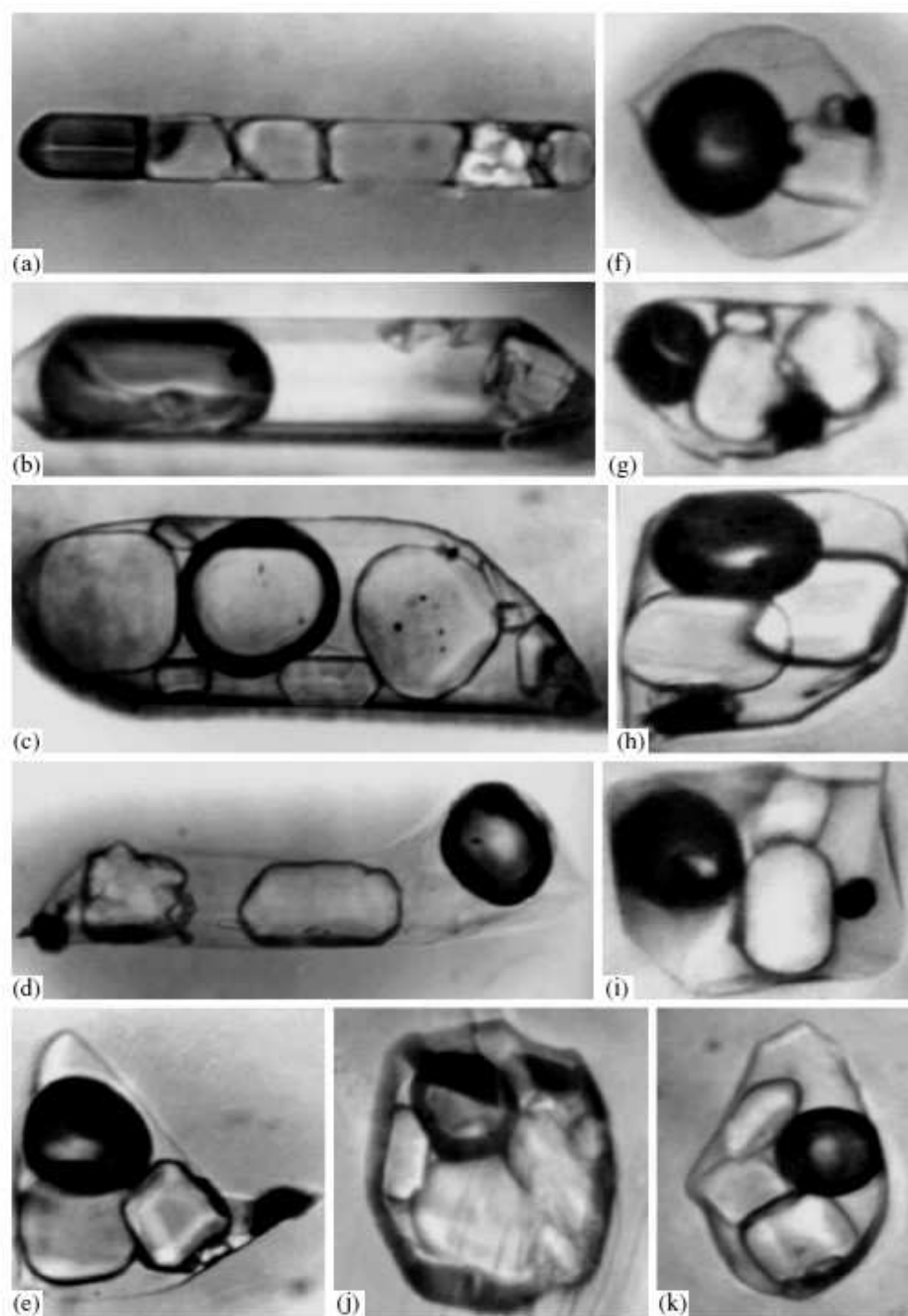


Fig. 1. Multiphase inclusions with daughter crystals in various minerals.

(a) Quartz from a miarole in granite, Industrial'noe Sn deposit, North Eastern Russia. The homogenization temperature $T_h = 820^\circ\text{C}$, see [33, 34] for other data; (b) beryl from Mount Sherlovaya, Eastern Transbaikalia, $T_h = 615^\circ\text{C}$; (c) topaz from pegmatite in Volhynia, Ukraine, $T_h = 480^\circ\text{C}$; (d, e) fluorite from pyroxene-garnet skarn, Tyrnyauz deposit, Northern Caucasus, $T_h = 655^\circ\text{C}$ (gas disappears at 630°C , magnetite dissolves at 655°C [35]); (f) quartz, Eldzhurta granite, Northern Caucasus, dissolution temperatures: 200°C for the anisotropic crystal, 330°C for halite, 750°C for the ore mineral, 820°C for the gas [36]; (g, h) quartz from pegmatite, Vitosa, Bulgaria, $T_h = 505^\circ\text{C}$ (magnetite did not completely dissolve); (i) quartz from pegmatite, Kent, Kazakhstan, $T_h = 610^\circ\text{C}$; (j) scheelite from the Chorukh-Dairon wolframite deposit, Northern Tajikistan [37], $T_h = 530^\circ\text{C}$; (k) quartz from a vein of rock crystal in the Western Pamirs, $T_h = 440^\circ\text{C}$ [38].

cinnabar (99%), celestine (73%), and barite (74%). Histograms of the homogenization temperatures of fluid inclusions in some minerals are shown in Fig. 2.

The most favorable ranges of the crystallization temperatures of certain minerals identified will likely not be modified in the course of further studies because of the good representatives of data on which these ranges are based. The following example illustrates the validity of this conclusion. By 1980, 529 measurements of the homogenization temperatures of fluid inclusions in sphalerite were obtained, and the temperature range of 300–100°C comprised 76% of all measured values [18]. The number of measurements of these temperatures for sphalerite significantly increased by late 2007 (1983 measurements), but the temperature range of 300–100°C included practically the same percentage of the values: 75% (Table 5). In 1980, 80% of 84 measurements obtained for beryl fell within the temperature range of 450–250°C [18]. The number of the measurements currently increased to 299, but the same temperature range includes 75% of them (i.e., a closely similar percentage).

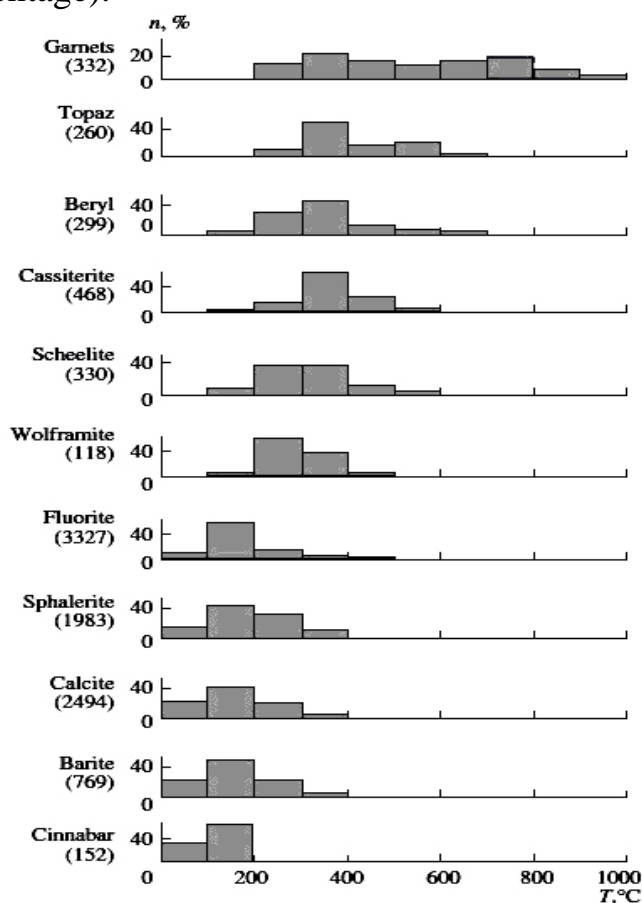


Fig. 2. Histograms for the homogenization temperatures of fluid inclusions in some minerals. Numerals in parentheses show the number of determinations.

Analogous examples for two other minerals (fluorite and calcite) are also similar. The temperature range of 250– 50°C includes 81% of 1278 measurements for

fluorite and 80% of 795 measurements for calcite according to [18]. Now this most favorable range of crystallization temperatures includes 80% of 3327 values for fluorite and 81% of 2494 measurements for calcite. Results close to earlier data in [18] were also obtained for other minerals (Table 6).

PRESSURES OF NATURAL MINERAL-FORMING FLUIDS

Pressure is one of the most important parameters of mineral-forming systems. Now the main source of quantitative information on the pressure of natural fluids is inclusions in minerals. While as few as 160 pressure measurements derived from information on fluid inclusions had been published by 1972 [39], the number of these measurements increased to 470 by 1977 [40], 880 by 1980 [41], and now reaches 5400 (Table 2). Note that data on fluid inclusions make it possible to characterize all geological processes: magmatic, metamorphic, pegmatite, skarn, greisen, hydrothermal, sedimentary, and diagenetic.

Table 6. Comparison of the most favorable temperature ranges for the crystallization of certain minerals reported in 1980 in [18] and in this publication

Mineral	Temperature range, °C	As of 1980		As of 2007	
		<i>n</i>	%	<i>n</i>	%
Cassiterite	450–300	190	78	468	75
Beryl	450–250	84	80	299	75
Tourmaline	400–250	84	78	173	65
Wolframite	350–250	76	80	118	68
Sphalerite	300–100	529	76	1983	75
Fluorite	250–50	1278	81	3327	80
Calcite	250–50	705	80	2494	81
Barite	200–50	182	82	770	74
Antimonite	150–50	52	84	88	75
Cinnabar	150–50	77	87	152	82

Note: *n* is the total number of measurements, % is the percentage of measurements within a given temperature range.

Table 7 shows data on the frequency of occurrence (in %) of temperatures and

pressures of natural mineral-forming fluids within ranges of 20–1200°C and 1–12000 bar. As follows from this table, more than half of the 5262 measurements fall within the temperature range of 200–500°C (55%) and the pressure range of 1–2000 bar (57%). Figure 3 presents all available measurements of temperatures (20–1400°C) and pressures (1–13000 bar) of natural fluids (the current number of such determinations amounts to 5390). This figure does not display 15 measurements with pressures >13000 bar, among which the maximum values of fluid pressure reaches 21000 bar [42]. This figure also shows that the best thickening of the data points occurs at temperatures below 400°C and pressures below 2000 bar. At the same time, only very few measurements occur within the range of 500–900°C and pressures of <1000 bar, i.e., the region characterized by a low density of the fluid (this region was previously referred to as pneumatolitic) is unfavorable for the crystallization of minerals.

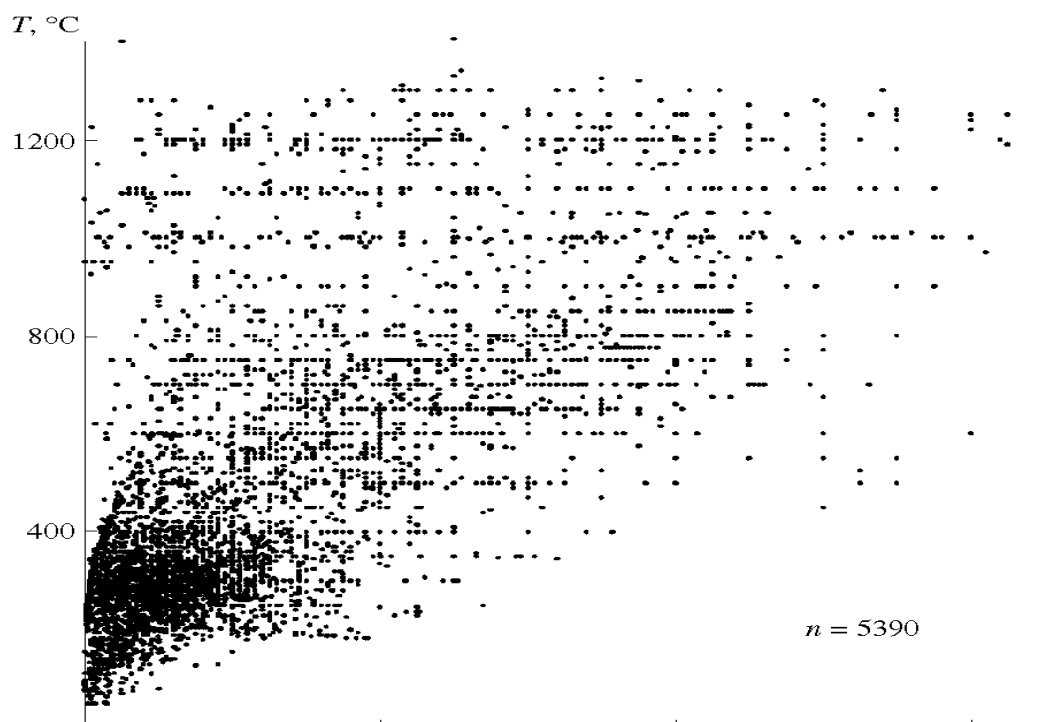


Fig. 3 Pressures of natural mineral-forming fluids within the ranges of 20–1400°C and 1–13000 bar.

The composition of fluid within such broad temperature and pressure ranges was proven to vary: the regions of high temperatures (> 600–700°C) and pressures (>4000 bar) are dominated by H₂O-free CO₂, CH₄, N₂, and CO fluids, whereas fluids at temperatures below 600°C and pressures <400 bar are typically aqueous. The variations in the component composition of fluids are shown in Fig. 4a (predominantly H₂O-free fluids) and 4b (predominantly aqueous fluids), and Table 8 reports data on the frequencies of occurrence (in %) of these fluid types within

the

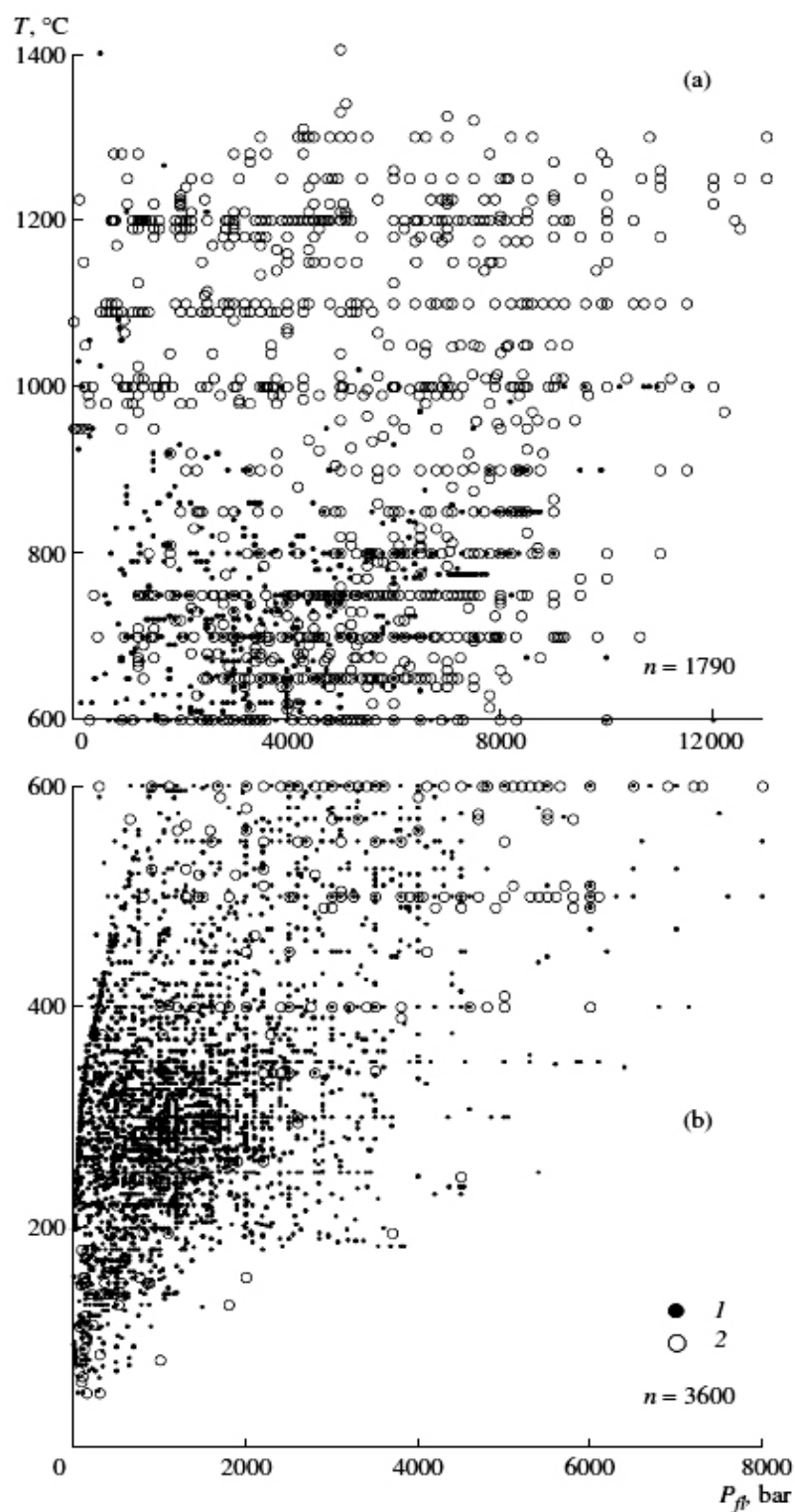


Fig. 4. Pressures of natural mineral-forming fluids within the ranges of (a) 600–1400°C and 1–13000 bar and (b) 20–600°C and 1–8000 bar.
 (1) Fluids of predominantly aqueous composition, (2) water-poor and water-free fluids (CO_2 , CH_4 , N_2).

temperature range of 20–1200°C and the pressure range of 1–12000 bar.

Water-poor high-temperature (>1000°C) fluids commonly consist of carbon dioxide, which is provided mostly by basaltic magmas. The ascent of these magmas to the Earth's surface is associated with their degassing and the origin of an individual ee_2 fluid phase. The major fluid component of deep xenoliths in alkali basalts and kimberlites that represent the upper mantle is also ee_2 , and these inclusions sometimes also contain up to 8–12 mol % CO, N₂, or minor amounts of S-bearing gases. A generalized characteristic of deep fluids and a review of all currently available data was published in our earlier paper [43]. It was demonstrated that the studies of syngenetic melt and fluid inclusions provide evidence of the widespread degassing of natural magmas with the release of volatile components in the form of an individual phase. It was also shown that the composition of this volatile phase differs for various magmas: this is CO₂ for mafic and ultramafic melts and H₂O for acid melts. Data obtained after the aforementioned paper was published completely confirm these conclusions.

The temperature range of 600–1000°C, at which metamorphic processes are widespread, is characterized by water-poor fluids also dominated by carbon dioxide. Pre dominantly CO₂ fluids are most typical of rocks of the granulite metamorphic facies.

Figure 4a shows that the high-temperature (>600°C) region includes numerous measurements of high fluid pressures (>5 kbar). As was mentioned above, these fluids are dominated by CO₂. In numerous recently published papers, data on inclusions in minerals point to fluid pressures higher than 10 kbar [42, 44–60]. Note that a pressure of 5 kbar corresponds to the lithostatic pressure of overlying rocks at a depth of 18–20 km, and a pressure of 10 kbar occurs at 35–40 km. It is thus reasonable to conclude that fluids of predominantly CO₂ composition can exist as an individual phase at significant depths within the crust (20–40 and even 70–75 km, according to [43]) at high temperatures and pressures. These deep fluids of magmatic or metamorphic genesis can be involved in hydrothermal solutions when ascending to the surface and form ore deposits. In this situation, they control the movements of the solutions.

Figure 4 also shows that many measurements at 600–900°C correspond to aqueous fluids. One of their principal sources are acid magmas, whose water concentrations are often as high as 5–8 wt % and occasionally reach 13.9 wt % [61]. Studies of inclusions in minerals make it possible to visually observe a high-density liquid aqueous phase in acid melts, to conduct thermometric and cryometric measurements, and to calculate the concentrations and pressures of volatile components in magmatic melts [36, 61–74]. Figure 5 presents micrographs of melt inclusions with high-density magmatic water in quartz, sanidine, and anorthoclase. The degassing of such water-rich acid melts results in the liberation of high-temperature aqueous fluids under high pressure (from a few to 10–15 kbar). These fluids can undoubtedly participate in hydrothermal ore-forming processes [75].

Here we do not analyze the role of magmatic fluids in the genesis of ore deposits;

some aspects of relations between rare-metal ore mineralization and acid magmatism were considered in our earlier publications [76, 77] based on data obtained on inclusions in minerals.

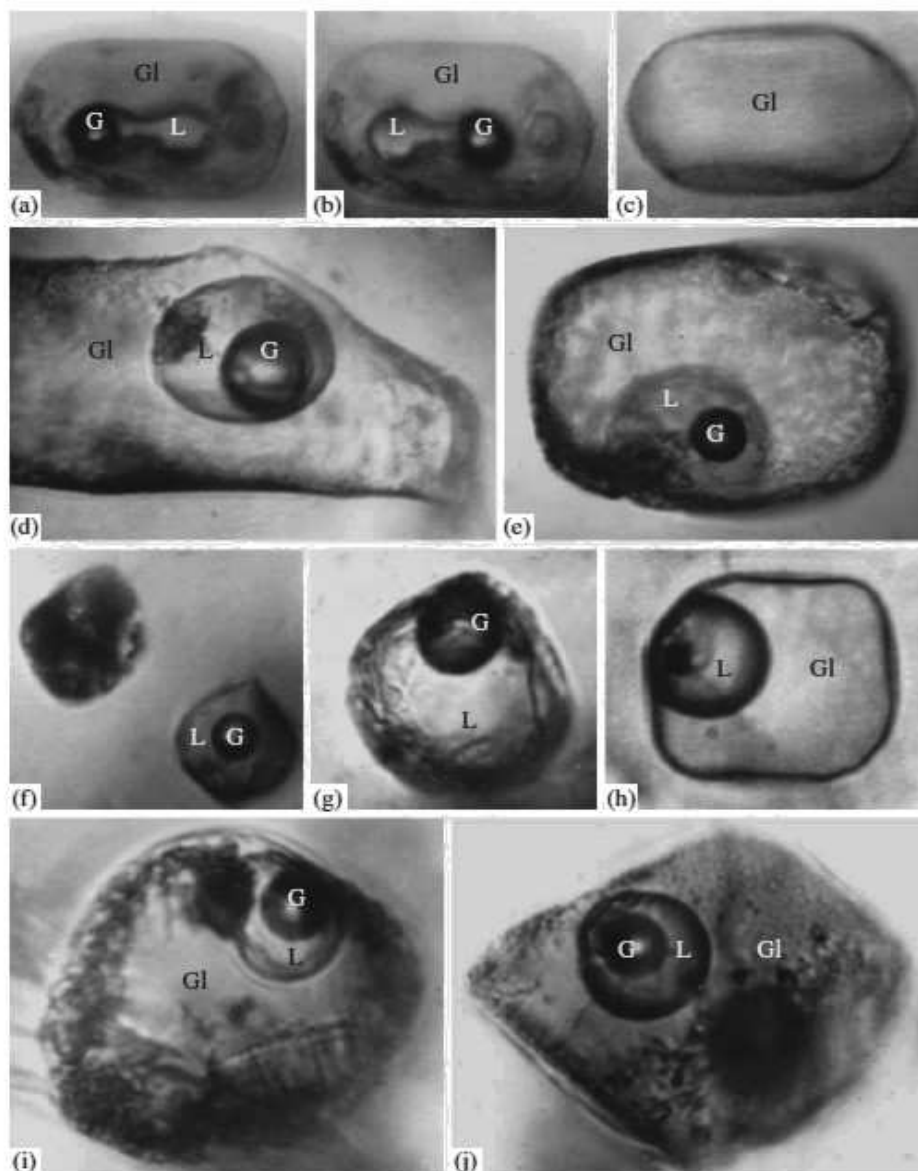


Fig. 5. Silicate melt inclusions with high-density magmatic water. (a–e) Quartz from topaz rhyolite, Spore Mountain, United States [67, 68]: (a) 8-shaped fluid segregation at room temperature, the gas phase (G) on the left-hand side has $T_h = 270^\circ\text{C}$, (b) same inclusion after its heterogenization, a gas phase appeared on the right-hand side, (c) inclusion after homogenization in a bomb under a pressure of 3.1 kbar and a temperature of 700°C , (d, e) inclusions at room temperature, the homogenization temperatures of the fluid constituents of the inclusions are (d) 255°C , (e) 136°C ; (f) quartz in rhyolite from central Slovakia [66, 71]; (g) sanidine in rhyolite from central Slovakia [66, 71]; (h) sanidine in andesite from central Slovakia [69, 72]; (i, j) anorthoclase, Pantelleria Island, fluids of the inclusions homogenized at (i) 305°C and (j) 235°C [65]; Gl is silicate glaucophane, G is a gas phase, L is the liquid water phase.

The depths at which ore deposits are formed usually do not exceed 3–5 km [78], which corresponds to a lithostatic pressure of 800–1300 bar. As follows from Table 7 and Fig. 4b, the pressures of mineral-forming fluids at temperatures lower than 400°C quite often exceed 1500–2000 bar. In many instances when the depths

of ore formation were evaluated from geological evidence and the pressures were calculated from data obtained on inclusions in minerals, the actual values of the latter parameter turned out to be significantly higher not only than the hydrostatic load but also than the lithostatic pressure [18, 39, 40, 76, 77, and others]. This means that the excess pressure is exerted by fluids coming from greater depths, and these fluids can be either CO₂- or H₂O dominated (see above). This is illustrated by the following example. We thoroughly examined fluid inclusions in quartz samples taken at various depths (up to 3100 m) at the Kolar gold deposit in India [79]. It was determined that the fluid pressure gradients varied from 0.33 to 6.07 bar/m (at an average value of 1.35 bar/m) and significantly exceeded the pressure gradient of 0.27 bar/m due to the lithostatic load of the overlying rocks. This led us to conclude that the CO₂-dominated fluids could come from a fairly deep source, which maintained the high pressure gradients during the lengthy evolutionary history of the deposit.

SALINITY AND DENSITY OF NATURAL MINERAL-FORMING FLUIDS

Studying inclusions in minerals is a reliable and straightforward method for evaluating the chemistry, salinity, and density of mineral-forming fluids. Table 2 illustrates the tendency in the accumulation of factual data (publications and analyses) on the salinity of natural fluids. Currently available information on the chemical composition of fluid inclusions indicates that, in spite of the great diversity of endogenic mineral-forming media, their common major components, along with water, are alkali systematic evolution of their composition with temperature.

Solutions richest in CO₂ (with CO₂ concentrations varying in these solutions from a few dozen to a few hundred grams per 1 kg of H₂O) are typical of intermediate temperatures (200–350°C). The presence of such high CO₂ concentrations results in the fact that these inclusions at room temperatures contain both aqueous solution and carbon dioxide as an individual phase. Some examples of multiphase inclusions with liquid CO₂ in various minerals are shown in Fig. 6.

High-temperature (>300–350°C) solutions contain notably more chlorides of Na, K, and other elements, and the total salinity of these fluids may reach 50–80 wt % equiv. NaCl (Fig. 7). Such high-salinity fluids can be regarded as chloride melts; inclusions can occasionally contain sulfate melts [87].

Based on 18378 determinations, Table 9 lists the frequencies of occurrence of temperatures and the salinity of natural hydrothermal mineral-forming fluids within the ranges of 20–1000°C and 0–80 wt % NaCl equiv. It is interesting to note that as few as 1124 such determinations were available as of 1980 for a narrower temperature range of 20–700°C [18]. As follows from Table 9, more than

Table 7. Frequency of occurrence (%) of temperature and pressure values of natural mineral-forming fluids within the ranges of 20–1200°C and 1–12,000 bar (based on the data of 5262 determinations)

Pressure, bar	Temperature, °C												
	20–100	100–200	200–300	300–400	400–500	500–600	600–700	700–800	800–900	900–1000	1000–1100	1100–1200	20–1200
1–500	1.03	3.31	5.13	3.95	1.25	0.10	0.10	0.02	–	0.29	0.15	0.02	15.35
500–1000	0.10	2.45	6.42	3.94	1.08	0.72	0.19	0.13	0.08	0.13	0.32	0.15	15.71
1000–1500	–	0.59	6.40	4.54	1.31	0.93	0.40	0.36	0.11	0.17	0.25	0.28	15.34
1500–2000	–	0.15	3.91	3.29	1.16	0.65	0.28	0.44	0.17	0.15	0.08	0.30	10.58
2000–2500	–	0.21	1.93	2.26	0.82	0.78	0.32	0.38	0.19	0.11	0.11	0.27	7.38
2500–3000	–	0.15	0.87	1.20	0.65	1.05	0.89	0.57	0.13	0.08	0.21	0.25	6.05
3000–3500	–	0.17	0.51	0.63	0.53	0.97	0.70	0.42	0.27	0.10	0.11	0.23	4.64
3500–4000	–	0.11	0.10	0.38	0.51	0.78	0.80	0.57	0.06	0.19	0.21	0.30	4.01
4000–4500	–	–	0.11	0.17	0.36	0.42	0.61	0.63	0.11	0.06	0.13	0.30	2.90
4500–5000	–	–	0.06	0.15	0.13	0.46	0.78	0.66	0.23	0.15	0.10	0.28	3.00
5000–6000	–	–	0.04	0.11	0.34	0.44	1.12	1.31	0.36	0.27	0.27	0.19	4.45
6000–7000	–	–	–	0.08	0.10	0.23	1.01	0.93	0.49	0.36	0.19	0.44	3.83
7000–8000	–	–	–	0.02	0.06	0.10	0.48	1.06	0.42	0.30	0.25	0.49	3.18
8000–9000	–	–	–	–	–	0.04	0.11	0.36	0.82	0.36	0.28	0.27	2.24
9000–10000	–	–	–	–	0.04	0.06	0.10	0.11	0.04	0.11	0.15	0.19	0.80
10000–11000	–	–	–	–	0.04	0.06	0.02	0.02	0.02	0.10	0.10	0.04	0.40
11000–12000	–	–	–	–	–	–	0.02	–	0.02	0.06	0.04	–	0.14
1–12000	1.13	7.14	25.48	20.72	8.38	7.79	7.93	7.97	3.52	2.99	2.95	4.00	100.00

half (53%) of all salinity determinations in hydrothermal fluids do not exceed 10 wt %.

When captured in minerals and cooled to room temperature, such fluids form two-phase inclusions consisting of gas and liquid. Examples of such inclusions in

various minerals are shown in Fig. 8. The overwhelming majority (84%) of determinations in Table 9 are constrained to the temperature range of 100–400 °C. Although the information available in 1980 was much more scant, the percentage of measured values falling within the same temperature range of 100–400 °C was the same: 84% [18]. This means that the number of measurements obtained by various researchers and exceeding 1000 is adequately representative.

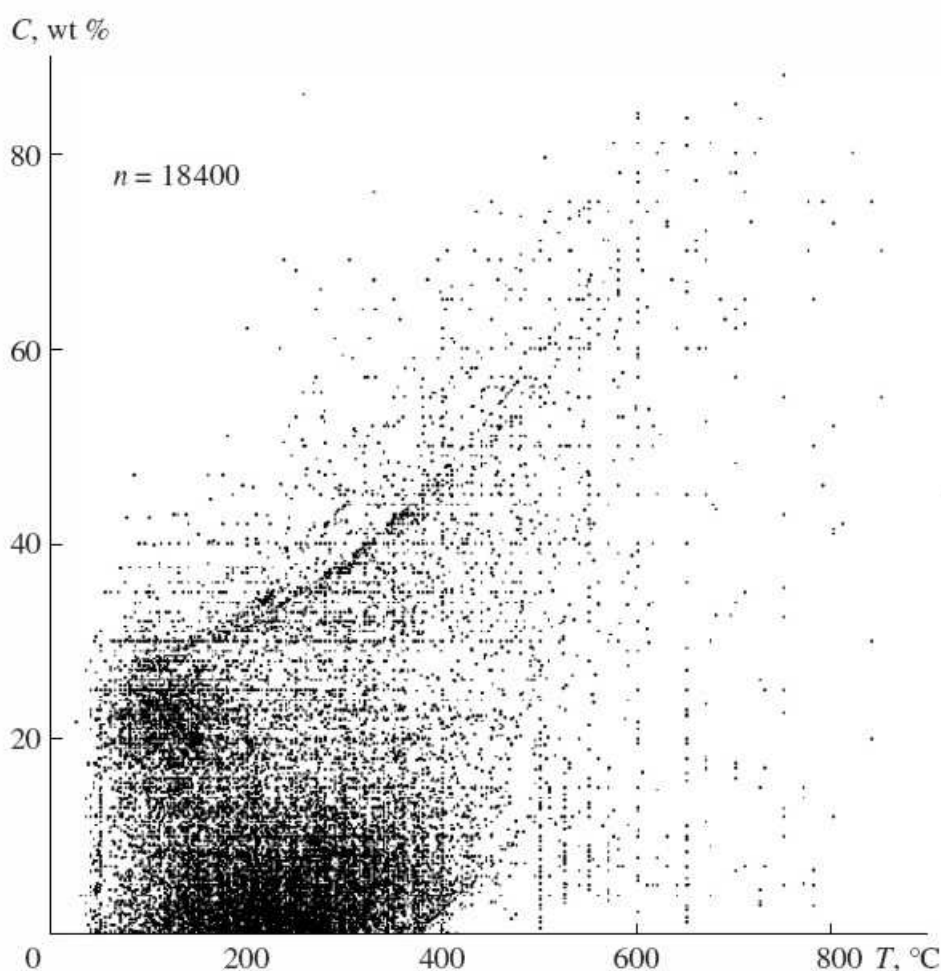


Fig. 7. Distribution of temperature and salinity (wt % equiv. NaCl) values of natural mineral-forming fluids.

Data on inclusions in minerals provide quantitative characteristics of the density of hydrothermal fluids. The density of two-phase (gas + liquid) inclusions is calculated from the salinity of the solution and its homogenization temperature.

The density of multiphase inclusions (gas + liquid + crystalline phases) is calculated based on the experimentally determined density of the gas, liquid, and solid phases at room temperature. Upon determining the density of each of the phases, one can calculate the density of the fluid captured when the mineral crystallized. The procedure is discussed in much detail in [92]. Our database contains information on 18437 determinations of the density of natural fluids, and these data are shown in Fig. 9, while Table 10 presents data on the frequency of the occurrence of temperature and density values of hydrothermal mineral-forming fluids within the

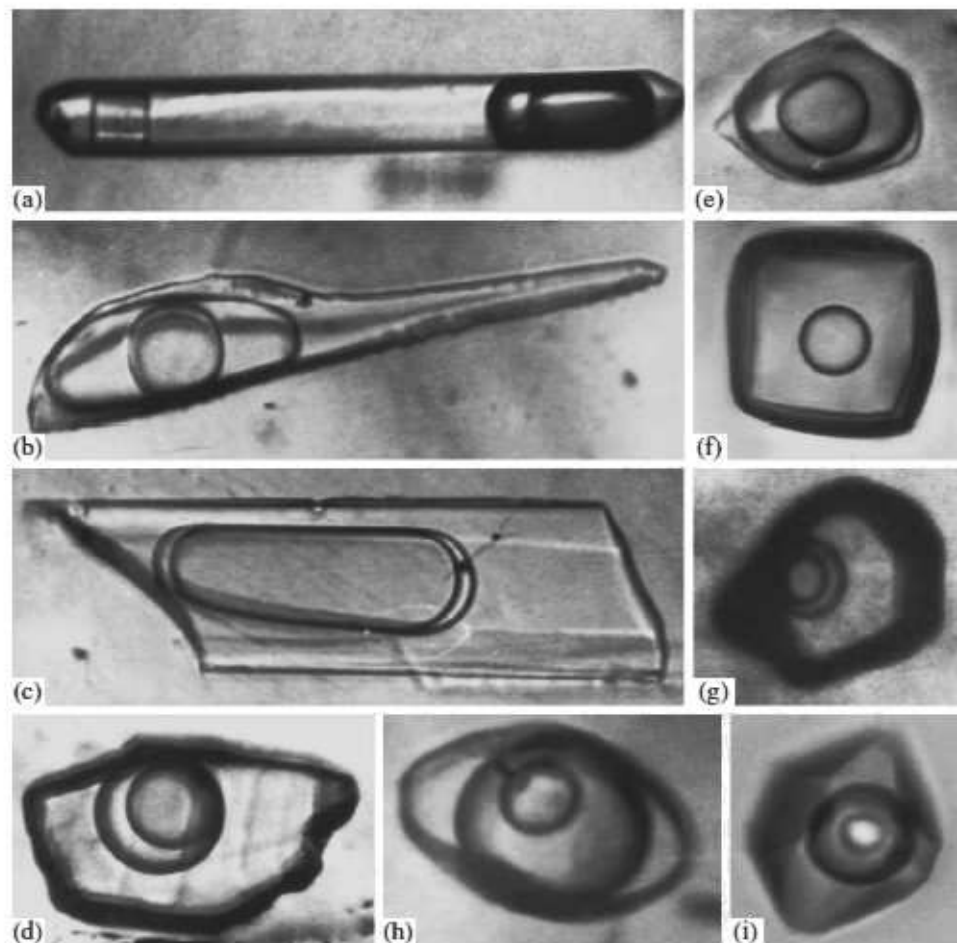


Fig. 6. Multiphase inclusions with liquid CO₂ in various minerals.

(a) Quartz from a rock crystal-bearing vein in the Western Pamirs [38]; (b) beryl, Spokoinoe W deposit, Eastern Transbaikalia, $T_h = 295^\circ\text{C}$ [80]; (c) topaz, Modoto wolframite deposit, Mongolia, $T_h = 317^\circ\text{C}$ [80, 81]; (d) siderite, Ivigtut cryolite deposit, SW Greenland, $T_h = 285^\circ\text{C}$ [82, 83]; (e) fluorite from fluorite–muscovite greisen, Belukha W deposit, Eastern Transbaikalia [80, 84]; (f) halite, Devonian rock salt, core of a borehole, depth 1380 m, Dnepr–Donets depression, Ukraine, micrograph at -7°C , Raman spectroscopic data: CO₂ = 79.1 mol %, CH₄ = 20.9 mol %; (g) orpiment, Minkyule deposit, Verkhoyansk Range, Yakutia [85]; (h) quartz, rock crystal-bearing veins in Southern Urals; (i) quartz, Berezovsk gold deposit, Urals, $T_h = 288^\circ\text{C}$ [86].

(76%) of the determinations span the density range of $0.8\tilde{1}.2$ g/cm³, i.e., natural fluids mostly have very high density values. Note that when the 1015

determinations available as of 1980 were analyzed, the density range of 0.8–1.2 g/cm³ included practically the same percentage of these determinations: 75% [18].

GAS COMPOSITION OF NATURAL MINERAL-FORMING FLUIDS

One of the most important factors of natural mineral-forming processes is the chemical composition of solutions from which minerals crystallized. An important role in evaluating this composition is played by the study of fluid inclusions. The exact knowledge of the gas composition of a fluid not only provides direct

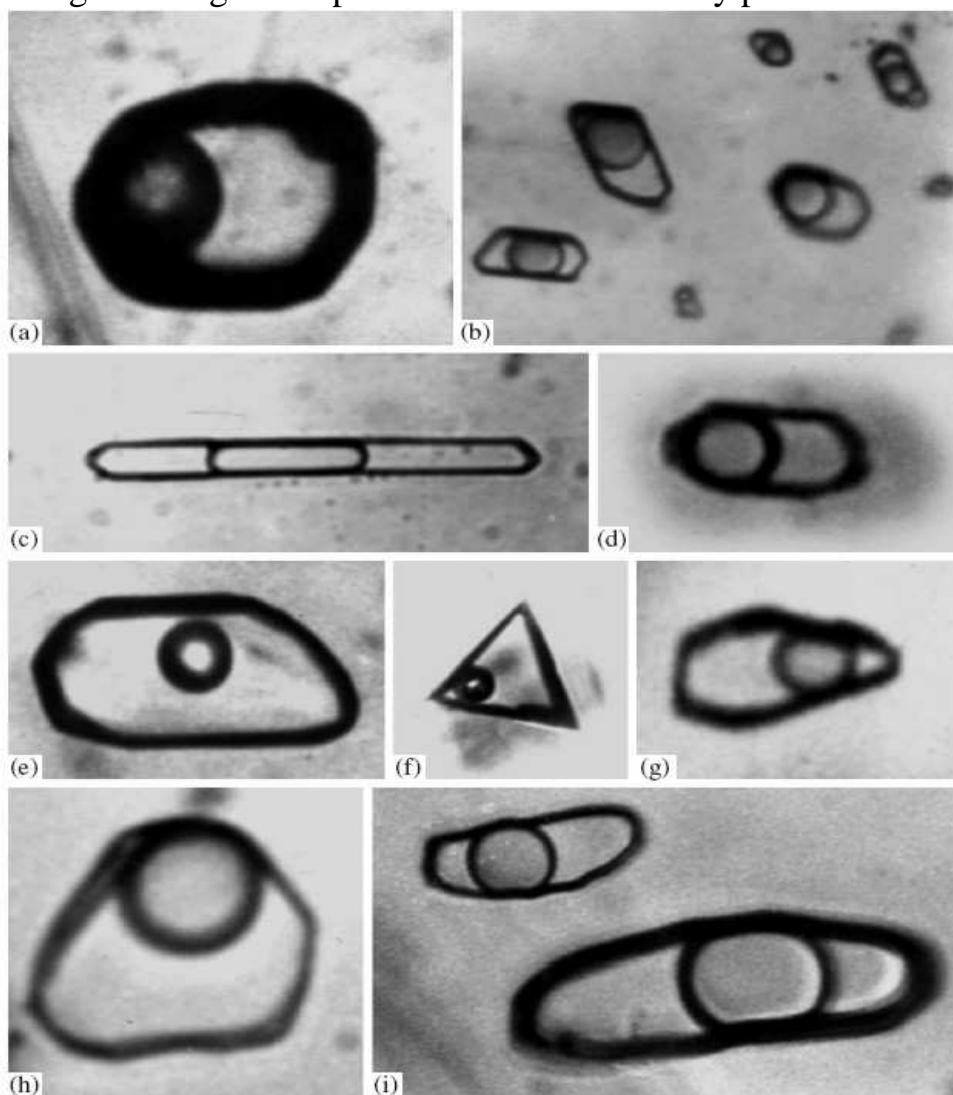


Fig. 8. Two-phase (gas + liquid) fluid inclusions in various minerals.

(a, b) Sphalerite: (a) Dzhida wolframite deposit, South Western Transbaikalia, $T_h = 239^\circ\text{C}$, $C = 9.5$ wt % equiv. NaCl [88]; (b) Sadovoe base-metal deposit, Southern Russian Far East, $T_h = 350^\circ\text{C}$, $C = 3.6$ wt % equiv. NaCl [89]; (c, d) topaz: (c) Svetloe Sn–W deposit, Chukotka, $T_h = 329^\circ\text{C}$, $C = 4.8$ wt % equiv. NaCl [89]; (d) Yugodzyr Mo–W deposit, Eastern Mongolia, $T_h = 376^\circ\text{C}$, $C = 7.2$ wt % equiv. NaCl [90]; (e) barite, Abagatui fluorite deposit, Eastern Transbaikalia, $T_h = 142^\circ\text{C}$, $C = 3.5$ wt % equiv. NaCl; (f) fluorite, Lastochka deposit, Russian Far East, $T_h = 152^\circ\text{C}$, $C = 4.7$ wt % equiv. NaCl; (g) huebnerite, Tumen-Tsogto wolframite deposit, Eastern Mongolia, $T_h = 272^\circ\text{C}$, $C = 7.2$ wt % equiv. NaCl [80, 81]; (h) quartz, Banska Stiavnica Au–Ag–Pb–Zn deposit, Central Slovakia, $T_h = 305^\circ\text{C}$, $C = 2.7$ wt % equiv. NaCl [91]; (i) cassiterite, Svetloe Sn–W deposit, Chukotka, $T_h = 330^\circ\text{C}$, $C = 4.3$ wt % equiv. NaCl [89].

evidence on the concentrations of certain components and their spatiotemporal evolution but also makes it possible to remarkably widen the

characteristics of mineral-forming fluids with the application of thermodynamic methods.

The very first direct determinations of gas components in fluid inclusions were accomplished in the second half of the 20th century (Table 2). In 1950 Ermakov [1] described in much detail the techniques applicable for studying inclusions in minerals. The publication of this paper stimulated the development of more advanced techniques and methods, with mass spectrometric techniques [93–100 and others] finding the widest application. Simultaneously gas chromatographic methods were more and more widely used after the publication of [101–104]. The advantages and disadvantages shared by all of these methods are underlain by the fact that they provide data only on the bulk composition of inclusions [99, 105, 106]. The analysis of the gas phases of individual inclusions was first conducted by.

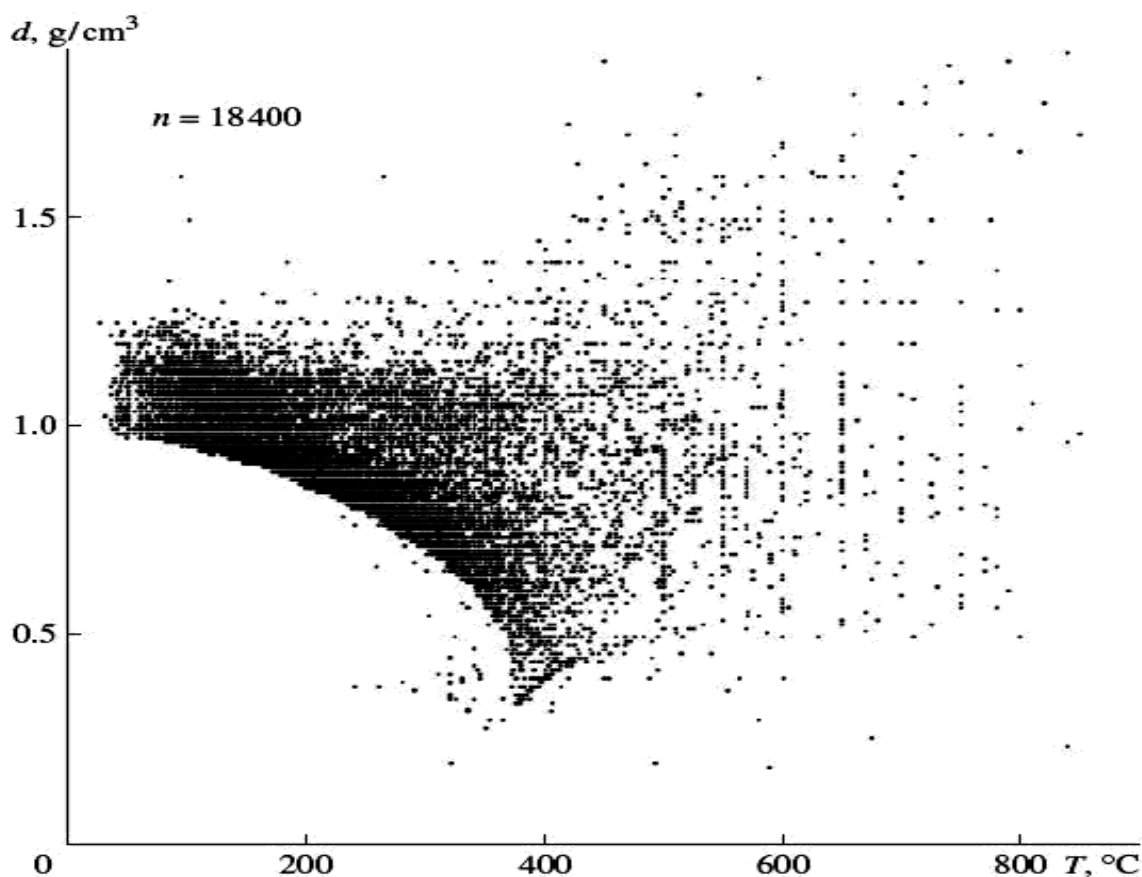


Fig. 9. Distribution of temperature and density values of natural mineral-forming fluids.

Maslova [107], and this technique was later modernized by Shugurova [108] but eventually has not found wide use because of its high labor intensity and low accuracy. The most reliable data can be obtained by means of the direct analysis of the material of fluid inclusions. Because of this, the publication of [109] in 1976

marked the onset of a new phase in studying microinclusions and displayed the potentialities and outlooks of the application of Raman spectroscopic techniques in studying individual fluid inclusions without their opening. The continuous modernization of these techniques resulted in their broad utilization at various laboratories worldwide [110–115 and many others]

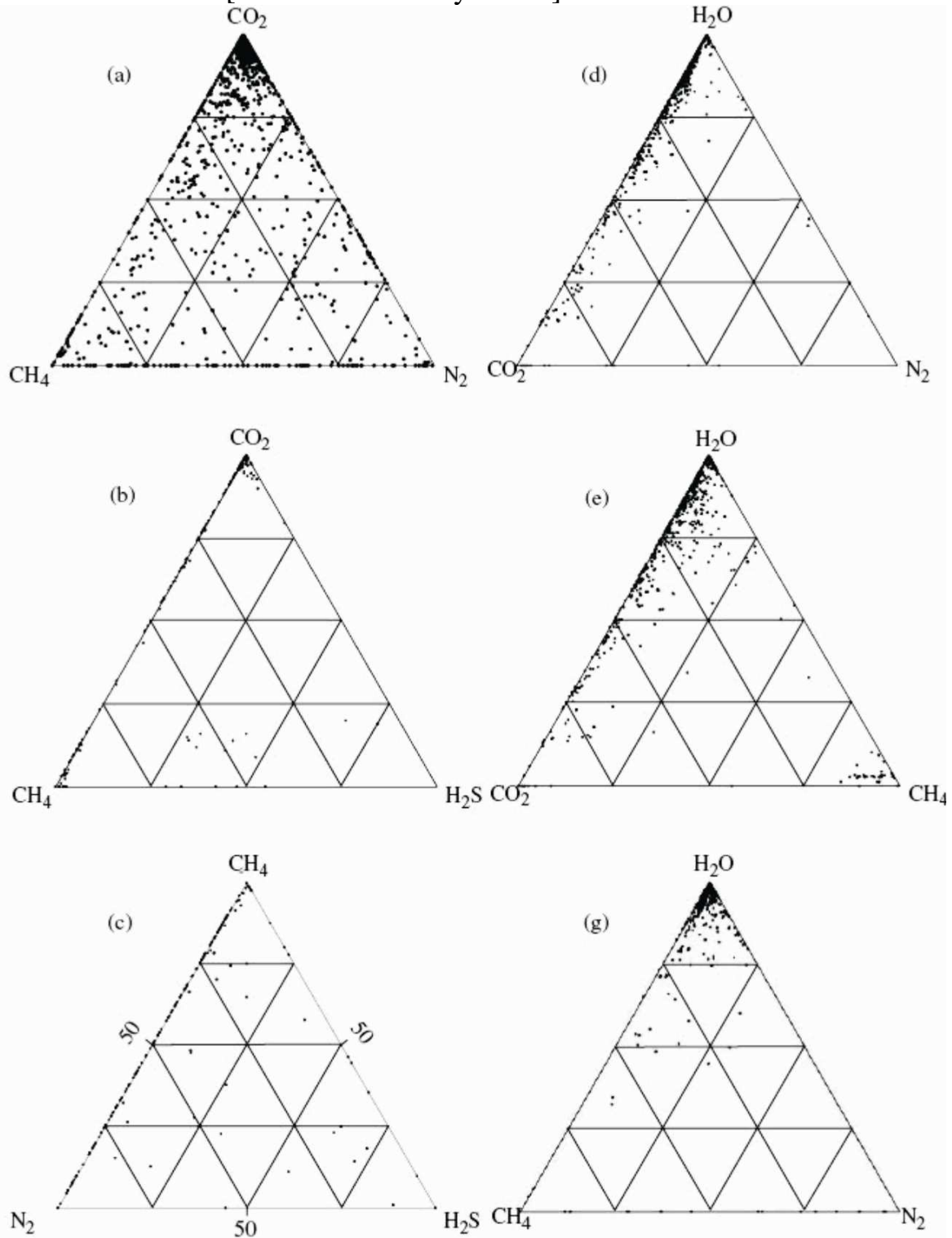


Fig. 10. Diagrams showing proportions of gas components in natural mineral-forming fluids. Numbers of determinations: (a) 1200, (b) 376, (c) 313, (d) 683, (e) 770, (f) 641.

Table 8. Frequency of occurrence (%) of (I) H₂O-dominated and (II) H₂O-poor or H₂O-free fluid inclusions in minerals within the ranges of 20–1200°C and 1–12000 bar

Temperature, °C	Number of measurements	%		Pressure, bar	Number of measurements	%	
		I	II			I	II
20–100	59	76	24	1–1000	1642	94	6
100–200	376	81	19	1000–2000	1373	91	9
200–300	1342	92	8	2000–3000	717	81	19
300–400	1090	85	15	3000–4000	462	70	30
400–500	441	78	22	4000–5000	330	47	53
500–600	410	71	29	5000–6000	246	35	65
600–700	415	45	55	6000–7000	212	40	60
700–800	425	48	52	7000–8000	177	40	60
800–900	187	46	54	8000–9000	133	40	60
900–1000	160	16	84	9000–10000	47	45	55
1000–1100	159	4	96	10000–11000	27	45	55
1100–1200	215	1	99	11000–12000	10	20	80

Table 9. Frequency of occurrence (%) of temperature and salinity values of natural hydrothermal mineral-forming fluids at 20–1000°C and 0–80 wt % equiv. NaCl (based on the data of 18378 measurements)

Salinity, wt %	Temperature, °C										
	20–100	100–200	200–300	300–400	400–500	500–600	600–700	700–800	800–900	900–1000	20–1000
0–5	1.61	10.17	14.33	5.80	0.48	0.09	0.08	0.04	–	–	32.60
5–10	0.83	5.59	7.82	4.98	0.69	0.28	0.06	0.04	–	–	20.29
10–15	0.89	3.86	3.68	2.28	0.57	0.20	0.02	0.04	–	–	11.54
15–20	1.33	3.81	1.67	1.23	0.32	0.11	0.08	0.01	0.01	–	8.57
20–25	1.90	5.33	1.39	0.85	0.41	0.06	0.03	0.02	–	–	9.99
25–30	0.83	2.36	0.90	0.67	0.29	0.10	0.02	0.01	0.01	–	5.19
30–35	0.20	0.87	1.58	0.89	0.33	0.13	0.03	0.01	–	–	4.04
35–40	0.08	0.26	0.80	0.93	0.35	0.16	0.02	0.01	–	–	2.61
40–45	0.01	0.08	0.22	0.92	0.34	0.14	0.02	0.02	0.01	0.01	1.77
45–50	0.01	0.02	0.11	0.34	0.47	0.14	0.02	0.01	–	–	1.12
50–60	–	0.01	0.08	0.26	0.60	0.25	0.05	0.01	0.01	–	1.27
60–70	–	0.01	0.03	0.08	0.19	0.34	0.07	0.02	0.01	–	0.75
70–80	–	–	–	0.01	0.03	0.12	0.06	0.03	0.01	–	0.26
0–80	7.69	32.37	32.61	19.24	5.07	2.12	0.56	0.27	0.06	0.01	100.00

The variations in the number of publications and measurements by techniques predominantly utilized in the analysis of natural fluids and applied in studying fluid inclusions in minerals with time is shown in Table 11. Although Raman spectroscopic techniques were applied to studying inclusions in minerals much later than other techniques, the former have a strong lead in this field and now

Table 10. Frequency of occurrence (%) of temperature and density values of natural hydrothermal mineral-forming fluids at 20–1000°C and 0.01–1.90 g/cm³ (based on the data of 18437 measurements)

Density, g/cm ³	Temperature, °C										
	20–100	100–200	200–300	300–400	400–500	500–600	600–700	700–800	800–900	900–1000	20–1000
0.01–0.20	–	–	–	0.01	0.01	0.01	–	–	–	–	0.03
0.20–0.40	–	–	0.03	0.38	0.07	0.02	0.01	–	0.01	–	0.52
0.40–0.60	–	–	–	1.77	0.90	0.13	0.04	0.04	–	–	2.88
0.60–0.70	–	–	0.02	4.21	0.62	0.15	0.03	0.04	–	–	5.07
0.70–0.80	–	–	6.01	5.69	0.73	0.20	0.06	0.02	–	–	12.71
0.80–0.90	–	2.28	16.41	2.27	0.58	0.38	0.11	0.05	–	–	22.08
0.90–1.00	1.39	14.75	5.31	1.78	0.67	0.41	0.10	0.03	0.01	–	24.45
1.00–1.10	2.50	9.36	3.28	2.20	0.67	0.25	0.05	0.03	0.01	–	18.35
1.10–1.20	3.44	5.54	1.24	0.68	0.39	0.19	0.04	0.01	–	0.01	11.54
1.20–1.30	0.34	0.26	0.18	0.18	0.22	0.15	0.04	0.02	–	–	1.39
1.30–1.40	0.01	0.01	0.02	0.06	0.10	0.10	0.03	0.01	–	–	0.34
1.40–1.50	–	0.01	0.01	0.01	0.06	0.12	0.04	0.01	–	–	0.26
1.50–1.60	–	–	–	–	0.05	0.08	0.03	–	–	–	0.16
1.60–1.70	–	–	–	–	0.02	0.04	0.03	0.02	0.01	–	0.12
1.70–1.80	–	–	–	–	0.01	0.01	0.01	0.01	0.01	–	0.05
1.80–1.90	–	–	–	–	0.01	0.01	0.01	0.01	0.01	–	0.05
0.01–1.90	7.68	32.21	32.51	19.24	5.11	2.25	0.63	0.30	0.06	0.01	100.00

Table 11. Methods and techniques most frequently used to analyze the gas composition of natural fluids and applied in studying fluid inclusions in minerals in various periods of time (I is the number of publications, II is the number of measurements)

Method	1965–1990			1991–2007			1965–2007		
	I	II		I	II		I	II	
		n	%		n	%		n	%
Gas chromatography	23	214	19	44	569	13	67	783	15
Mass spectrometry	22	184	17	31	740	18	53	924	17
Raman spectrometry	49	499	45	1422	2550	61	171	3049	58
Other methods	9	214	19	18	330	8	27	544	10
Total	103	1111	100	215	4189	100	318	5300	100

account for more than 60% of all measurements. However, “bulk-analysis” techniques are still widely used, results obtained with various approaches to the analysis of the same samples are still actively discussed in the literature, and

conclusions are drawn concerning the advantages and disadvantages of such techniques [99, 105, 106, and others].

The authors of numerous publications devoted to the comparison of a great diversity of analytical techniques concur that Raman spectroscopic techniques are accurate enough to determine the composition of individual inclusions but the data thus obtained can sometimes be not representative of the average composition of fluids in the sample as a whole. This pertains, first of all, to the analysis of inclusions of heterogeneous phase composition, and hence, it is pertinent to stress here once again that the analysis of fluid inclusions is not a routine operation but involves assiduous research. Table 12 lists the average composition of the gas phase of natural mineral-forming fluids obtained by Raman spectroscopic analysis. Already very early in the course of studying fluid inclusion, it became obvious enough that CO₂ is one of the predominant gas components of most mineral-forming fluids. For example, CO₂ was identified in 1881 analyses (66%) (Table 12) of the 3049 analyses of the gas composition of fluid inclusions by Raman spectroscopy (Table 11), with CO₂ accounting for 100% of the filling of the inclusions in 223 analyses (no other gases were identified in them). An ever growing number of determinations indicates that reduced carbon-bearing species (such as CH₄) can broadly participate in naturally occurring processes, as was first emphasized in [93]. Methane was identified in 1835 of the 3049 Raman spectroscopic analyses

Table 12. Average composition (mol %) of the gas phase of natural fluids (Raman spectroscopic data)

Component	Number of analyses	Range of concentrations and average values	Average composition of gas phase
CO ₂	1881	0.00–100 (63.65)	61.46
CH ₄	1835	0.00–100 (19.91)	19.23
N ₂	1508	0.00–100 (16.76)	16.18
H ₂ S	463	0.00–75.0 (2.25)	2.17
C _n H _m	111	0.00–12.0 (0.75)	0.72
H ₂	70	0.00–3.20 (0.12)	0.12
CO	54	0.00–4.30 (0.12)	0.12
SO ₂	19	0.00	0.00
Total	5941	–	100.0

(65%) (Table 11), and the methane concentrations in 71 of the analyses reach 100%. The third most widely spread and most abundant component is nitrogen, as was first noted in [104] and was confirmed by information accumulated later. Nitrogen was found in 1508 of 3049 analyses of the gas composition of fluid inclusions (53%) (Table 11) and accounted for 100% in 26 of these analyses. Figure 10 illustrates the relations between the concentrations of various volatile

components in natural mineral-forming fluids. For example, when H₂O and other major components were analyzed (Fig. 10a), 51% of the 1200 data points corresponds to the presence of all of the three major components, and 36% are diverse combinations of two-component systems. Unicomponent systems account for 13% of the total number of the analyses. Systems with H₂O (Figs. 10d, 10e) are most commonly three-component: H₂O–CO₂–CH₄ (76% of 770 analyses) and H₂O–CO₂–N₂ (72% of 683 analyses).

CONCLUSIONS

1. We compiled a database comprising materials from more than 17500 publications on fluid and melt inclusions in minerals and generalized the results on the major physicochemical parameters of natural mineral-forming fluids (the temperature, pressure, salinity, and density of hydrothermal solutions and the gas composition of fluids). Data on the frequency of occurrence of certain ranges of the homogenization temperatures of fluid inclusions allowed us to identify the temperature ranges most favorable for the crystallization of the host minerals of the inclusions.

2. The frequencies of occurrence of H₂O-dominated and H₂O-poor inclusions were determined for the ranges of 20–1200°C and 1–12000 bar. Mostly aqueous inclusions are predominant at temperatures below 600°C and pressures below 4000 bar, while water-poor and waterfree inclusions dominate at temperatures of 600–1200°C and pressures of 4000–12000 bar. The paper presents examples of inclusions with visually observable water, which exists as an individual high-density phase in melt inclusions in minerals collected worldwide.

3. Extensive data indicate that pressures during hydrothermal mineral-forming processes can be very high, up to 1000–1500 bar. Such pressures are much higher not only than the hydrostatic pressure but also than the pressures of the overlying rocks. This means that the excess pressures are exerted by fluids coming from greater depths; the composition of these fluids can be either CO₂- or H₂O-dominated.

4. The frequencies of occurrence of the temperatures and salinity of hydrothermal fluids are calculated based on more than 18000 determinations within the ranges of 20–1000°C and 0–80 wt % equiv. NaCl. More than a half (53%) of all determinations of the salinities of hydrothermal fluids correspond to values no higher than 10 wt %, and the great majority (84%) of temperature measurements

for hydrothermal fluids falls within the range of 100–400°C. The frequencies of occurrence of the temperatures and densities of hydrothermal mineral-forming fluids are calculated for the ranges of 20–1000°C and 0.01–1.90 g/cm³. Most (76%) of the determinations corresponds to density values of 0.8–1.2 wt %; i.e., most natural mineral-forming fluids have a very high density.

5. The paper discusses the most commonly used techniques used to analyze gases in natural fluids in application to studying inclusions in minerals of various age. More than 3000 analyses made by Raman spectroscopy (the most widely utilized technique) are used to calculate the average composition of the gas phase of natural fluids.

ACKNOWLEDGMENTS

This study was supported by the Russian Foundation for Basic Research, project no. 07-05-00497.

REFERENCES

1. **N. P. Ermakov**, Studies of Mineral-Forming Solutions (Khark. Univ., Kharkov, 1950) [in Russian].
2. **G. G. Lemmlein**, "Healing of Cracks in Crystal and Changes in the Cavity Shapes of Secondary Liquid Inclusions," Dokl. Akad. Nauk SSSR 78 (4), 685–688 (1951).
3. **G. G. Lemmlein**, Morphology and Genesis of Crystals (Nauka, Moscow, 1973) [in Russian].
4. **E. Roedder**, "Technique for the Extraction and Partial Chemical Analysis of Fluid-Field Inclusions from Minerals," Econ. Geol. 53 (3), 235–269 (1958).
5. **E. Roedder**, "Fluid Inclusions," Rev. Mineral. 12, 644 (1984).
6. **V. A. Kalyuzhnyi**, "Improvement of Microstage for Analysis of Liquid Inclusions," Tr. VNIIP 2 (2), 43–47 (1958).
7. **V. A. Kalyuzhnyi**, Principles of Study of Mineral-Forming Fluids (Naukova dumka, Kiev, 1982) [in Russian].
8. **Yu. A. Dolgov**, "Thermodynamics of the Genesis of Mirolitic Pegmatites," Tr. Inst. Geol. Geofiz. Sib. Otd. Akad. Nauk SSSR 15, 113–165 (1963).
9. **Yu. A. Dolgov, A. A. Tomilenko, and V. P. Chupin**, "Inclusions of Salt Melt-Brines in Quartz of Anatectites from the Western Part of the Aldan Shield," in Studying Inclusions in Minerals and Genetic Mineralogy (Novosibirsk, 1975), pp. 5–16 [in Russian].
10. **B. Poty**, "Inclusions Solides Et "Fil a Plomb Mineralogique": L'Age Du Filon De La Gardette (Isere)," Sciences de la Terre 11 (1), 41–53 (1966).
11. **B. P. Poty, H. A. Stalder, and A. M. Weisbrod**, "Fluid Inclusions Studies in Quartz from Fissures of Western and Central Alps," Schweiz. Min. Petr. Mitt 54 (2/3), 717–752 (1974).
12. **R. Clochiatti**, "Divers Aspects des Reliquats Magmatiques des Phenocristaux de Quartz des Porphyries de la Region de Bolzano (Italie)," C. R. Acad. Sci. 265 (25), 1861–1863 (1967).
13. **R. Clochiatti**, "Les Cristaux de Quartz des Ponces de la Vallee des dix Mille Fumees (Katmai, Alaska)," C. R. Acad. Sci. 274 (23), 3037–3040 (1972).
14. **R. J. Bodnar**, "A Method of Calculating Fluid Inclusion Volumes Based on Vapor Bubble Diameters and P-V-T-X Properties of Inclusion Fluids," Econ. Geol. 78 (3), 535–542 (1983).
15. **R. J. Bodnar and S. M. Sterner**, "Synthetic Fluid Inclusions in Natural Quartz. II. Application to PVT Studies," Geochim. Cosmochim. Acta 49 (9), 1855–1859 (1985).

16. **A. V. Sobolev and V. B. Naumov**, “First Direct Evidence for the Presence of H₂O in Ultrabasic Melt and Estimation of its Concentration,” *Dokl. Akad. Nauk SSSR* 280 (2), 458–461 (1985).
17. **A. V. Sobolev**, “Melt Inclusions in Minerals as a Source of Principle Petrological Information,” *Petrologiya* 4 (3), 228–239 (1996) [*Petrology* 4, 209–220 (1996)].
18. **V. B. Naumov and G. B. Naumov**, “Mineral-Forming Fluids and Physicochemical Trends of Their Evolution,” *Geokhimiya*, No. 10, 1450–1460 (1980).
19. **L. Bailly, V. Bouchot, C. Beny, and J.-P. Milesi**, “Fluid Inclusion Study of Stibnite Using Infrared Microscopy: An Example from the Brouzils Antimony Deposit (Vendee, Armorican Massif, France),” *Econ. Geol.* 95 (1), 221–226 (2000).
20. **S. G. Hageman and V. Luders**, “P–T–X Conditions of Hydrothermal Fluids and Precipitation Mechanism of Stibnite-Gold Mineralization at the Wiluna Lode-Gold Deposits, Western Australia: Conventional and Infrared Microthermometric Constraints,” *Miner. Deposita* 38 (8), 936–952 (2003).
21. **K. Germann, V. Luders, D. A. Banks, et al.**, “Late Hercynian Polymetallic Vein-Type Base-Metal Mineralization in the Iberian Pyrite Belt: Fluid-Inclusion and Stable-Isotope Geochemistry (S–O–H–Cl),” *Miner. Deposita* 38 (8), 953–967 (2003).
22. **A. R. Campbell and S. Robinson-Cook**, “Infrared Fluid Inclusion Microthermometry on Coexisting Wolframite and Quartz,” *Econ. Geol.* 82 (6), 1640–1645 (1987).
23. **A. R. Campbell, S. Robinson-Cook, and C. Amindyas**, “Observation of Fluid Inclusions in Wolframite from Panasqueira, Portugal,” *Bull. Mineral.* 111 (3-4), 251–256 (1988).
24. **V. Luders**, “Contribution of Infrared Microscopy to Fluid Inclusions Studies in Some Opaque Minerals (Wolframite, Stibnite, Bournonite): Metallogenic Implications,” *Econ. Geol.* 91, 1462–1468 (1996).
25. **L. Bailly, L. Grancea, and K. Kouzmanov**, “Infrared Microthermometry and Chemistry of Wolframite from the Baia Sprie Epithermal Deposit, Romania,” *Econ. Geol.* 97 (2), 415–423 (2002).
26. **V. Luders, J. Gutzmer, and N. J. Beukes**, “Fluid Inclusion Studies in Cogenetic Hematite, Hausmannite, and Gangue Minerals from High-Grade Manganese Ores in the Kalahari Manganese Field, South Africa,” *Econ. Geol.* 94 (4), 589–596 (1999).
27. **V. Luders, R. L. Romer, A. R. Cabral, et al.**, “Genesis of Itabirite-Hosted Au–Pd–Pt-Bearing Hematite–(Quartz) Veins, Quadrilatero Ferrifero, Minas Gerais, Brazil: Constraints from Fluid Inclusion Infrared Microthermometry, Bulk Crush-Leach Analysis and U–Pb Systematics,” *Miner. Deposita* 40 (3), 289–306 (2005).
28. **D. P. Mancano and A. R. Campbell**, “Microthermometry of Enargite-Hosted Fluid Inclusions from the Lepanto, Philippines, High-Sulfidation Cu–Au Deposit,” *Geochim. Cosmochim. Acta* 59 (19), 3909–3916 (1995).
29. **V. Luders and M. Ziemann**, “Possibilities and Limits of Infrared Light Microthermometry Applied to Studies of Pyrite-Hosted Fluid Inclusions,” *Chem. Geol.* 154 (1–4), 169–178 (1999).
30. **K. Kouzmanov, L. Bailly, C. Ramboz, et al.**, “Morphology, Origin and Infrared Microthermometry of Fluid Inclusions in Pyrite from the Radka Epithermal Copper Deposit, Srednogorie Zone, Bulgaria,” *Miner. Deposita* 37 (6–7), 599–613 (2002).
31. **S. E. Lindaas, J. Kulis, and A. R. Campbell**, “Near-Infrared Observation and Microthermometry of Pyrite-Hosted Fluid Inclusions,” *Econ. Geol.* 97 (3), 603–618 (2002).
32. **V. Luders, B. Pracejus, and P. Halbach**, “Fluid Inclusion and Sulfur Isotope Studies in Probable Modern Analogue Kuroko-Type Ores from the JADE Hydrothermal Field (Central Okinawa Trough, Japan),” *Chem. Geol.* 173 (1–3), 45–58 (2001).

33. **V. B. Naumov and V. S. Kamenetskii**, "Silicate and Salt Melts in the Genesis of the Industrial Tin Deposit: Evidence from Inclusions in Minerals," *Geokhimiya*, No. 12, 1279–1289 (2006) [*Geochem. Int.* 44, 1181–1190 (2006)].
34. **V. S. Kamenetsky, V. B. Naumov, P. Davidson**, et al., "Immiscibility between Silicate Magmas and Aqueous Fluids: a Melt Inclusion Pursuit Into the Magmatic-Hydrothermal Transition in the Omsukchan Granite (NE Russia)," *Chem. Geol.* 210 (3–4), 73–90 (2004).
35. **V. B. Naumov and V. V. Shapenko**, "Fluid Inclusion Data on Iron Content in the High-Temperature Chloride Solutions," *Geokhimiya*, No. 2, 231–238 (1980).
36. **V. B. Naumov and N. E. Uchameishvili**, "Thermometric Study of Inclusions in Minerals of Magmatic Rocks of the Tyrnauz Area (North Caucasus)," *Geokhimiya*, No. 4, 525–532 (1977).
37. **G. A. Milovskii, B. F. Zlenko, and A. M. Gubanov**, "Formation Conditions of the Scheelite Ores of the Deposit of the Chorukh-Dairon Ore Field: Evidence from the Study of Gas-Liquid Inclusions," *Geokhimiya*, No. 1, 79–86 (1978).
38. **V. B. Naumov, A. Kh. Khakimov, and I. L. Khodakovskii**, "Solubility of Hydrocarbonic Acid in the Concentrated Solutions at High Temperatures and Pressures," *Geokhimiya*, No. 1, 45–55 (1974).
39. **A. I. Tugarinov and V. B. Naumov**, "Physicochemical Parameters of Hydrothermal Mineral Formation," *Geokhimiya*, No. 3, 259–265 (1972).
40. **G. B. Naumov and V. B. Naumov**, "Influence of Temperature and Pressure on Acidity of Endogenic Solutions and Staging of Ore Formation," *Geol. Rudn. Mestorozhd.*, No. 1, 13–23 (1977).
41. **V. B. Naumov and G. B. Naumov**, "Mineral-Forming Fluids and Physicochemical Trends of Their Evolution," *Geokhimiya*, No. 10, 1450–1460 (1980).
42. **I. P. Solovova, V. B. Naumov, V. I. Kovalenko**, et al., "History of the Formation of Spinel Lherzolite (Dreiser Weiher, W. Germany) on the Basis of Microinclusion Data," *Geokhimiya*, No. 10, 1400–1411 (1990).
43. **V. B. Naumov and V. I. Kovalenko**, "Characteristics of Major Volatiles of Natural Magmas and Metamorphic Fluids: Evidence from Fluid Inclusion Study," *Geokhimiya*, No. 5, 590–600 (1986).
44. **N. V. Berdnikov and V. S. Prikhod'ko**, "Hydrocarbonic Degassing of Alkali Basaltic Magmas," *Dokl. Akad. Nauk SSSR* 259 (3), 708–710 (1981).
45. **T. Andersen, S. Y. O'Reilly, and W. L. Griffin**, "The Trapped Fluid Phase in Upper Mantle Xenoliths from Victoria, Australia: Implications for Mantle Metasomatism," *Contrib. Mineral. Petrol.* 88, 72–85 (1984).
46. **R. G. Schwab and B. Freisleben**, "Fluid CO₂ Inclusions in Olivine and Pyroxene and Their Behaviour under High Pressure and Temperature Conditions," *Bull. Mineral.* 111 (3–4), 297–306 (1988).
47. **B. De Vivo, M. L. Frezzotti, A. Lima, and R. Trigila**, "Spinel Lherzolite Nodules from Oahu Island (Hawaii): A Fluid Inclusion Study," *Bull. Mineral.* 111 (3–4), 307–319 (1988).
48. **T. Andersen, H. Austrheim, and E. A. J. Burke**, "Fluid Inclusions in Granulites and Eclogites from the Bergen Arcs, Caledonides of W. Norway," *Mineral. Mag.* 54, 145–158 (1990).
49. **B. De Vivo, A. Lima, and V. Scribano**, "CO₂ Fluid Inclusions in Ultramafic Xenoliths from the Iblean Plateau, Sicily, Italy," *Mineral. Mag.* 54 (375), 183–194 (1990).
50. **T. H. Hansteen, T. Andersen, E.-R. Neumann, and H. Jelsma**, "Fluid and Silicate Glass Inclusions in Ultramafic and Mafic Xenoliths from Hierro, Canary Islands: Implications for Mantle Metasomatism," *Contrib. Mineral. Petrol.* 107, 242–254 (1991).

51. **N. L. Dobretsov, I. V. Ashchepkov, V. A. Simonov, and S. M. Zhmodik**, “Interaction of Upper Mantle Rocks with Deep-Seated Fluids and Melts of the Baikal Rift Zone,” *Geol. Geofiz.*, No. 5, 3–20 (1992).
52. **M. L. Frezzotti, E. A. J. Burke, B. De Vivo**, et al., “Mantle Fluids in Pyroxenite Nodules from Salt Lake Crater (Oahu, Hawaii),” *Eur. J. Mineral.* 4 (5), 1137–1153 (1992).
53. **P. Schiano and R. Clochiatti**, “Worldwide Occurrence of Silica-Rich Melts in Sub-Continental and Sub-Oceanic Mantle Minerals,” *Nature* 368, 621–624 (1994).
54. **P. Schiano, R. Clochiatti, N. Shimizu**, et al., “Cogenetic Silica-Rich and Carbonate-Rich Melts Trapped in Mantle Minerals in Kerguelen Ultramafic Xenoliths: Implications for Metasomatism in the Oceanic Upper Mantle,” *Earth Planet. Sci. Lett.* 123, 167–178 (1994).
55. **M. E. Varela, E. A. Bjerg, R. Clochiatti**, et al., “Fluid Inclusions in Upper Mantle Xenoliths from Northern Patagonia, Argentina: Evidence for an Upper Mantle Diapir,” *Mineral. Petrol.* 60, 145–164.
56. **T. H. Hansteen, A. Klugel, and H.-U. Schmincke**, “Multi-Stage Magma Ascent beneath the Canary Islands: Evidence from Fluid Inclusions,” *Contrib. Mineral. Petrol.* 132, 48–64 (1998).
57. **A. V. Golovin, V. V. Sharygin, and V. G. Mal’kovets**, “Melt Evolution during the Crystallization of the Bele Basanite Pipe (North Minusinks Depression),” *Geol. Geofiz.* 41 (12), 1760–1782 (2000).
58. **M. Santosh and T. Tsunogae**, “Extremely High Density Pure CO₂ Fluid Inclusions in a Garnet Granulite from Southern India,” *J. Geol.* 111, 1–16 (2003).
59. **M. Santosh, T. Tsunogae, and S.-I. Yoshikura**, “‘Ultra-high Density’ Carbonic Fluids in Ultra-high-Temperature Crustal Metamorphism,” *J. Mineral. Petrol. Sci.* 99(2004).
60. **M. Cuney, Y. Coulibaly, and M.-C. Boiron**, “High-Density Early CO₂ Fluids in the Ultra-high-Temperature Granulites of Ihouhaouene (In Ouzal, Algeria),” *Lithos* 96 (3–4), 402–414 (2007).
61. **V. B. Naumov and V. I. Kovalenko**, “Water Content and Pressure in Felsic Magmas: Evidence from Fluid Inclusion Study,” *Dokl. Akad. Nauk SSSR* 261 (6), 1417–1420 (1981).
62. **I. T. Bakumenko and O. N. Kosukhin**, “Water in Felsic Melt Inclusions,” *Dokl. Akad. Nauk SSSR* 234 (1), 164–167 (1977).
63. **V. B. Naumov**, “Determination of Concentration and Pressure of Volatiles in Magmatic Melts Based on Inclusions in Minerals,” *Geokhimiya*, No. 7, 997–1007 (1979).
64. **V. B. Naumov, V. I. Kovalenko, R. Clochiatti, and I. P. Solovova**, “Crystallization Parameters and Phase Composition of Melt Inclusions in Quartz of Ongonites,” *Geokhimiya*, No. 4, 451–464 (1984).
65. **V. B. Naumov, I. P. Solovova, V. I. Kovalenko, and I. D. Ryabchikov**, “Fluid Inclusion Data on Composition and Concentration of Fluid Phase and Water Content in the Pantellerite and Ongonite Melts,” *Dokl. Akad. Nauk SSSR* 295 (2), 456–459 (1987).
66. **V. B. Naumov, I. P. Solovova, V. A. Kovalenker**, et al., “First Data on High-Density Fluid Inclusions of the Magmatic Water in the Rhyolite Phenocrysts,” *Dokl. Akad. Nauk SSSR* 318 (1), 187–190 (1991).
67. **G. M. Tsareva, V. I. Kovalenko, V. B. Naumov**, et al., “Melt Inclusions in High-Density Aqueous Phase in Quartz of the Spor Mountain Rare-Metal Topaz Rhyolites (USA),” *Dokl. Akad. Nauk SSSR* 314 (3), 694–697 (1990).
68. **G. M. Tsareva, V. B. Naumov, V. I. Kovalenko**, et al., “Melt Inclusion Data on the Composition and Crystallization Conditions of the Spor Mountain Topaz Rhyolites (USA),” *Geokhimiya*, No. 10, 1453–1462 (1991).
69. **V. B. Naumov, I. P. Solovova, V. A. Kovalenker**, et al., “Magmatic Water at Pressures of 15–17 Kbar and Its Concentration in the Melt: First Inclusion Data on Plagioclase Andesites,” *Dokl. Akad. Nauk SSSR* 324 (3), 654–658 (1992).

70. **M. L. Frezzotti**, “Magmatic Immiscibility and Fluid Phase Evolution in the Mount Genis Granite (Southeastern Sardinia, Italy),” *Geochim. Cosmochim. Acta* 56, 21–33 (1992).
71. **V. B. Naumov, V. A. Kovalenker, V. L. Rusinov, and N. N. Kononkova**, “High-Density Fluid Inclusions of Magmatic Water in Phenocrysts of Acid Volcanics from Petrologiya 2 (5), 480–494 (1994).
72. **V. B. Naumov, M. L. Tolstykh, V. A. Kovalenker, and N. N. Kononkova**, “Fluid Overpressure in Andesite Melts from Central Slovakia: Evidence from Inclusions in Minerals,” *Petrologiya* 4 (3), 283–294 (1996) [*Petrology* 4, 265–276 (1996)].
73. **P. Davidson and V. S. Kamenetsky**, “Primary Aqueous Fluids in Rhyolitic Magmas: Melt Inclusion Evidence for Pre- and Post-Trapping Exsolution,” *Chem. Geol.* 237, 372–383 (2007).
74. **S. Wallier, R. Rey, K. Kouzmanov, et al.**, “Magmatic Fluids in the Breccia-Hosted Epithermal Au–Ag Deposit of Rosia Montana, Romania,” *Econ. Geol.* 101 (5), 923–954 (2006).
75. **V. B. Naumov, V. I. Kovalenko, and V. A. Dorofeeva**, “Magmatic Volatile Components and Their Role in the Formation of Ore-Forming Fluids,” *Geol. Rudn. Mestorozhd.* 39 (6), 520–529 (1997) [*Geol. Ore Dep.* 39, 451–460 (1997)].
76. **V. B. Naumov and G. F. Ivanova**, “On Relation of Rare-Metal Mineralization with Felsic Magmatism: Evidence from the Study of Mineral Inclusions,” *Geol. Rudn. Mestorozhd.* 22 (3), 95–103 (1980).
77. **V. B. Naumov and G. F. Ivanova**, “Geochemical Criteria of Genetic Relation of Rare-Metal Mineralization with Acid Magmatism,” *Geokhimiya*, No. 6, 791–804 (1984).
78. **I. P. Kushnarev**, *Depth of the Formation of Endogenic Ore Deposits* (Nedra, Moscow, 1982) [in Russian].
79. **V. B. Naumov, Yu. G. Safonov, and O. F. Mironova**, “Some Tendencies in Spatial Variations of the Fluid Parameters of the Kolar Gold-Bearing Deposit (India),” *Geol. Rudn. Mestorozhd.* 30 (6), 105–109 (1988).
80. **V. B. Naumov and G. F. Ivanova**, “Barometrical Characterization of the Formation of Tungsten Deposits,” *Geokhimiya*, No. 6, 627–641 (1971).
81. **V. B. Naumov, G. F. Ivanova, and Z. M. Motorina**, “Formation Conditions of Tungsten, Tin–Tungsten, and Molybdenum–Tungsten Deposits,” in *Main Parameters of Natural Processes of Endogenic Ore Formation* (Nauka, Novosibirsk, 1979), Vol. 2, pp. 53–62 [in Russian].
82. **V. Yu. Prokof’ev, V. B. Naumov, G. F. Ivanova, and N. I. Savel’eva**, “Study of Fluid Inclusions in the Cryolite and Siderite of the Ivigtut Deposit (Greenland),”
83. *Geokhimiya*, No. 12, 1783–1788 (1990).
84. **V. Yu. Prokof’ev, V. B. Naumov, G. F. Ivanova, and N. I. Savel’eva**, “Fluid Inclusion Studies in Cryolite and Siderite of the Ivigtut Deposit (Greenland),” *Neues Jahrb. Mineral. Monatsh.*, No. 1, 32–38 (1991).
85. **V. B. Naumov and G. F. Ivanova**, “P–T Conditions of Fluorite Crystallization at Tungsten Deposits,” *Geokhimiya*, No. 3, 387–400 (1975).
86. **E. I. Sergeeva, V. B. Naumov, and I. L. Khodakovskii**, “Formation Conditions of Arsenic Sulfide at Hydrothermal Deposits,” in *Geochemistry of Hydrothermal Ore Formation* (Nauka, Moscow, 1971), pp. 210–222 [in Russian].
87. **I. A. Baksheev, V. Yu. Prokof’ev, and V. I. Ustinov**, “Genesis of Metasomatic Rocks and Mineralized Veins at the Berezovskoe Deposit, Central Urals: Evidence from Fluid Inclusions and Stable Isotopes,” *Geochem. Int.* 39 (Suppl. 2), 129–144 (2001).

88. **V. B. Naumov, V. S. Kamenetskii, R. Thomas**, et al., “Inclusions of Silicate and Sulfate Melts in Chrome Diopside from the Inagli Deposit, Yakutia, Russia,” *Geokhimiya*, No. 6, 603–614 (2008) [*Geochem. Int.* 46 554–564 (2008)].
89. **V. V. Shapenko**, “Genetic Features of Tungsten Mineralization of the Dzhida Ore Field (Southwestern Transbaikalia),” *Geol. Rudn. Mestorozhd.*, No. 5, 18–29 (1982).
90. **V. B. Naumov and B. N. Naumenko**, “Formation Conditions of the Svetloe Tin–Tungsten Deposit (Chukotka),” *Geol. Rudn. Mestorozhd.*, No. 5, 84–92 (1979).
91. **G. F. Ivanova, V. B. Naumov, V. S. Karpukhina, and E. V. Cherkasova**, “Genesis of Rare-Metal (W, Mo, Sn, and Be) Mineralization in Southeastern Mongolia: Geochemical Features and Physicochemical Parameters,” *Geokhimiya*, No. 8, 834–845 (2002) [*Geochem. Int.* 40, 751–761 (2002)].
92. **V. A. Kovalenker, V. B. Naumov, V. Yu. Prokof'ev**, et al., “Compositions of Magmatic Melts and Evolution of Mineral-Forming Fluids in the Banska Stiavnica Epithermal Au–Ag–Pb–Zn Deposit, Slovakia: A Study of Inclusions in Minerals,” *Geokhimiya*, No. 2, 141–160 (2006) [*Geochem. Int.* 44, 118–136 (2006)].
93. **V. B. Naumov**, “Possibility of Determination of Pressure and Density of Mineral-Forming Media Based on Mineral Inclusions,” in *Studying Inclusions in Minerals in Application to the Exploration and Study of Ore Deposits* (Nedra, Moscow, 1982), pp. 85–94 [in Russian].
94. **R. C. Murray**, “Hydrocarbon Fluid Inclusions in Quartz,” *Am. Assoc. Petrol. Geol. Bull.* 41 (5), 950–952 (1957).
95. **R. Goguel**, “Die Chemische Zusammensetzung der in den Mineralen Einiger Granite und Ihrer Pegmatite ein Geschlossenen Gaz und Flussigkeiten,” *Geochim. Cosmochim. Acta* 27 (2), 155–181 (1963).
96. **J.-L. Zimmermann**, “Etude par Spectrometrie de Masse des Fluids Occlus dans Quelques Echantillons de Quartz,” *C. R. Acad. Sci.* 263 (5), 461–464 (1966).
97. **V. A. Kalyuzhnyi, I. M. Svoren', and E. L. Platonova**, “Composition of Gas–Fluid Inclusions and Problems of Hydrogen Discovery in Them: Results of Mass-Spectrometric Chemical Analysis,” *Dokl. Akad. Nauk SSSR* 219 (4), 973–976 (1974).
98. **I. Bonev and N. B. Piperov**, “Precipitation of Ores, Boiling, and Vertical Interval of Lead–Zinc Mineralization in the Madan Ore Field,” *Geologica Balcanica*, Sofia 7 (4) (1977).
99. **D. I. Norman and F. J. Sawkins**, “The Tribag Breccia Pipes: Precambrian Cu–Mo Deposits, Batchawana Bay, Ontario,” *Econ. Geol.* 80 (6), 1593–1621 (1985).
100. **J. N. Moore, D. I. Norman, and B. M. Kennedy**, “Fluid Inclusion Gas Compositions from an Active Magmatic-Hydrothermal System: A Case Study of the Geysers Geothermal Field, USA,” *Chem. Geol.* 173 (1–3), 3–30 (2001).
101. **F. Q. Yang, J. W. Mao, Y. T. Wang**, et al., “Geology and Metalogenesis of the Sawayaerdunn Gold Deposit in the Southwestern Xinjiang, China,” *Resour. Geol.* 57 (1), 57–75 (2007).
102. **M. M. Elinson**, “Methods of Extraction and Study of Gas and Liquid from Mineral Inclusions,” in *Mineralogical Thermometry and Barometry* (Nauka, Moscow, 1968), pp. 23–31 [in Russian].
103. **K. A. Kvenvolden and E. Roedder**, “Fluid Inclusions in Quartz Crystals from South-West-Africa,” *Geochim. Cosmochim. Acta* 35, 1209–1229 (1971).
104. **O. F. Mironova**, “Gas-Chromatographic Analysis of Inclusions in Minerals,” *Zh. Analyt. Khim.* 28 (8), 1561–1564 (1973).
105. **O. F. Mironova, V. B. Naumov, and A. N. Salazkin**, “Nitrogen in Mineral-Forming Fluids. Gas-Chromatographic Determination during Studying Inclusions in Minerals,” *Geokhimiya*, No. 7, 979–992 (1992).
106. **C.-J. Bray and E. T. C. Spooner**, “Fluid Inclusion Volatile Analysis by Gas Chromatography with Photoionization/ Microthermal Conductivity Detectors:

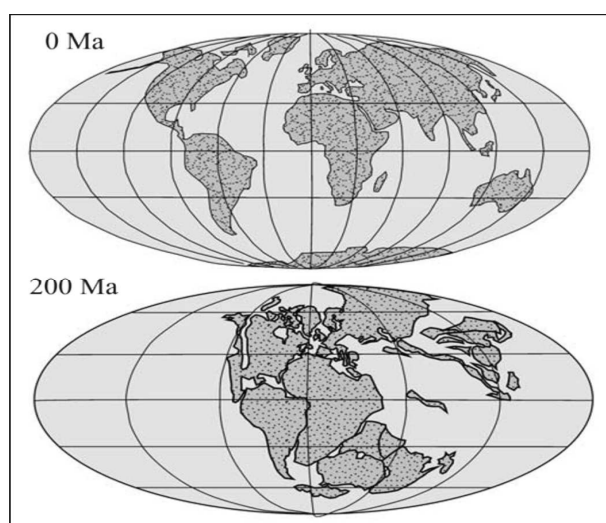
- Applicationsto Magmatic MoS₂ and Other H₂O–CO₂ and H₂O–CH₄ Fluids,” *Geochim. Cosmochim. Acta* 56, 261–272 (1992).
107. **T. Graupner, U. Kempe, E. T. C. Spooner**, et al., “Microthermometric, Laser Raman Spectroscopic, and Volatile-Ion Chromatographic Analysis of Hydrothermal Fluids in the Paleozoic Muruntau Au-Bearing Quartz Vein Ore Field, Uzbekistan,” *Econ. Geol.* 96 (1), 1–23 (2001).
108. **I. N. Maslova**, “Ultramicrochemical Study of Composition of Liquid and Gas Phase in Two-Phase Inclusions from Quartz of Volhynia,” *Geokhimiya*, No. 2, 169–173(1961).
109. **Yu. A. Dolgov and N. A. Shugurova**, “Compositional Study of Individual Gas Inclusions,” in *Materials on Genetic and Experimental Mineralogy* (Nauka, Novosibirsk, 1966), Vol. 4, pp. 173–181 [in Russian].
110. **G. J. Rosasco and E. Roedder**, “Application of a New Laser-Excited Raman Spectrometer to Nondestructive Analysis of Sulfate in Individual Phases in Fluid Inclusions in Minerals,” in *Proceedings of 25th International Geological Congress, Canberra, Australia, 1976* (Canberra, 1976), Vol. 3, pp. 812–813.
111. **N. Guilhaumou, P. Dhamelincourt, J.-C. Touray, and J. Barbillat**, “Analyse a la Microsonde a Effet Raman d’Inclusions Gazeuses du Systeme N₂–CO₂,” *C. R. Acad. Sci.* 287 (15), 1317–1319 (1978).
112. **P. Dhamelincourt, J.-M. Beny, J. Dubessy, and B. Poty**, “Analyse d’Inclusions Fluids a la Microsonde MOLE a Effet Raman,” *Bull. Mineral.* 102 (5–6), 600–610 (1979).
113. **V. B. Naumov, M. V. Akhmanova, A. V. Sobolev, and P. Dhamelincourt**, “Application of Laser Raman–Microprobe in Study of Gas Phase of Inclusions in Minerals,” *Geokhimiya*, No. 7, 1027–1034 (1986).
114. **J. Konnerup-Madsen, J. Dubessy, and J. Rose-Hansen**, “Combined Raman Microprobe Spectrometry and Microthermometry of Fluid Inclusions in Minerals from Igneous Rocks of the Gardar Province (South Greenland),” *Lithos* 18 (4), 271–280 (1985).
115. **M. Nishizawa, Y. Sano, Y. Ueno, and S. Maruyama**, “Speciation and Isotope Ratios of Nitrogen in Fluid Inclusions from Seafloor Deposits at ~3.5 Ga,” *Mar. Geol.* 254 (3–4), 332–344 (2007).
116. **A. S. Borisenko, A. A. Borovikov, L. M. Zhitova, and G. G. Pavlova**, “Composition of Magmatogenic Fluids and Factors of their Geochemical Specialization and Metal Potential,” *Geol. Geofiz.* 47 (12), 1308–1325 (2006).

The Recent Supercontinent in the Northern Hemisphere of the Earth (North Pangea): Magmatic and Geodynamic Evolution

Kovalenko V. I., Yarmolyuk V. V., and Bogatikov O. A.

*Institute of Geology of Ore Deposits, Petrography, Mineralogy, and Geochemistry,
Russian Academy of Sciences, Staromonetnyi per. 35, Moscow, 119017 Russia;
e-mail: yarm@igem.ru*

Spatially united continental associations that differ from ordinary continents only in size are referred to as supercontinents. Unfortunately, we failed to find a clear and justified definition for the term “supercontinent” in the literature, and that is why we will use in this work the above-mentioned simple definition. If it is true, then all features of continents, except their sizes, are retained in supercontinents as well. Evidently, the main feature of such global structural elements of the Earth is the presence of the continental crust in them. With the understanding that the supercontinent Pangea, which was ascertained by A. Wegener and which incorporated almost all principal continents, was the last supercontinent on the Earth and incorporated nearly all the main continents that existed at the boundary between the Paleozoic and the Mesozoic, we should introduce one more constraint on the term “supercontinent”: precisely, incorporation of the majority of continents. This follows from the fact that, according to [1], Pangea did not incorporate such continents as Amuria, North and South China, Malaysia, and other smaller continental blocks separated from Pangea by the Tethys and Paleotethys oceans (Fig. 1a). Hence, it should be accepted that supercontinents incorporate most of the continental blocks, but not necessarily all of them.



In the present-day structure of the Earth's lithosphere, considerable fragments of Pangea turned out to be interrelated in one way or another. This is true of the set of continents (Fig. 1) that unites Eurasia, North and South America, and Africa. Only Australia and Antarctica appear to be separated from this part of Pangea.

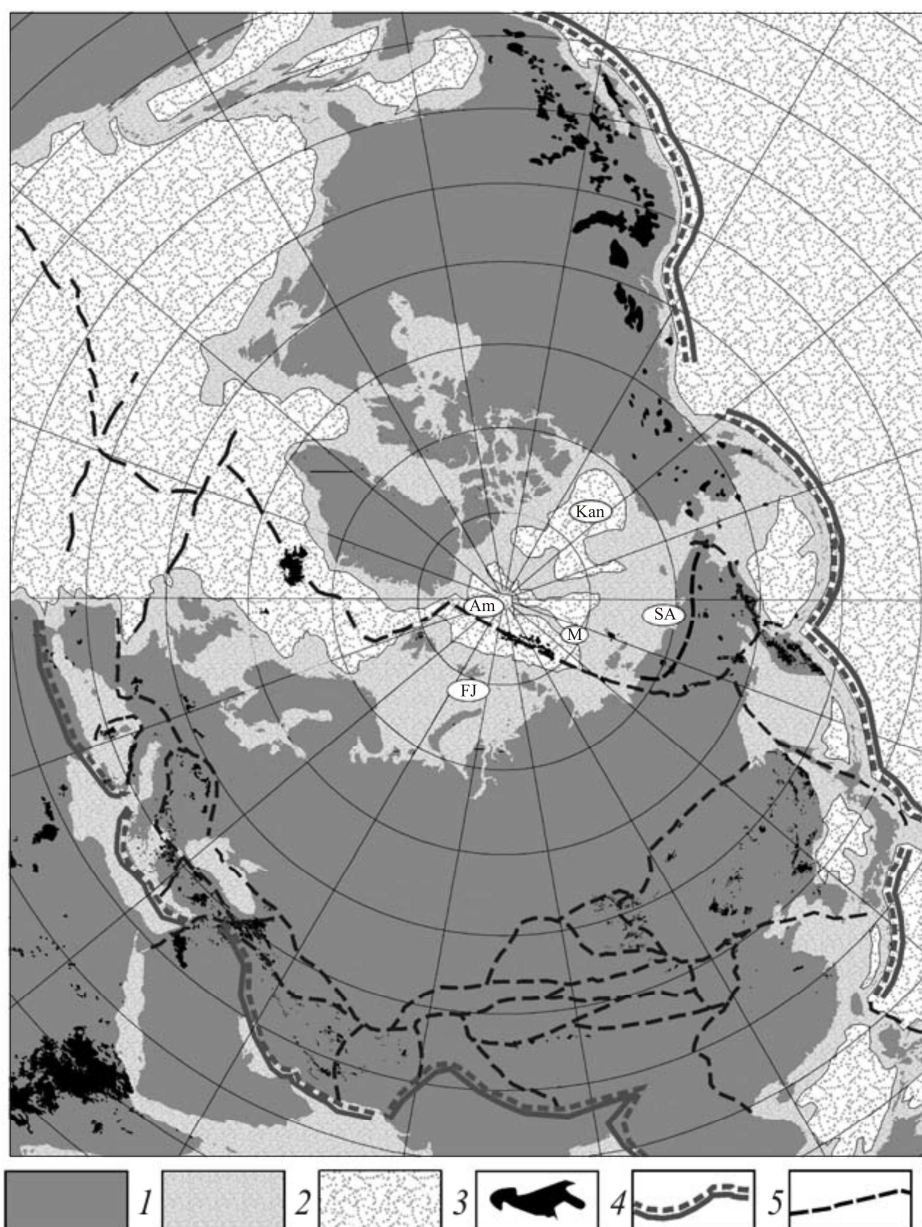
Fig. 1. Position of continents on the modern surface of the Earth (0 Ma) and in the Pangea structure (200 Ma ago)[1].

One may find an answer to the question whether these spatially close Pangea fragments can be attributed to a recent continent, first of all, from the structure of the Pangea northern part and especially the Arctic region [2–6], since even the above-mentioned continental blocks such as Amuria, North and South China, and others not incorporated into the Pangea structure, have amalgamated with Eurasia at present.

Figure 2 demonstrates the map of spatial distribution of the continental and oceanic crusts, as well as manifestation of recent volcanism [7] on the territory of the Northern Hemisphere. The map clearly fixes the prevalence of the continental crust in these spatially contiguous remains of the late Paleozoic Pangea. In the region of contiguous continents, the oceanic crust occupies a limited space, probably, in areas of the Canada Basin (the oceanic crust formed there in the Cretaceous [8]) and Amerasian Basin representing a prolongation of the Atlantic Ocean. In this connection, the continental area of the Northern Hemisphere can be regarded as a retained northern part of Pangea, which is under destruction on the side of the Atlantic Ocean (expansion of the Atlantic to the Arctic regions, according to the terminology suggested by Yu.M. Pushcharovskii [4] and E.V. Shepilov [6]). However, Fig. 2 also shows that the generation of the Atlantic and its oceanic crust changed only the shape and structure of the supercontinent as due to separation of Eurasia and America these continents amalgamated in the region of the Chukchi Peninsula and Alaska. Therefore, this part of Pangea has retained all features of a supercontinent up to the present. Let us consider this inference in detail in light of the geodynamic and magmatic evolution of North Pangea.

During the formation of Pangea, collision of numerous terranes at the base of Western Siberia from Spitsbergen to the eastern boundary of the Laptev Sea resulted in consolidation of the Arctic shelf as a single continental block by the Middle Triassic. In that epoch, a vast shallow-water continental basin with numerous islands separated by rifts with an intense manifestation of trap volcanism occupied the place of the Arctic Ocean [8]. The South Anyui Sea, the lithosphere of which was subducted under eastern Eurasia in the Early Cretaceous and from which only the South Anyui suture zone remained, was the only sea basin with oceanic crust which separated the Eurasian and North American plates and which joined the Pacific Ocean [8].

The Canadian abyssal basin, which is a constituent of the Amerasian Basin, opened in the Early Cretaceous in the Arctic region, and the Franz Josef major volcanic plateau is generated. The plateau is related in time to Cretaceous vast dike belts and volcanics in Canadian Arctic Islands and Greenland, which are referred to the high Arctic large igneous province (HALIP) [9, 10]. Reconstructed for the moment prior to disintegration of Greenland, Svalbard, and Franz Josef Land, the center of these radial dike belts is located on the northeastern edge of Queen



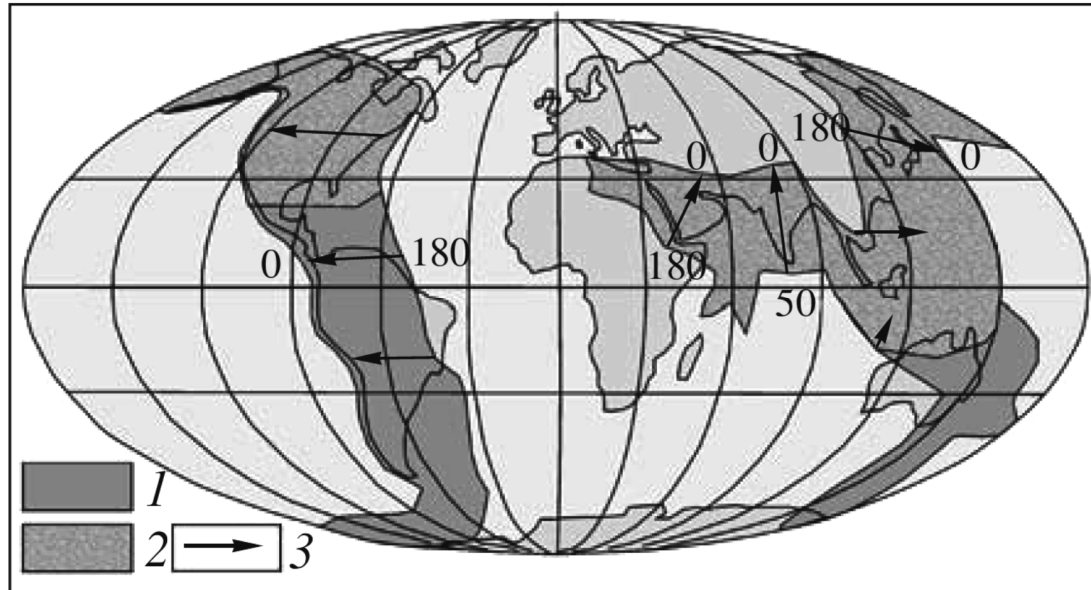
Elizabeth Island and is related to the mantle plume effect. According to preliminary data, these dike belts formed in the Cretaceous and Tertiary. At nearly the same time, the Makarov Basin opened with spreading in the axial part and

Fig. 2. Lay-out scheme for continents of the Northern Hemisphere (pole view).

(1, 2) Continental plates: (1) continents, (2) shelf of continents; (3) oceanic plates; (4) areas of late Cenozoic magmatism; (5) convergent plate boundaries; (6) microplate boundaries. Structures of the Arctic Basin: (Can) Canada Basin, (Am) Amerasian Basin, (M) Makarov Basin, (FJ) Franz Josef Islands, (SA) South Anyui Suture.

subduction in its eastern part, which were accompanied by island-arc volcanism. According to N.A. Bogdanov's data [8], the Alpha-Mendelev volcanic plateau originated above the subduction zone at the end of the Cretaceous, and intraplate basic rocks formed on the continental shelf of Eurasia, Hyperborean dome (De-Longa Dome [11]), in the Arctic

Archipelago, and in the region of Cape Washington (northern Greenland). In the Paleocene, about 53 Ma ago, the spreading in the Gakkel Ridge set in, and the Eurasian oceanic basin opened [12]. The basin with MOR-type tholeiitic basite volcanism has been under spreading



with a low rate through the present time. Figures 2 and 3 demonstrate that the geodynamic position of North Pangea is determined by two differently directed processes:

Fig. 3. Calculations for plate burial for the last 180 Ma, after [13].

(1) Subducted plates; (2) the same, subducted under Eurasia; (3) vectors and linear values for lithospheric plate motion. The origin of arrows shows a trench edge at the onset of convergence, the end of arrows shows its modern position. Numerals denote the time interval (Ma) for plate motions. According to reconstructions, trenches migrated towards the Pacific Ocean, and within the Tethys, northwards.

subduction of lithospheric plates on the west (on the side of the Pacific Ocean), south (on the side of India and the Arabian Peninsula), and southwest (on the side of the Mediterranean Sea) which results in consolidation of Laurasia, and spreading of oceanic plates on the side of the Atlantic Ocean, which results in the wedging of the supercontinent.

Subduction processes are not typical for the Arctic part of the supercontinent, and the geodynamics of active areas of the Arctic part is close to local spreading.

When comparing the northern and southern parts of Wegener's Pangea, we should infer a weakness of even local spreading in the northern part of this supercontinent compared to its southern part in the course of the evolution from the late Paleozoic to the present (Fig. 1), especially when the now-predominant continental part of the Arctic Ocean is considered. In the southern part of Pangea, practically all present-day continents separated during that time (Figs. 1, 3). In the northern part of Pangea, the Gakkel Ridge originated only in the Cenozoic on the

extension of the Mid-Atlantic Ridge (MAR) as a result of the above-mentioned Atlantic “expansion” into the Arctic region, which, in the opinion of some researchers, is likely to lead in the future to a similar, like in southern Pangea, breakage of North America and Eurasia. The breakage is not occurring at the moment, and the effects of rifting in the Arctic region are of local rather than global nature. This was, in particular, emphasized in [6] and noted that rifting and spreading in the Arctic region were of incomplete nature with numerous “jumps-over” of the spreading axes. Distinctions in the geodynamics of North and South Pangea seem to indicate a general retention of the supercontinent nature of North Pangea that is possible only in the case of a relatively cold (and heavier) asthenosphere and mantle in general, in the area of which lithospheric plates have remained like in a trap during the time interval from the late Paleozoic to the present. As many researchers have shown, these areas are located in zones of lowering of the geoid surface. In this case, unaccomplished rifting in the Arctic region accompanied by spreading represents a reflection of local “breaks” of the hot mantle through the predominant cold mantle. Such a “break-through” of the hot mantle to the Arctic region is likely to have global consequences only on the side of the Atlantic (Fig. 3), and the rest of the hot mantle plumes caused by subduction were “suppressed.” In general, the Cenozoic history of the Arctic region is more akin to the last stages of the evolution of supercontinents [14], and the Arctic Ocean itself represents an intracontinental sedimentary basin typical of a developed supercontinent [14]. The formation of basins with the oceanic crust within it, and the connection of them first (in the Cretaceous) with the Pacific Ocean and later (in the Cenozoic) with the Atlantic Ocean, the separation of North America and Greenland are indications of the local breakage of this supercontinent which did not result in the prevalence of spreading (the Atlantic tendency) over compression (the Pacific tendency). Data on the episodic manifestation of the breakage in the Arctic part of the supercontinent can probably be related to the presence of the mantle plume in its base, the activity of which was most likely suppressed by subduction on Laurasia boundaries. Such an assumption follows from ideas presented in [15], according to which zones of lithospheric breakage are formed between mantle plumes. This suggests the occurrence of such an Arctic plume near the eastern flank of the Gakkel Ridge. The occurrence of this plume in the region of the De-Longa Rise is highly probable [11]. This inference is in good agreement with the distribution of recent high-alkaline volcanics in the Arctic region. The rocks occur in continental areas along the Gakkel Ridge margins beyond the sphere of the spreading center effect just as analogous rocks have formed along margins of the Red Sea and Gulf of Aden, which are opening above the Afar plume.

The model of generation of recent volcanism in the Arctic region resides in shorthand form in the following (Fig. 4). Subduction of lithospheric plates under Eurasia (and its different parts), as well as under North America (Fig. 3) resulted in

its collision with the continents of India, Africa, and Arabia and the formation of numerous microplates along their boundaries (Fig. 2). Due to stability of subduction processes over hundreds of millions of years, a great volume of the hot mantle material accumulated under the continent. The processes initiated a compensated removal of the hot mantle material near convergent plate boundaries and caused the appearance of numerous mantle plumes, with sources of basite and alkaline magmas within convergent boundaries of Eurasia (in the Far East and within the Alpine–Himalayan belt) [7]. Since the time of the break-up of Pangea, which little affected the supercontinent part located in the Northern Hemisphere (North Pangea), a sea basin began forming in the place of the Arctic Ocean with

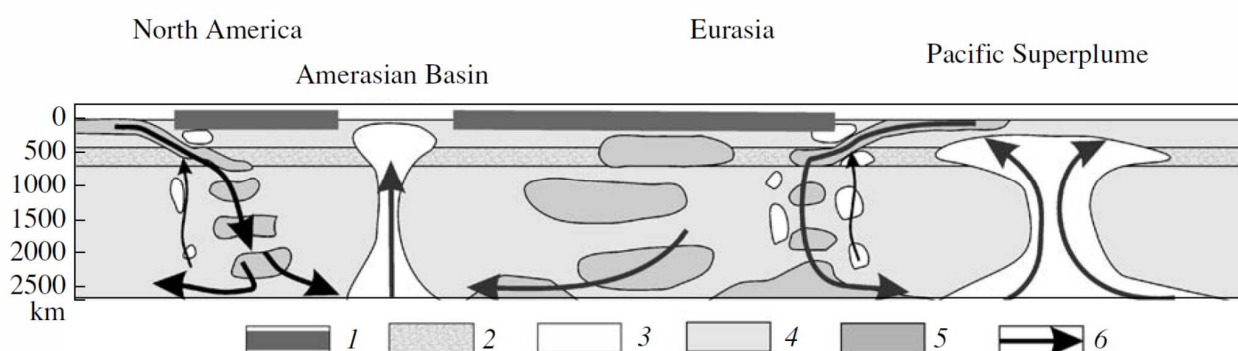


Fig. 4. Model of geodynamic processes resulting in the formation of the North Pangea supercontinent.

(1) Continental lithosphere; (2) transitional mantle layer; (3) hot (low-velocity) mantle; (4) standard mantle; (5) subducted lithosphere and cold (high-velocity)

generation of the oceanic crust in the Cretaceous and the Cenozoic. The generation of the oceanic crust of the Cenozoic Arctic Basin is likely to fix the breakage of the supercontinent of the Northern Hemisphere under the effect of mantle plumes evolving in the course of their migration northwards from the central Atlantic region (the Iceland, Jan Mayen, and probable Arctic plumes).

Such a long retention (over 200 Ma) of the tectonic stability in Laurasia and the supercontinent status of North Pangea is most likely determined by subduction processes along its boundaries (Figs. 2, 3). The processes inhibit major breakages of the lithosphere in this part of the Earth as they cause the compression regime within it. The supercontinent volume is built up along these convergent boundaries (Fig. 4), and long-term stable subduction of lithospheric plates under Eurasia and North America resulted in accumulation of cold lithospheric material and cessation of hot mantle convection in the interior of the region (Fig. 4). It is likely that these processes suppressed the activity of the mantle plume which has been active in the polar region of the Earth since the terminal

Triassic right up to the present time and regularly forced its way toward the Earth's surface.

ACKNOWLEDGMENTS

This work was supported by the Russian Foundation for Basic Research, project nos. 08-05-00347 and 0805-00472, and Program 16 of the Presidium of the Russian Academy of Sciences.

REFERENCES

1. **Scotese C. R.** Paleogeographic Atlas. Univ. Texas, Arlington (TX) (1997).
2. **Pushcharovskii Yu. M., Mossakovskii A. A., and Ruzhentsev S. V.** Dokl. Akad. Nauk 364 (1), 88–91 (1999). [Dokl. 364 (1), 9–12 (1999)].
3. **Pushcharovskii Yu. M., Melankholina E. N., Mossakovskii A. A., et al.** Dokl. Akad. Nauk 366 (1), 88–99 (1999) [Dokl. 366 (4), 447–451 (1999)].
4. **Pushcharovskii Yu. M.** Geotektonika, No. 1, 3–12 (2002) [Geotectonics 36 (1), 1–11 (2002)].
5. **Gramberg I. S.** Geotektonika, No. 6, 3–19 (2001) [Geo tectonics 35 (6), 423–438 (2001)].
6. **Shipilov E. I.** Geotektonika, No. 2, 1–23 (2008) [Geo Geotectonics 42 (2), 105–125 (2008)].
7. Recent volcanism in North Eurasia: Consistent Patterns of Development, Volcanic Hazard, Relationship with Underground Processes and Changes in the Environment and Climate. Changes in the Environment and Climate: Natural Catastrophes and Technogenic Catastrophes Caused by These Changes, Ed. by V. I. Kovalenko, V.V.Yarmolyuk, and O.A. Bogatikov (IGEM Ros. Akad. Nauk, Moscow, 2008) [in Russian].
8. **Bogdanov N. A.**, Geotektonika, No. 3, 13–30 (2004) [Geotectonics 38 (3), 166–182 (2004)].
9. **Maher H. D., Jr.**, J. Geol.109, 91 (2001).
10. **Buchan K. L. and Ernst R. E.**, The High Arctic Large Igneous Province (HALIP). Evidence for an Associated Giant Radiating Dyke Swarm. www.largeigneousprovinces.org/LOM.html.
11. **Filatova N. I. and Khain V. E.**, Geotectonics 41 (3), 171–195 (2007) [Geotektonika, No. 3, 3–29 (2007)].
12. **Glebovskii V. Yu., Kaminskii V. D., Minakov A. N., et al.**, Geotectonics 40 (4), 263–282 (2006) [Geotektonika, No. 4, 21–42 (2006)].
13. **Lithgow-Bertelloni C. and Richards M. A.**, Rev. Geophys. 36 (1), c78 (1998).
14. **Maruyama S.**, J. Geol. Soc. Jap. 100, 24–49 (1994).
15. **Burke K. and Dewey J. F.**, J. Geol. 81, 406–433 (1973).

Composition and thermal structure of mantle beneath the Western Part of Congo-Kasai craton according to xenocrysts from Angola kimberlites.

Ashchepkov I.V.¹, Rotman A.Y.², Nossyko S.⁴, Somov S.V.², Shimupi J.⁵, Vladykin N.V.³, Palessky S.V.¹, Saprykin A.I.¹, Khmelnikova O.S.¹.

¹ *Institute of Geology and Mineralogy, SD RAS Novosibirsk 630090, Russia;*

² *Central Science and Research Geology And Prospecting Institute Of The Stock Company "ALROSA", Chernyshevsky Str,7, Mirny, 678170 Russian Federation;*

³ *Institute of Geochemistry SD RAS, Favorsky str. 1a, Irkutsk, 66403;*

⁴ *Mining-Ore Association, SCatoca Angola;*

⁵ *Endiama Co. (Angolan Government).*

ABSTRACT

Three pipes from the Angola- South West of Congo-Kasai craton Caquele, Camitongo 1 and 2 reveal close mineralogy of the xenocrysts of the deep-seated mantle minerals: garnets clinopyroxenes and ilmenites.

PT estimates reveal also close geothermal condition ~37 - 40 mvm-2, slightly higher then the determined for the biggest pipe in the World Catoca locate data the same region. But this is lower then thermal gradients beneath South Africa kimberlites which may be explained by higher thickness of the subcratonic lithospheric mantle(SCLM) beneath Congo-Kasai craton (to 400 km) then beneath Kaapvaal craton 250- 300 км.

The layering and major horizons the 5-9 is close for Camitongo 1-2 pipes as well as the mantle lithology despite on close general mineralogy. The heating in the basement from 75 up to 55 kbar is a general feature of the mantle lithosphere beneath this kimberlite pipes.

Mantle columns have individual geochemical features of the minerals suggesting pervasive metasomatism from the lower part of mantle. Caquelle CPx patterns reveal lherzolitic REE are LILE – enriched with the Ba peaks due to Plh melting while Camitongo 1-2 show Ta-Nb enrichments possibly due to interactions with the protokimberlites and Pb dips.

Ilmenite trend tracing the mantle column from bottom up to shallow mantle evolve to Fe- ilmenites and correlates with the abundance of the clinopyroxenes enriched in Fe in the mantle as well as the abundance of TREE in ilmenite due to AFC differentiation.

INTRODUCTION

Africa kimberlites are the most investigated for the [35] nevertheless the information about the some large kimberlite fields like in Angola is rather scarce [10,51]. Largest in the World and less eroded kimberlite pipes like Catoca [17, 41, 53] that were found in Angola are of the great interest not only for the prospecting and industrial geologist but for the petrologists because it is the most modern and

representative information about the composition of the upper mantle in the Central Africa [27, 53] which is studied less then in Kaapvaal craton [18, 23, 30, 31, 34, 36] and other parts of Africa continent. Congo - Kasai craton have the most deep root in the Africa to 400 km [38] as the other such craton may have another thermal regime more typical for those with deep roots like Slave [5] or Siberian craton.

GEOGRAPHIC LOCATION

Kimberlites from Angola [16] are distributed on the vast territory of the Congo –Kasai craton. Most of them are located in NE-SW belt. Some kimberlites fields and form separate groups scattered in Western part of Angola in 50-150 km from the coast. In this paper we give some information for the kimberlites from Camitongo (8 57' 00 'S - 19 08'E) ~ 250 km from Luanda and Caquele (12° 7' 0S, - 14° 6' 60E) ~250 SE from Luanda. The largest in the World kimberlite pipe Catoca (10° 9' 0S -14° 55' 0E) is located at the same meridian as previous 200 to the south.

SAMPLES.

All the data were obtained from the mineral concentrate – natural from the laterite soil and the drilling samples. Climatic conditions in Angola allow only several minerals to be preserved in the kimberlite matrix. We used garnet, ilmenites and clinopyroxenes to recognize the variation of geochemistry and major elements. The grains used had the typical dimensions 0.5-1 mm and some larger grains and intergrowths were taken as the microxenoliths to determine the associations. The grains were mostly taken from the sandy tuff kimberlites. All of them are rounded most likely during the eruption when they were in the hot explosion cloud.

ANALYTICAL METHODS

From each pipes about 100- 150 grains of the each type of the minerals were taken. The populations for the analyzed grains in each concentrate exceed 700. After the estimations of the variations for major components the representative varieties were analyzed by LAM ICP method.

All the analyses were obtained in the Analytic Centre IGM SB RAS. The EPMA data were determined by OS Khmelnikova and on the Camebax Micro mass spectrometer. With the 20 mv acceleration voltage and 15 ma in epoxy mounts of the polishes mineral grains ~500 -600 in each cassette.

The LAM ICP data were obtained on Finnegan Element mass spectrometer with the Nd UV laser on Laserprobe. The laser diameter does not exceed 10-20 microns with the scanning of the surface – 30 scans for samples. The concentration 33 trace elements were determined using 2- 3 isotopes for the most complicated elements (48 isotopes together) and compared to chose better values. The scanning time for the

Table 1.

Major and trace element composition of the minerals from the concentrate of Caquele pipe Angola. Caquele pipe.

Component Mineral	caq104 Ilm	caqD104 Cr-Dl	caqD53 Cr-dlDl	caqD35 Cr-dlDl	kaK94 Garnet	kaK92 Garnet	cG57 Garnet	cG55 Garnet	cG56 Garnet	cG54 Garnet	cG132 Garnet	Zirc	Zirc
SiO2		55.01	55.55	55.42	41.74	40.49	41.33	41.62	41.63	42.43	42.4	31.92	32.01
TiO2	46.18	0.32	0.28	0.33	0.05	0.25	0.05	0.16	1.01	0.68	0.97	1.04	1.04
Al2O3	0.55	3.31	2.18	2.03	20.39	12.98	19.4	18.24	15.85	20.05	17.78	0	0.007
Cr2O3	0.44	3.08	0.95	1.12	5.89	13.31	5.49	6.34	7.68	2.78	6.74	66.04	66.09
FeO	45.49	3.24	3.72	3.61	7.89	6.99	8.97	8.99	7.98	7.28	7.49	0	0
MnO	0.2	0	0	0.35	0.35	0.24	0.38	0	0	0	0.24	0	0
MgO	6.95	14.3	17.82	18.13	20.98	18.5	18.27	18.02	17.78	21.25	20.11	0	0
CaO		16.78	17.51	18.21	2.95	6.46	5.37	5.79	7.14	4.59	5.06	0.016	0.038
Na2O		3.89	1.91	2	0.11	0.11	0.11	0.05	0.1	0.09	0.11	0	0.39
K2O		0.03	0.04	0.03	0.05	0.05	0.05	0	0	0.01	0.05		
NiO	0.21	0.05	0.05	0.08				0.02	0.05	0.02		1.29	
Total	100.02	100.01	100.01	100.96	100.2	99.38	99.42	99.23	99.22	99.18	99.17	99.035	99.575
Ba	147.7	2154	2.286	302	0.677	0.358	1.834	0.569	7.284	1.072	1.03	26.39	55.05
La	2.175	6.381	4.49	0.528	0.037	0.053	0.046	0.045	0.072	0.132	0.068	0.061	0.343
Ce	6.366	23.3	16.81	1.128	0.294	0.514	0.327	0.263	0.319	0.39	0.52	0.84	0.688
Pr	1.277	4.233	3.131	0.207	0.108	0.178	0.11	0.1	0.103	0.139	0.18	0.07	0.07
Nd	6.863	21.44	16.2	1.466	1.182	1.772	1.356	2.304	1.002	1.37	1.702	0.505	0.26
Sm	1.986	5.813	4.435	0.695	0.865	1.438	0.88	0.632	0.722	1.207	1.559	1.151	0.737
Eu	0.593	1.909	1.246	0.221	0.463	0.615	0.404	0.199	0.363	0.574	0.673	0.51	0.191
Gd	1.967	5.601	3.984	0.733	2.009	2.795	2.034	0.696	1.602	2.92	3.293	2.795	1.114
Th	0.268	0.715	0.492	0.115	0.411	0.541	0.41	0.089	0.34	0.627	0.748	0.738	0.361
Dy	1.367	3.975	2.769	0.828	3.278	4.343	3.472	0.571	2.79	5.211	6.349	8.255	4.25
Ho	0.219	0.601	0.39	0.143	0.723	0.877	0.731	0.113	0.614	1.177	1.405	2.16	1.306
Er	0.482	1.307	0.874	0.41	2	2.486	2.28	0.366	1.919	3.685	4.586	8.217	5.519
Tm	0.066	0.144	0.091	0.058	0.302	0.375	0.344	0.073	0.299	0.579	0.699	1.557	1.027
Yb	0.288	0.769	0.44	0.48	2.101	2.45	2.203	0.548	2.011	3.731	4.807	13.88	7.409
Lu	0.031	0.092	0.055	0.101	0.327	0.362	0.342	0.115	0.322	0.617	0.778	1.886	1.389
Hf	1.041	17.02	3.257	0.226	1.426	2.614	1.769	0.618	1.285	2.578	3.428	1926	634.6
Ta	0.244	0.253	0.086	0.078	0.022	0.012	0.025	0.043	0.027	0.037	0.045	2.332	1.75
Pb	1.579	1.2	1.148	0.554	0.305	0.378	0.376	0.592	0.256	0.696	0.441	1.22	2.043
Th	0.012	0.601	0.122	0.144	0.025	0.008	0.024	0.047	0.021	0.018	0.032	4.456	3.585
U	0.012	0.219	0.013	0.356	0.009	0.007	0.014	0.073	0.02	0.01	0.015	12.69	8.902
Sc	16.93	127	41.99	104.2	75.58	68.04	65.05	103.8	69.24	94.21	96.68	177.1	80.19
V	154.1	681.7	360.4	132.6	156.1	161.7	144.5	181.6	148.9	199.4	204.1	1.046	0.221
Co	23.42	47.35	41.96	23.82	30.74	26.25	28.54	20.82	30	37.23	41.11	0.02	0.239
Cu		14.72	32.86	23.77	4.627	5.166	7.318	9.487	3.635	6.388	13.01	5.069	23.12
Ni	263.2	376.7	277.7	77.78	77.61	80.5	75.25	14.17	78.28	102.2	95.51	0.443	14.44
Rb	0.485	20.96	0.068	1.544	0.04	0.04	0.047	0.118	0.323	0.058	0.057	0.221	0.277
Sr	99.49	399.7	201.6	8.379	0.423	0.542	0.547	0.247	0.729	0.667	1.464	0.583	2.655
Y	5.448	13.84	9.217	3.892	18.46	23.24	19.2	2.994	15.23	29.89	36.06	54.46	35.81
Zr	7.073	11.12	19.81	5.806	25.77	42.41	27.91	10.32	22.08	40.62	52.51	35540	8717
Nb	1.179	4.61	0.359	0.776	0.166	0.096	0.194	0.077	0.222	0.249	0.524	2.356	2.353
Cs	0.01	0.123	0.004	0.083	0.003	7E-04	0.004	0.002	0.009	0.005	0.004	0.007	0.011

Table 2.

Camitongo 1 pipe.

Component	cam1g22	cam1g23	cam1g24	cam1g26	cam1f25	cam1f26	cam1f27	cam1f28	cam1f30	cam1f31	cam1f96	cam1f97	cam1f98
Mineral	Garnet	Garnet	Garnet	Garnet	Cr-dBi	Cr-dDi	Cr-dDi	Cr-dDi	Cr-dDi	Cr-Di	Ilm	Ilm	Ilm
SiO2	41.09	40.64	41.43	40.97	53.78	53.52	54.32	56.25	54.97	54.75	50.99	52.96	49.31
TiO2	0.23	0.16	0.06	0.05	0.10	0.07	0.22	0.20	0.18	0.13	0.32	0.23	0.39
Al2O3	19.91	18.59	19.74	18.83	2.34	3.16	2.91	2.96	1.64	0.86	0.018	0.11	1.16
Cr2O3	4.19	6.02	4.69	5.96	2.58	3.14	1.24	1.97	2.90	2.31	1.00	36.74	36.56
FeO	6.86	7.72	8.82	8.18	2.56	2.41	2.77	2.63	2.13	3.04	0.40	1.01	1.39
MnO	0.29	0.33	0.38	0.35							9.30	8.18	10.16
MgO	20.66	20.13	18.96	18.76	15.79	15.61	15.66	15.61	15.27	15.05			
CaO	4.95	4.60	4.55	5.73	17.49	16.71	17.69	18.54	19.36	20.34			
Na2O	0.05	0.06	0.06	0.03	3.43	3.81	3.23	2.95	2.41	1.93			
K2O	0.00	0.00	0.01	0.00	0.01	0.01	0.02	0.00	0.01	0.03			
NiO	0.09	0.08	0.06	0.07	0.10	0.13	0.12	0.10	0.15	0.11			
Total	98.32	98.33	98.76	98.94	98.17	98.57	98.18	99.60	99.02	8.55	0.09	0.09	0.08
Ba	0.017	0.021	0.026	0.189	0.203	0.179	4.188	1.321	0.716	0.457	96.89	99.31	99.06
La	0.012	0.004	0.004	0.046	1.047	4.59	3.55	1.79	29.07	14.94	0.002	0.006	0.016
Ce	0.084	0.059	0.047	0.085	3.56	12.5	11.1	5.735	81.27	43.01	0.004	0.006	0.027
Pr	0.084	0.026	0.019	0.082	0.718	2.183	2.226	1.057	12.08	5.867	0.006	0.0006	0.002
Nd	0.308	0.29	0.181	0.339	3.637	10.57	11.77	4.876	52.58	23.2	0.013	0.01	0.009
Sm	0.314	0.248	0.162	0.254	1.05	3.106	3.196	1.253	9.439	3.176	0.002	0.008	0.004
Eu	0.176	0.125	0.078	0.139	0.322	0.821	1.002	0.391	2.586	0.796	0.0007	0.002	0.002
Gd	0.753	0.47	0.361	0.563	0.898	1.83	3.166	1.181	7.078	2.016	0.003	0.008	0.006
Tb	0.126	0.098	0.068	0.107	0.12	0.112	0.401	0.148	0.697	0.22	0.0008	0.001	0.0006
Dy	1.042	0.653	0.601	0.81	0.729	0.393	2.318	0.801	3.341	1.174	0.003	0.006	0.003
Ho	0.232	0.137	0.142	0.137	0.102	0.043	0.359	0.146	0.429	0.169	0.0009	0.001	0.0007
Er	0.71	0.379	0.429	0.382	0.225	0.072	0.741	0.326	0.726	0.323	0.002	0.004	0.003
Tm	0.112	0.069	0.069	0.053	0.032	0.007	0.087	0.041	0.072	0.034	0.001	0.002	0.0004
Yb	0.701	0.505	0.474	0.347	0.153	0.03	0.427	0.19	0.294	0.149	0.003	0.004	0.006
Lu	0.125	0.082	0.066	0.049	0.016	0.004	0.046	0.027	0.031	0.019	0.001	0.001	0.002
Hf	0.162	0.149	0.25	0.393	0.278	2.769	6.91	0.384	3.739	3.73	8.838	5.901	4.493
Ta	0.005	0.008	0.005	0.006	0.004	0.03	0.084	0.016	0.203	0.012	69.28	61.64	27.76
Pb	0.012	0.023	0.025	0.011	0.084	0.459	0.239	0.142	1.409	0.981	0.011	0.136	0.011
Th	0.004	0.001	0.001	0.002	0.01	0.144	0.184	0.026	0.453	0.329	4E-04	0.014	1E-04
U	0.007	0.003	0.002	0.003	0.002	0.039	0.029	0.008	0.056	0.094	0.028	0.02	0.013
Sc	32.35	29.68	26.04	31.75	9.123	44.53	56.37	14.19	57.18	40.24	7.099	6.171	3.069
V	51.97	67.9	56.82	70.77	109.3	424.5	445.6	134.2	554.3	623.4	431.5	302.8	214
Co	12.7	12.45	11.12	10.33	19.43	11.93	24.83	27.59	23.36	30.55	19.73	17.65	12.8
Cu	0.247	0.511	0.32	0.421	2.382	0.346	1.096	3.545	0.379	1.083	2.604	3.138	2.272
Ni	10.86	17.25	17.04	19.8	250.3	188.9	351.9	381.3	388.8	180.6	15.43	19.07	14.76
Rb	0.057	0.053	0.099	0.022	0.017	0.033	0.58	0.059	0.106	0.061	0.067	0.074	0.119
Sr	0.081	0.106	0.056	0.122	66.25	185.4	185.1	92.24	734.1	456.3	0.023	0.144	0.023
Y	6.193	3.992	3.541	4.131	2.566	1.028	8.139	3.302	9.579	3.482	0.003	0.01	0.005
Zr	5.236	3.761	5.04	7.762	1.988	24.33	47.12	3.444	68.48	33.34	115.6	90.23	75.05
Nb	0.036	0.043	0.033	0.052	0.079	0.214	1.212	0.691	1.312	0.337	534.2	498.6	267.1
Cs	0.001	0.001	0.002	0.001	7E-04	8E-05	0.009	0.003	0.004	0.004	0.002	0.002	0.004

Camitongo 2 pipe.

Table 3.

Component Mineral	cam23 Garnet	cam2G4 Garnet	cam25 Garnet	cam26 Garnet	cam2G7 Garnet	cam2G8 Garnet	cam29 Garnet	cam210 Garnet	cam211 Cr-Di	cam22 Cr-Di	cam23 Cr-Di	cam24 Cr-Di	cam215 Ilm	cam217 Ilm	cam2115 Ilm	cam21 Zircon	cam22 Zircon
SiO2	41.98	42.55	42.77	41.72	42.17	42.06	41.98	42.71	54.39	54.36	54.32	54.31	43.74	45.84	46.95	32.91	32.85
TiO2	0.91	0.07	0.01	0.5	0.76	0.07	0.31	0.07	0.47	0.29	0.28	0.53	0.07	0.74	0.15	0.805	0.485
Al2O3	17.22	21.27	21.11	18.02	21.49	19.34	20.47	19.03	3.17	2.5	2.16	3.22	3.99	0.4	1.71	0.004	0.004
Cr2O3	7.11	3.16	6.16	7.23	1.49	6.01	3.34	6.07	0.27	2.52	3.81	1.01	43.91	42.85	40	65.12	65.24
FeO	6.65	8.28	6.67	6.76	8.87	6.87	7.1	6.99	5.93	2.75	2.43	3.8	0.21	0.21	0.5	0	0
MnO	20.45	19.65	21.1	19.91	21.3	20.1	21.37	20.36	16.22	14.41	14.37	17.13	6.44	8.93	11.37	0.009	0
MgO	5.09	4.67	3.47	5.4	4.21	5.57	4.66	5.62	15.94	19.03	17.73	15.5				0.011	0.017
CaO	0.13	0.05	0.03	0.09	0.12	0.03	0.07	0.03	2.42	2.75	3.07	2.55				0.012	0.074
K2O	0.01	0	0.02	0	0	0	0	0.01	0.03	0.01	0.04	0.02					
NiO	99.89	99.25	101.65	99.98	101.68	100.41	100.58	101.29	99	98.73	98.31	98.19	0.08	0.08	0.08	98.871	98.666
Total	1.225	0.048	0.095	16.9	0.004	0.008	0.109	1.774	0.372	0.109	0.342	30.53	98.55	99.05	100.79	14.17	0.041
Ba	0.284	0.004	0.008	25.3	0.003	0.004	0.091	0.091	22.5	2.212	2.371	26.84	0.066	0.066	0.281	0.472	0.006
La	1.497	0.034	0.081	68.43	0.013	0.027	1E-04	0.183	63.25	8.511	7.619	79.76	0.046	0.008	0.135	17.81	0.836
Ce	0.11	0.013	0.029	11.13	0.007	0.014	7E-04	0.035	10.42	1.949	1.323	13.79	0.003	0.005	0.013	0.361	0.035
Pr	0.648	0.209	0.302	50.8	0.127	0.19	0.002	0.375	50.14	11.53	6.588	66	0.021	0.011	0.019	2.428	0.449
Nd	1.007	0.739	0.557	11.23	0.32	0.327	0.059	0.37	9.738	3.864	1.744	13.65	0.024	0.011	0.019	1.308	1.269
Sm	0.379	0.161	0.177	2.988	0.121	0.133	0.008	0.134	2.674	1.182	0.505	3.656	0.003	0.003	3E-04	0.453	0.495
Eu	2.409	0.371	0.715	8.609	0.517	0.486	0.005	0.675	7.394	3.718	1.377	10.32	0.008	0.008	0.012	1.883	2.607
Gd	0.659	0.069	0.166	1.001	0.091	0.084	0.002	0.145	0.93	0.465	0.172	1.177	0.001	0.002	0.002	0.367	0.705
Tb	7.475	0.505	1.534	5.51	0.674	0.622	0.002	1.404	5.332	2.444	0.816	6.114	0.006	0.004	0.005	3.045	7.578
Dy	1.962	0.125	0.39	0.824	0.17	0.129	0.0009	0.336	0.819	0.334	0.112	0.628	0.002	0.003	0.001	0.849	2.129
Ho	6.94	0.366	1.258	2.015	0.559	0.471	0.006	1.078	2.128	0.734	0.219	1.768	0.004	0.002	0.002	2.816	8.796
Er	1.244	0.063	0.176	0.248	0.106	0.078	0.0004	0.192	0.273	0.077	0.025	0.209	0.002	0.0005	0.0008	0.52	1.609
Tm	9.972	0.445	1.017	1.435	0.767	0.63	0.0008	1.263	1.794	0.386	0.128	1.071	0.006	0.011	0.003	4.869	15.19
Yb	1.254	0.077	0.142	0.198	0.144	0.116	3E-04	0.218	0.258	0.043	0.015	0.137	8E-04	0.002	0.001	0.632	2.198
Lu	31.44	0.232	0.654	5.414	0.248	0.275	0.028	0.345	3.131	4.589	0.572	10.09	2.852	2.533	6.578	27.98	22.94
Ta	2.862	0.002	0.007	0.397	0.003	0.004	9E-04	0.007	0.429	0.175	0.014	0.11	26.16	87.79	100.2	0.739	1.585
Pb	0.772	0.029	0.048	0.985	0.018	0.015	0.011	0.032	0.773	0.2	0.221	1.154	0.013	0.034	0.023	0.201	0.817
Th	7.948	0.002	0.006	0.475	0.002	0.002	0.011	0.012	0.215	0.027	0.02	0.59	7E-04	0.002	5E-04	1.324	6.092
U	14.49	0.004	0.011	0.069	0.002	0.004	0.0002	0.014	0.028	0.011	0.003	0.13	0.01	0.009	0.034	3.891	16.58
Sc	265.7	34.66	26.81	106.8	29.1	46.77	0.188	55.46	100.9	42.16	19.04	131.8	4.98	5.004	8.576	273.9	302.8
V	0.456	51.82	64.89	470.1	58.31	77.05	0.134	83.01	415.3	396.3	189.1	548.6	185.1	236.2	183.7	3.511	0.112
Co	11.04	11.04	11.04	16.03	12.42	13.34	0.129	15.13	13.93	28.47	23.19	14.64	25.9	24.91	13.15	1.365	0.277
Cu	0.443	0.132	0.501	0.414	0.077	0.172	0.009	0.217	0.406	1.511	2.633	0.994	6.302	3.771	1.809	1.326	1.156
Ni	1.395	7.305	23.12	272	3.825	5.572	0.542	7.548	260.3	116.1	398.2	212.2	100.6	100.6	14.68	0.253	0.328
Rb	0.015	0.034	0.0001	0.367	0.043	0.078	0.042	0.149	0.126	0.05	0.027	0.275	0.008	0.001	0.003	4.778	0.101
Sr	0.491	0.063	0.153	688.2	0.036	0.05	0.021	0.755	707.5	207.9	131.5	902.6	0.058	0.033	0.116	4.778	0.101
Y	51.27	3.019	9.837	21.86	4.55	3.986	0.001	8.904	22.17	8.193	2.772	20.16	4E-04	0.007	0.007	23.27	57.18
Zr	72803	3.789	11.04	97.69	3.419	5.609	0.002	8.053	67.29	89.15	4.923	79.48	36.48	36.79	97.9	69571	71444
Nb	3.755	0.247	0.042	2.556	0.026	0.025	0.002	0.099	1.515	0.786	0.153	1.716	179.6	648.9	802.2	0.897	1.283
Cs	0.004	0.002	0.003	0.005	0.002	6E-04	0.002	0.002	0.002	6E-04	0.073	0.003	3E-04	9E-04	0.003	0.002	0.078

Notes: Analyses were made in Analytical Center of UIGGM SB RAS, Novosibirsk. Major components are determined by CamebaxMicro (O.S. Khmelnikova, January, 2003). Trace elements are determined using ICP MS "ELEMENT" (Finnigan) with laser UV LaserProbe (S.V. Palesky, A.I. Saprykin).

each grain do not exceed 3 minutes. Analyst of the LAM ICP analyses

Palessky S.V., establishment and developing of the method in IGM SB RAS - A.I.Saprykin.

MAJOR ELEMENT CHEMISTRY OF THE MINERALS

Garnets from the kimberlite pipes of Angola [17, 43] reveal rather unusual compositions. Most of the compositional variation concentrate within the Iherzolite field at Cr₂O₃-CaO discriminant diagram [47, 49] reaching 14 %Cr₂O₃ for those from Caquele and Camitongo kimberlite pipe (Fig.1). This is high comparing to the variations from Chicuatite, Chikolongo, Palue, Viniaty and Ochinjau pipes from the NE zone [16] traced by kimberlites. Deviation to the harzburgite field [13, 19, 23, and 47] was found only starting from 12% of Cr₂O₃ and several points of sub-calcium garnets were found within the 5-7%Cr₂O₃ interval. For Camitongo 1 kimberlite pipe the major trend is restricted by 10%Cr₂O₃ which is close to those found for garnets from Catoca [50]. The later largest and most productive Catoca pipe [14] (under the exploration) reveal a large amount of the harburgitic and dunitic garnets constituting about half of the whole population. Eclogitic garnets [24, 29] are more typical for Camtingo 2 pipe then for Camitongo1 and then for Caquele pipes.

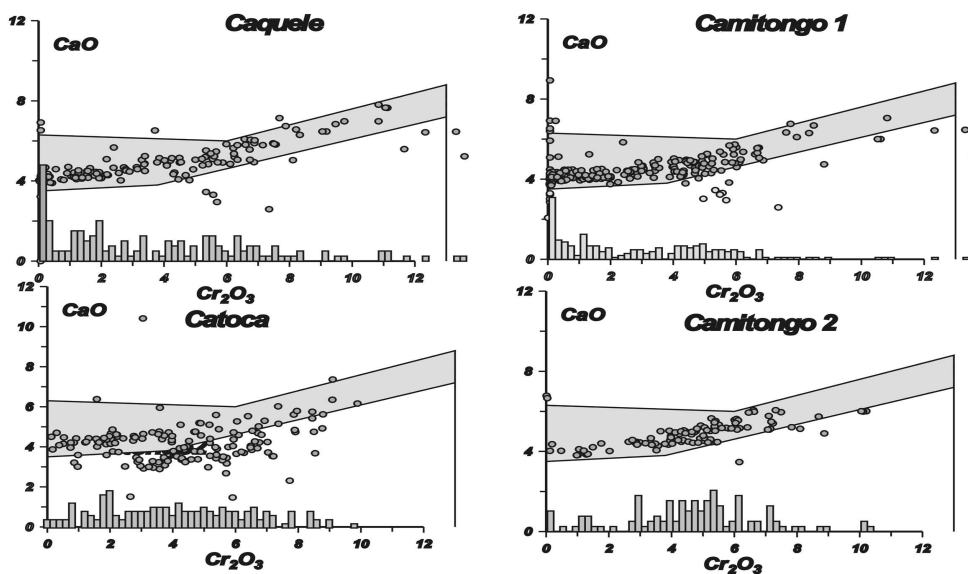


Fig. 1. Discrimination diagram for the Garnets from Angola pipes Caquele, Camitongo 1, Camitongo 2, Catoca.

Clinopyroxenes. in the concentrate of the three studied pipes are similar and in the variation diagram are nearly overlapping but the amount of the separate groups in each pipe highly differs. One can recognize three major groups of clinopyroxenes (Fig.2).

Most of the typical Cr- diopsides with 2-3% FeO are correspondent to the compositions that are found at the middle part of the lithospheric mantle sections worldwide [35, 47]. They are relatively low in Al₂O₃ content from 0.5 to 4%. The TiO₂ concentration rise with the FeO content and Cr₂O₃ decrease but the most Fe-rich compositions are divided from the main trend by the break. Fe enriched varieties of clinopyroxenes may be subdivided into three groups according to Al₂O₃ content. Minor part of the Ti-low compositions with the high sodium content refer to typical eclogites plotting in the Group B - C field in MgO-Na₂O diagram. Some of them (C) are typical omphacites with 7% Na₂O and 10-12% Al₂O₃. The pipe Camitongo 1 containing less Cr- garnets is characterized by the higher Al content of the Fe- rich pyroxenes close to eclogitic ones. An opposite in Caquele pipe with the relatively scarce eclogitic garnets in the concentrate the practically do not contain typical omphacites [15, 32] or close compositions. It possibly means that more deep interval is composed from the hot garnet- low pyroxenites that do not refer to the so called eclogites A – though are plotted in this field.

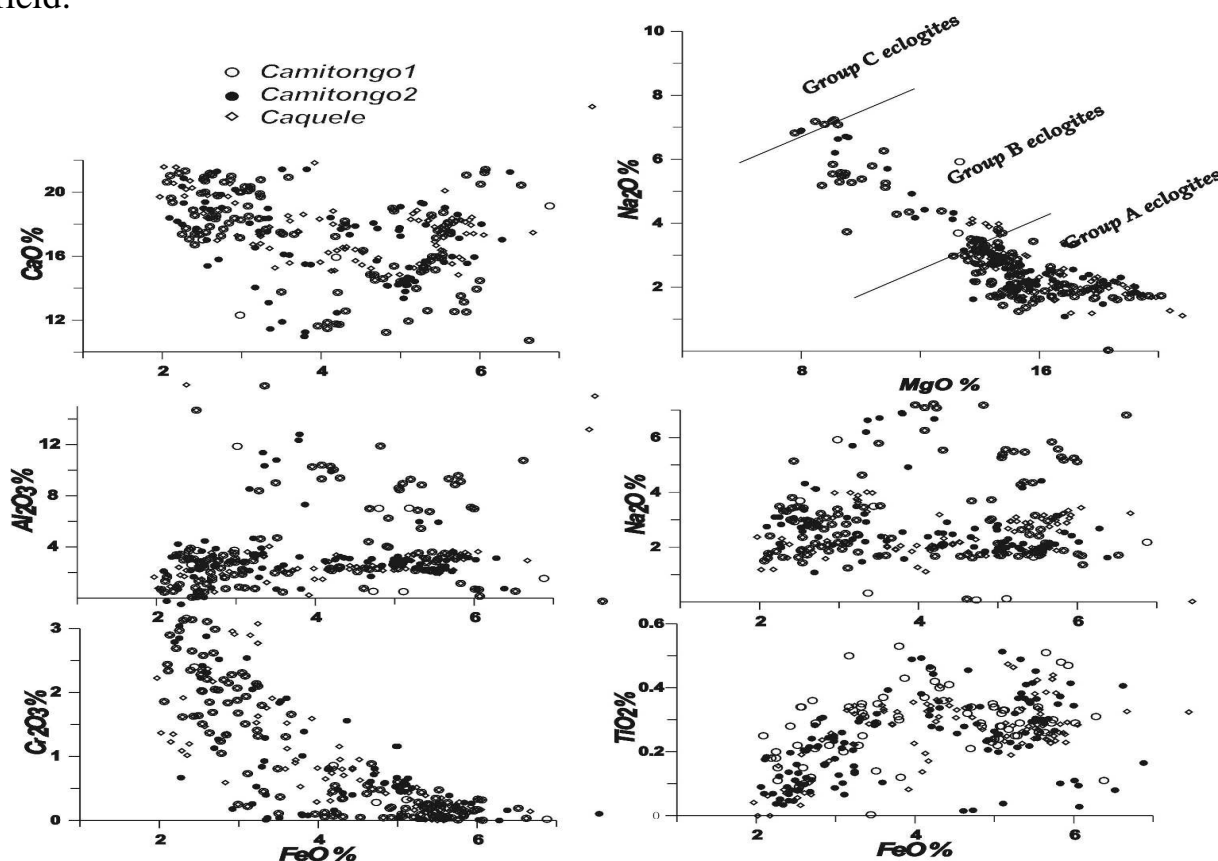


Fig. 2. Variation diagram for the Clinopyroxenes from Angola pipes: Caquele, Camitongo 1, Camitongo 2.

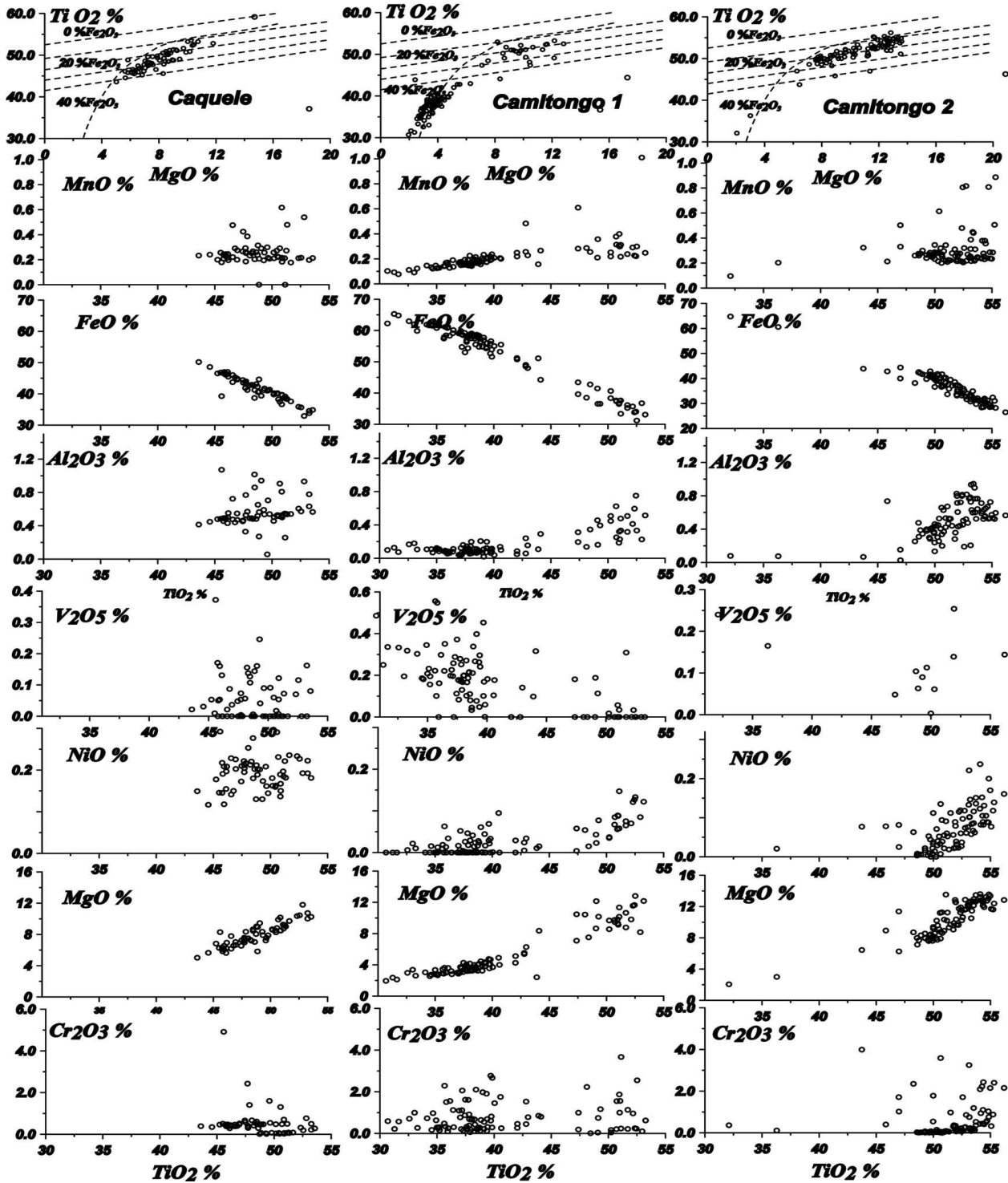


Fig. 3. Variation diagram for the microilmenites from Angola pipes: Caquile, Camitongo 1, Camitongo 2.

The most ferriferous (to 8%FeO) and Cr-low with the high TiO₂ content are close to the pigeonite compositions but with relatively high Na₂O content (2-4%). In CaO component decrease together with FeO rise which is an indication the hot

interaction with Fe- rich magma with peridotites.

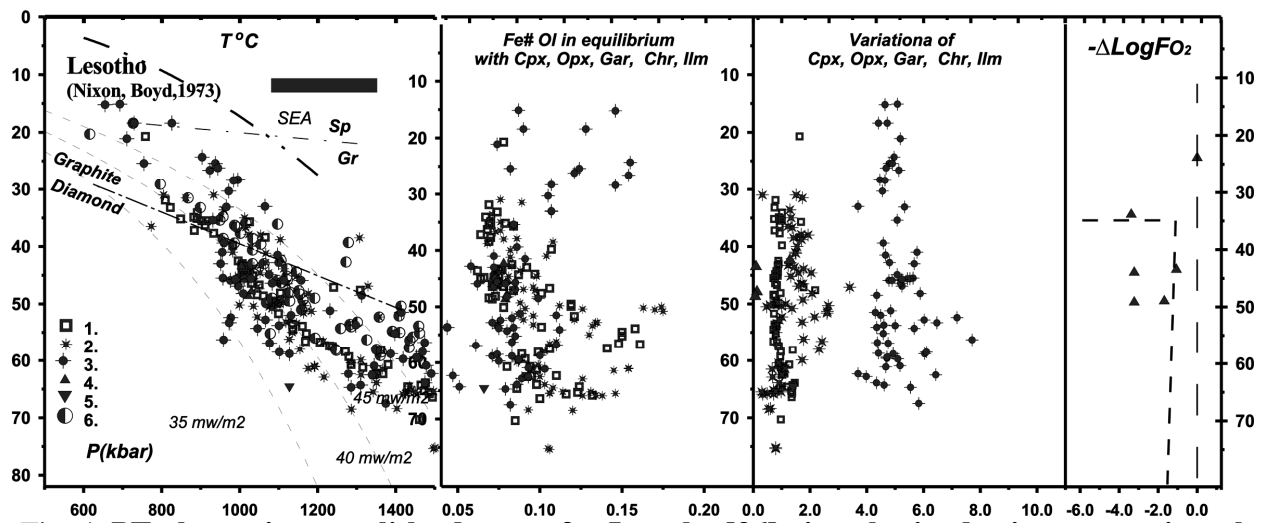


Fig. 4. PT plots using xenoliths data set for Lesotho [36] pipe obtained using monomineral thermobarometry.

1. orthopyroxene: $T^{\circ}\text{C}$ [12] - P (kbar) [28]. 3. clinopyroxene: $T^{\circ}\text{C}$ [33 corrected] - P kbar [3]; Garnet: $T^{\circ}\text{C}$ [26], monomineral- P (kbar) [2]; 4. chromite: $T^{\circ}\text{C}$ (O'Neil,Wall,1987 , monomineral MT)- P (kbar) (Ashchepkov, Vishnyakova 2006,Chr); 5. ilmenite: $T^{\circ}\text{C}$ [52]- P (kbar)(Ashchepkov, Vishnyakova 2006, Ilm); 6. $T^{\circ}\text{C}$ and P (kbar) [12].

Rare richterite amphiboles were met in the concentrate from Camitongo 1 pipe.

Ilmenites from these three pipes have diverse compositions overlapping only partly in high MgO field. At the variation diagram TiO_2 - MgO - FeO they display typical fractionation trends [22, 30, 31] but the minor components reveal the more complicated trends and origin. Concentrations of MgO for Caquele and Camitongo1 pipes are typical for cratonic kimberlites (6-14% MgO) [46, 54] (Fig.3). They are occurring more rarely in Camitongo 2 pipe ilmenites where lower in MgO concentrations are typical. The trend from the Comitongo I and are complementally and together compile long fractionation trends typical for the Southern Africa [30].

The highest differences were determined for the Cr_2O_3 concentrations. The larger concentrations of this element which are typical for the metasomatites [4] were determined for the Comitongo pipes where it has bi-modal distribution with the picks near 55 and 40% TiO_2 .

Study of the ilmenites from Catoca [42] reveal 4 different groups including: high Mg -type common for kimberlites and diamond bearing associations [39], Fe-rich ilmenites (enriched in hematite), Mn- ilmenites, and common Mg-low ilmenites [46] as common for the groundmass kimberlites on any region. It was found that sometimes Mg - rich ilmenites were porous and surrounded by the Fe-rich varieties. Such intergrowths were not detected in the studied kimberlites

though the compositional varieties of ilmenites from Catoca and studied pipes are close.

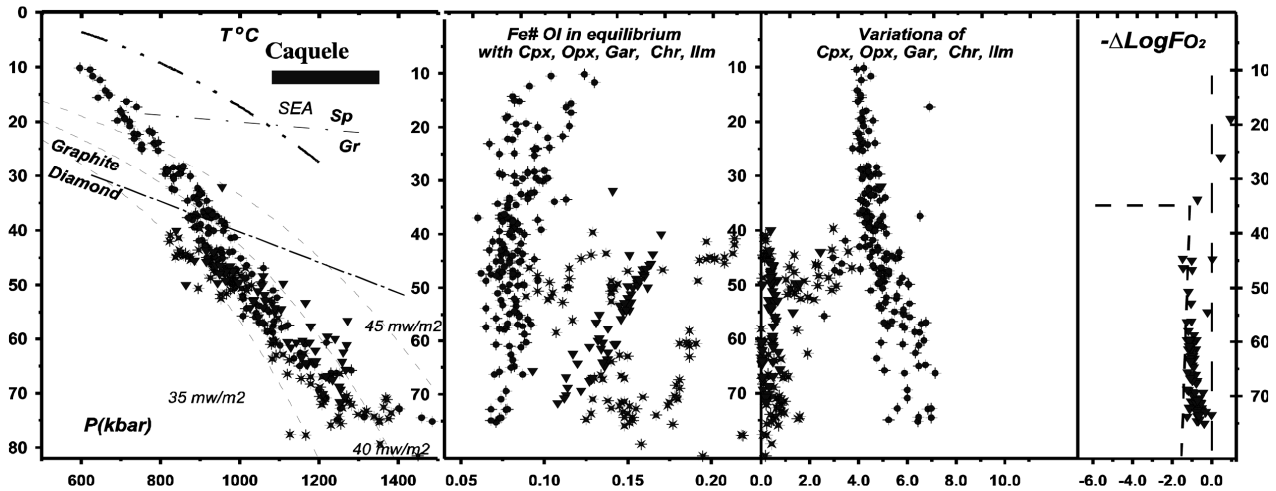


Fig. 5. PT plots using xenoliths from Caquele pipe obtained using monomineral thermobarometry. Signs are the same.

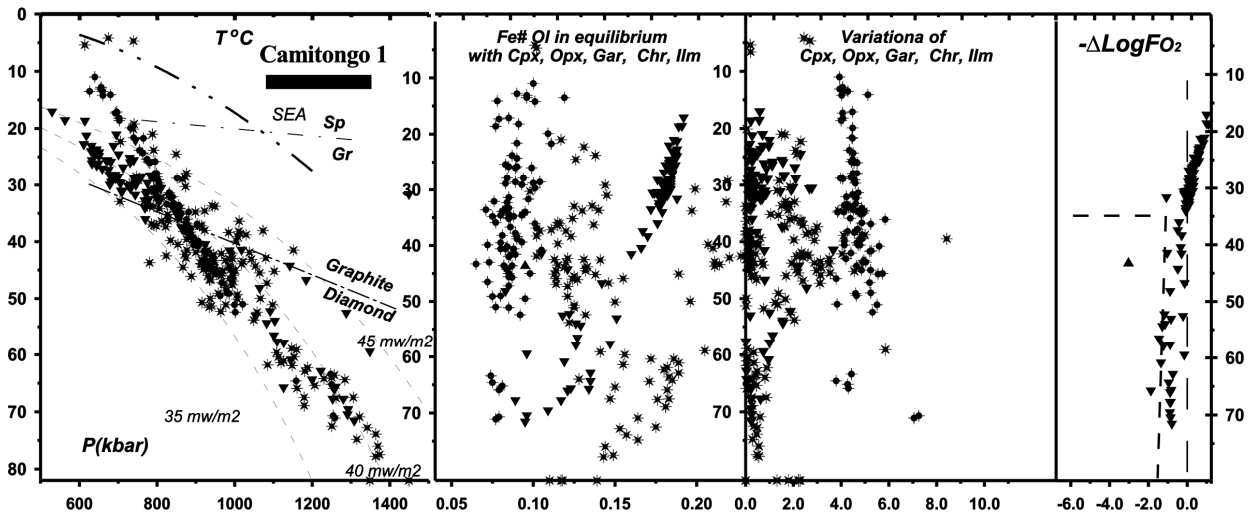


Fig. 6. PT plots using xenoliths from Camitongo 1 pipe obtained using monomineral thermobarometry. Signs are the same.

THERMOBAROMETRY

TP conditions for the mineral from concentrate were determined for clinopyroxenes garnet and ilmenites according to clinopyroxene [3] barometer and [33] thermometer, thermometer methods for garnets [2] and [79] thermometer and ilmenite [4] with the [52] thermometer. The configuration of the obtained geotherms is specific for the all studied pipes. Clinopyroxenes geotherms for the all studied pipes have typical inflection near 65 kbar at 1200°C determined by [36]

for Lesotho. (Fig 4).

We add for the calculations all the analyses from the P.Nixon issue [35] and some new and receive the more complex structure of the thermal state and geothermal regime in the mantle using [12] thermobarometry. The monomineral thermobarometry give close values (Fig.4).

The geotherms from the western part of the Angola of in Southwestern part of Congo –Kasai craton reveal more colder conditions corresponding to the South Africa [9] an from Namibia. [27]. Unlikely to the previous versions of thermobarometry [20, 45] our version of garnet thermobarometry [3] give the pressure conditions up to 80kbar. Previous versions of the garnet thermobarometry [20,45] plot most of Lherzolithic garnets near 40 kbars or lower and then project them on the geotherm for the reconstruction of mantle layering [6]. Relatively cold geotherms with the gradients higher then conductive were obtained both with the garnets and clinopyroxenes and even metasomatic Cr- rich ilmenites (Fig.5-7).

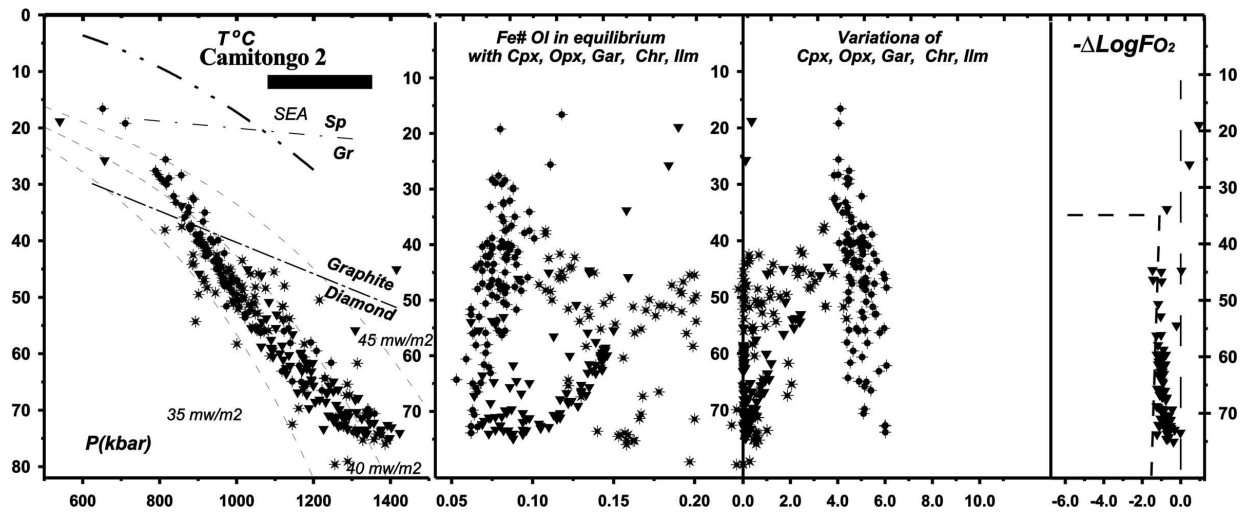


Fig. 7. PT plots using xenoliths data set for Camitongo 2 pipe obtained using monomineral thermobarometry. Signs are the same.

Mantle xenocrysts from Camitongo 1-2 generally refer to 38 mvm-2 while pipes Caquele (Fig.5) for the Catoca pipe the geotherm (Fig.8) are slightly higher then those determined for the cratons of the northern continents (Siberian [11], Slave [5], etc). The lower temperature conditions are determined mainly for Na-rich pyroxenes then for garnets. The lack of the pronounced inflection on the geotherm and the pipes give the conclusion about the lack of the pyroxenite lens which is typical for the Siberian craton.

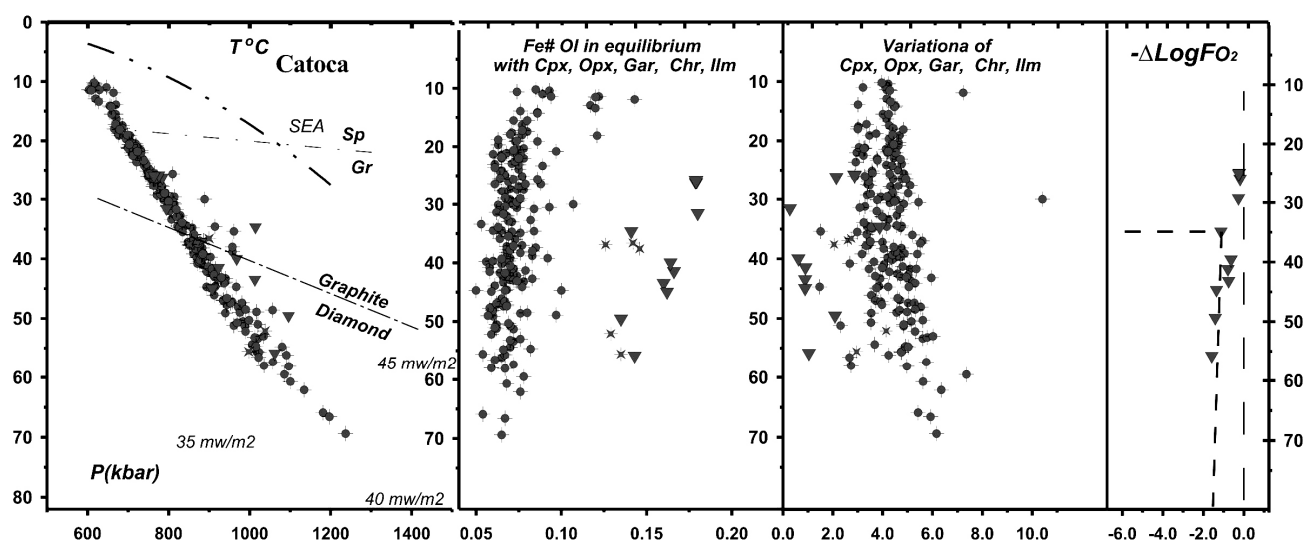


Fig. 8. PT plots using xenoliths data set for Catoca pipe obtained using monomineral thermobarometry. Signs are the same.

Thermal gradients of SCLM beneath two pipes Camitongo 1-2 (Fig.6-7) are close to 38 mvm-2 at 60-55 kbar with the elevations of these gradients in the lower pressure conditions. The mantle lithosphere is divided there in to two parts. Xenocrysts from the 1 one shows mainly the lower pressure conditions while Camitongo 2 – the higher part. Caquele pipe reveal the close set of the pressures for garnets clinopyroxenes and ilmenites which give the pressures 35-70 kbar. Garnets and pyroxenes from Catoca give the TP conditions which in the lower part are close to the 36 mvm-2 geotherm but this TP trend is more steeper then conductive geotherm and cross 40 mvm-2 geotherm and diamond stability boundary [24] in near 35 kbar forming subadiabatic branch.

Judging by the PT and the frequency of the points lying within the diamond stability field all studied the pipes should be diamondiferous. The Camitongo 1 pipe is the most abundant in such grains in concentrate.

The Mesozoic mantle geotherm from Angola are colder then Mesozoic (Fig.4) and Proterozoic [53] (Fig.9) geotherms from South Africa.

GEOCHEMISTRY OF THE MINERALS

The trace elements were determined for clinopyroxenes garnets ilmenites, zircons.

All clinopyroxenes from the studied pipes corresponds to the garnet facies with positive Gd/Yb_n and negative La/Sm_n ratios which are varying from one pipe to another and negatively correlates. Only one flattened TRE spectrum in Caquele pipe (Fig.10) corresponds to the garnet free peridotite. The clinopyroxenes spectrums reveal specific features in each pipe. Those from Caquele have the hampered rounded REE spectrums conform each other typical for peridotites and

pyroxenites to -5-7% of garnet in modal rock abundances and Cpx/Gar ratios~1:3 according to geochemical modeling. They in general are depleted in HFSE but they all reveal very high Ba (Rb) peaks as those found for phlogopites in metasomatites [17]. One has U peak and one more peak in Th. This is not typical for the clinopyroxenes from the Camitongo pipes. Such peaks may be sign of the subduction related fluids or the hybrid melts occurred due to melting of metasomatites. Two of them have small positive Pb anomalies the others more TRE enriched sample negative ones. They reveal Zr – minimums and most TRE rich show the Hf peak possibly referred to metasomatites with ilmenite. Spectrum of Cpx from spinel facie has U peak.

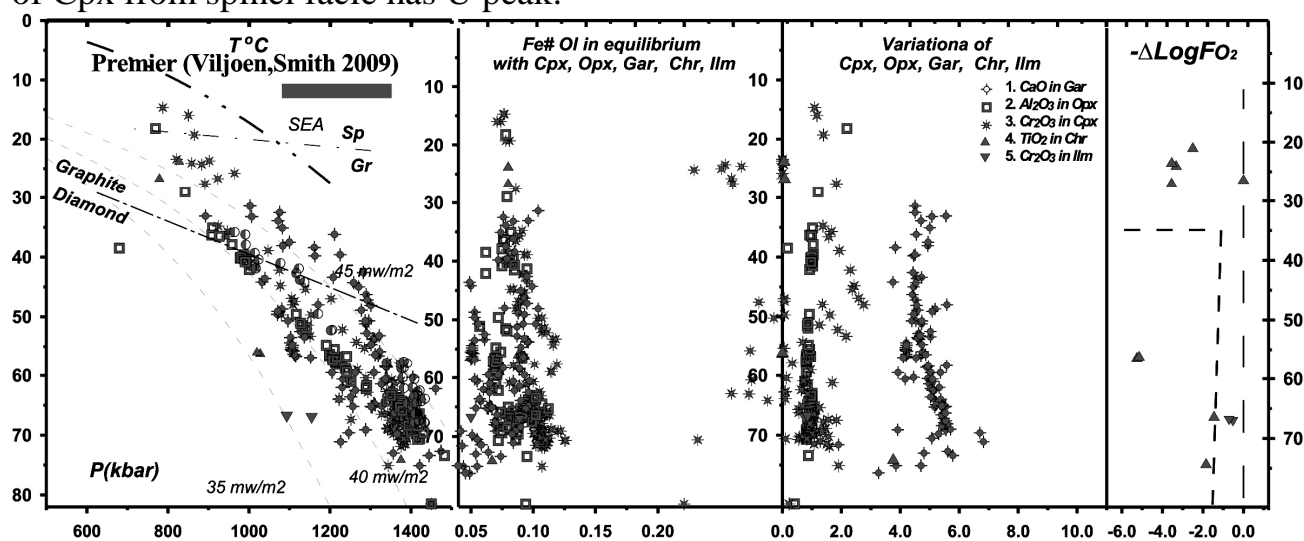


Fig. 9. PT plots using xenoliths data set for Premier pipe [54] obtained using monomineral thermobarometry. Signs are the same.

Clinopyroxenes from Camitongo 1 pipe reveal 3 types of spectrums (Fig.11). First is Lherzolithic with the 7-9 % of modal garnets the others are more enriched in garnet and more deep seated. Two are correspondent to typical primitive garnet peridotites similar to those from Caquele pipe. They are depleted in LILE – HFSE components, have strong Pb (as well as the other clinopyroxenes from this pipe) and display the strong Zr minimum Two more rich in TRE (hump REE~10) reveal enrichment in Th, U what may be the sign of the carbonatite metasomatism which is associated with the lack or negative Nb-Ta dips. Clinopyroxenes with REE enrichment factor (hump REE) near 100-50 PM are characterized by Th – U peaks, Zr dips and may refer to the metasomatism associated with zirconium precipitation. The Cpx from Camitongo 2 are divided in two groups. One has REE (~10) moderate level

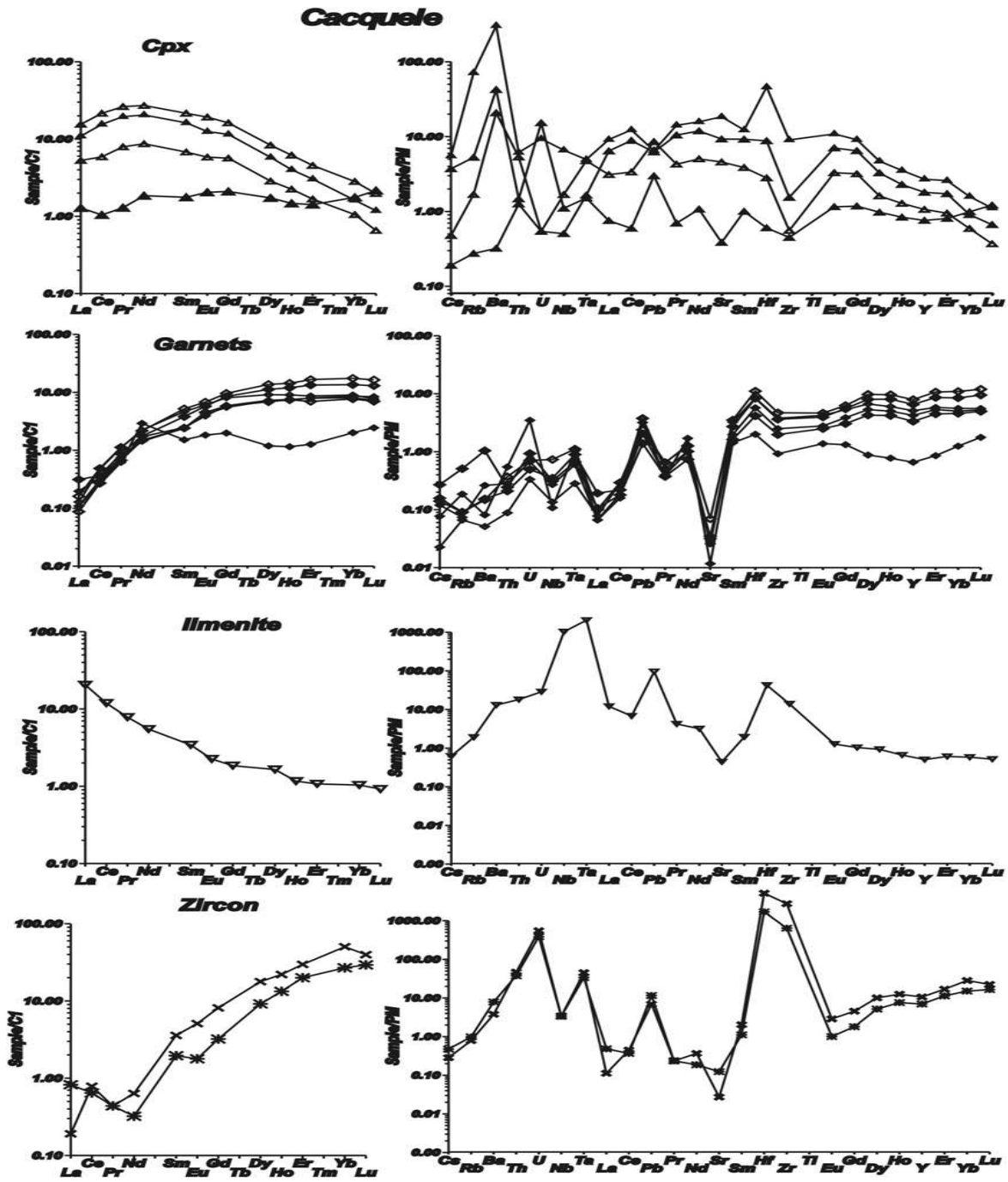


Fig. 10. Rare earth patterns and trace element spidergrams for the minerals from the Cacquele pipe.

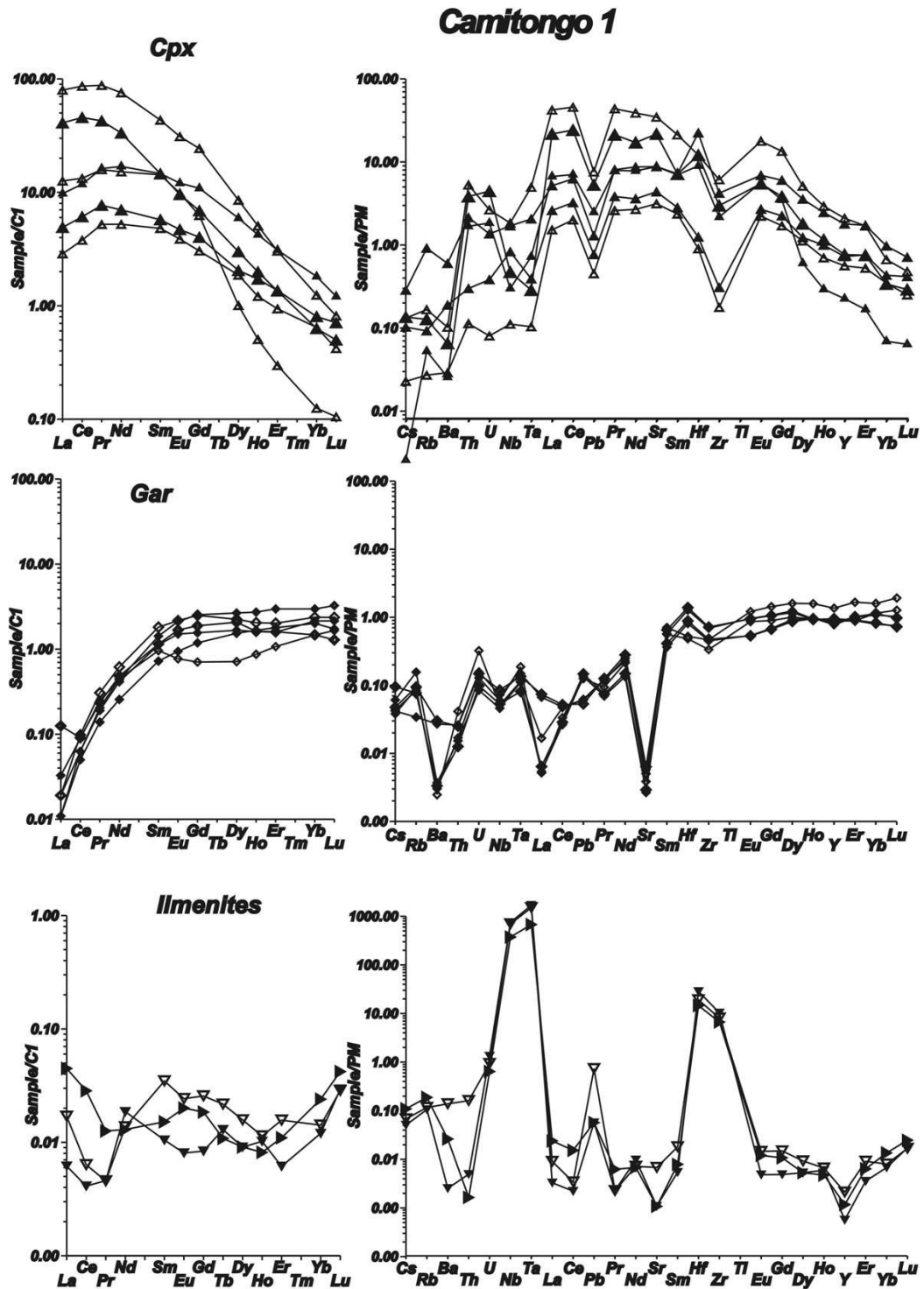


Fig. 11. Rare earth patterns and trace element spidergrams for the minerals from the Camitongo 1 pipe.

and TRE nearly primitive spectrum with the Ba depletion and Zr minima for those with lower TRE concentration. The three others are much enriched (~100 PM) with the HREE depletions. They reveal Ba-Th-U hamper, the Pb dip and nearly

flat HFSE except Zr – which is low as for the most of samples.

Garnets from the three pipes differ in REE level. Those from Caquele reveal higher HREE level close to 10/PM (primitive mantle) one display the flexed pattern with the depletion MHREE. The entire are moderately enriched in LILE-HFSE – have Pb and Hf peaks. Those from Camitongo 1 have lower HREE ~1 and reveal strong U-Rb peaks and heavy Ba-Sr minima. Garnets from Camitongo 2 reveal moderate HREE and low LREE (Fig.12) with the inflected REE spectrum in general. They display Rb peak higher then U and elevated in general left part of the spider diagram, small Pb and Hf peaks and negative deep Ba- Sr dips.

Zircons from two pipes in general display rather typical elevated REE and TRE distributions with the HREE enrichment strong Ce Th-U Zr -Hf peaks and saw – like spidergrams. Three zircons from Camitongo 2 pipe display fan- like rotations of the REE spectrums on Sm. The Ce anomaly is much higher for the pattern lower in REE in general.

Ilmenites from all pipes also differ in TREE spectrums. The spiderdiagram for one ilmenite from Caquele pipe display rather enriched TRE with quite different inclination of REE spectrums and LREE enrichment typical for melts saturated in fluids.

It display high Nb Ta and relatively high Zr –Hf and Pb and low LILE and Sr. Ilmenites form Camitongo 1 display gently inflected W-shaped low in REE (~0.2 PM) patterns very strong Nb-Ta and lower Pb and Zr-Hf peaks. Ilmenites from Camitongo 2 reveal U – shaped with LREE enrichment distributions, they display much enriched Nb-Ta lower Zr – Hf spiderdiagrams nearly without or with small Pb peaks. Comitongo 1-2 ilmenites display Y dips and probably are referring to depleted in Al peridotites

DISCUSSION

Interpretation of the composition of the mantle beneath western part of Congo-Kasai craton.

General mineral chemistry of the garnets an pyroxenes from S Western part of the Camitongo craton reveal the rather enriched compositions do nor differ much from the other localities of the South Africa [6, 9, 10, 12, 13, 17, 26, 29, 30, 34, 35 52, 53]. Amount of the metasomatites should be rather high judging by the geochemistry of the minerals. This is Typical for the many pipes from South Africa including Kimberly [17], for the depleted associations are much higher for the Catoca pipe comparing with the other studied localities.

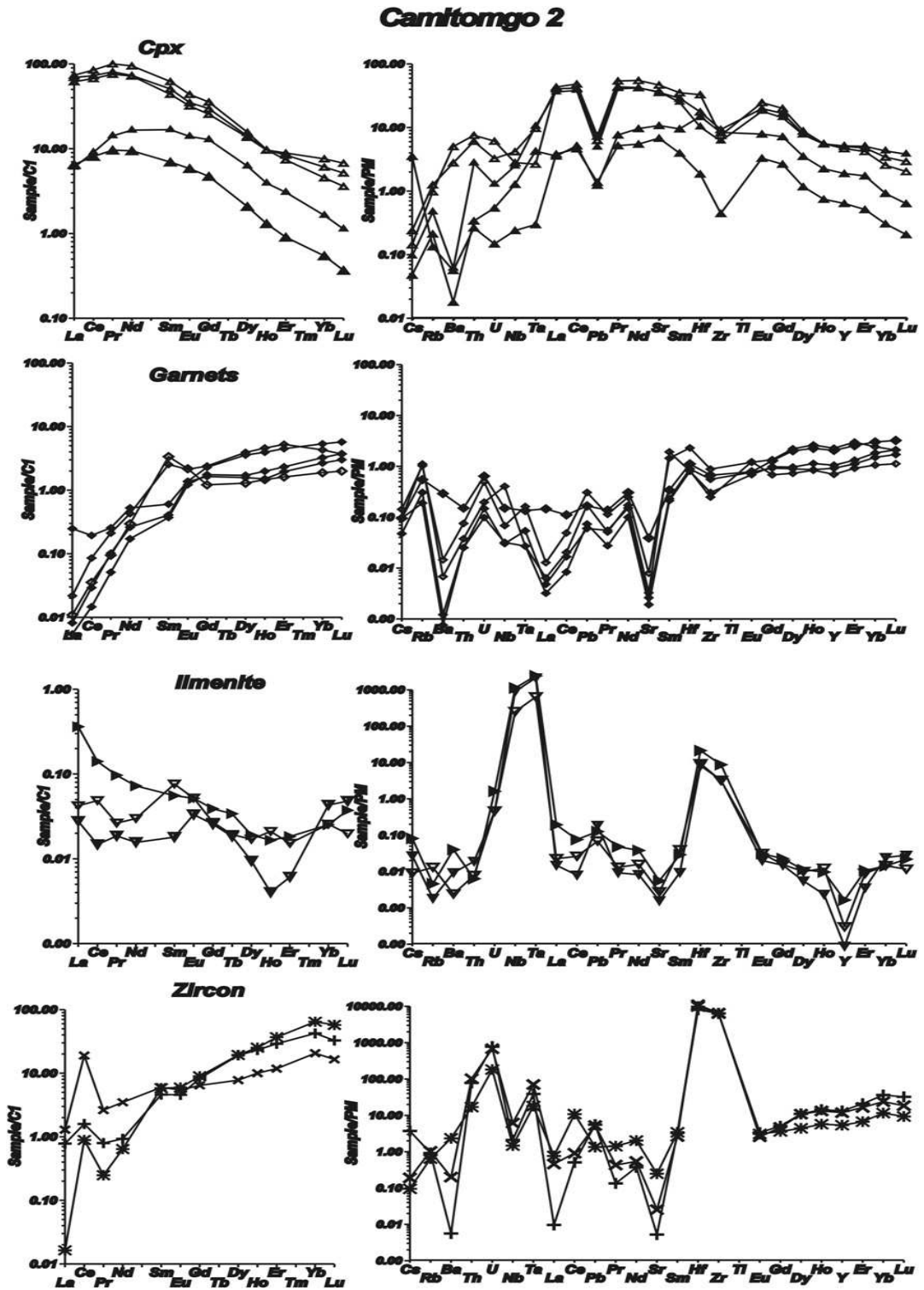


Fig. 12. Rare earth patterns and trace element spidergrams for the minerals from the Camitongo 2 pipe.

Thermal structures and construction of the mantle columns.

Thermal gradients within the most of the South Africa kimberlite pipes are mainly correspondent to the 40 mvm-2 geotherms but some depleted rock including diamond bearing associations reveal the colder conditions. The same is

determined for some of the coldest eclogites. This means that South Africa lithosphere was heated probably during the low- Proterozoic – Paleozoic time by the numerous plumes which caused the break up of Rodinia and Gondwana. Thicker lithosphere of the Congo craton reaching in the central parts 400km [38] were the reason of colder thermal state determined for the studied pipes.

The TPX diagram allows determining the layering of the mantle. Layering beneath the Catoca pipe may be determined by the fluctuation of the Fe#. About 5-6 layers exist in the 70=40 kbar interval and 3-4 in the upper part. The lithosphere beneath the Caquele may be divided from the top it ma be found three intervals to 40 kbars. The most enriched compositions were detected from 40 to 50 kbar where the pyroxenites are common in the mantle section [39]. The layer ~45 kbar is traced by the eclogites. Ilmenite trend stop near this levels commonly [4]. Two more layers may be roughly determined in more heated 60- 670 kbar and then 70-75 kbars where two more eclogitic lenses are present. The Cr –low pyroxenites are tracing the trend of the ilmenite compositions.

For the Camitongo 1 pipe the sharper layering is seen on P-Fe#Ol diagram. The Upper part from 15 to 35 kbar contain two layers Upper from top to 25 kbars contain pyroxenites and lherzolites / Te lower is the wall rock of the magmatic system where the Fe-rich ilmenites were crystallized. They were surrounded by the metasomatites where the clinopyroxenes became more ferriferous with descending pressures as well as the ilmenites. The later are pertly contaminated with Cr. The lower part from 35 to 55 kbars is represented mainly by the ilmenite bearing metasomatites and peridotite s with the high variations of the Fe#. And the lower part from 75 to 55 kbar is represented by the heated rocks forming convective branch and surrounding the lower magmatic chamber crystallizing ilmenites and Cr- less pyroxenites.

Mantle xenocrysts from the Camitongo 2 pipe mostly represent the lower part of mantle section. The Upper part probably is similar to those from previous pipe. Cr- Fe-rich metasomatites are found within the 35-55 kbar intervals. Cr-low pyroxenites and eclogites in this part are most abundant there. And the ilmenite low –Cr fractionation trend is tracing the magmatic system probably responsible for the heating mante. The more Fe-rich pyroxenites ($Fe\# > 0.15$) should represent more Fe-rich probably plume melts. And eclogites are more Fe- rich and are situated in lowermost part near 75 kbar.

Ilmenite trends as the indicator of the development of the feeding system for the kimberlite eruptions.

The concentration of minor components (NiO, MnO, Al₂O₃, V₂O₅, and Cr₂O₃) is regulated by different phases accompanied AFC fractionation ilmenite: Al₂O₃ is controlled by garnet, NiO by olivine, Cr₂O₃ – by chromite etc. These phases may play role of assimilants or precipitates.

We assume the ilmenite fractionation trend in kimberlites to be produced in the long vertical feeding system in the mantle similar to augite trend in alkali basalts [1]. The most simple crystallization scheme is suggested for Camitongo 2. The HT (P) conditions are correspondent to HT metasomatites produced by the interaction of the hot plume magma with the peridotite substrate. The differentiation assemblages are represented by the olivine and minor garnet as well as ilmenite itself according to modeling calculations. But natural ilmenite assemblages are mainly garnet pyroxenites [43]. Ilmenite peculiarities are rather specific for the field's kimberlite fields [47] but the difference between the populations of closely located pipes Camitongo 1-2 is very high. For Camitongo 1 pipe the dissolution of Cr rich phase probably clinopyroxene and chromite in the protokimberlite magma is negligible. For the Camitongo 1 volcano the two levels of the protokimberlite magma – is pronounced. The HT (P) line is close to the Camitongo 2 but with the minor garnet fraction. The upper floor is characterized by the new differentiation and interaction accompanied by the crystallization olivine and garnet in different proportions. Thus the branching system seems to be the most probable variant explaining the dispersion of the ilmenite and clinopyroxene in the middle part of the mantle section.

But it seems to be that the enrichment in the chromium is mainly regulated by the dissolution of the Cr- bearing phases from the surrounding feeding system peridotite substrate. Zonation and difference in the compositions of the porous and hard grains [41] is common for the ilmenites. Zonation in Cr may be of different type [45]. It should be noted that ilmenites are crystallizing within and near the magmatic channels. The small xenocrysts or the ilmenite mush may be transported by the magma at the upper horizons and there can be cemented by the Fe- rich ilmenite aggregates.

Trace elements for the ilmenites from Caquele refer to the metasomatites (W-shaped and low concentration) and to differentiation (LREE enriched from melts precipitated garnets) while for those from the Camitongo 1 mainly to the metasomatites. The hydrous metasomatites are developed mainly within the middle part of the mantle section.

The inflected in Eu-Gd patterns means of the garnets and clinopyroxenes and garnets probably means the hybridization with the melts contaminated in eclogites.

The difference beneath the Camitongo 1- and 2 mantle sections probably are formed by the capturing. The pipe Camitongo 1 should refer to the first phase and developing of the magmatic system. At the next state differentiated protokimberlite melts were migrated to the higher part to 50 kbar level of the mantle section and differentiated producing wall rock and vein metasomatites.

CONCLUSIONS

1. Mantle lithosphere beneath the Western part of the Congo Kasai craton is

rather fertile and is similar to the Kaapwaal craton. Mantle metasomatites here are situated mainly.

2. The thick lithospheric mantle beneath in the South Western part of Congo Kasai craton is responsible for his colder TP gradient.

3. The mantle sections beneath the Camitongo 2 and 1 pipes represent the two stages of the developing of protokimberlite melts with the migration of the magma differentiation level from the lower part to 40kbar which was influenced to the capturing of the mantle xenoliths.

REFERENCES

1. **Ashchepkov I.V. & André L.** Pyroxenite xenoliths in picrite basalts (Vitim plateau): origin and differentiation of mantle melts. // Russian Geology and Geophysics, 2002, v.43/4, p.343-363.
2. **Ashchepkov I.V.** Empirical garnet thermobarometry for mantle peridotite. // Russian Geology and Geophysics, 2006, v.47 (10), p. 1071-1085.
3. **Ashchepkov I.V.** More precise equation of the Jd-Di barometer. // Herald of Earth Sciences department Russian Academy of Sciences, 2003, N1 (21). http://www.scgis.ru/russian/cp1251/h_dgggms/CD-R/hitariada/informbul-1_2003/term-7e.pdf
4. **Ashchepkov I.V., Pokhilenko N.P., Vladykin N.V., Rotman A.Y., Afanasiev V.P., Logvinova A.M., Kostrovitsky S.I., Pokhilenko L.N., Karpenko M.A., Kuligin S.S., Malygina E.V., Stegnitsky Y.B., Alyмова N.A. & Khmelnikova O.S.** Reconstruction of mantle sections beneath Yakutian kimberlite pipes using monomineral thermobarometry. // Geological Society of London Special Publication., 2008, v.293, p.335-352.
5. **Aulbach S., Pearson N.J., O'Reilly S.Y., & Doyle B.J.** Origins of Xenolithic Eclogites and Pyroxenites from the Central Slave Craton, Canada. Journal of Petrology, 2007. v.48, pp.1843 - 1873.
6. **Batumike J.M., Griffin W.L., O'Reilly S.Y.** Lithospheric mantle structure and the diamond potential of kimberlites in southern D.R. Congo. // Lithos . 2009 v.112.
7. **Baumgartner M., Ankar E., Grutter H.** Compositional Classification Of "Kimberlitic" And "Non-Kimberlitic Ilmenite, With Implications For Visual Selection And Discrimination. // 8th International Kimberlite Conference Long Abstract. Victoria, Canada, 2003. FLA0281.
8. **Beard B.L., Fraracci K.N., Taylor L.A., Snyder G.A., Clayton R.N., Mayeda T.K. & Sobolev N.V.** (1996). Petrography and geochemistry of eclogites from the Mir kimberlite, Yakutia, Russia. //Contributions to Mineralogy and Petrology, v.125, pp.293–310.
9. **Bell D.R., Schmitz M.D., Janney P.E.** Mesozoic thermal evolution of the southern African mantle lithosphere . Lithos. 2003. v. 71./ 2-4. pp. 273-287..
10. **Boyd F.R. and Danchin R.V.,** 1980. Lherzolites, eclogites and megacrysts from some kimberlites of Angola // American Journal of Science, v.280A, pp.528-549.
11. **Boyd F.R., Pokhilenko N.P., Pearson D.G., Mertzman S.A., Sobolev N.V.& Finger L.W.,** 1997. Composition of the Siberian cratonic mantle: evidence from Udachnaya peridotite xenoliths. // Contrib. Mineral. Petrol. 128, 228-246.
12. **Brey G, Kohler T.** Geothermometry in four phase lherzolites II. New thermobarometers, and practical assessment of existing thermobarometers. // J. Petrol. 1990, v.31, v.1353-1378
13. **Burgess S.R., Harte B.,** 1999. Tracing Lithosphere Evolution Through the Analysis of Heterogeneous G9/G10 Garnets in Peridotite Xenoliths, I: Major Element Chemistry. In:

- Gurney J.J., et al. (Eds.), Proceedings of the VII th International Kimberlite Conference. Red Roof Design, Capetown, South Africa, pp. 66-80.
14. **Correia E.A., Laiginhas F.A.** Garnets from the Camafuca-Camazambo kimberlite (Angola). // *An Acad Bras Cienc.* 2006 v. 78(2), pp.309-15.
 15. **Dawson, J.B., Stephens, W.E.,** 1975. Statistical classification of garnets from kimberlite and associated xenoliths. // *J. Geol.* V.83, pp.589-607.
 16. **Egorov K.N., Roman'ko E.F. , Podvysotsky V.T., Sablukov S.M., Garanin V.K., D'yakonov D.B.** New data on kimberlite magmatism in southwestern Angola. *Russian // Geology and Geophysics.* 2007. v.48, pp. 323–336.
 17. **Ganga J., Rotman A.Ya., and Nosiko S.** Pipe Catoca, an example of the weakly eroded kimberlites from north-east of Angola // 8th International Kimberlite Conference Long Abstract. 2003. FLA312.
 18. **Gregoire M, Bell D.R., Le Roex A.P.** Garnet Lherzolites from the Kaapvaal Craton (South Africa): trace element evidence for a metasomatic history. // *J Petrol.* v. 2003, v.44, pp. 629–657.
 19. **Griffin W. L., Fisher N.I., Friedman J.H., O'Reilly S.Y., Ryan C.G.** Cr-pyrope garnets in the lithospheric mantle 2. Compositional populations and their distribution in time and space. // *Geochemistry, Geophysics, Geosystems* 2002 V 3, pp.12.
 20. **Griffin W.L., Ryan C.G.** An experimental calibration of the "nickel in garnet" geothermometer with applications, by D. Canil: discussion. // *Contrib Mineral Petrol.* 1996, v. 124, pp.216-218.
 21. **Griffin W.L., Fisher N.I., Friedman J., Ryan, C.G., O'Reilly S.Y.,** 1999. Cr–pyrope garnets in the lithospheric mantle. I. Compositional systematics and relations to tectonic setting. // *J. Petrol.* v40, pp.679–704.
 22. **Griffin W.L., Moore R.O., Ryan, CG., Gurney J.J. & Win T.T.** 1997. Geochemistry of magnesian ilmenite megacrysts from southern African kimberlites. // *Russian Geology and Geophysics.* V. 38/2, pp. 421-443.
 23. **Griffin W.L., Shee S.R., Ryan C.G., Win T.T., Wyatt B.A.** Harzburgite to lherzolite and back again: metasomatic processes in ultramafic xenoliths from the Wesselton kimberlite, Kimberley, South Africa. *Contrib. Mineral. Petrol.* 1999. v.134, pp.232-250.
 24. **Grutter H.S., Quadling K.E.** Can sodium in garnet be used to monitor eclogitic diamond potential? In: Gurney, J.J., Gurney, J.L., Pascoe, M.D., Richardson, S.H. (Eds.), J. B. Dawson volume, // Proceedings of the 7th International Kimberlite Conference, Red Roof Design, Capetown, 1999. pp.314-320.*
 25. **Kennedy S.C., Kennedy G.C.** The equilibrium boundary between graphite and diamond. *J Geophys Res* 1976, v.81, pp. 2467-2470
 26. **Krogh, E.J.** The garnet-clinopyroxene Fe-Mg thermometer – a reinterpretation of existing experimental data.// *Contrib. Mineral. Petrol.* 1988. v.99, pp.44-48.
 27. **Leost I., Stachel T., Brey G.P., Harris J.W., Ryabchikov I.D.** Diamond formation and source carbonation: mineral associations in diamonds from Namibia. // *Contrib. Mineral. Petrol.* 2003. V. 145. P. 12-24.
 28. **MacGregor I.D., Carter J.L.,** 1970. The chemistry of clinopyroxenes and garnets of eclogite and peridotite xenoliths from the Roberts Victor Mine, South Africa. // *Phys. Earth Planet. Interiors.* 1970, v.3, pp. 391-397.
 29. **McCandless T.E., Gurney J.J.** Sodium in garnet and potassium in clinopyroxene: criteria for classifying mantle eclogites. // In Ross, J. (Ed), *Kimberlites and related rocks Vol 2 Their mantle/crust setting, diamonds and diamond exploration.* Blackwell, Carlton, 1989. pp. 827-832.
-

30. **Moore A. & Belousova E.**, 2005. Crystallization of Cr-poor and Cr-rich megacryst suites from the host kimberlite magma: implications for mantle structure and the generation of kimberlite magmas. // *Contributions to Mineralogy and Petrology*, v.49, pp.462–481.
31. **Moore R.O., Griffin W.L., Gurney J.J., Ryan C.G., Cousens D.R., Sie S.H. and Suter G.F.** Trace element geochemistry of ilmenite megacrysts from the Monastery kimberlite, South Africa. // *Lithos*, 1992. v.29, pp. 1-18.
32. **Morimoto N.** Nomenclature of pyroxenes. // *Mineral Mag.*, 1988, v.52, pp.535–550.
33. **Nimis P., Taylor W.**, 2000. Single clinopyroxene thermobarometry for garnet peridotites. Part I. Calibration and testing of a Cr-in-Cpx barometer and an enstatite-in-Cpx thermometer. // *Contrib. Mineral. Petrol.* v.139 (5), vv.541-554.
34. **Nixon P.H., Rogers N.W., Gibson I.L., Grey A.** Depleted and fertile mantle xenoliths from southern African kimberlites. // *Annu Rev Earth Planet. Sci.* 1981, v. 9 pp.13 –22.
35. **Nixon P.H.**, / Ed. Lesotho Kimberlites. Cape and Transvaal, Capetown, 1973, pp. 48–56.
36. **Nixon P.H., Boyd F.R.**, Petrogenesis of the granular and sheared ultrabasic nodule suite in peridotite xenoliths. // *Ext Abstrts*, 5 th IKC, Cape Town, 1973. pp. 122-126.*
37. **O'Neill H.St.C, Wood B.J.** An experimental study of Fe-Mg- partitioning between garnet and olivine and its calibration as a geothermometer. // *Contrib. Mineral. Petrol.* 1979, v. 70. p. 5970.
38. **O'Reilly S.Y., Zhang M., Griffin W.L., Begg G., Hronsky J.** Ultradeep continental roots and their oceanic remnants: A solution to the geochemical “mantle reservoir” problem? // *Lithos*, 2009. v.112 , In Press,
39. **Pokhilenko, N. P., Sobolev N.V., Sobolev V.S. & Lavrentiev Y.G.** Xenoliths of diamond bearing ilmenite-pyrope lherzolites from the kimberlite pipe Udachnaya (Yakutia). // *Doklady AN SSSR.* 1976, 231, 438-442
40. **Pokhilenko N. P., Sobolev N.V., Kuligin S. S. & Shimizu N.** 2000. Peculiarities of distribution of pyroxenite paragenesis garnets in Yakutian kimberlites and some aspects of the evolution of the Siberian craton lithospheric mantle. *Proceedings of the VII International Kimberlite Conference, The P.H. Nixon volume.* 690-707.
41. **Pollack H.N., Chapman D.S.**, 1977. On the regional variation of heat flow, geotherms, and lithospheric thickness. // *Tectonophysics* 1977. v.38, pp. 279-296.
42. **Robles-Cruz S.E., Watangua M., Isidoro L., Melgarejo J.C., Galí S., Olimpio A.** Contrasting compositions and textures of ilmenite in the Catoca kimberlite, Angola, and implications in exploration for diamond. // *Lithos.* 2009, v. 112 in press.
43. **Rodionov A S, Amshinsky & Pokhilenko N P.** 1988. Ilmenite-Pyrope wehrlite – a new type of kimberlite xenoliths paragenesis. // *Russian Geology and Geophysics* v.19/7, pp.53-57.
44. **Roman'ko E.F., Egorov K.N., Podvysotskii V.T., Sablukov S.M., D'yakonov D.B.**, 2005. A new diamondiferous kimberlite region in southwestern Angola. // *Dokl. Earth Sci.* v.403A (6), pp. 817–821.
45. **Ryan C.G., Griffin W.L., Pearson N.J.** Garnet geotherms pressure-temperature data from Cr-pyrope garnet xenocrysts in volcanic rocks. // *J Geophys Res* v.101 B3, pp. 5611–5625.
46. **Schulze D.L, Anderson P.F.N., Hearn Jr., B.C. & Hetman, C.M.**, 1995. Origin and significance of ilmenite megacrysts and macrocrysts from kimberlite. // *International Geology Review*, v.37, pp.780-812.
47. **Sobolev N.V.** Significance of picroilmenite for the localization of kimberlite fields. // *Russian Geology and Geophysics* 1980, v. 24/5, pp.149-151.
48. **Sobolev N.V.** Deep seated inclusions in kimberlites and the problem of the composition of the upper mantle. AGU, Washington, DC. 1977. 350p.

49. **Sobolev N.V.**, Significance of picroilmenite for locating kimberlite fields. // *Geologiya i Geofizika (Soviet Geology and Geophysics)* 1980 V.(10), pp.149–151 (127–129).
50. **Sobolev N.V., Lavrent'yev Y.G., Pokhilenko N.P., Usova L V.** Chrome-rich garnets from the kimberlites of Yakutia and their paragenesis. // *Contrib. Mineral. Petrol.* 1973. v.40, pp.39-52.
51. **Sobolev N.V., Mankenda A., Kaminsky F.V., Sobolev V.N.**, 1990. Garnets from kimberlites of northeastern Angola and their composition–diamond potential relationship. // *Dokl. Akad. Nauk SSSR* v.315, pp.1225–1229.
52. **Taylor W.L., Kamperman M., Hamilton R.**, 1998. New thermometer and oxygen fugacity sensor calibration for ilmenite and Cr-spinel-bearing peridotite assemblage. // In: Gurney, J.J., 7th IKC Extended abstracts, Capetown. FLA891.
53. **Van Achtebergh E., W. L. Griffin, and J. Stiefenhofer.** Metasomatism in mantle xenoliths from the Letlhakane kimberlites: Estimation of element fluxes, // *Contrib. Mineral. Petrol.*, 2001. v.141, pp. 397–414.
54. **Viljoen F., Dobbe R., Smit B.** 2009 Geochemical processes in peridotite xenoliths from the Premier diamond mine, South Africa: Evidence for the depletion and refertilisation of subcratonic lithosphere. *Lithos* 2009. v. 112.
55. **Wyatt B. A., Baumgartner M., Anckar E. & Grutter H.** Compositional classification of “kimberlitic” and “non-kimberlitic” ilmenite. // *Lithos* 2004. v.77, pp.819–840.
56. **Zuev V.M., Khar'kiv A.D., Zinchuk N.N., Mankenda A.** Weakly eroded kimberlite pipes of Angola. // *Geologiya i Geofizika (Soviet Geology and Geophysics)*, 1988., v. 29 (3), pp. 56–62 (50–57).

Trace Elements in Plutonic Alkaline Rocks from the Oceanic Islands

Asavin A. M.

Vernadsky Institute of Geochemistry and Analytical Chemistry, Russian Academy of Sciences, ul. Kosygina 19, Moscow, 119991 Russia;

INTRODUCTION

The intraplate oceanic magmatism is one of the largest geological processes in geological history. There is a volcanic magmatism mainly. Ore potential of these type of magmatism depends on the other magmatic stage – plutonic facieses. The hidden deep part of the volcanic structure on the oceanic island there is the main object for the search of the potential ore bodies into the magmatic cameras.

There are a lot of the ore deposit connected with intraplate magmatic alkaline magmas observed on the continental environment. There is mainly a trace elements deposit.

Therefore to make a prognostication of the deposit which connected with this type of the magma in the ocean we must study plutonic rocks of the oceanic islands.

Into the task of this work we developed the compositional analysis of the plutonic rocks, make their petrochemical classification, estimated the prevalence of different types and their rare-metal specialization. The attempt to compare oceanic species with their continental analogs is made on the limited material on the oceanic islands of Atlantic ocean.

INFORMATION RESOURCE

We developed the database for geochemistry of intra-plate oceanic magmatism GIM (geochemistry of the intraplate magmatism). The database is represented on the portal “Geology” (<http://Earth.jscs.ru/gim>). In database in the present moment are represented about 35 thousand records of the chemical analyses of volcanic and plutonic rocks of oceanic islands and seamounts of the Atlantic and Indian Ocean. In particular in the database are represented about 500 analyses in the main and rare elements of the plutonic rocks of oceanic islands. Using this data set we estimated the prevalence of different petrochemical types of the intrusive rock.

CLASSIFICATION

On the classification diagram the SiO_2 - sum of alkaline (Fig. 1) are represented the compositions of plutonic rocks. On the whole it is possible to distinguish two groups of species. The first are the samples of the mantle substance of different degree of melting and alteration - ultrabasic peridotites, wehrlites. These mantle nodules are the xenolites, raised from the partial melting mantle source to the surface.

The second group is the wide spectrum of basic and acid plutonic rocks and being appeared, apparently, partly of cumulus which formed during the crystallization differentiation.

For the completeness of description should be mentioned third group of diverse subvolcanic bodies - dikes, stocks, sills and other. Actually these are the complete analogs of volcanic rocks, simply their cooling occurs more slowly, also, due to these degree of crystallized state more size grains.

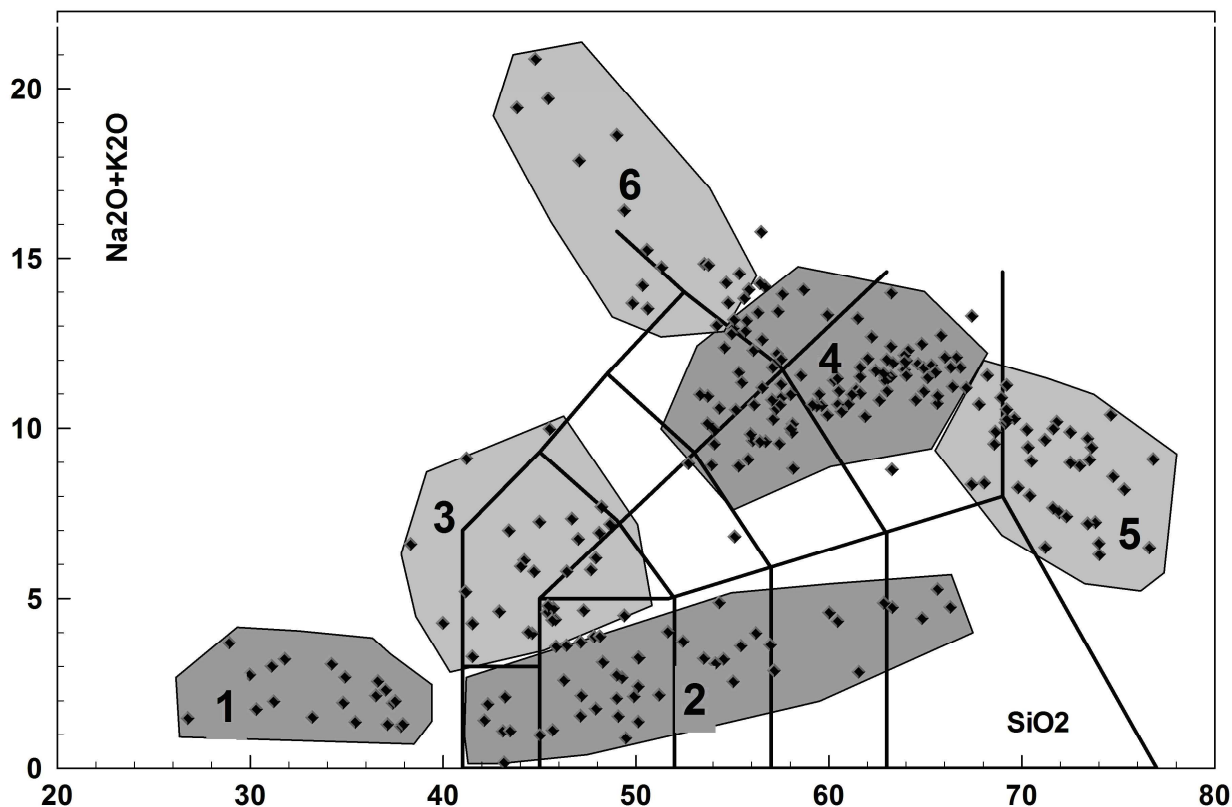


Fig.1. **Classification of the plutonic rocks from oceanic islands (Atlantic ocean)** 1- ultrabasic foidite and gabbroid group, 2 – alkaline granite and quartz syenite, 3 –syenite and other alkaline rocks, 4 – diorite and granite normal alkalinity.

Thus, for evaluating the processes of proceeding in the magma chambers and determining the potential ore level of alkaline melts are most interesting the alkaline plutonic rocks, which fall into the second group. Among these species it is possible to discriminate three main groups of the species:

1. gabbroids of different alkalinity,
2. alkaline syenite
3. alkaline granites.

Fist set also include rare local of foidite type of the rock - iolite, turiate. Gabbroids give a continuous series of the species of normal alkalinity without the breaks of compositions apparently connected with the process of differentiation.

It is most interesting, the fact that most frequently are encountered the intrusive rock with the high the content of silica (Fig.2). On the diagram of CIPW normative minerals (Fig. 3) are given the compositions of these three groups in the terms of the content CIPW norms. The analysis of data revealed the lower content dark-colored into the quartz normative group of the rocks in comparison with nepheline normative species.

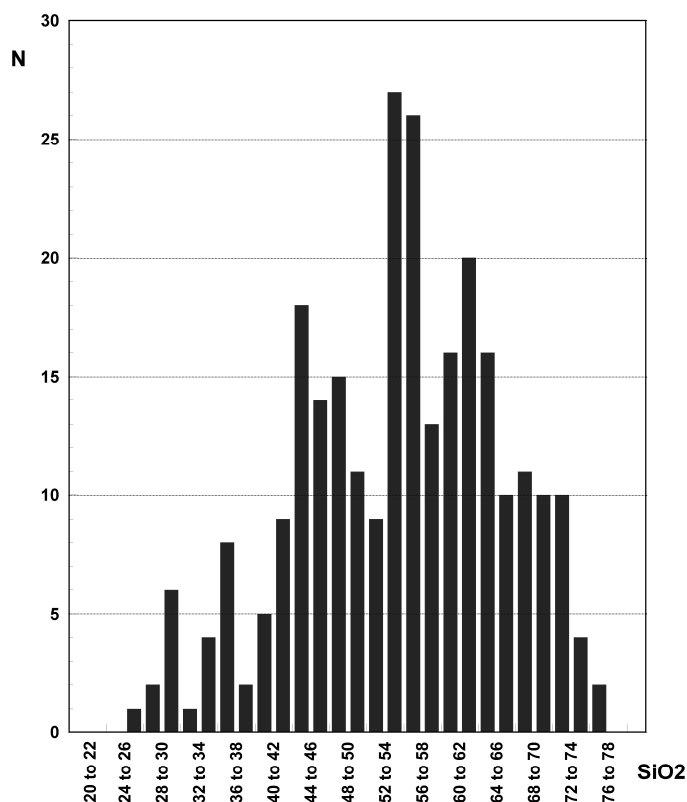


Fig.2. Histogram SiO2 content in plutonic rocks from oceanic islands (Atlantic Ocean).

From the figure 3 we can see that more part of points contains less than 10% normative pyroxene and ore minerals (magnetite, ilmenite, perovskite, hematite) in the rocks.

They make obvious the presence of such highly siliceous melts, that as a whole the differentiation of mantle melting under the oceanic islands have a long way of the differentiation, i.e., it is the evidence that in the magmatic cameras realize the conditions of complete fractionating to the quite last stages of close

ones to the points of eutectic composition – plagioclase-feldspar, nepheline-feldspar, quartz-feldspar.

This circumstance is contributory factor for the forming of the ore body in the magmatic stage.

The potential of ore productivity is directly proportionally from the volume of magmatic cameras, the stability of magma chamber (long period for the process of concentration ore components), the possibility of the realization of the processes of the concentration of ore phases and forms the ore horizons.

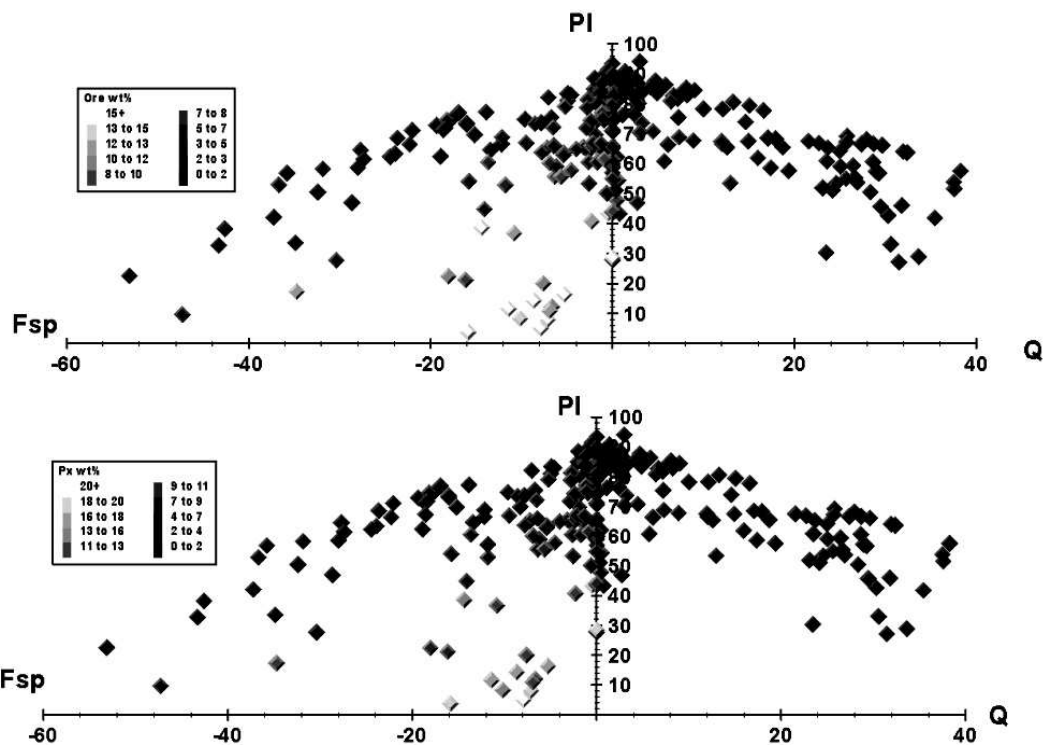


Fig.3. Composition plutonic rocks from oceanic islands (Atlantic Ocean) as abundances CIPW minals: Fsp= Ort+Ne; PI= Ab+An; Ore – Mgt+Ilm+He; Px= Wo+Fs+En.

As this is shown in the models of magmatic deposit of the apatite- rare-metal body of Khibinski and Lovozero massive, Illimaussac, Gulinskyi pluton, largest of the deposite of Nb and Ta of alkaline apo-granite in the province of Nigeria and Russian intrusive into Western Sayan (Ulug-Ttanzeq and others).

Thus, the revealed special two features in macro composition of the plutonic rocks of the oceanic islands:

1. predominance of the leucocratic varieties of intrusive comagmate of volcanic process.
2. lower abundance of the rock-forming dark phases (pyroxene, ilmenite, perovskite) which concentrate the trace elements.

All those makes it possible to expect that the concentration of incoherent (trace) elements in the residual melts must increase in sudden large amount.

Taking into account the total accumulation of rare elements up to the moment of the forming of final differentiates, the content in the liquid easily can reach the level of solubility trace element in the melts – level of the ore saturation, when the own trace element ore phase will be crystallized.

TRACE ELEMENTS

Thus, the first analysis of obtained data testifies about the prospect of this type of magmatism as the source of ore deposits, and the gigantic volumes of magmatism make it possible to expect, the forming of the large or very large volumes of ore deposit.

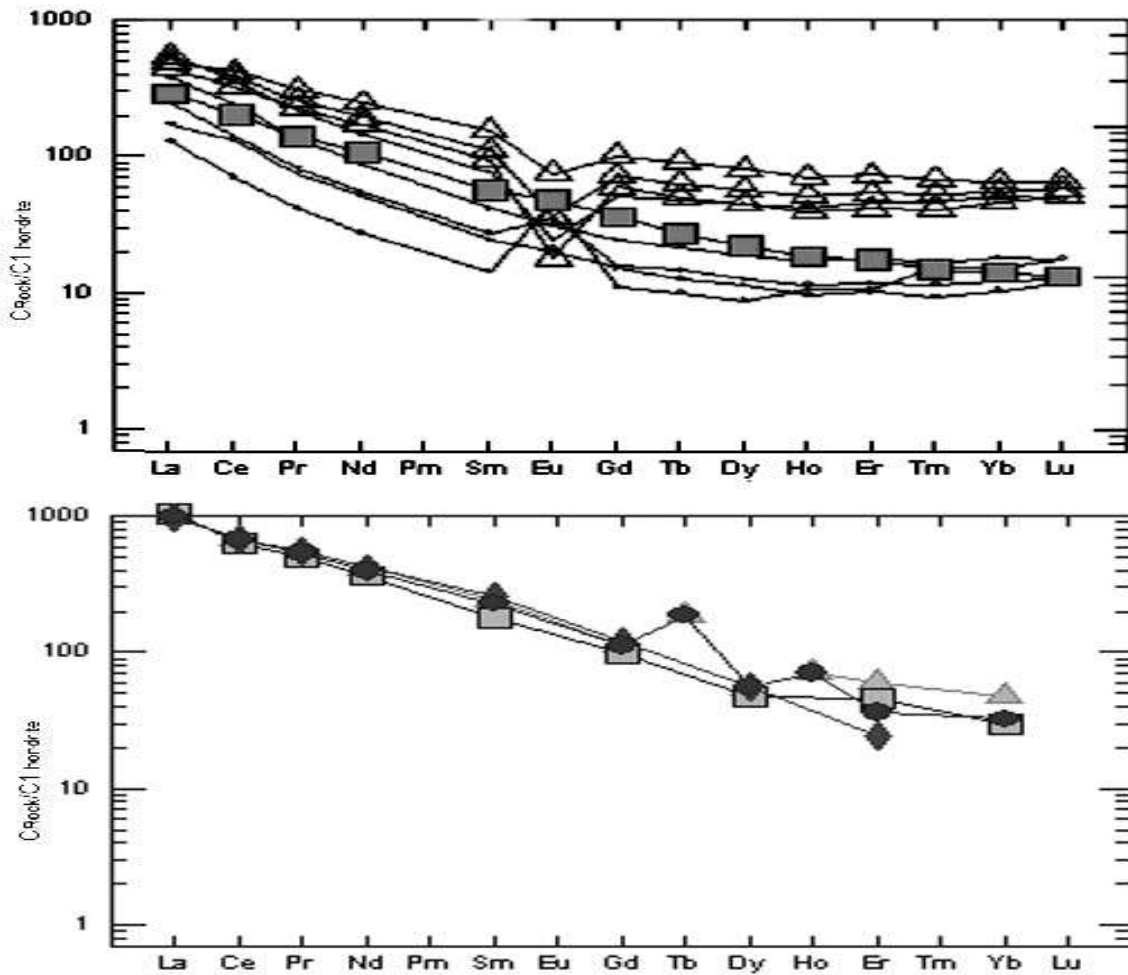


Fig.4. TR concentration norm C1 hondrite concentration from: A- syenite from the oceanic islands (square – mean concentration, triangle – quartz syenite, dots – nepheline syenite); B- syenite from the Lovozero (Gerasimovsky V.I. et al 1966) massive (square – nepheline concentration, triangle – quartz syenite).

For evaluating the level of trace elements composition we calculated the averaged values on the rare-earth elements for the nepheline and quartz syenite (fig 4) for the comparison of these given with the compositions continental alkaline plutonic rocks analog. Fig 4 was built for the syenite of Lovozero massif, largest alkaline intrusion of Kola peninsula and trace (Zr, Nb,-TR, U) metal deposit (Gerasimovsky V.I. and others 1966).

The influence of the trace-metal mineralization connected with the plutonic stage is reflected in the increased contents of the trace elements of the majority of the dike and subvolcanic species of this massif. The anomalous contents of trace elements are the clear sign of the ore mineralization. One should expect that also the promising manifestations of oceanic alkaline magmatism will be characterized by the high level of the contents of rare elements. The analysis of the graphs of the distribution of rare-earth elements revealed the sufficiently unexpected fact. Oceanic species proved to be substantially they were depleted with respect to rare elements. I.e., in spite of identical macro is the composition (both there are syenite) of the content of rare-earth elements in the oceanic intrusive rock almost two orders lower than continental. This circumstance refutes our previous thesis about the high ore potential of oceanic intrusive systems.

DISCUSSION

The reasons for this paradox needs more attention, and it is extremely important for evaluating the ore potential of alkaline magmatism as a whole. As the draft hypothesis possible to assume that there is a powerful process, which exists into intermediate magmatic cameras by lithophile and incoherent elements, thus, that also cumulative species and eutectic melts are as a result impoverished of trace elements. Possibly, such process is scattering in the alkaline melts of rare elements due to their high capacity with respect to trace cations, as this for example realizes in the Mongolia from ongonite's melt. However, the appearance of such enriched melts it is unknown on the oceanic islands, although they are known in the regions of alkaline volcanism on the continents. The relatively not high contents of volatile components in the alkaline magmas of the majority of oceanic islands (weak prevalence of hornblende and micas in vulcanite) and processes of the high-temperature metasomatic processing in the oceanic islands plutonic and volcanic complexes makes it impossible assumption about the active transfer of trace elements by fluid phase.

Thus, and this explanation does not make it possible to solve problem. In a number of island series are revealed the manifestations of the carbonatite magmatism [Kogarko L.N 1993, Kai Hoernle et al 2002]; however, these manifestations are not characterized by the anomalously high level of the contents of rare elements. But where is the trace elements? Where is the enormous volumes of mantle trace elements accumulated in process differentiation of oceanic melts

during the millions years of evolution, which must concentrate as a result of this differentiation in relative small volume of the residual melts?

REFERENCES

1. **Gerasimovsky V.I., Volkov V.P., Kogarko L.N., Polikov A.I., Saprukina U.A. Balashov U.A.** Geochemistry of the Lovozero alkaline massive. Nayka 1966 PP.381. (cyrilic)
2. **Kogarko L.N.** Geochemical characteristics of oceanic carbonatites from the Cape Verde Islands // S.Afr.J. Geol 1993 96 (3) P.119-125.
3. **Kai Hoernle, Tilton G., Le Bas Mike, Duggen S, Garbe-Schonberg Dieter** Geochemistry of the oceanic carbonatites compared with continental carbonatites; mantle recycling of oceanic crustal carbonatite // Contrib Mineral Petrol 2002 142 P.520-542.

HENDRICKSITE AND ZN-CONTAINING PHLOGOPITE FROM PERALKALINE PHONOLITES OF THE OKTYABRSKY MASSIF, AZOV REGION, UKRAINE

Sharygin V.V.

V.S.Sobolev Institute of Geology and Mineralogy SD RAS, Koptyuga pr. 3, 630090 Novosibirsk,
Russia

ABSTRACT

Hendricksite and Zn-containing phlogopite were observed in the groundmass of two types of dike peralkaline phonolites from the Okryabrsky massif, Azov region, Ukraine. These micas are associated with nepheline, K-feldspar, albite, sodalite, Zn-containing Zn-kupletskite, aegirine, fluorite, Na-catapleiite, serandite, REE-rich eudyalite, fluorapatite, cerite-(Ce), Na-REE-apatite, U-REE-pyrochlore, cryolite, thorite, thorianite and mineral of the cancrinite group. The fine-grained phonolite of the Oktyabrsky massif is the first occurrence of hendricksite in peralkaline magmatic rocks. The simplified formula of hendricksite from this phonolite species can be expressed as $K_2(Zn_3Mg_2Mn)[Al_2Si_6O_{20}](OH)_3F$. This mica is variable in composition (in wt.%): SiO_2 (37.7-38.7), TiO_2 (up to 0.3), Al_2O_3 (10.1-10.9), FeO_t (0.3-1.4), ZnO (21.5-25.8), MgO (6.9-9.7), MnO (6.4-7.7), K_2O (8.4-9.1), Rb_2O (0.5-0.8), Li_2O (up to 0.3), F (1.5-2.3) and H_2O (2.1-2.5 wt.%). Zn-Li-containing phlogopite were found only in the porphyric phonolite. Its simplified formula can be expressed as $K_2(Mg_4Zn_{0.75}Mn_{0.5}Li_{0.75})[Al_{1.25}Si_{6.75}O_{20}]F_{2.5}(OH)_{1.5}$, indicating that is Zn-Li-Mn-F-bearing mica intermediate between phlogopite $KMg_3[AlSi_3O_{10}](OH)_2$ and tainiolite $KLiMg_2[Si_4O_{10}]F_2$. Its composition is (in wt.%): SiO_2 (46.1-46.9), TiO_2 (up to 0.3), Al_2O_3 (7.5-8.4), FeO_t (up to 0.3), MnO (4.0-5.0), ZnO (5.3-6.8), MgO (17.6-18.5), K_2O (10.2-10.5), Rb_2O (0.2-0.6). The appearance of ^{61}Zn -containing minerals (kupletskite, hendricksite, phlogopite) in the Oktyabrsky phonolites indicate low fS_2 , high fO_2 , high alkalinity (peralkalinity) and high contents of volatiles during their crystallization. These rocks represent the latest derivatives of the massif. They lack sulphide mineralization and contain the high abundance of H_2O - or F -bearing minerals, all Fe as Fe^{3+} is mainly accumulated in aegirine.

Keywords: *hendricksite, phlogopite, tainiolite, peralkaline phonolite, Oktyabrsky massif, Ukraine*

INTRODUCTION

Zincian trioctahedral micas occur very rarely in nature. Hendricksite, ideally $K(Zn,Mg,Mn)_3[AlSi_3O_{10}](OH)_2$, a Zn-dominant member of the mica group, was first described by [10] and by [9] in the skarn zones of the Mn-Zn-deposit at

Franklin Furnace, New Jersey, USA. Since then, according to the Internet (www.mindat.org/min-1864.html) this mineral was also indicated in Argentina (mine no. 6, San Miguel Group, Córdoba) and Tasmania (Grieves Siding deposit, Oceana mine area, Zeehan). Zn-rich mica from the latter occurrence was identified by XRD and is not supported still by chemical data (personal communication of R. Bottrill, Mineral Resources Tasmania). However, zincian phlogopite and biotite (up to 12.5 wt.% ZnO) are common of Mn-Zn skarns and ores of both Franklin Furnace and nearby Sterling Hills [6,10,11;35]. A moderate Zn-enrichment (0.2-1.5 wt.% ZnO) is also observed in biotite, protolithionite and zinnwaldite from some A-type granites [1,8,19,32,33,34].

Hendricksite has been found in peralkaline fine-grained phonolite of the Oktyabrsky massif, Ukraine [31] that is the first occurrence of this mineral in igneous alkaline rocks. Later zincian phlogopite was observed in porphyric phonolite of this massif. The aim of this study is to discuss the specific features of chemical composition for Zn-rich micas in peralkaline phonolites and the behaviour of Zn in plutonic alkaline environments.

BRIEF DATA FOR THE OKTYABRSKY MASSIF

The Oktyabrsky massif (former name - Mariupol) is one of the oldest and largest alkaline complexes of the Azov sea region, Ukrainian shield (age -1.8 Ga, square $\approx 40 \text{ km}^2$). The complex is mainly composed of alkaline syenites and foyaites. Mariupolites and their pegmatites, subalkaline gabbros and their derivatives (peridotites, pyroxenites and olivinites) are minor [16-18]. Dyke rocks (aegirine foyaites, phonolites and nepheline syenite porphyries) are also not abundant and predominantly localized beyond of the massif in the country Proterozoic granitoids. They are the latest differentiated products of the Oktyabrsky alkaline complex [16,18]. The majority of alkaline syenites and foyaites within the massif show miaskitic features. Mariupolites are miaskitic to agpaitic and contain accessory minerals (zircon, pyrochlore, britholite) common of miaskitic nepheline syenites. Only melanocratic mariupolites indicate peralkaline character with $(\text{Na}+\text{K})/\text{Al}$ up to 1.5 due to the abundance of aegirine and Na-foids. The dyke rocks (aegirine foyaites and phonolites) show strong agpaitic features, $(\text{Na}+\text{K})/\text{Al} > 1.1$ and occasionally contain eudialyte, catapleiite and the astrophyllite-group minerals [7,16,18].

PETROGRAPHY OF PERALKALINE PHONOLITES

The studied peralkaline phonolites are localized in 4 km to the north of the Oktyabrsky massif (gully Kamennaya, upper reaches of the Kalka River). These rocks are seemed to form a small plug (50×20 m) in granites. [21] described them as dyke mariupolitic phonolites.

Two textural species of phonolites occur on this locality. The main species is

fine-grained phonolite. This rock is holocrystalline, massive and gray-colored. Rare phenocrysts (up to 5 mm) and microphenocrysts (<0.5 mm) of K-feldspar, nepheline and Zn-kupletskite are set in the fine-grained groundmass composed of leucocratic minerals (nepheline, K-feldspar, albite and sodalite), aegirine and fluorite. The associated minor and accessory phases in the groundmass are Zn-kupletskite, Na-catapleiite, serandite, mineral of the cancrinite group, REE-Zr-Mn-rich mineral of the eudialyte group, hendricksite, cryolite, cerite-(Ce), fluorapatite with Na-REE-fluorapatite rim, thorianite, thorite and U-REE-rich pyrochlore [31]. The second rock type is porphyric and occasionally occurs as small clasts (up to 2-3 cm) in the fine-grained phonolite. It contains up to 50% of phenocrysts (2-7 mm) in finer-grained and more melanocratic groundmass than that in the host phonolite (Fig. 1). Besides textural signature, the porphyric phonolite strongly differs from the fine-grained phonolite in higher contents of F-bearing minerals. This species contains abundant F-bearing phenocrysts (cerite-(Ce), Zn-kupletskite and fluorite) and groundmass phosphates (fluorapatite rimmed by Na-REE-fluorapatite). In addition, copper as rounded inclusions in fluorapatite, zincian phlogopite and an unidentified silicate containing Na, Ca, Y, Ti, Nb and F (the götzenite group ?) occur in this phonolite. The appearance of two phonolite species strongly suggests the two-stage emplacement or crystal fractionation of an initial phonolite melt in an intermediate magmatic chamber before emplacement.

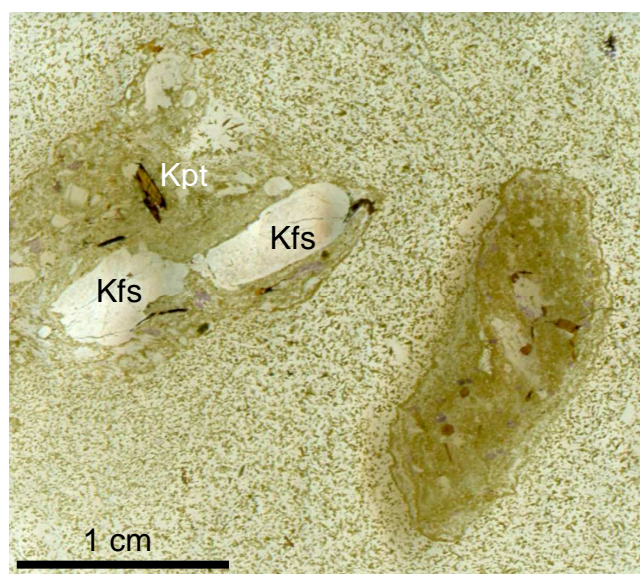


Fig 1. Porphyric clasts in fine-grained phonolite, Oktyabrsky massif (transmitted light). K-feldspar, Zn-kupletskite, cerite-(Ce) and fluorite are the main phenocrysts in porphyric phonolite. Symbols: Kpt = Zn-kupletskite; Kfs = K-feldspar.

The variations of chemical composition of the fine-grained phonolites are (in wt.%): SiO₂ -54.8-55.3; TiO₂ - 0.03-0.8; Al₂O₃ - 18.8-20.2; Fe₂O₃ - 5.9-6.0; FeO -

0.1-1.2; MnO - 0.5-0.6; MgO - 0.3-0.7; CaO - 0.9-1.7; Na₂O - 10.8-11.3; K₂O - 4.2-4.5; P₂O₅ - up to 0.1, F - up to 0.4, Peralkaline Index - 1.12-1.25 [16,21]. The average contents of some trace elements are (in ppm): Li - 13; Rb - 405; Sr - 35; Ba - 50; Zr - 3050; Nb - 532; Y - 243; La - 240; Ce - 390; Nd - 235 [18]. New determinations (three analyses by ICP-MS, unpublished data) also show high concentrations of Zn (300-400), Ta (30-35); Th (30-45), U (8-11); Pb (25-30) and Be (15-20 ppm).

ANALYTICAL METHODS

Double-polished rock sections (~ 50-100 μm in thickness) were used for optical examination of phonolite samples in transmitted and reflected light. Zn-rich micas very resemble Zn-kupletskite in optical and morphological properties, so their preliminary identification was provided by energy-dispersive spectra (EDS), back-scattered electron (BSE) images and elemental mapping (EDS system), using JEOL 6380LA and Leo 1430VP scanning electron microscopes at the V.S. Sobolev Institute of Geology and Mineralogy (IGM), Novosibirsk, Russia. The operating conditions were as follows: accelerating voltage of 20 kV and a probe current of 1 nA, low vacuum of 40-60 Pa or high vacuum.

Electron microprobe analyses (EMPA) of Zn-micas were made at IGM, Novosibirsk, using a "CAMEBAX-micro" electron microprobe. The operating conditions were as follows: beam diameter of 1-2 μm, accelerating voltage of 20 kV and a beam current of 15-25 nA, counting time of 10 s (for all elements). Data reduction was performed using a PAP routine. Overlap corrections for Si(Kα)-Sr(Lα), Si(Kα)-Rb(Lα), Mn(Kβ)-Fe(Kα), Mn(Lα)-F(Kα), Fe(Lα)-F(Kα) and Zn(Lα)-Na(Kα) were done. Precision for major elements was better than 2 rel.%. A total of 12 elements were sought following standards were employed: orthoclase (K-Kα and Al-Kα), diopside (Si-Kα, Ca-Kα and Mg-Kα), rhodonite (Mn-Kα), synthetic ZnFe₂O₄ (Zn-Kα), pyrope (Fe-Kα), synthetic RbNd(WO₄)₂ (RbLα), albite (Na-Kα), ilmenite (Ti-Kα) and synthetic fluorphogopite (F-Kα). Also sought but not detected by microprobe were Ba, Sr, Y, Th, La, Ce, Nd, Zr, Nb and Ta. Microprobe analyses were performed on the grains larger than 5-10 μm. Total iron in Zn-mica compositions from the Oktyabrsky phonolite is labeled as FeO. However, the presence of Fe₂O₃ is not excluded because the rock-forming pyroxene is dominant in Fe³⁺ (aegirine). All manganese is suggested to be Mn²⁺, as other Mn-rich minerals (Zn-kupletskite, serandite) contain only MnO.

The concentrations of some trace elements (Be, Li, B, Rb, Ba, Sr and Cs), water and F in the largest hendricksite blades (>20 μm) were analyzed by secondary-ion mass spectroscopy (SIMS), using a Cameca IMS-4f ion probe at the Yaroslavl' branch of the Physicotechnological Institute (YBPTI), Yaroslavl', Russia. The operating conditions were as follows: primary O²⁻ beam of 20 μm, a beam current of 2-4 nA, energy offset of 100 eV and energy slit of 50 eV.

Concentrations of elements were determined from the ratios of their isotopes to ^{30}Si , using calibration curves for standard samples [15]. Low background contents of H_2O (<0.03 wt.%) were due to the 24 h high-vacuum exposure of the samples in the mass spectrometer. The conditions for fluorine determination were described by [26].

ZINCIAN MICAS IN PHONOLITES

Hendricksite

Hendricksite was identified in the fine-grained phonolite samples. This Zn-rich mica forms brown blades (20-40 μm), which commonly confined to Zn-kupletskite phenocrysts and microphenocrysts, sometimes overgrowing those (Figs. 2-3). Discrete small blades (up to 20 μm) and larger grains (microphenocrysts, up to $150\times 20\ \mu\text{m}$) of hendricksite rarely occur in the fine-grained groundmass (Fig. 2). The strong chemical difference between and Zn-kupletskite is clearly shown on the BSE images and elemental maps (Fig. 3). Their relationships indicate that Zn-kupletskite crystallised earlier than hendricksite.

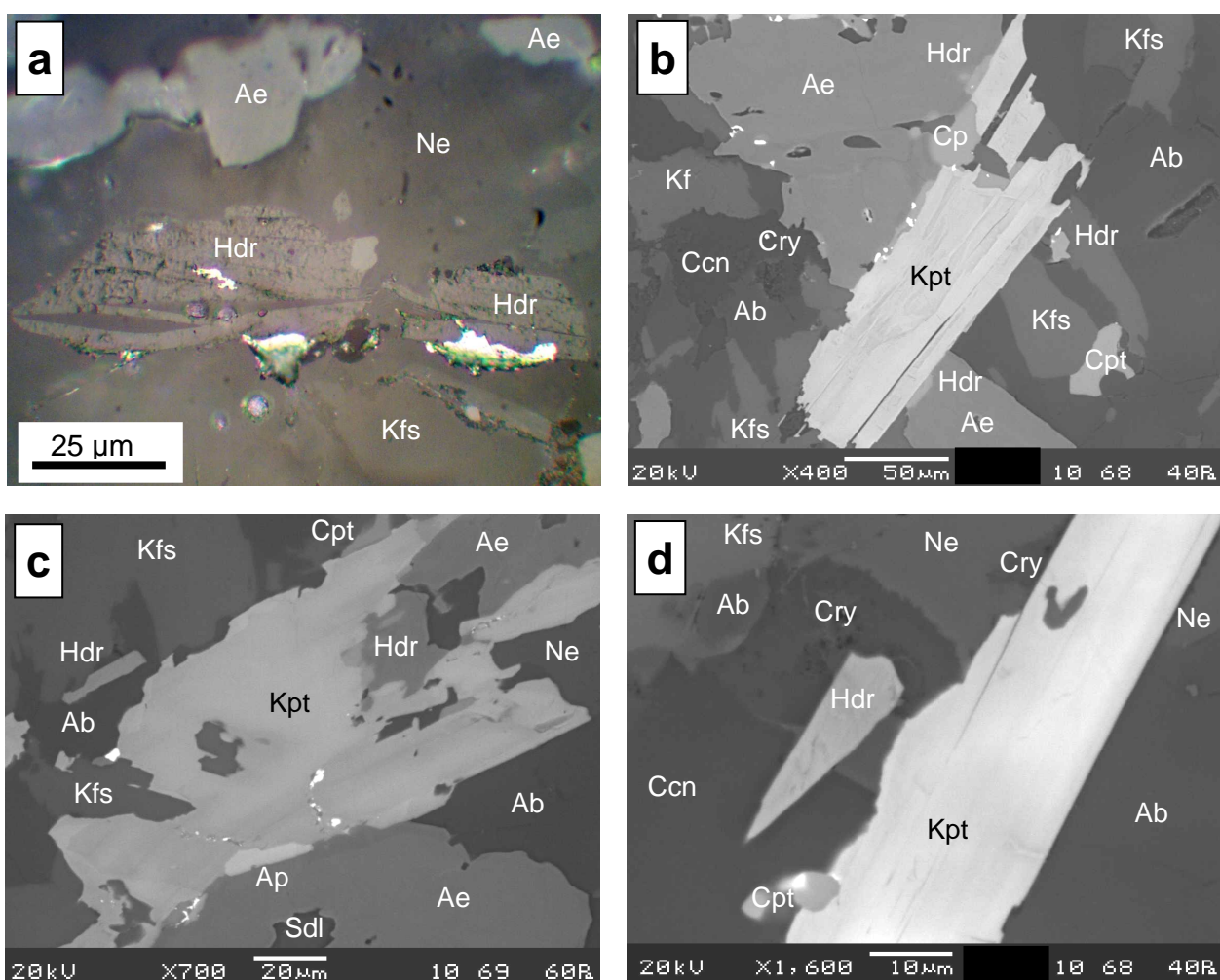
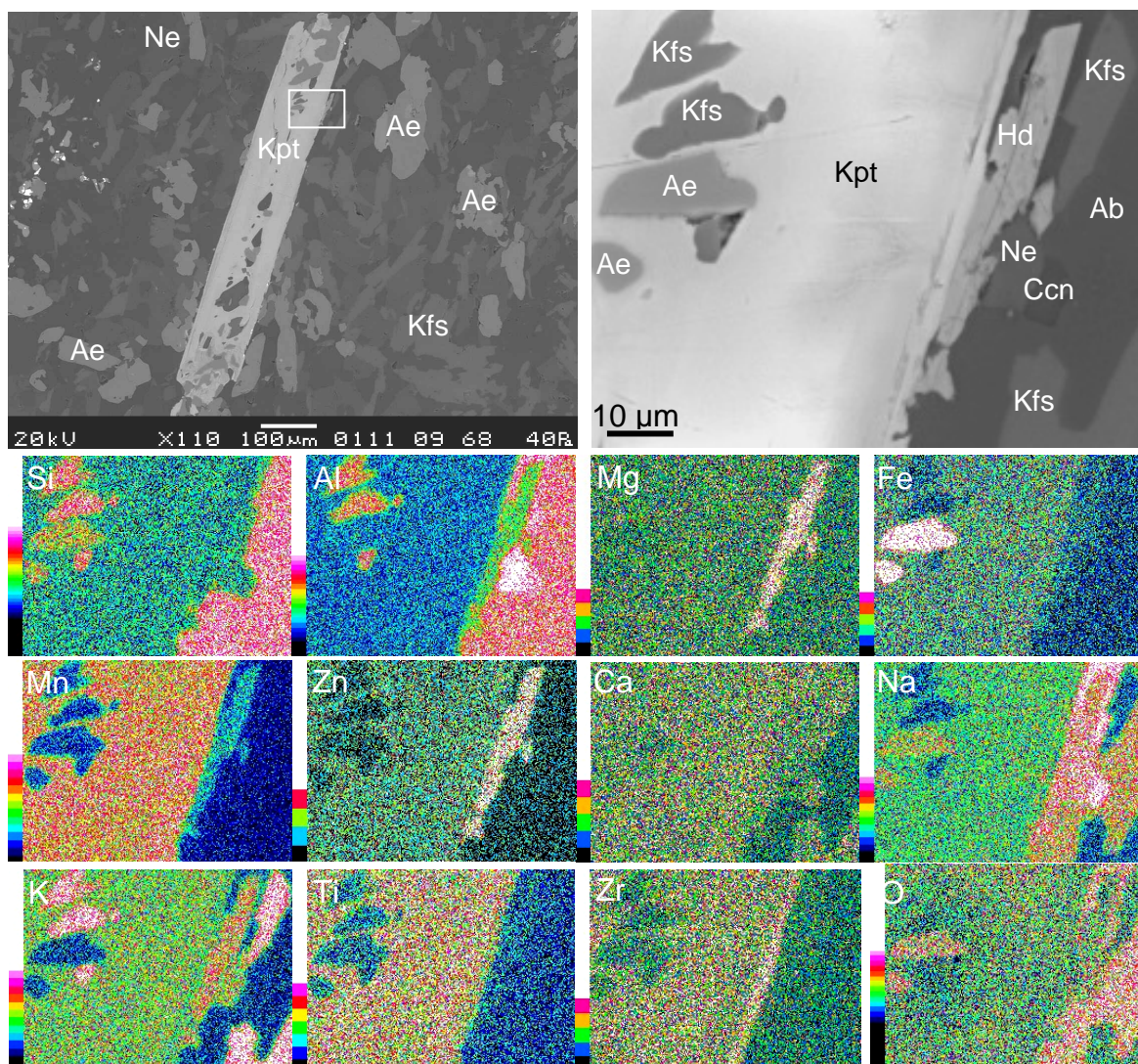


Fig. 2. **Hendricksite in peralkaline fine-grained phonolite, Oktyabrsky massif.**

a - large grain (microphenocryst) of hendricksite in groundmass, reflected light (after microprobe); b-d - small grains of hendricksite in association with Zn-kupletskite, BSE images. Symbols: Hdr = hendricksite; Kpt = Zn-kupletskite; Ae = aegirine; Kfs = K-feldspar; Ab = albite; Ne = nepheline; Ccn = a mineral of the cancrinite group; Sdl = sodalite; Cpt = Na-catapleiite; Cry = cryolite; Ap - Na-REE-rich fluorapatite.

Zincian phlogopite

This Zn-rich mica is observed in porphyric phonolite clasts. It forms large colorless blades (microphenocrysts, 20-50×100-200 μm) in the groundmass (Fig. 4). The relations among groundmass minerals are shown that Zn-phlogopite



crystallized after aegirine and fluorite and before or together with Zn-kupletskite.

Fig. 3. **BSE images and elemental maps for hendricksite overgrown on a Zn-kupletskite phenocryst.** Symbols see Fig. 2.

CHEMICAL COMPOSITION

The EMPA data for hendricksite from the Oktyabrsky fine-grained phonolite show high SiO₂ (37.7-38.7), ZnO (21.5-25.8), MgO (6.9-9.7), F (1.5-2.3) and low Al₂O₃ (10.1-10.9), TiO₂ (up to 0.3), FeO_t (0.3-1.4) and MnO (6.4-7.7 wt.%). Representative analyses are given in Table 1. Namely in these components, the Oktyabrsky hendricksite strongly differs from the holotype of Mn-Zn-skarns at Franklin Furnace [9,10,12].

Most grains of the Oktyabrsky hendricksite show relatively little compositional variation. Pronounced chemical zoning was observed only in one groundmass microphenocryst (Fig. 1a) indicating an increase in ZnO and depletion in MgO, MnO and F from the core to rim (Table 1). Like Zn-kupletskite [31], the Zn-mica from the fine-grained phonolite contains appreciable Rb₂O (0.5-0.8 wt.%).

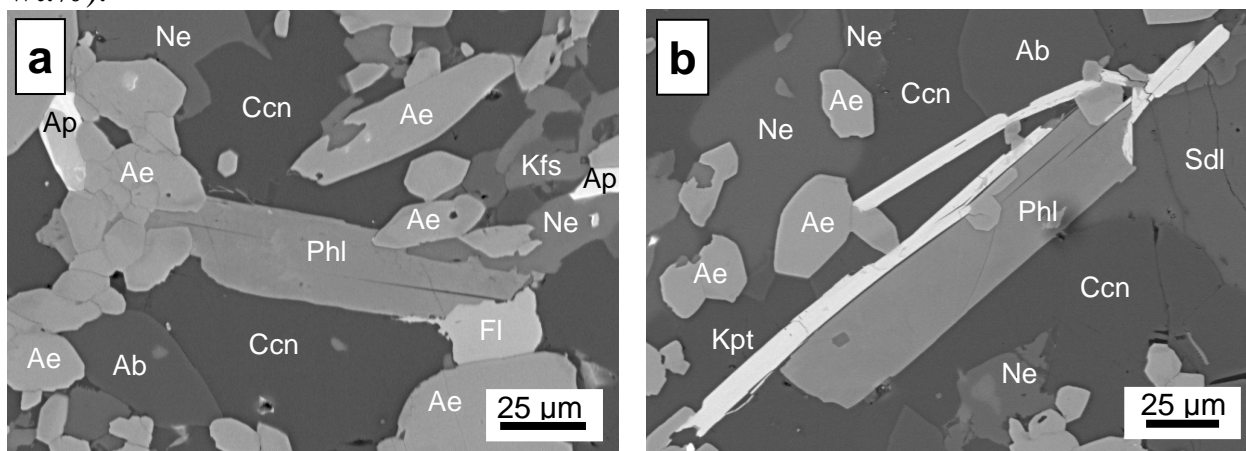


Fig. 4. **BSE images of Zn-bearing phlogopite in the groundmass of porphyric phonolite.**

a) in association with fluorite; b) in association with Zn-kupletskite. Phl = Zn-bearing phlogopite; Fl = fluorite; Ap - fluorapatite with rim of Na-REE-fluorapatite, other symbols see Fig. 2.

The SIMS data confirmed the high concentrations of Rb and F obtained by EMPA (Table 1, analyses 1-2) and showed high contents of H₂O (2.1-2.5 wt.%) and Li (1350-1390 ppm) and low amounts of other trace elements (in ppm): Ba - <33; Cs - <66; Sr - <66; Be - <20; B - <1. In comparison, hendricksite at Franklin Furnace contains lower Li₂O (0.04 wt.%, [9]) and higher BaO (0.3-1.3 wt.%, [9,10,12]).

Unlike hendricksite, Zn-containing mica from the porphyric phonolite is more siliceous and magnesian compositions (in wt.%): SiO₂ - 46.1-46.9; TiO₂ - up to 0.3; Al₂O₃ - 7.5-8.4; FeO_t - up to 0.3; MnO - 4.0-5.0; ZnO - 5.3-6.8; MgO - 17.6-18.5; Na₂O - up to 0.1; K₂O - 10.2-10.5; Rb₂O - 0.2-0.6; F - 5.3-5.9. Chemical zoning of individual grains is not indicated on the BSE images (Fig. 4) due to weak variations in ZnO, MgO, and Al₂O₃. The core-to-rim compositions of three individual grains from the groundmass are given in Table 2. Besides high concentrations of SiO₂, MgO and F, compositions show the 2-3 wt.% deficit to total 100 wt.%, that strongly suggests the presence of H₂O and Li₂O.

Table 1.

EMPA and SIMS analyses of hendricksite in fine-grained peralkaline phonolite

	1	2	3	4	5	6	7	8	
wt. %	core	rim							
SiO₂	37.86	38.01	37.78	37.48	37.90	37.89	38.04	37.89	31.58
TiO₂	0.11	0.07	0.24	0.10	0.15	0.18	0.10	0.17	0.32
Al₂O₃	10.00	10.19	10.15	10.44	10.14	10.11	10.39	10.11	13.72
FeO_t	0.61	0.47	0.39	0.50	1.39	0.38	1.11	0.28	2.36
MnO	7.40	7.04	7.53	6.49	7.17	6.93	6.35	7.39	12.28
ZnO	22.62	24.85	22.87	25.81	24.30	23.10	24.46	23.14	22.97
MgO	7.84	6.63	7.61	7.18	6.30	8.63	6.88	7.50	3.69
CaO	0.01	0.05	0.06	0.00	0.03	0.00	0.05	0.02	-
Na₂O	0.00	0.00	0.00	0.02	0.04	0.02	0.07	0.04	0.24
K₂O	8.94	8.78	8.79	8.68	8.65	8.65	8.48	8.73	7.91
Rb₂O	0.73	0.77	0.74	0.75	0.70	0.73	0.74	0.74	-
Li₂O_{SIMS}	0.29	-	0.30	-	-	-	-	-	-
H₂O*	2.62	2.34	2.82	2.72	2.46	2.74	2.55	2.27	3.65
F	2.23	1.70	1.78	1.60	1.50	1.62	1.38	1.94	0.45
Sum	101.25	100.90	101.04	101.78	100.73	100.97	100.60	100.22	99.82
O=F	-0.94	-0.72	-0.75	-0.67	0.63	-0.68	-0.58	-0.82	-0.19
Sum	100.31	100.18	100.29	101.11	100.10	100.29	100.02	99.40	99.63
SIMS									
H₂O, wt. %	2.13		2.53						
F, wt. %	2.64		1.76						
Rb₂O, wt. %	0.58		0.81						
B, ppm	0.4		0.9						
Be, ppm	13.7		19.6						
Ba, ppm	32.9		16.5						
Cs, ppm	66.2		40.5						
Sr, ppm	25.7		65.8						
Formulae based on 14 cations									
Si	6.159	6.286	6.146	6.134	6.277	6.165	6.267	6.263	5.338
Al^{IV}	1.841	1.714	1.854	1.866	1.723	1.835	1.733	1.737	2.662
Σ T	8.000	8.000	8.000	8.000	8.000	8.000	8.000	8.000	8.000
Al^{VI}	0.076	0.272	0.092	0.148	0.256	0.104	0.284	0.233	0.071
Ti	0.014	0.009	0.029	0.012	0.019	0.022	0.013	0.022	0.041
Fe	0.083	0.065	0.053	0.069	0.193	0.051	0.153	0.039	0.334
Mn	1.020	0.985	1.037	0.900	1.006	0.955	0.885	1.034	1.758
Zn	2.717	3.034	2.748	3.119	2.972	2.775	2.975	2.825	2.867
Mg	1.901	1.634	1.845	1.751	1.555	2.093	1.689	1.848	0.929
Li	0.190	-	0.196	-	-	-	-	-	-
Σ M	6.000	6.000	6.000	6.000	6.000	6.000	6.000	6.000	6.000
Ca	0.001	0.008	0.010	0.000	0.005	0.001	0.008	0.004	-
Na	0.000	0.000	0.000	0.007	0.013	0.007	0.023	0.013	0.079
K	1.854	1.852	1.823	1.812	1.828	1.796	1.782	1.840	1.706
Rb	0.077	0.082	0.077	0.079	0.075	0.076	0.079	0.079	-
Σ I	1.932	1.943	1.910	1.899	1.846	1.879	1.892	1.935	1.827
OH	2.848	2.583	3.065	2.966	2.718	2.973	2.803	2.504	4.115
F	1.146	0.889	0.914	0.828	0.786	0.835	0.720	1.016	0.241
O	0.006	0.527	0.020	0.206	0.496	0.192	0.477	0.479	-
Σ cations	15.932	15.943	15.910	15.899	15.920	15.879	15.892	15.935	15.827
End-members, mole %									
K₂Zn₆(AlSi₃O₁₀)₂(OH,F)₄	47.50	53.06	48.35	53.42	51.91	47.24	52.17	49.17	48.69
K₂Mn₆(AlSi₃O₁₀)₂(OH,F)	17.83	17.23	18.25	15.41	17.57	16.26	15.52	18.00	29.86
K₂Mg₆(AlSi₃O₁₀)₂(OH,F)	33.23	28.57	32.47	29.99	27.16	35.62	29.62	32.16	15.79
K₂Fe₆(AlSi₃O₁₀)₂(OH,F)₄	1.45	1.14	0.93	1.18	3.36	0.88	2.69	0.67	5.67

Note: 1 - core and rim of a large grain (microphenocryst) in groundmass; 2-4 - small blades around Zn-kupletskite microphenocrysts; 5-7 - individual small blades in groundmass; 8 - holotype from Franklin Furnace (Frondel and Ito, 1966). Total includes 0.65 wt.% BaO (0.043 apfu Ba). Initial FeO (0.34 wt.%) and Fe₂O₃ (2.25

wt.%) are recalculated as FeO. H₂O* = calculation on the basis of total positive charge and (OH+F+O)=4 apfu.

Table 2.

. EMPA analyses of Zn-bearing lithian phlogopite in porphyric peralkaline phonolite

wt.%	1		2		3		4
	core	rim	core	rim	core	rim	ideal
SiO₂	46.55	46.26	46.73	46.53	46.20	46.39	46.43
TiO₂	0.28	0.21	0.26	0.28	0.19	0.21	
Al₂O₃	7.92	8.25	7.59	8.07	8.48	8.36	7.30
FeO	0.18	0.05	0.23	0.12	0.10	0.17	
MnO	4.34	4.55	4.39	4.21	4.72	4.11	4.06
ZnO	5.30	6.65	5.36	6.62	6.82	5.94	6.99
MgO	17.95	18.18	18.38	18.01	17.78	18.48	18.46
Na₂O	0.07	0.00	0.05	0.00	0.09	0.10	
K₂O	10.33	10.31	10.39	10.40	10.40	10.36	10.78
Rb₂O	0.55	0.30	0.29	0.21	0.27	0.25	
Li₂O*	1.32	1.09	1.19	1.18	1.15	1.17	1.28
F	5.80	5.53	5.93	5.76	5.84	5.55	5.44
H₂O*	1.11	1.30	1.01	1.18	1.18	1.31	1.55
Sum	101.70	102.68	101.81	102.56	103.20	102.41	102.29
O=F	2.44	2.33	2.50	2.42	2.46	2.34	2.29
Sum	99.26	100.35	99.31	100.14	100.74	100.07	100.00
Formulae based on 14 cations							
Si	6.796	6.718	6.820	6.758	6.697	6.718	6.750
Al^{IV}	1.204	1.282	1.180	1.242	1.303	1.282	1.250
Σ T	8.000	8.000	8.000	8.000	8.000	8.000	8.000
Al^{VI}	0.159	0.129	0.125	0.140	0.145	0.145	
Ti	0.030	0.023	0.029	0.031	0.020	0.023	
Fe	0.022	0.007	0.028	0.015	0.012	0.021	
Mn	0.537	0.560	0.543	0.517	0.579	0.504	0.500
Zn	0.571	0.713	0.578	0.710	0.730	0.636	0.750
Mg	3.906	3.934	3.998	3.898	3.841	3.989	4.000
Li	0.775	0.634	0.700	0.689	0.673	0.683	0.750
Σ M	6.000	6.000	6.000	6.000	6.000	6.000	6.000
Na	0.020	0.000	0.014	0.000	0.024	0.028	
K	1.924	1.910	1.935	1.927	1.923	1.914	2.000
Rb	0.052	0.028	0.028	0.019	0.025	0.023	
Σ I	1.996	1.938	1.976	1.946	1.972	1.965	2.000
F	2.678	2.540	2.737	2.646	2.677	2.542	2.500
O	0.237	0.197	0.278	0.216	0.181	0.191	
OH	1.085	1.263	0.985	1.139	1.142	1.267	1.500
Σ cations	15.996	15.938	15.976	15.946	15.972	15.965	16.000

Note: BaO, CaO are below detection limits (0.01 wt.%).

1-3 - core and rim of individual grains from the groundmass; 4 - ideal composition $K_2(Mg_4Zn_{0.75}Mn_{0.5}Li_{0.75})[Al_{1.25}Si_{6.75}O_{20}]F_{2.5}(OH)_{1.5}$.
 Li_2O^* = quoted from formula calculations on the basis of 44 positive charges

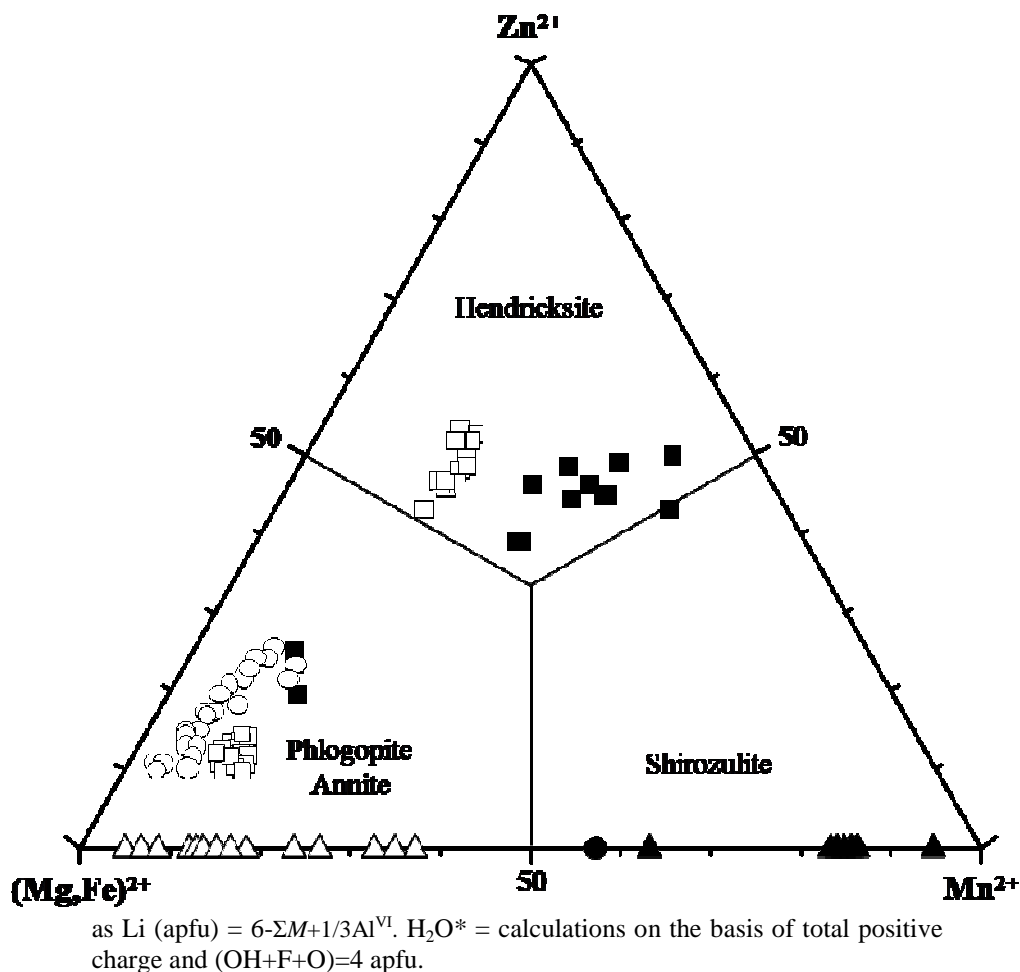


Fig. 5. Compositional variations of hendricksite and Zn-bearing phlogopite from phonolites of the Oktyabrsky massif in comparison with Zn- and Mn-rich micas from Zn-Mn deposits. Open squares – hendricksite and Zn-bearing phlogopite from fine-grained and porphyric phonolites, respectively, Oktyabrsky massif, Ukraine (original data); solid squares - hendricksite (holotype) and Zn-bearing phlogopite, Franklin Furnace, NJ, USA [9,10,12,29]; open circles - Zn-bearing phlogopite and other Zn-bearing micas, Sterling Hill, NJ, USA [6,11,35]; solid circles - shirozulite (holotype), Taguchi, Aichi Prefecture, Japan [14]; solid triangles - Al-poor tetrasilicic Mn-mica (shirozulite ?), Mn-deposits of South Urals, Russia [3]; open triangles - manganooan phlogopite (manganophyllite) and annite, worldwide Mn-deposits and granites [4,5,34,36].

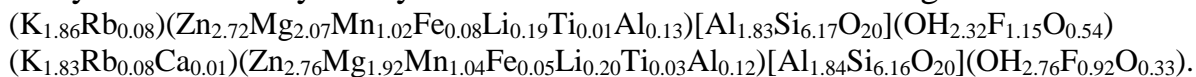
This mica seems to be an intermediate member of the phlogopite-tainiolite series. However, no compositions strongly enriched in ZnO and MnO are previously found elsewhere for this series ([23] and references herein; [2]).

CRYSTAL CHEMISTRY

Crystal structure refinement were provided only for zincian manganooan

phlogopite (9.38 wt.% ZnO, 6.03 wt.% MnO) from the Franklin Furnace deposit [29]. According to these data, all Zn^{2+} occupies exclusively the octahedral sites in the mica structure and there is no order among six-folded coordinated cations.

Calculations based on of 24(O,OH,F) for two complete (EMPA+SIMS) analyses of the Oktyabrsky hendricksite showed the following formulae:



These calculations indicate some cation deficiency (0.06-0.08 apfu) in the interlayer site and minor presence of octahedral Al and absence of tetrahedral Fe^{3+} . In general, those are consistent with calculations on the basis of 14 cations (tetrahedral and octahedral sites) given in Table 1. However, the latter method is also non-ideal variant to calculate formula for the Oktyabrsky hendricksite when composition was determined by microprobe only (without Li_2O). Even moderate content of Li_2O (0.3 wt.%) which commonly occupies the octahedral site in the structure of the trioctahedral micas has an essential influence on the contents of octahedral Al and oxygen in the (OH,F,O) position. In case of the Oktyabrsky hendricksite, the absence of Li in formula calculations does lead to some increase of these components (Table 1).

The simplified formula of the Oktyabrsky hendricksite may be expressed as $K_2(Zn_3Mg_2Mn)[Al_2Si_6O_{20}](OH)_3F$, which strongly differs from that of holotype $K_2(Zn_3MgMn_2)[Al_2Si_6O_{20}](OH)_4$ at Franklin Furnace [9,10,12]. Both hendricksite species can be related due to isomorphism $Mg^{2+} + F^{-1} \leftrightarrow Mn^{2+} + (OH)^{-1}$. The compositional variations of hendricksite are seen clearly on the ternary diagram $(Mg,Fe)^{2+} - Zn^{2+} - Mn^{2+}$, showing the ideal end-members (phlogopite-annite, hendricksite, shirozulite) (Fig. 5). In general, compositions of hendricksite both from the Oktyabrsky phonolite and from the Franklin skarns are so far from ideal $K_2Zn_6[AlSi_3O_{10}]_2(OH,F)_4$ and are localized near medians of the hendricksite-phlogopite and hendricksite-shirozulite lines, respectively. It generally reflects the different isomorphous schemes for hendricksite: $Mg^{2+} \leftrightarrow Zn^{2+}$ for the Oktyabrsky specimen and $(Mg,Fe)^{2+} \leftrightarrow (Zn,Mn)^{2+}$ for the Franklin sample (Fig. 5).

In addition, mineral from both occurrences strongly differs in the Si/Al ratio in the tetrahedral site: 3.3-3.7 for the Oktyabrsky specimen and 2.0-2.2 for the Franklin sample. Low-Ba zincian phlogopite and biotite at Franklin Furnace and Sterling Hill indicate the Si/Al ratio in the range of 2.1-2.9 [6,11,29,35].

In general, the appreciable high contents of Si in the Oktyabrsky hendricksite can be explained by following schemes of the heterovalent isomorphism: ${}^{IV}Al^{3+} + {}^{VI}M^{2+} + 2(OH,F)^{-1} \leftrightarrow {}^{IV}Si^{4+} + {}^{VI}Al^{3+} + 2O^{2-}$ [31] or ${}^{IV}Al^{3+} + {}^{VI}M^{2+} \leftrightarrow {}^{IV}Si^{4+} + {}^{VI}Li^{1+}$, where $M^{2+} = Mg, Zn, Mn, Fe$.

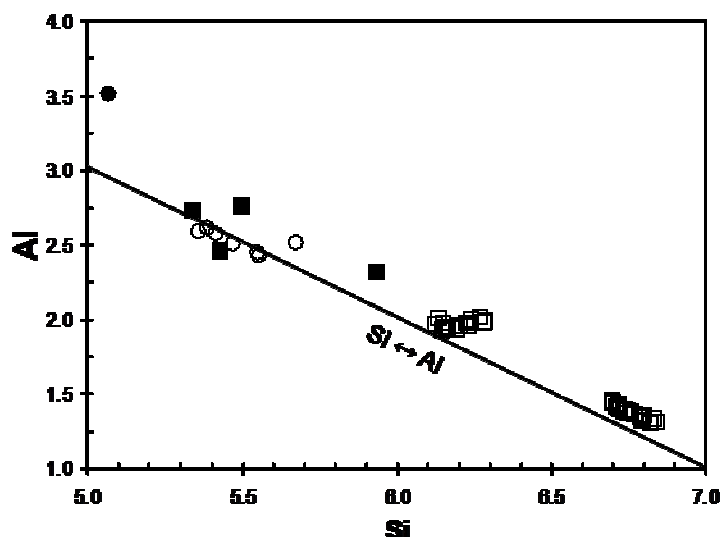
The undetermined Li_2O and H_2O gave particular difficulties in calculations of formula for Zn-containing phlogopite from the porphyric phonolite (see above). We used the following way: the Li_2O contents were estimated from formula calculations on the basis of 44 positive charges as $Li \text{ (apfu)} = 6 - \Sigma M + 1/3Al^{VI}$; these

values were quoted for calculations on the basis of 14 cations (tetrahedral and octahedral sites); the H₂O contents have been obtained from charge balance and (OH+F+O)=4 apfu. Thus, the simplified formula of the Oktyabrsky phlogopite can be expressed as K₂(Mg₄Zn_{0.75}Mn_{0.5}Li_{0.75})[Al_{1.25}Si_{6.75}O₂₀]F_{2.5}(OH)_{1.5} (Table 2), that is Zn-Li-Mn-F-containing phlogopite intermediate between phlogopite KMg₃[AlSi₃O₁₀](OH)₂ and tainiolite KLiMg₂[Si₄O₁₀]F₂ via the isomorphism ^{IV}Al³⁺ + ^{VI}Mg²⁺ + OH¹⁻ ↔ ^{IV}Si⁴⁺ + ^{VI}Li¹⁺ + F¹⁻. The incorporation of Zn and Mn in the octahedral sites is due to the schemes Mg²⁺ ↔ Zn²⁺ and Mg²⁺ ↔ Mn²⁺.

Discussion

Behavior of Zn in alkaline magmatic system

The occurrence of minerals, containing ^[6]Zn in the crystal structure (kupletskite, hendricksite), in alkaline rocks indicate low *f*S₂, high *f*O₂, high alkalinity (peralkalinity) and high fluid contents of environment [22,25]. Similar conditions are most common of the latest crystallization products of the large peralkaline magmatic complexes such as Khibini, Lovozero and Mont Saint-Hilaire. In this



sense, the peralkaline phonolites of the Oktyabrsky massif are also the remarkable

Fig. 6. Si plotted against total Al (a.p.f.u.) for hendricksite, Zn-bearing micas and shirozulite.

Symbols see Fig. 5. Zn-bearing micas with high BaO (>9 wt.%, Sterling Hill) are not shown here.

example. These rocks represent the latest derivatives of the massif. They lack sulfide mineralization; Fe as Fe³⁺ is mainly accumulated in aegirine. There are also significant amounts of silicates containing ^[6]Zn (kupletskite, hendricksite), and H₂O- or F-bearing minerals (fluorite, cryolite, cerite-(Ce), Na-catapleiite, serandite,

REE-eudialyte, Na-REE-fluorapatite, U-REE-pyrochlore, and others). In case of the fine-grained phonolite, hendricksite crystallized later than Zn-kupletskite, and during crystallization a gradual increase in ^{67}Zn and F is indicated. In particular, ^{67}Zn in kupletskite occupies 12.5-18.7% of the octahedral sites, and F accounts for 14.5–20% of 5(OH,F,O). In hendricksite, these values increase up to 45.2-52% for ^{67}Zn and to 18-32.5% of 4(OH,F,O) for F [31]. In porphyric phonolite the increasing of F is more drastical, whereas the Zn abundance is near constant for the kupletskite – mica pair. It should be noted that both phonolite types of the Oktyabrskii massif contain fluorite CaF_2 and cryolite Na_3AlF_6 . However, the very high abundance of F in crystallizing environment seems to be not promoted the complete accumulation of Zn in phyllosilicates and this element may be incorporated by other silicates. It is indicated in the porphyric phonolites which contain higher amount of F-rich minerals than the fine-grained species. Both kupletskite and mica in porphyric phonolite are poorer in ZnO. The phenocrystal and groundmass kupletskite in this rock contains 4-4.5 wt.% ZnO (author's data), whereas mineral from the fine-grained phonolite is richer in ZnO (6.3-7.9 wt.%, [31]). Hendricksite with 21.5-25.8 wt.% ZnO is dominant mica in the fine-grained phonolite, whereas phogopite from porphyric phonolite contains 5.3-6.8 wt.% ZnO.

Stability of Zn- and Mn-dominant trioctahedral micas

Synthetic micas of the ideal end-members $\text{KZn}_3[\text{AlSi}_3\text{O}_{10}](\text{OH})_2$ and $\text{KMn}_3[\text{AlSi}_3\text{O}_{10}](\text{OH})_2$ were made by the hydrothermal crystallization from stoichiometric gels and mixture (oxides + $\text{K}_2\text{Si}_2\text{O}_5$) at 1-3 kb and 250-650°C [10,13]. [24] synthesized a Zn-containing phlogopite at 55-85°C from gels with low ZnO concentration. However, [14] stated that ideal shirozulite composition $\text{KMn}_3[\text{AlSi}_3\text{O}_{10}](\text{OH})_2$ seems to be an unstable phase in natural conditions as the octahedral layer is very larger in size than tetrahedral layer. The Mn^{2+} ion completely occupies the octahedral sites in the structure, but its ionic radius (0.83 Å) are significantly larger than common six-coordinated Mg^{2+} and Fe^{2+} (0.72 and 0.78 Å, respectively, [30]) in trioctahedral micas. There are no variants to compensate the difference in the size between the octahedral and tetrahedral layers. Unlike the ideal composition, the holotype shirozulite from Taguchi, Japan [14] is Mg-rich species with simplified formula $(\text{K}_{0.9}\text{Ba}_{0.1})(\text{Mn}_{1.5}\text{Mg}_{1.0}\text{Fe}^{2+}_{0.2}\text{Al}_{0.3})[\text{Al}_{1.5}\text{Si}_{2.5}\text{O}_{10}](\text{OH})_2$. The additional $^{\text{IV}}\text{Al}$ increases the size of the tetrahedral layer, promoting linkage between the tetrahedral layer and a large octahedral layer. Increasing amounts of six-coordinated Mg, Fe^{2+} , Al and Fe^{3+} have a similar effect diminishing the size of the octahedral layer. The higher Mn^{2+} content ($\gg 50\%$) in the octahedral site will increase the disproportion between the octahedral and tetrahedral layers. [3] proposed another way to compensate this disproportion due to incomplete Mn^{2+} occupation of the octahedral layer according to the isomorphic scheme $^{\text{VI}}\text{R}^{2+} + 2^{\text{IV}}\text{Al}^{3+} \leftrightarrow ^{\text{VI}}\square + 2^{\text{IV}}\text{Si}^{4+}$ what is common of phyllosilicates. This isomorphism lead

to tetrasilic composition $\text{KMn}_{2.5}[\text{Si}_4\text{O}_{10}](\text{OH})_2$, which is an intermediate between the trioctahedral and dioctahedral micas. [3] described similar Al-undersaturated mica from the Mn deposits of the South Urals as shirozulite, but it seems to be a new Mn-member of the mica family and close to montdorite $\text{KFe}^{2+}_{1.5}\text{Mn}^{2+}_{0.5}\text{Mg}_{0.5}[\text{Si}_4\text{O}_{10}]\text{F}_2$ [20,27,28].

Thus, the numerous occurrences of manganophlogopite (manganophyllite) and annite [4,5,34,36] and the discovery of magnesian shirozulite [14] strongly suggest the existence of limited solid solutions phlogopite (annite) - magnesian shirozulite with miscible gap in the region close to the composition $\text{KMn}_3[\text{AlSi}_3\text{O}_{10}](\text{OH})_2$.

In case of the composition $\text{KZn}_3[\text{AlSi}_3\text{O}_{10}](\text{OH})_2$, the octahedral ionic radius of Zn (0.74 Å) is intermediate between Mg^{2+} and Fe^{2+} (0.72 and 0.78 Å, respectively, [30]) that does not lead to the disproportion between the octahedral and tetrahedral layers. Therefore, the complete solid solutions between phlogopite (annite) and ideal hendricksite are highly possible. The Zn-containing micas from the Oktyabrsky phonolites are intermediate members of the phlogopite-hendricksite series. On the line $\text{KZn}_3[\text{AlSi}_3\text{O}_{10}](\text{OH})_2$ - $\text{KMn}_3[\text{AlSi}_3\text{O}_{10}](\text{OH})_2$ it is suggested the existence of the limited solid solution hendricksite – manganese hendricksite – zincian shirozulite with miscible gap in the region close to the composition $\text{KMn}_3[\text{AlSi}_3\text{O}_{10}](\text{OH})_2$. The Franklin hendricksite with the highest Mn content is a member of this series.

ACKNOWLEDGEMENTS

The author thanks L.N. Pospelova, E.N. Nigmatullina, A.T. Titov (IGM, Novosibirsk), S.G. Simakin and Ye.V. Potapov (YBPTI, Yaroslavl') and S.V. Kovyazin (IGM, Novosibirsk) for help in the EMPA, EDS and SIMS analyses of zincian micas. S.G. Krivdik (IGMOF, Kiev) is specially thanked for providing the samples of phonolites. This work was supported by Siberian Division of Russian Academy of Sciences (integration project 6.15).

REFERENCES

1. **Abdalla H., Matsueda H., Ishihara S. and Miura H.** (1994) Mineral chemistry of albite-enriched granitoids at Um Ara, Southeastern Desert, Egypt. // *International Geology Review*, 36, 1067-1077.
2. **Armbruster T., Richards R., Gnos E., Pettke T. and Herwegh M.** (2007) Unusual fibrous sodian tainiolite epitactic on phlogopite from marble xenoliths of Mont Saint-Hilaire, Quebec, Canada. // *The Canadian Mineralogist*, 45, 541-549
3. **Brusnitsyn A.I. and Nesterov A.R.** (2006) Shirozulite in manganese ore deposits of the South Urals, its chemical composition and the formulae of manganese micas. // *Zapiski Vserossiyskogo Mineralogicheskogo Obshchestva*, 135 (2), 93-98 (in Russian with English abstract).
4. **Chen S. and Wu G.** (1987) Mineralogical study of Mn-biotite in miarolitic granite from Kuiqi, Fujian. // *Dizhi Lun ping (Geological Review)*, 33, 222-228 (in Chinese).

5. **Chukhrov F.B., ed.** (1992) Minerals (hand-book). Volume IV. Issue 1. Phyllosilicates. Nauka Publishing, Moscow, 598 pp. (in Russian).
6. **Craig J.R., Sandhaus D.J. and Guy R.E.** (1985) Pyrophanite, $MnTiO_3$, from Sterling Hill, New Jersey. // *The Canadian Mineralogist*, 23, 491-494.
7. **Dubina A.V., Sharygin V.V., Krivdik S.G. and Bondarenko, I.N.** (2008) Mineralogical and geochemical features of agpaitic alkaline rocks of the Oktyabrsky massif, Ukraine. Abstract. Geochemistry of magmatic rocks. Workshop "Alkaline magmatism of the Earth", Saint-Petersburg-Moscow, pp. 47-48 (in Russian).
8. **du Bray E.A.** (1994) Compositions of micas in peraluminous granitoids of the eastern Arabian Shield. Implications for petrogenesis and tectonic setting of highly evolved, rare-metal enriched granites. // *Contributions to Mineralogy and Petrology*, 116, 381-397.
9. **Evans B.W. and Strens, R.G.J.** (1966) Zinc mica from Franklin Furnace, New Jersey. // *Nature*, 211, 619-619.
10. **Fron del C. and Ito J.** (1966) Hendricksite, a new species of mica. // *American Mineralogist*, 51, 1107-1123.
11. **Fron del C. and Einaudi M.** (1968) Zinc-rich micas from Sterling Hill, New Jersey. // *American Mineralogist*, 53, 1752-1754.
12. **Guggenheim S., Schulze W.A., Harris G.A. and Lin J.-C.** (1983) Noncentric layer silicates: An optical second harmonic generation, chemical and X-ray study. // *Clays and Clay Minerals*, 31, 251-260.
13. **Hazen R.M. and Wones D.R.** (1972) The effect of cation substitutions on the physical properties of trioctahedral micas. // *American Mineralogist*, 57, 103-129.
14. **Ishida K., Hawthorne F.C. and Hirowatari F.** (2004) Shirozulite, $KMn^{2+}_3(Si_3Al)O_{10}(OH)_2$, a new manganese-dominant trioctahedral mica: Description and crystal structure. // *American Mineralogist*, 89, 232-238.
15. **Jochum K.P., Dingwen D.B., Rocholl A., Stoll B., Hofmann A.W., Becker S., Besmehn A., Besesette D., Dietze H.-J., Dulski P., Erzinger J., Hellebrand E., Hoppe P., Horn I., Janssens K., Jenner G., Klein M., McDonough W.M., Maetz M., Mezger K., Münker C., Nikogosian I.K., Pickhart C., Raczek I., Rhede D., Seufert H.M., Simakin S.G., Sobolev A.V., Spettel A.V., Straub S., Vincze L., Wallianos A., Weckwerth G., Weyer S., Wolf D. and Zimmer M.** (2000) The preparation and preliminary characterization of eight geological MPI-DING reference glasses for in-situ microanalysis. *Geostandard Newsletters*, 24, 87-133.
16. **Krivdik S.G. and Tkachuk V.I.** (1988) Eudyalite-bearing agpaitic phonolites and dike nepheline syenites of the Oktyabrsky massif, Ukrainian Shield. // *Geokhimiya*, 26, 1133-1139 (in Russian).
17. **Krivdik S.G. and Tkachuk V.I.** (1990) The petrology of alkaline rocks of the Ukrainian Shield. Naukova Dumka Publishing, Kiev, 408 pp. (in Russian).
18. **Krivdik S.G. and Tkachuk V.I.** (1998) Geochemical and petrological features of alkaline rocks of the Oktyabrsky massif, Ukraine. // *Geokhimiya*, 36, 362-371 (in Russian).
19. **Lowell R. and Ahl M.** (2000) Chemistry of dark zinnwaldite from Bom Futuro tin mine, Rondônia, Brazil. // *Mineralogical Magazine*, 64, 699-709.
20. **Melcher F.** (1995) Genesis of chemical sediments in Birimian greenstone belts: evidence from gondites and related manganese-bearing rocks from northern Ghana. // *Mineralogical Magazine*, 59, 229-251.
21. **Morozewicz J.** (1930) Der Mariupolit und seine Blutsverwandten. *Mineralogische und Petrographische Mitteilungen*. // *Neue Folge*, 40 (5-6), 335-436.

22. **Pekov I.V.** (2005) Genetic Mineralogy and Crystal Chemistry of Rare Elements in High-Alkaline Postmagmatic Systems. D.Sc. thesis, Moscow State University, Russia, 652 pp. (in Russian).
23. **Pekov I.V., Chukanov N.V., Ferraris G., Ivaldi G., Pushcharovsky D.Yu. and Zadov A.E.** (2003) Shirokshinite, $K(NaMg_2)Si_4O_{10}F_2$, a new mica with octahedral Na from Khibiny massif, Kola Peninsula: descriptive data and structural disorder. // *European Journal of Mineralogy*, 15, 447–454.
24. **Perrotta A.J. and Garland T.J.** (1975) Low temperature synthesis of zinc-phlogopite. // *American Mineralogist*, 60, 152-154.
25. **Piilonen P.C, Pekov I.V, Back M., Steede T. and Gault R.A.** (2006) Crystal-structure refinement of a Zn-rich kupletskite from Mont Saint-Hilaire, Québec, with contributions to the geochemistry of zinc in peralkaline environments. // *Mineralogical Magazine*, 70, 565-578.
26. **Portnyagin M.V., Simakin S.G. and Sobolev A.V.** (2002) Fluorine in primitive magmas of the Troodos ophiolite complex, Cyprus: technique of analysis and main results. // *Geochemistry International*, 40, 625-632.
27. **Rieder M., Cavazzini G., D'yakonov Yu.S., Frank-Kamenetskii V.A., Gottardi G., Guggenheim S., Koval' P.V., Müller G., Neiva A.M.R., Radoslovich E.W., Robert J.-L., Sassi F.P., Takeda H., Weiss Z. and Wones D.R.** (1998) Nomenclature of the micas. // *The Canadian Mineralogist*, 36, 905-912.
28. **Robert J.-L. and Maury R.C.** (1979) Natural occurrence of a (Fe,Mg,Mn) tetrasilicic potassium mica. *Contributions to Mineralogy and Petrology*, 68, 117-123.
29. **Robert J.-L. and Gaspérin M.** (1985) Crystal structure refinement of hendricksite, a Zn- and Mn-rich trioctahedral potassium mica: a contribution to the crystal chemistry of zinc-bearing minerals. // *Tschermaks Mineralogische und Petrographische Mitteilungen*, 34, 1-14.
30. **Shannon R.D.** (1976) Revised effective ionic radii and systematic studies of interatomic distances in halides and chalcogenides. *Acta Crystallography*, A32, 751-767.
31. **Sharygin V.V., Krivdik S.G., Pospelova L.N. and Dubina A.V.** (2009) Zn-kupletskite and hendricksite in the agpaitic phonolites of the Oktyabrskii massif, Azov region, Ukraine. *Doklady Earth Sciences*, 425A, 499-504.
32. **Sobachenko V.N., Matveyeva L.N. and Khaltuyeva V.K.** (1989) The evolution of mica composition in granitization and near-fracture metasomatic processes in Precambrian trough structures. // *Geologiya i Geofizika*, 30 (12), 73-81 (in Russian).
33. **Tischendorf G., Förster H.-J. and Gottesmann B.** (2001) Minor- and trace-element composition of trioctahedral micas: a review. // *Mineralogical Magazine*, 65, 249-276.
34. **Tischendorf G., Förster H.-J., Gottesmann B. and Rieder M.** (2007) True and brittle micas: composition and solid-solution series. // *Mineralogical Magazine*, 71, 285-320.
35. **Tracy R.J.** (1991) Ba-rich micas from the Franklin Marble, Lime Crest and Sterling Hill, New Jersey. // *American Mineralogist*, 76, 1683-1693.
36. **Yoshii M., Togashi Y. and Maeda K.** (1973) On the intensity changes of basal reflections with relation to barium content in manganoan phlogopites and kinoshitalite. // *Bulletin of the Geological Survey of Japan*, 24, 543-550.

